

THESIS

THE EFFECT OF TOW SHEARING ON REINFORCEMENT POSITIONAL FIDELITY IN
THE MANUFACTURE OF A CONTINUOUS FIBER REINFORCED THERMOPLASTIC
MATRIX COMPOSITE VIA PULTRUSION-LIKE PROCESSING OF COMMINGLED
FEEDSTOCK

Submitted by

Kent M. Warlick

Department of Mechanical Engineering

In partial fulfillment of the requirements

For the Degree of Master of Science

Colorado State University

Fort Collins, Colorado

Summer 2017

Master's Committee:

Advisor: Donald W. Radford

Troy Holland
Paul Heyliger

Copyright by Kent M. Warlick 2017

All Rights Reserved

ABSTRACT

THE EFFECT OF TOW SHEARING ON REINFORCEMENT POSITIONAL FIDELITY IN THE MANUFACTURE OF A CONTINUOUS FIBER REINFORCED THERMOPLASTIC MATRIX COMPOSITE VIA PULTRUSION-LIKE PROCESSING OF COMMINGLED FEEDSTOCK

While the addition of short fiber to 3D printed articles has increased structural performance, ultimate gains will only be realized through the introduction of continuous reinforcement placed along pre-planned load paths. Most additive manufacturing research focusing on the addition of continuous reinforcement has revolved around utilization of a prefabricated composite filament or a fiber and matrix mixed within a hot end prior to deposition on a printing surface such that conventional extrusion based FDM can be applied. Although stronger 3D printed parts can be made in this manner, high quality homogenous composites are not possible due to fiber dominated regions, matrix dominated regions, and voids present between adjacent filaments. Conventional composite manufacturing processes are much better at creating homogeneous composites; however, the layer by layer approach in which they are made is inhibiting the alignment of reinforcement with loads. Automated Fiber Placement techniques utilize in plane bending deformation of the tow to facilitate tow steering. Due to buckling fibers on the inner radius of curves, manufacturers recommend a minimum curvature for path placement with this technique. A method called continuous tow shearing has shown promise to enable the placement of tows in complex patterns without tow buckling, spreading, and separation inherent in conventional forms of automated reinforcement positioning. The

current work employs fused deposition modeling hardware and the continuous tow shearing technique to manufacture high quality fiber reinforced composites with high positional fidelity, varying continuous reinforcement orientations within a layer, and plastic elements incorporated enabling the ultimate gains in structural performance possible.

A mechanical system combining concepts of additive manufacturing with fiber placement via filament winding was developed. Paths with and without tension inherent in filament winding were analyzed through microscopy in order to examine best and worst case scenarios. High quality fiber reinforced composite materials, in terms of low void content, high fiber volume fractions and homogeneity in microstructure, were manufactured in both of these scenarios. In order to improve fidelity and quality in fiber path transition regions, a forced air cooling manifold was designed, printed, and implemented into the current system. To better understand the composite performance that results from varying pertinent manufacturing parameters, the effect of feed rate, hot end temperature, forced air cooling, and deposition surface (polypropylene and previously deposited glass polypropylene commingled tow) on interply performance, microstructure, and positional fidelity were analyzed. Interply performance, in terms of average maximum load and average peel strength, was quantified through a t-peel test of the bonding quality between two surfaces. With use of forced air cooling, minor decreases in average peel strength were present due to a reduction in tow deposition temperature which was found to be the variable most indicative of performance. Average maximum load was comparable between the forced air cooled and non-air cooled samples. Microstructure was evaluated through characterization of composite area, void content, and flash percentage. Low void contents mostly between five to seven percent were attained. Further reduction of this void content to two percent is possible through higher processing temperatures;

however, reduced composite area, low average peel strength performance, and the presence of smoke during manufacturing implied thermal degradation of the polypropylene matrix occurred in these samples with higher processing temperatures. Positional fidelity was measured through calculations of shear angle, shift width, and error of a predefined path. While positional fidelity variation was low with a polypropylene deposition surface, forced air cooling is necessary to achieve fidelity on top of an already deposited tow surface as evident by the fifty-six percent reduction in error tolerance profile achieved. Lastly, proof of concept articles with unique fiber paths and neat plastic elements incorporated were produced to demonstrate fiber placement along pre-planned load paths and the ability to achieve greater structural efficiency through the use of less material.

The results show that high positional fidelity and high quality composites can be produced through the use of the tow shearing technique implemented in the developed mechanical system. The implementation of forced air cooling was critical in achieving fidelity and quality in transition regions. Alignment of continuous reinforcement with pre-planned load paths was demonstrated in the proof of concept article with varying fiber orientations within a layer. Combining fused deposition modeling of plastic with the placement of continuous reinforcement enabled a honeycomb composite to be produced with higher specific properties than traditional composites. Thus, the current system demonstrated a greater capability of achieving ultimate gains in structural performance than previously possible.

ACKNOWLEDGEMENTS

This research would have not been possible without the support of a number of individuals. I would first like to thank the Department of Mechanical Engineering at Colorado State University for accepting me into the program to serve as a graduate teaching assistant in the process of acquiring my Master of Science Degree. To my committee members, Dr. Troy Holland and Dr. Paul Heyliger, thank you for challenging me in the classroom and fostering confidence in my abilities as a graduate student. To Dr. Donald Radford, thank you for sharing your knowledge with me of a field I was interested in but knew little about when I started. You forced me to think, learn new skills, and developed me into a more well-rounded engineer. I have accomplished even more than what I envisioned in my advanced degree. I also want to thank my parents, Tim and Nadine Warlick. Without their continual support, I would not have been able to finish this degree. To my family and friends, thank you for constantly encouraging me and reminding me my identity should not be based in my research. Lastly, I want to extend gratitude to my God, a God that has blessed me with the ability to conduct this research and write this thesis. “For from Him and through Him and for Him are all things. To Him be the glory forever.”—Romans 11:36.

TABLE OF CONTENTS

| | |
|---|----|
| ABSTRACT..... | ii |
| ACKNOWLEDGEMENTS | v |
| TABLE OF CONTENTS..... | vi |
| LIST OF FIGURES | ix |
| 1. CHAPTER 1:INTRODUCTION | 1 |
| 1.1 NEED FOR ALIGNING CONTINUOUS FIBER WITH ACTUAL PART LOADS | 1 |
| 1.2 DESIGN FREEDOMS OFFERED THROUGH COMBINING FDM AND CONTINUOUS FIBER PLACEMENT | 3 |
| 1.3 METHODS OF INCORPORATING CONTINUOUS FIBER INTO FDM..... | 6 |
| 1.3.1 Prefabricated Composite Filament Technique..... | 7 |
| 1.3.2 Mixing in the Print Head Technique..... | 8 |
| 1.3.3 Mixing at Point of Contact Technique..... | 13 |
| 1.4 COMPOSITE AUTOMATED FIBER PLACEMENT TECHNIQUES | 14 |
| 1.5 THE FUTURE OF AFP: CONTINUOUS TOW SHEARING..... | 20 |
| 1.6 CURRENT RESEARCH..... | 27 |
| 2. MACHINE DEVELOPMENT | 28 |
| 2.1 REQUIREMENTS FOR FABRICATING A HIGH QUALITY COMPOSITE..... | 28 |
| 2.1.1 Filament Winding 3D Printer Combination System | 29 |
| 3. PRELIMINARY STUDIES..... | 35 |
| 3.1 MATERIALS USED | 35 |
| 3.2 NONGEODESIC TRIAL PRINT..... | 36 |
| 3.3 INITIAL STUDY ASSESSING COMPOSITE QUALITY | 38 |
| 3.3.1 Visual Evaluation Results | 39 |
| 3.3.2 Metallographic Evaluation Results | 41 |
| 3.3.3 Discussion | 44 |
| 3.4 ACTIVE FORCED AIR COOLING | 45 |
| 4. EXPERIMENTAL..... | 49 |
| 4.1 MANUFACTURING OF SAMPLES | 50 |
| 4.2 HEAT TRANSFER ANALYSIS TO ESTIMATE ACTUAL DEPOSITION TEMPERATURE..... | 54 |
| 4.3 POST-PROCESSING FOR POSITIONAL FIDELITY | 58 |
| 4.4 POST-PROCESSING FOR MECHANICAL PERFORMANCE..... | 60 |
| 5. RESULTS | 63 |
| 5.1 TOW POSITIONAL FIDELITY GRAPHS..... | 63 |
| 5.1.1 Shear Angle..... | 66 |
| 5.1.2 Shift Width Graphs | 71 |
| 5.1.3 Error Graphs..... | 76 |

| | |
|---|-----|
| 5.2 COMPOSITE BEAM ANALYSIS..... | 79 |
| 5.2.1 T-Peel Results | 79 |
| 5.2.2 Microstructure Results | 83 |
| 6. DISCUSSION | 86 |
| 6.1 EFFECTS OF TENSION ON TOW SLIDING AND TOW SHIFTING..... | 86 |
| 6.2 EFFECT OF CONSOLIDATION MECHANISMS | 88 |
| 6.3 EFFECT OF FORCED AIR COOLING AND DEPOSITION SURFACE..... | 89 |
| 6.4 POLYPROPYLENE BEHAVIOR AT ELEVATED TEMPERATURES | 91 |
| 6.5 QUALITY OF COMPOSITE BEAMS..... | 93 |
| 6.6 IRREGULARITIES..... | 98 |
| 7. VERIFICATION OF FUTURE POTENTIAL..... | 100 |
| 7.1 VARYING FIBER ORIENTATIONS WITHIN A LAYER..... | 100 |
| 7.2 COMBINING CONVENTIONAL FDM WITH FIBER PLACEMENT..... | 101 |
| 7.3 OUT OF PLANE FIBER PLACEMENT AND FIBER VOLUME FRACTION MODIFICATION | 105 |
| 7.4 BARRIERS TO MAKING DIGITAL COMPOSITES A REALITY..... | 106 |
| 8. CONCLUSIONS..... | 108 |
| 9. REFERENCES | 111 |
| 10. APPENDICES | 115 |
| 10.1 MARLIN FIRMWARE MODIFICATIONS..... | 115 |
| 10.2 TOW POSITIONAL FIDELITY G-CODE | 138 |
| 10.3 MATLAB PROGRAMS FOR PROCESSING | 160 |
| 10.3.1 Tow_edge.m Program:..... | 160 |
| 10.3.2 Get_Results.m Program: | 162 |
| 10.3.3 transform_data.m User Written Function: | 168 |
| 10.4 MICROSTRUCTURE ANALYSIS PHOTOMICROGRAPHS | 170 |
| 10.5 COMPOSITE BEAM SPECIMEN PICTURES..... | 204 |
| 10.6 SHEAR ANGLE GRAPHS..... | 213 |
| 10.7 SHIFT WIDTH GRAPHS | 220 |
| 10.8 ERROR GRAPHS..... | 227 |

LIST OF TABLES

| | |
|--|----|
| Table 1: Tensile and flexural strength results for neat PLA, carbon fiber reinforced PLA, and modified carbon fiber reinforced PLA. [15] | 11 |
| Table 2: A description of the geometric features is shown..... | 26 |
| Table 3: Results of the sample thickness based on optical microscopy are shown. | 43 |
| Table 4: The sample names along with the varying process parameters are shown..... | 53 |
| Table 5: The symbols, values, and units used for the time dependent conduction heat transfer model are shown. | 55 |
| Table 6: Resultant temperatures of the glass fiber at different processing conditions obtained through a time dependent conduction model. | 57 |
| Table 7: Resultant temperatures of the PP filament at different processing conditions obtained through a time dependent conduction model. | 57 |

LIST OF FIGURES

| | |
|---|----|
| Figure 1: Conventional composite manufacturing methods involve stacking laminae with different fiber orientations to create a laminate [3]. | 2 |
| Figure 2: Non-geodesic fiber paths are shown in (a) and (b). Localized buildup of material is also shown in (b). | 2 |
| Figure 3: The tooling (a) required to create a composite cascade basket (b) is one of the barriers to widespread use of composites..... | 3 |
| Figure 4: Varying fiber volume fraction and out of plane fiber placement are additional design freedoms that can be realized through combining FDM with fiber placement techniques. Figure 4(b) from source [2]. | 5 |
| Figure 5: Scaffolding, in the form of cellular structures, can be printed onto a fiber reinforced facesheet as shown in (a). A top fiber reinforced face sheet can be placed on top of the scaffolding to create structures with out fo plane features as shown in (b). | 6 |
| Figure 6: Conventional FDM slicing techniques create an isotropic layer as shown in (a). Internal printed structures could be oriented in the loading direction to create a more anisotropic structure as shown in (b) [2]. | 6 |
| Figure 7: Voids present in a 6 layer carbon fiber composite in (a) and a 2 layer carbon fiber composite fabricated using the Mark One(R) printer [7]. | 7 |
| Figure 8: A schematic of the mixing in the print head method to create continuous fiber reinforced composite filament is shown [12]. | 9 |
| Figure 9: Carbon fiber bundles visible on the inside radii of (a) and (b) demonstrate wetout is not occurring [16]. | 10 |
| Figure 10: The cross section of an ABS carbon fiber composite details the different interfaces present [14]. | 12 |
| Figure 11: The cross-section of a fiber rod shows a hexagonal yarn packing with high fiber volume fraction and low void content [17]. | 13 |
| Figure 12: Fiber steering strategies to maintain desired fiber orientation include (a) parallel path strategy, (b) shifted path strategy and (c) shifted path with tow drops strategy [31]. | 17 |
| Figure 13: The tow drop pattern (a) and tow overlap pattern (b) of tow steered composite panels is shown [34]. | 18 |
| Figure 14: Tow deformation that is occurring using conventional fiber placement techniques [39]. | 20 |
| Figure 15: Ideal dry tow deformation (a) and real dry tow deformation (b) that occurs on a turn with the embroidery process of tailored fiber placement [38]. | 21 |
| Figure 16: A preform made by an embroidery machine demonstrates local buckling of the tow as a result of in plane bending [39]. | 21 |
| Figure 17: The tow arrangement and head rotation for conventional AFP with tow gaps (a), conventional AFP with tow overlaps (b), and CTS (c) [39]. | 22 |
| Figure 18: As a result of shifting of the fibers, a thickness change occurs as shown in (a). A better view of the change in thickness can be seen in (b) [39]. | 22 |
| Figure 19: Unidirectional non crimped fabric steered by a CMTS head [40]. | 24 |
| Figure 20: The reference tow paths and actual tow paths for a constant angle variation is shown [41]. | 25 |

| | |
|---|----|
| Figure 21: Geometric features determined in the study by Kim et al. [41]. | 26 |
| Figure 22: Shift width (a) and Average shear angle (b) graphs were made to characterize manufacturing layup accuracy [41]. | 27 |
| Figure 23: The Pico hot end utilized in controlling the temperature of the commingled tow. | 29 |
| Figure 24: The tailored nozzle with (a) bottom, (b) front and (c) top views used to consolidate the composite. | 31 |
| Figure 25: The developed machine with heated mandrel (u axis), fiber carriage (v, w) and two print head gantries (x, y, z). | 32 |
| Figure 26: The tailstock shown from the (a) front and (b) back without carbon fiber reinforced face sheets demonstrates the ability to hold different diameter mandrels and an internal tubular heater. | 33 |
| Figure 27: The designed mechanical system with all the previously described elements can be seen. | 34 |
| Figure 28: The coded path for a trial print incorporating nongeodesic features. | 36 |
| Figure 29: The actual path for the trial print with nongeodesic features; tow splitting, tow sliding, rounded corners and width variation are shown. | 37 |
| Figure 30: Band width, as shown above, is synonymous with the width of the tow and the center to center distance between adjacent tows. | 38 |
| Figure 31: The experimental part shown was used to evaluate composite quality. The 3 layer part starts and finishes at the point crossing the V axis line. | 39 |
| Figure 32: The hoop and longitudinal transition part as the build progresses: (a) placing the 1st layer; (b) placing the 2nd layer; (c) finishing the 3rd layer; (d) finished parts of 2.75, 2.5, and 2.25 mm. | 40 |
| Figure 33: Photomicrographs of the cross section of (a) 2.25 mm hoop, (b) 2.5 mm hoop, (c) 2.75 mm hoop, (d,e) two views of 2.5 mm longitudinal and (f) 2.75 mm longitudinal samples taken at a magnification of 50X. | 42 |
| Figure 34: High magnification photomicrographs of the 2.5 mm hoop (a) and the 2.5 mm longitudinal (b) samples. | 42 |
| Figure 35: The designed cooling manifold that allows for forced air cooling in all directions. | 46 |
| Figure 36: The forced air cooling manifold at different stages of the printing process; internal cavities can be seen in (a) and (b). | 47 |
| Figure 37: An L bracket produced without AC (a) and with AC (b) demonstrates the effectiveness of the cooling manifold. | 48 |
| Figure 38: The coded path including the tow fidelity portion of the study and the samples for quantifying mechanical performance are shown. | 49 |
| Figure 39: The placement of the 3rd glass PP layer of the specimens used for peel strength and microscopy is shown. | 51 |
| Figure 40: Placement of the first deposition layer is shown in (a) while the large amount of tow sliding present in a sample without AC can be seen in (b). | 52 |
| Figure 41: Unprocessed commingled tow with large PP filaments and small glass fibers is shown. | 54 |
| Figure 42: Temperatures of the constituents as it leaves the nozzle as a function of hot end temperature. | 57 |
| Figure 43: The manifold forces air in the direction of the arrows at the deposited tow in order to allow for rapid solidification. | 58 |

| | |
|--|----|
| Figure 44: The process from a scanned image to an image with just the fiber paths is shown for a PP deposition surface (Sample 2) (a) and a glass fiber PP deposition surface (Sample 19) (b)... | 60 |
| Figure 45: Instron mechanical testing machine setup for a t-peel specimen. | 61 |
| Figure 46: Adobe Photoshop was used to select and quantify the area of the composite (a), flash (b), intraply voids (c), and interply voids (d)..... | 62 |
| Figure 47: The tow edges (solid lines) and programmed tow path (dotted lines) for Sample 33 are shown. | 63 |
| Figure 48: The tow edges (solid lines) and programmed tow path (dotted lines) for Sample 34 are shown. | 64 |
| Figure 49: The shift-width for Sample 33 (a) and Sample 34 (b) as it progresses along the mandrel axis. | 65 |
| Figure 50: The shear angle for Sample 33 (a) and Sample 34 (b) as it progresses along the mandrel axis. | 66 |
| Figure 51: The shear angle as the path progresses along the mandrel axis for samples with no air cooling and a PP deposition surface. | 67 |
| Figure 52: The shear angle as the path progresses along the mandrel axis for samples with air cooling and a PP deposition surface. | 67 |
| Figure 53: The shear angle as the path progresses along the mandrel axis for samples on a PP/GF deposition surface with a feedrate of 400 mm/min (a) and 200 mm/min (b). | 69 |
| Figure 54: The shear angle as the path progresses along the mandrel axis for samples on a PP/GF deposition surface with a hot end set temperature of 400°C (a) and 300°C (b). | 70 |
| Figure 55: The shear angle as the path progresses along the mandrel axis for samples on a PP/GF deposition surface with a feed rate of 400 mm/min..... | 71 |
| Figure 56: The shift width as the path progresses along the mandrel axis for samples on a PP deposition surface without AC (a) and with AC (b). | 72 |
| Figure 57: The shift width as the path progresses along the mandrel axis for samples on a PP/GF deposition surface without AC (a) and with AC (b). | 73 |
| Figure 58: The shift width as the path progresses along the mandrel axis for samples on a PP/GF deposition surface with a hot end set temperature of 400°C (a), 350°C (b) and 300°C (c)..... | 74 |
| Figure 59: The tow width as the path progresses along the mandrel axis for samples on a PP/GF deposition surface without AC (a) and with AC (b). | 75 |
| Figure 60: Error as the path progresses along the mandrel axis for samples on a PP deposition surface without AC (a) and with AC (b)..... | 76 |
| Figure 61: Error as the path progresses along the mandrel axis for samples on a PP/GF deposition surface without AC (a) and with AC (b)..... | 78 |
| Figure 62: The manufactured specimens shown were classified based on their appearance as discreet (a), non-discreet (b) and in between (c)..... | 79 |
| Figure 63: T-peel samples were tested in accordance with ASTM D1876-08. Failure was classified as adhesive (a) or adherend (b) failure..... | 80 |
| Figure 64: Fiber pullout was evident in most of the adherend surfaces after peeling occurred. .. | 81 |
| Figure 65: The load separation chart for all five of the beams tested for Sample 4. | 81 |
| Figure 66: The average maximum load and average peel strength for each sample set are shown. | 82 |
| Figure 67: The average area for each of the samples analyzed was determined through microscopy. | 83 |
| Figure 68: An average width (a) and thickness (b) were calculated via microscopy. | 84 |

| | |
|---|-----|
| Figure 69: Average flash percentage was determined from each sample through microscopy.... | 85 |
| Figure 70: Average void percentage was determined from each sample through microscopy. ... | 85 |
| Figure 71: Tension inherent to filament winding and to head movement affect the transition from longitudinal to constant shear angle (a) differently than the transition from constant shear angle to longitudinal (b). | 88 |
| Figure 72: Consolidation of a longitudinal path (a) occurs fully by the nozzle while consolidation of a 70 degree path (b) occurs mostly by tension inherent to filament winding..... | 89 |
| Figure 73: The melt viscosity as a function of temperature for polypropylene and other plastics is shown [46]. | 92 |
| Figure 74: The thermal decomposition of PP in nitrogen and air is shown in the above TGA curves. A heating rate of 9.1 and 8.2 K/min was used for nitrogen and air [47]...... | 93 |
| Figure 75: The composite cross section for Sample 6 Section 1. | 95 |
| Figure 76: The cross section of Sample 14 section 1..... | 96 |
| Figure 77: The cross section for Sample 17 section 2A. | 98 |
| Figure 78: Outside and inside layer views of the fiber paths for a composite with a built in hole. | 100 |
| Figure 79: Honeycomb composites can be produced through combining conventional FDM with fiber placement. Printing of the plastic honeycomb on top of the base layer is shown in (a), while the placement of continuous reinforcement on top of the honeycomb is shown in (b). ... | 102 |
| Figure 80: The de-tooled honeycomb composite with edge closeouts and a minimal amount of flash..... | 103 |
| Figure 81: The manufacturing of the base layer (a), honeycomb core (b) and top face sheet (c) for a composite tube with longitudinal reinforcement is shown. | 104 |

1. CHAPTER 1:INTRODUCTION

1.1 Need for Aligning Continuous Fiber with Actual Part Loads

Limitations in mechanical and physical properties of 3D printed neat thermoplastics have led to the initiation of research into the addition of fibrous reinforcements. Tekinalp *et.al.*, used a fused deposition modeling (FDM) based technique to create chopped carbon fiber-ABS resin dog bone samples with a fiber volume fraction of 30%, resulting in specific tensile strength values higher than aluminum [1]. The approach applied used short fiber reinforcement which limited property gains and resulted in nozzle clogging at higher fiber volume fractions. Only through the introduction of continuous fiber reinforcement and placement of the reinforcement along pre-planned load paths will the ultimate gains be realized as mechanical properties such as stiffness and strength significantly decrease when the reinforcement deviates from the loading direction.

Current composite manufacturing methods, as well as 3D printing methods, involve stacking layers to build a component. In addition, continuous reinforcement within laminae is often oriented completely in one direction as shown in Figure 1. Although the direction of reinforcement is better aligned with pre-planned load paths, rarely do uniform stress states exist in a part. Loads often travel out of plane or through the thickness of a component. Mechanical properties out of plane are significantly reduced in comparison with in-plane properties because of the current fabrication method [2]. This global positioning technique is restricting local or regional variation in reinforcement orientation. Ultimate gains cannot be achieved here as well.

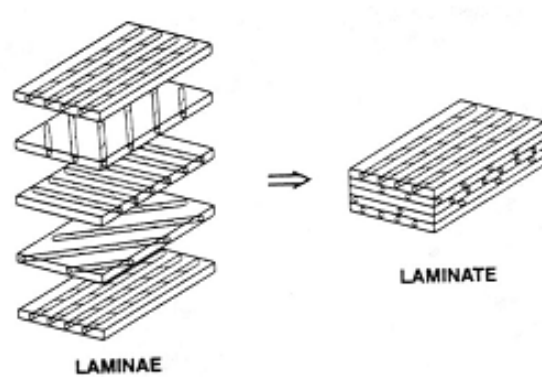


Figure 1: Conventional composite manufacturing methods involve stacking laminae with different fiber orientations to create a laminate [3].

Varying fiber direction within a layer would enable better alignment of fibers with actual load paths. Consider a part with a hole as shown in Figure 2 (a). Post-process drilling results in cut fibers and reduced efficiency in the localized area around the hole. The ability to place reinforcement around the holes would more efficiently distribute the loads going through the hole to the rest of the part. This is an example of a non-geodesic fiber path. A geodesic path is the shortest distance between two points on a surface. Figure 2 (b) shows both a geodesic path and a non-geodesic path. The non-geodesic fiber path starts as a $+45^\circ$ wind, transitions to a -45° wind, transitions again to a 0° wind, and then goes back on itself. Unfortunately, traditional fiber placement processes are not capable of producing paths in a non-geodesic manner like this one.



Figure 2: Non-geodesic fiber paths are shown in (a) and (b). Localized buildup of material is also shown in (b).

Non-geodesic fiber paths can be created through combining FDM with conventional composite fiber placement techniques. FDM is a process in which plastic filament in a molten form is extruded through a nozzle and hardens immediately to produce objects layer by layer. This local melting and solidification of a thermoplastic allows for any two dimensional path to be created. If this principle is extended to the deposition of continuous reinforcement, non-geodesic fiber paths that can follow complex load paths within a structure can be produced. The current work focuses on combining fused deposition modeling and continuous fiber placement.

1.2 Design Freedoms Offered Through Combining FDM and Continuous Fiber Placement

One of the main barriers to widespread use of composite materials is the tooling requirements. Figure 3 (a) depicts the tooling required to create a cascade basket shown in Figure 3 (b). Another barrier is the initial capital investment in the equipment (autoclaves, ovens, and automated fiber placement machines) to make composites. Combining fused deposition modeling and continuous fiber placement results in a method to create Digital Composites (DC). DC do not require tooling or capital investment in equipment due to the Direct Digital Manufacturing approach used.



Figure 3: The tooling (a) required to create a composite cascade basket (b) is one of the barriers to widespread use of composites.

“Direct Digital Manufacturing (DDM) is the ability to manufacture parts directly from a computer-aided design (CAD) file” [4]. Typically additive fabrication technologies are used to

manufacture end use parts, although some types of subtractive manufacturing can be used in this process [5] [4]. Constraints imposed by traditional manufacturing processes are eliminated by DDM; this means design for manufacturability and design for assembly rules no longer apply. Unlimited complexity can be implemented enabling parts to be designed for the best performance; in addition, part consolidation can take place [6].

With DDM, production can begin immediately after the design is completed [5] [6]. The time to market is significantly reduced as tooling is eliminated. Redesign can be done at any time in the product life cycle to better meet the needs of the product, company, and consumer. There is no penalty in terms of additional manufacturing expenses or delays in production for redesign. For all of these reasons, DDM has been labeled as the next industrial revolution.

Many other design freedoms can be realized through incorporating FDM and fiber placement. As shown in Figure 2 (b), local fiber reinforced regions of increased thickness can be integrated into designs. From a joining standpoint, this material addition can be useful for fit up regions. Structural benefits can be integrated as well through the use of rib stiffeners on the exterior surface.

Conventional composite techniques require a uniform fiber volume fraction within a part. Combining fiber placement and FDM can allow for local adjustment of fiber volume fraction. The amount of matrix material can be varied simply by adjusting the rate plastic is being extruded. This design freedom enables more efficient usage of the more expensive material: the continuous fiber. Figure 4 (a) depicts this local variation in fiber volume. As the distance from the mandrel increases, the fiber volume fraction decreases.

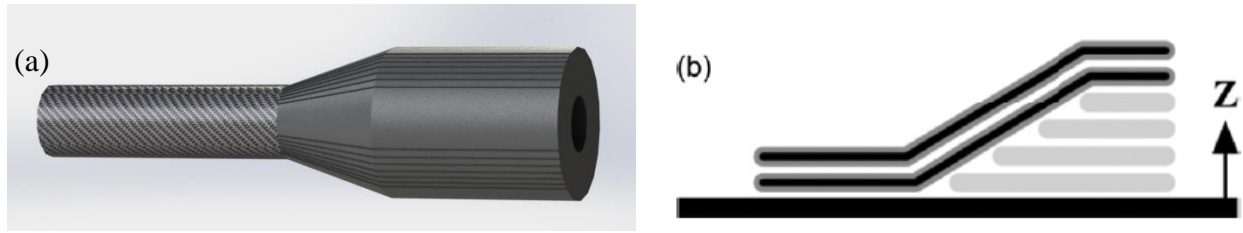


Figure 4: Varying fiber volume fraction and out of plane fiber placement are additional design freedoms that can be realized through combining FDM with fiber placement techniques. Figure 4(b) from source [2].

Another design freedom that can be achieved is the ability to adjust the fiber path out of the plane of the majority of the reinforcement. As previously mentioned, mechanical properties through the thickness of a composite are significantly reduced due to the layer by layer method in which they are fabricated. In components where loading through the thickness is a concern, the addition of fiber reinforcement through the thickness would be extremely beneficial.

Multiple methods can be utilized to orient fiber out of plane. Continuous reinforcement can be placed on top of already deposited layers as shown in Figure 4 (b). Plastic tooling could be printed through FDM and used as a deposition surface. As shown in Figure 5, the deposition surface does not have to be solid. With FDM, only narrow gaps can be bridged as the molten plastic will elongate and sag [2]. Through embedding continuous reinforcement, larger gaps may be bridged as the fibers will be kept in tension. This capability implies that lower density cellular (sandwich) structures with reduced supports can be manufactured. HIPS or other dissolvable filament can be used in this non-solid scaffolding approach and then easily dissolved post-fabrication. As shown in Figure 6 (a), standard FDM slicing methods simply try and achieve quasi-isotropic mechanical properties within the layer. With this process, cellular structure infill can be printed with patterns tailored to better align with pre-planned loads as shown in Figure 6(b). If a geodesic path in or out of plane is desired, tooling may not be needed at all. The first layer would have increased thickness due to lack of consolidation. Gaps will be

present. However, the pressure from applying subsequent layers will help consolidate that first layer and possibly eliminate the gaps that exist. Scaffolding might only be needed at locations where changes in fiber direction are desired.

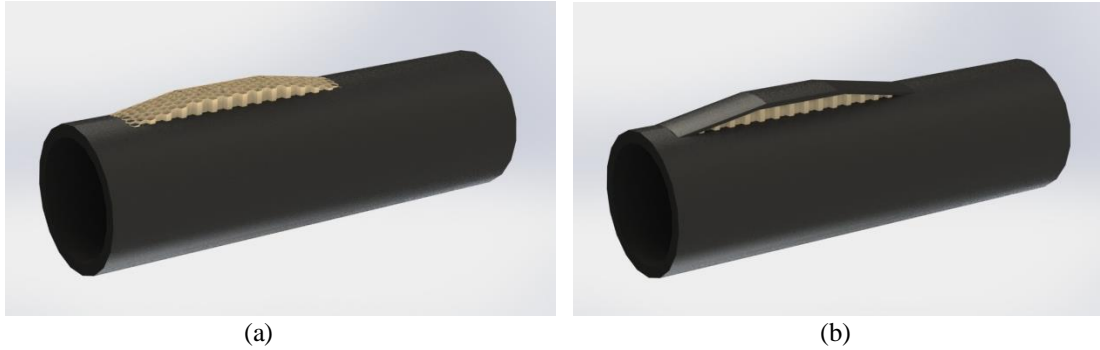


Figure 5: Scaffolding, in the form of cellular structures, can be printed onto a fiber reinforced facesheet as shown in (a). A top fiber reinforced face sheet can be placed on top of the scaffolding to create structures with out fo plane features as shown in (b).

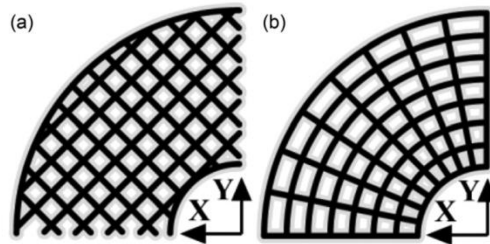


Figure 6: Conventional FDM slicing techniques create an isotropic layer as shown in (a). Internal printed structures could be oriented in the loading direction to create a more anisotropic structure as shown in (b) [2].

1.3 Methods of Incorporating Continuous Fiber into FDM

With all the potential benefits offered through incorporating continuous fiber into FDM, research in this area has increased. Three different techniques of achieving continuous fiber reinforced composites have been defined [2]. Each technique differentiates itself by the instant in which the fiber is wet out.

1.3.1 Prefabricated Composite Filament Technique

The first technique, embedding before the printing process, consists of using continuous reinforcement already in filament form to fabricate a finished component. The fiber is already wet out; it is simply heated up and extruded onto a deposition platform. The greatest advantage to this method is that no major changes are required to the 3D printer. As a result, a printer that can place continuous reinforced filament in plane is already commercially available: the Mark One [7].

The Mark One is capable of producing a composite with 34.5% fiber volume fraction but, unfortunately, with the void fraction increasing as the number of fiber reinforced thermoplastic layers increases [7] [8]. The 34.5% fiber volume fraction is deceptive in that it doesn't include excess matrix material that was grinded off. A completely composite part is never fabricated; the entire surface of the part is printed plastic as it enables dimensional accuracy within +/- 0.1 mm [7] [9]. Voids, some of which are very large, are present in composites produced by the Mark One. A 6 layer carbon fiber composite and a 2 layer carbon fiber composite with voids are shown in Figure 7 [7] [8]. Better properties, in terms of fewer voids, were achieved by alternating continuous reinforced filament layers and nylon layers.

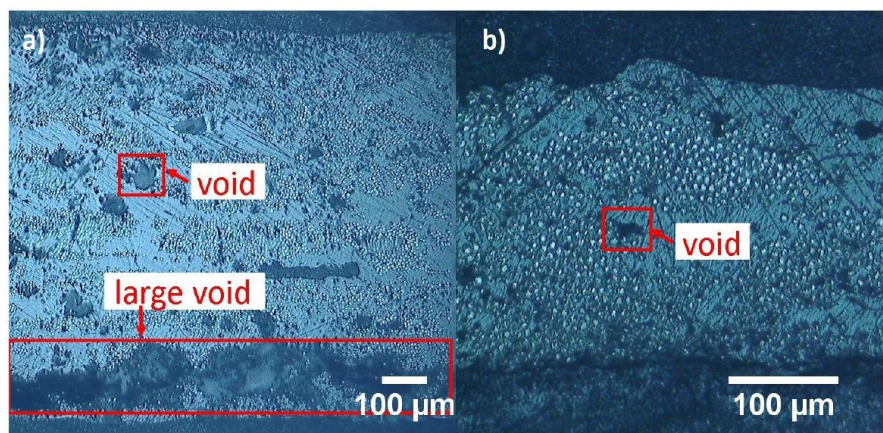


Figure 7: Voids present in a 6 layer carbon fiber composite in (a) and a 2 layer carbon fiber composite fabricated using the Mark One(R) printer [7].

The starting point for the continuous reinforcement creates a region of discontinuity that acts as a stress concentrator [7] [8] [9]. During tensile testing of dog bone samples produced with the Mark One, the failure location always occurred within that discontinuity area [9]. A separate study post-processed samples through a cutting and grinding operation to produce tensile specimens with and without these discontinuities [8]. Discontinuities reduced the tensile strength by roughly 30%.

There are some additional disadvantages associated with using a prefabricated composite filament. The feedstock filament used must have correct composition, strength, and a low enough processing viscosity to be extruded [10]. If the viscosity doesn't drop enough during processing, filament placed on turns will result in the continuous reinforcement bending in plane creating residual stress. Additionally, this prefabricated filament results in a constant fiber volume fraction [2]. Lastly, cost increases associated with using the proprietary processed filament form and not its simplest form are encountered.

1.3.2 Mixing in the Print Head Technique

The second technique, mixing in the print head, promises advantages based on the use of the lowest cost form of the microconstituents [2]. This method consists of dry fibers and a thermoplastic matrix combined inside a printhead with the wetting, extrusion and deposition processes occurring in sequence as shown in Figure 8. Like conventional FDM, a drive gear feeds solid plastic into the hot end which in turn pushes molten plastic further along in the heated zone until it is extruded out of the nozzle. The pressure from this extrusion process is enough to impregnate the continuous fiber which is fed into the system before or in the middle of the heated zone. Fiber preheating to reduce the difference in temperature between the constituents prior to their interaction resulted in better impregnation in one study [11]. A major advantage of

this technique is that the ability to change the fiber volume fraction through machine control does exist [2].

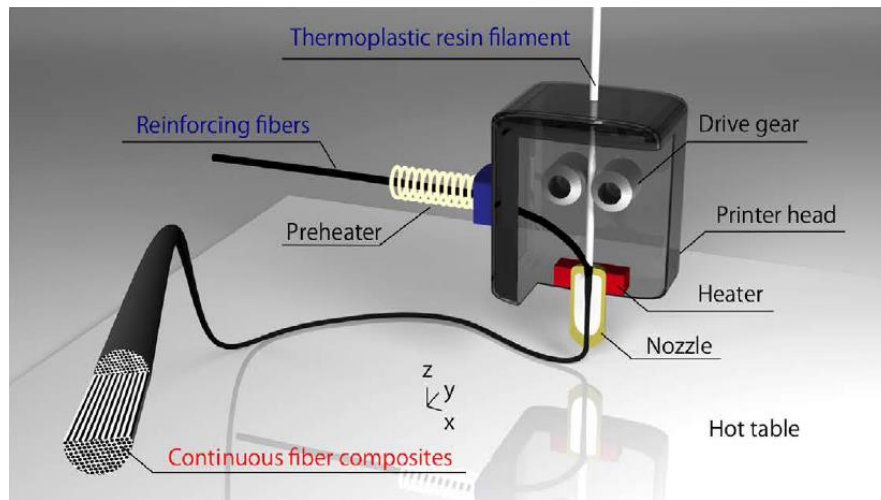


Figure 8: A schematic of the mixing in the print head method to create continuous fiber reinforced composite filament is shown [12].

Many studies have used the mixing in the print head technique to compare mechanical properties between fiber reinforced samples and neat plastic samples [12] [13] [14] [15] [11]. One study, with a fiber volume fraction of just 6.6%, reported tensile modulus and strength increases of 599% and 435% that of neat polylactic acid (PLA) [12]. Even greater property gains can be expected with higher fiber volume fractions. However, mostly low fiber volume fractions of less than 10% have been produced to-date [13] [11] [12] [14]. Fiber breaking and clogging in nozzles is preventing increasing fiber volume fractions using this method [13] [11] [12]. The large hole size necessary to prevent these issues from occurring reduces layer resolution. One approach avoided nozzle clogging by using tougher aramid fibers instead of glass or carbon [13]. On paths with sharp corners, difficulties with peeling prior to the solidification of the PLA matrix were encountered in this study.

Two studies demonstrated that higher fiber volume fractions than 10% are possible. Tian et al evaluated the influence of process parameters on the flexural strength and flexural modulus of carbon fiber PLA composites [16]. A maximum fiber volume fraction of 27% was achieved with the lowest hatch spacing or spacing between composite filaments. The maximum fiber volume fraction found using the mixing in the print head method was 34% [15]. Skepticism of this value exists as the localized area considered in the micrograph consisted of approximately one total fiber.

The viscous nature of thermoplastics fosters difficulty in achieving wetout. Improper sizing on the carbon fibers exacerbates this difficulty [11]. A weak bonding interface also exists between carbon fiber and PLA [15]. A poor interface can result in fiber dominated regions that are not even encapsulated fully in plastic [11] [16]. This effect is emphasized when curves are being produced as shown in Figure 9.

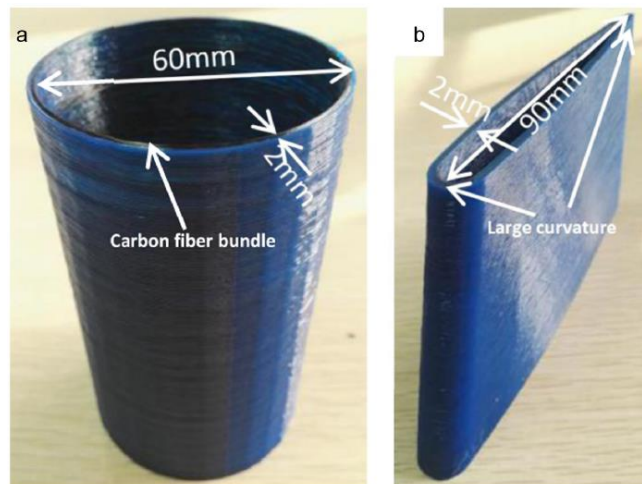


Figure 9: Carbon fiber bundles visible on the inside radii of (a) and (b) demonstrate wetout is not occurring [16].

Li, et al. conducted surface modification of the carbon fibers to improve its interfacial strength [15]. Scanning electron microscopy micrographs confirmed better wetout was achieved

in the modified carbon fibers than the unmodified. Voids were significantly reduced and a better distribution of PLA was evident as well. Tensile testing and flexural testing produced much better strengths as shown in Table 1.

Table 1: Tensile and flexural strength results for neat PLA, carbon fiber reinforced PLA, and modified carbon fiber reinforced PLA. [15]

| | PLA | Carbon Fiber Reinforced PLA | Modified Carbon Fiber Reinforced PLA |
|------------------------|-----|-----------------------------|--------------------------------------|
| Tensile Strength (MPa) | 28 | 80 | 91 |
| Flexure Strength (MPa) | 53 | 59 | 156 |

The major issue with embedding before the printing process, through creation of a composite filament, and embedding during the printing process, within the head, is that a homogeneous composite is not being created. Fiber dominated and matrix dominated areas are present throughout the component as shown in Figure 10. Yang et al. described how this manufacturing process creates interfaces at the meso-scale, micro-scale, and nano-scale [14]. The meso-scale interface is characterized by regularly repeating pores that exist due to the oval shape of the deposited and slightly consolidated fiber reinforced filament. The micro-scale interface is the interface between the continuous fibers and the plastic matrix. The infiltration of the matrix between and around the fibers is difficult; a poor interface often results. Fiber pullout was evident in this study and further confirms this reasoning. The nano-scale interface is defined as the interacting areas of adjacently deposited fiber reinforced filaments. Typically, full coalescence of filaments is not achieved due to the thermoplastics rapid solidification. Therefore, macromolecular chains within the thermoplastic cannot blend together at this interface. The poor interfacial properties exhibited in Yang's composite samples (2.81 MPa) resulted in interlaminar shear strength value of just 12% of that of injected molded neat ABS (2.81MPa). Poor interlaminar bonding as a result of these poor interfaces clearly had an effect.

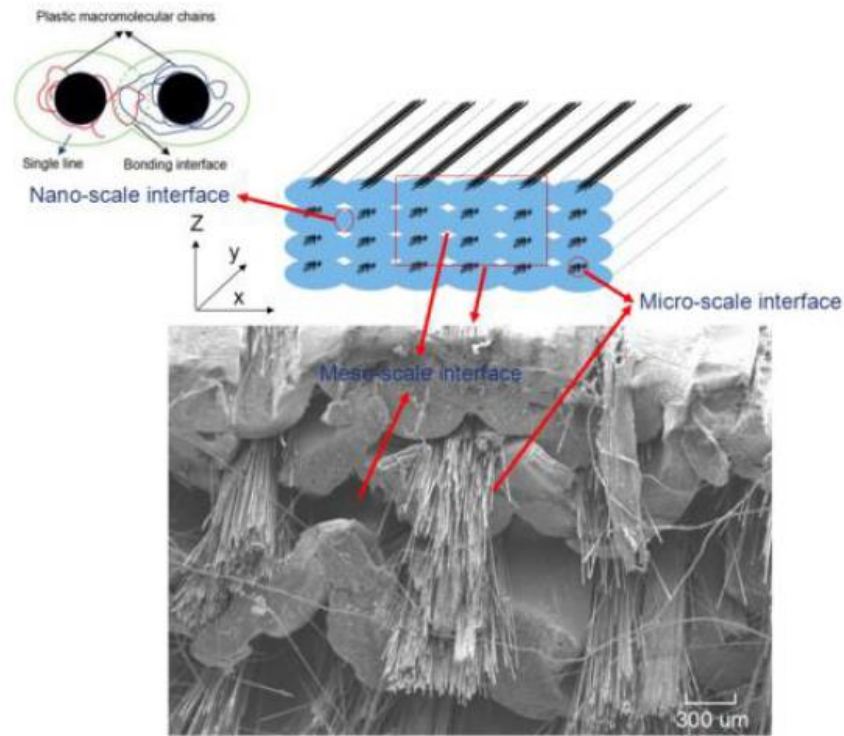


Figure 10: The cross section of an ABS carbon fiber composite details the different interfaces present [14].

Since a homogeneous composite could not be created with the mixing in the print head method, a study by Eichenhofer et al. used this technique to just create rods for lattice trusses [17]. This study had much more success in achieving wetout within the print head. Eichenhofer recognized that the distance the matrix has to travel to fully wetout the fibers is the most important parameter influencing the quality of the composite material [18]. Therefore, he used commingled reinforcement fibers and fibers of the thermoplastic matrix material to minimize this distance [17]. Material of this form is often referred to as commingled tow or hybrid yarn. The fabricated rods, which can be used to continuously manufacture fiber lattice trusses, consist of seven commingled tow yarns that undergo a pultrusion and extrusion process. Although fiber fractions were not determined in this study, the microscopy cross section of the fiber reinforced rod, shown in Figure 11 is significantly higher than previous studies. The areal void content

determined by light microscopy was between 7 and 13% between extrusion speeds of 100 and 200 mm/min. Void content and extrusion speed had a direct relationship. The authors implied that a slower speed allows the fibers to rearrange themselves within the die. This in turn reduces the spring-back force created by fiber waviness when the not yet solidified polymer leaves the die.



Figure 11: The cross-section of a fiber rod shows a hexagonal yarn packing with high fiber volume fraction and low void content [17].

1.3.3 Mixing at Point of Contact Technique

Combining the reinforcement and matrix at the point of contact on the tooling plate is the last and most difficult technique due to deposition through separate mechanisms [2]. There is a higher risk of defects and more machine axes are necessary to position the fiber and matrix using this method. Fiber wetout is occurring on the deposition surface. One study compared filament wound hoops created through embedding dry fiber into polyethylene terephthalate (PET) on a mandrel with the deposition of commingled tow [19]. The dry fiber FDM hot end filament

winding system produced better short beam shear results than that of similarly produced commingled tow samples.

The mixing at the point of contact technique is similar to conventional automated fiber placement (AFP) processes within composites manufacturing [2]. Each of these fiber placement processes has limitations inherent to each of them. To better understand the technology of the described mechanical system, an examination of the automated manufacturing processes that utilize continuous fiber reinforcement must be undertaken.

1.4 Composite Automated Fiber Placement Techniques

In filament winding, continuous fiber is wrapped around a rotating mandrel which defines the internal geometry of the resulting composite. The fiber spools are mounted onto a fiber carriage and an individual tow, or group of tows is attached to the mandrel surface to begin the winding process. Wet winding involves dry fiber traveling through a thermoset resin filled bath prior to contacting the mandrel surface; this method is advantageous as it uses the lowest cost constituent form of both the continuous fiber and the matrix. Prepreg tow winding utilizes thermoset or thermoplastic prepregs. The inherent tack of thermoset prepregs allows for adhesion to the mandrel and previous winding surfaces; thermoplastic prepregs must be heated just prior to contacting the surface to generate tack.

No matter the fiber form, the fiber path in filament winding is typically limited to the geodesic path. Placing pins onto the mandrel surface, around which the fiber can be wrapped, can enable low angle or even longitudinal winding. To avoid cutting fiber in the post processed machining of holes, placing cones onto the mandrel surface will displace the fibers to create a wound-in hole [20]. Since the fibers must remain in tension during this process, concave surfaces can be difficult to produce without some type of compaction method.

A similar process, not reliant on a rotating mandrel, is called automated tape laying or automated tape placement (ATP) as it uses prepreg thermoplastic or thermoset tape instead of the dry fiber form. If thermoset prepreg tape is used, curing is completed in an autoclave. Some thermoplastic tapes, such as APC-2 Carbon fiber reinforced polyether ether ketone (PEEK), are post-processed in an autoclave for void removal, macroscopic resin flow, and polymer infusion through the fiber network [21]. ATP is generally used to automate the manufacture of laminated composites, where all fibers in a given layer have the same orientation. Large equipment costs and part size constraints of the autoclave are limitations of this process [22]. Many recent developments in in-situ consolidation of thermoplastic tapes applied via ATP have made post autoclave processes less necessary [21] [23]. Mechanical properties of in-situ ATP laminates have surpassed 85% of that of ATP laminates autoclaved following placement; strengths have exceeded autoclave processed properties in some compression and open hole tension samples [21] [24].

Fiber paths are limited in automated fiber placement by other factors as well. Maximum steering radius was restricted to greater than 609.6 cm (240 in) in the past [25]. More modern machines have reduced this value significantly with current in situ consolidated tape laying heads capable of a steering radius of 127 cm on a flat plate [24]. This same study also described a filament winding head without a material feeder since the rotating cylindrical mandrel would allow for material deposition. The two separate heads enable in situ deposition and consolidation of plies so that $[0/90/+-\theta]$ cylinders could be fabricated. Results from that study showed compression properties exceeding those possible using thermoset matrix, autoclave processed composites.

Tailored fiber placement, a near net shape preforming technique, possesses additional freedom with fiber path generation. In this process, an embroidery machine is used to stitch a single roving into a base material [26] [27]. If the base material is dry fabric, the preform produced is injected with resin via a resin transfer molding or resin infusion molding operation. This technique was used to manufacture a simple tension-compression strut with a weight of 31grams, which was 47% of a comparable strut made of woven fabric (65 grams) [26]. Compared with AFP or ATL, embroidery machines are lower cost, more versatile, and more suitable for production of small highly loaded parts [27]. Other studies used preimpregnated epoxy woven fabrics as the base layer to achieve excellent results [28] [29]. When a shear loaded panel with 3% by weight hand stitched carbon tows was compared to a baseline panel, the failure load increased by 37%, stiffness by 18% and strain energy by 73% [28]. A robot placed fibers in optimum directions around a hole in another study resulting in a bolted joint composite coupon with an improved peak load of 18% and a bearing strength improvement of 14% with just 1% addition of fiber by weight [29]. Thus, the effect that optimization of fiber direction can have on a component is clear with this manufacturing process.

Filament winding's ability to simultaneously place multiple tows and ATP's cut and restart capabilities have been combined to create automated tow placement machines [30]. Automated tow placement is not confined to near geodesic paths like filament winding and ATP. The seven degrees of freedom in movement and placement of individual tows make fiber steering possible. Fiber steering allows for laminates to be fabricated with continuously varying fiber orientation angles. Fiber orientation determines components mechanical properties. Therefore, composites with varying fiber orientations are termed variable-stiffness composites because of the inherent fluctuations in mechanical performance throughout the component.

In automated tow placement, each tow is dispensed at its own rate allowing it to better conform to a tooling surface [30]. In addition, the width of the deposited fiber band can be increased or decreased through the cutting and restarting of individual tows within the tow placement head. This is necessary because of the difficulties inherent in using fiber steering to align reinforcement with pre-planned loads. Figure 12 depicts these difficulties [31]. Parallel tow bands placed side by side will result in an undesirable increase or decrease in fiber angle. Maintaining this fiber angle with each tow band will result in gaps or overlaps as seen in (b). The size of the tow band influences how much gap or overlap exists. Figure 12(c) shows the effect of starting and dropping tows within a band. The fiber orientation is maintained while the gaps are minimized throughout. Preserving continuous reinforcement through the turn with each tow is no longer possible; however, in situations where overlaps are not allowed this is the best option as gaps are significantly reduced [30]. These gaps form resin-rich regions which are believed to be one of the weaker regions in the composite.

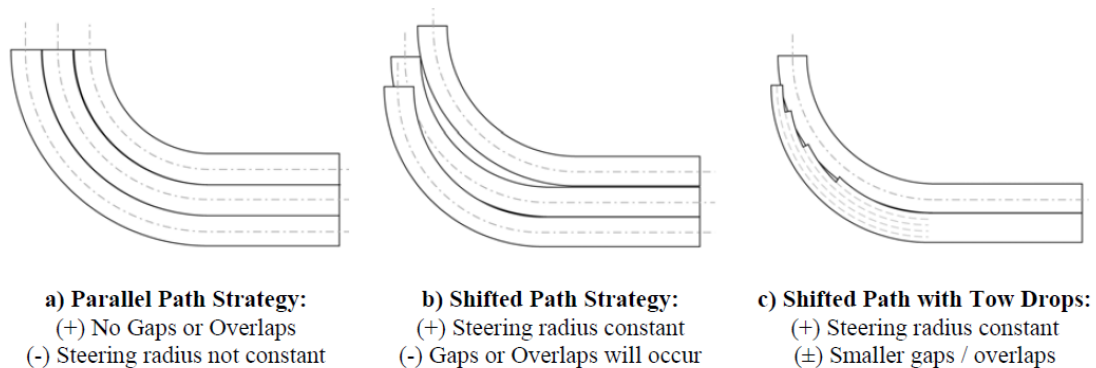


Figure 12: Fiber steering strategies to maintain desired fiber orientation include (a) parallel path strategy, (b) shifted path strategy and (c) shifted path with tow drops strategy [31].

The automated tow placement method can be utilized with dry tows in the creation of a preform [32] or with a carbon epoxy prepreg system [33] [34]. Creating a preform requires injection with resin via a resin infusion molding operation while autoclave curing is typically

required with prepreg systems. With the preform creation method, a processing window consisting of minimum radii for inner and outer contours was defined [32]. Outside this processing window, defects such as wrinkling, fiber shifting, and fiber bridging start to occur.

In order to analyze a highly non-uniform stress state configuration, one study compared panels of straight fibers, tow drop patterns and tow overlap patterns with a central hole subjected to in-plane loading [33] [34]. In the tow drop and tow overlap panels, the tow steering technique was used to curve fibers within the plane of the laminate. This allows the fibers to account for the non-uniform stress state and alter the principle load paths away from the edges of the hole. The tow drops allowed for no overlap in adjacent ply paths; the tow overlaps allowed for thickness increases that served as integrated stiffeners; each of these panels can be seen in Figure 13. Results confirmed tow steering enabled fibers to better carry the load. The tow drop panels supported buckling loads 10% greater than the straight-fiber panels, while the tow overlap panels supported almost double the straight-fiber panels.

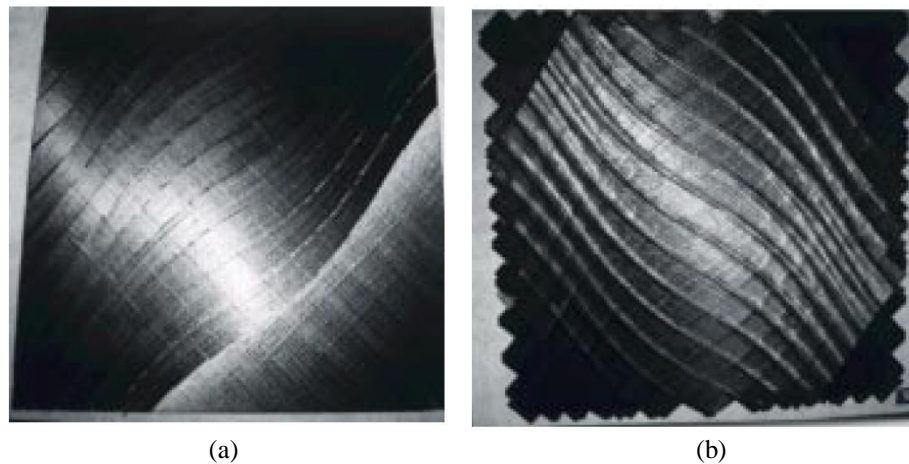


Figure 13: The tow drop pattern (a) and tow overlap pattern (b) of tow steered composite panels is shown [34].

Tow steering also offers additional benefits that are not as obvious. Studies by Wu, *et.al.*, incorporated design, manufacture, and compression testing of a tow steered composite shell

using graphite epoxy prepreg tape material [35] [36] [37]. The chosen pattern uses a variable stiffness concept to allow for improvements in buckling moments and static bending stiffness [36]. Since fiber angles vary continuously around the shell circumference in this design, the neutral axis shifts to the tension loaded-keel. Compression testing of this 18 cm (17 in) diameter shell showed a load shortening response consisting of a linear prebuckling zone, quick nonlinear postbuckling, nonlinear elastic unloading, and then linear elastic unloading [35] [37]. Despite each shell buckling response being accompanied by a single loud noise, a second test and nondestructive testing methods revealed no permanent damage occurred during the original test. A shell with tow overlaps and one with tow drop and add capability to ensure more uniform thickness was compared [35]. After adjusting for weight differences, the overlapping shell has a normalized prebuckling stiffness that is 28% higher and a normalized buckling load that is 78% higher than that of the other shell. These results show significant structural improvements can result through thought out placement of the load bearing fibers within the structure. Cutouts sized to represent a passenger access door on a commercial aircraft were made into this shell and compression testing was redone [37]. Results showed an average stiffness reduction of just 7% and an average global buckling reduction of 14%. If the tow steered design was done with cutouts in mind, even further reductions on structural performance may have resulted.

Although automated tow placement allows for the creation of components not possible via other automated methods which in turn increase mechanical performance, there are still some limitations to this process. The limitation in turning radius that exists within ATP is present in automated tow placement as well [30]. Too small of a radius causes the inner tows to wrinkle out of plane. Another limitation is the existence of a minimum cut length that the machine can properly lay down. This length is the distance from the nipping point on the deposition surface

to the tow cutting mechanism. After the tow is cut and tension is lost, inadvertent tow paths can be produced as a result of the tow transitioning to a geodesic path [38]. Lastly, the previously mentioned tow gaps create processed induced defects in the form of resin rich regions.

1.5 The Future of AFP: Continuous Tow Shearing

The central issue of the previously discussed AFP techniques is that they are trying to use in-plane bending deformation of the tow to achieve a curved path [38]. As shown in Figure 14, bending deformation creates buckling fibers on the inside of a tow and stretched fibers on the outside of the tow. To reduce these defects, manufacturers recommend a minimum curvature for the tow paths. This is not an adequate solution.

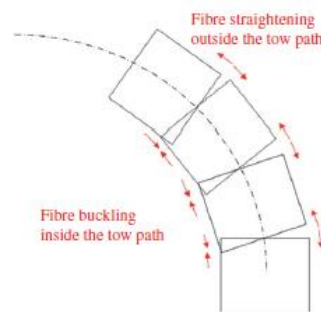


Figure 14: Tow deformation that is occurring using conventional fiber placement techniques [39].

Even the placement of dry tows, through a tailored fiber placement strategy, will experience local buckling as a result of in plane bending. Ideal tow deformation, shown in Figure 15 (a), induces local buckling of the fibers on the inside of the tow. Actual tow deformation, shown in Figure 15 (b), introduces many more defects. The tension in the stitching yarn must not be too high or the backup fabric will wrinkle. As a result, on a turn, the stitching yarns move upward creating space for the deposited tows; the tension induced from the machine head that pulls the tow further exasperates the movement of the tow to the interior edge of the

curve. This in turn increases the buckling intensity of the fibers. This effect is illustrated in an actual preform made by an embroidery machine in Figure 16.

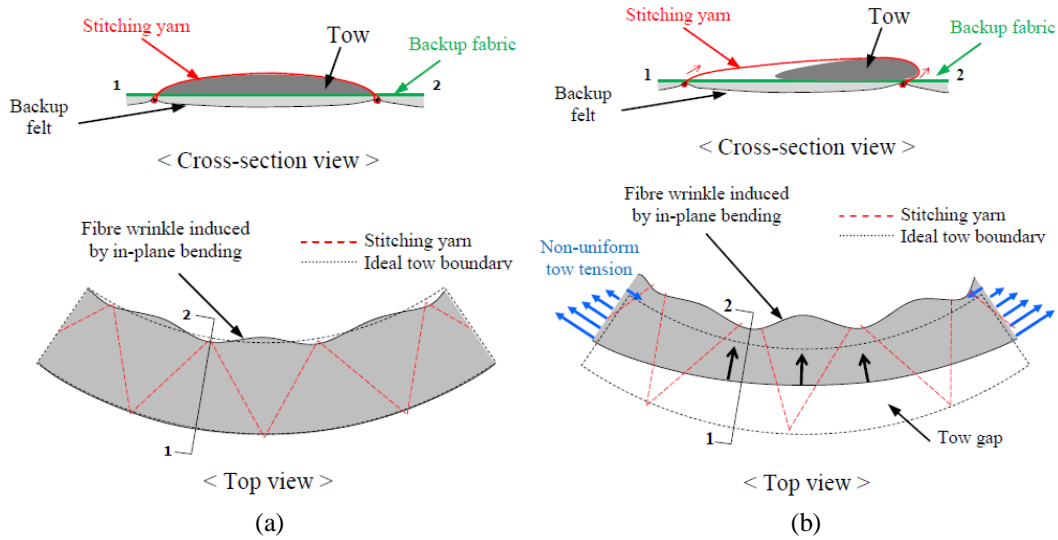


Figure 15: Ideal dry tow deformation (a) and real dry tow deformation (b) that occurs on a turn with the embroidery process of tailored fiber placement [38].

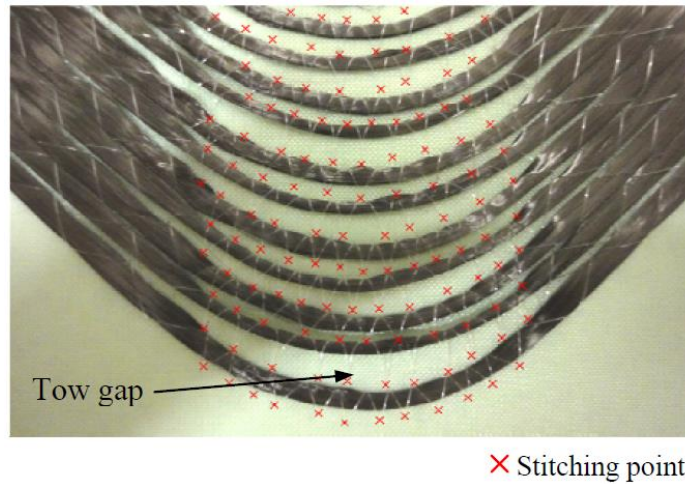


Figure 16: A preform made by an embroidery machine demonstrates local buckling of the tow as a result of in plane bending [39].

Kim et al. developed a novel method of using in-plane shear deformation of the tow instead of bending the tow [39]. This continuous tow shearing (CTS) technique involves fibers within a tow slipping in the shifting direction which further enables the fibers to tessellate to the

substrate surface. Unlike conventional AFP techniques, fibers exactly follow the designed tow path and avoid tow gaps and tow overlaps as shown in Figure 17.

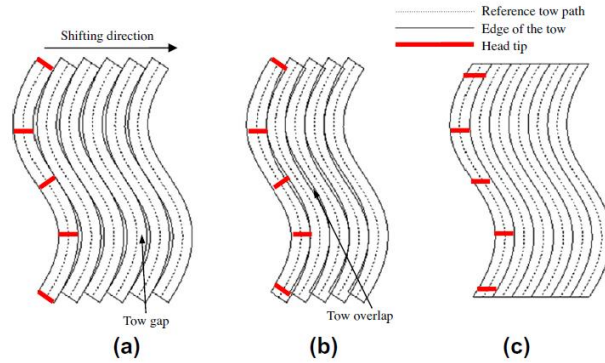


Figure 17: The tow arrangement and head rotation for conventional AFP with tow gaps (a), conventional AFP with tow overlaps (b), and CTS (c) [39].

The shifting of the fibers within a tow does cause volume redistribution [39]. The width of the cross section perpendicular to the fiber direction decreases and the tow thickness increases as shown in Figure 18. The resultant thickness can be calculated using $t = \frac{t_o}{\cos \theta}$ where t_o and θ are the average tow thickness before shearing and the shear angle.

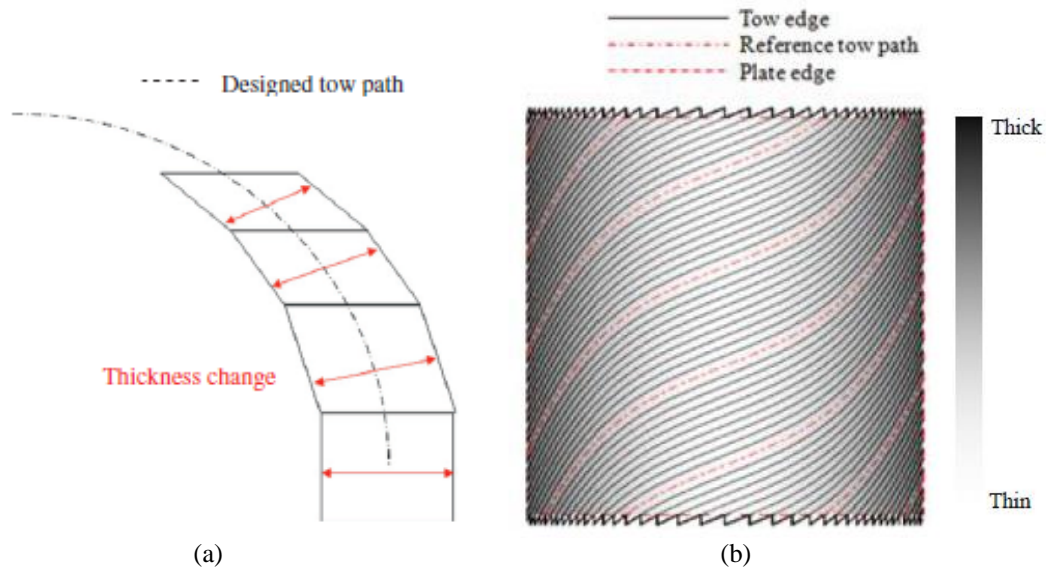


Figure 18: As a result of shifting of the fibers, a thickness change occurs as shown in (a). A better view of the change in thickness can be seen in (b) [39].

To demonstrate the CTS technique, a prototype continuous tow shearing head with a compaction shoe and a gripping shoe was developed [39]. The compaction shoe presses the tow onto a deposition surface while the gripping shoe pinches the other end of the tow so it moves along with the head. A resin and matrix system in which CTS can be utilized is not easily achieved. A dry tow without matrix impregnated can be easily sheared; however, fiber splitting can become a problem. The high viscosity of a prepreg system prevents shearing of tows as well. The head prototype used in this study produces a semi-impregnated tow in situ just before it is laid on the deposition surface. This tow has a dry top tow surface to prevent fiber damage during consolidation. A thermoplastics high viscosity will foster difficulty in shearing the tow as well. Commingled tow has the potential to mitigate this difficulty. Consolidation at the point of contact prevents fiber and matrix interface development until the fibers have already sheared past one another. Depending on the viscosity of the thermoplastic, a fully developed interface would promote bending instead of shearing of the tow.

Other than viscosity, the CTS technique is also influenced by the feedstock format. Thermoplastic prepreg tape or tow possesses a viscosity that drops upon heating allowing it to be easily sheared; however, the rigid region of the tape outside the heated zone constrains the fiber and matrix preventing shearing. Dry commingled tow is not constrained in that manner and can be continuously sheared.

CTS has its limitations. The slow rate in which the in-situ impregnation process occurs can limit the process speed [39]. In order to increase productivity, CTS was extended to create a continuous multi-tow shearing (CMTS) head that did not use the in-situ impregnation process [40]. A unidirectional non-crimp fabric (NCF) was used instead. During compaction, as long as the epoxy resin film impregnates the NCF fabric enough to fix the stitching yarns of the NCF,

the interior fibers can be held in their proper position. This CMTS head had the ability to place 40 bundles of 24K tows at a layup speed of 4 mm/sec. Figure 19 shows two adjacently placed paths placed with the CMTS head.

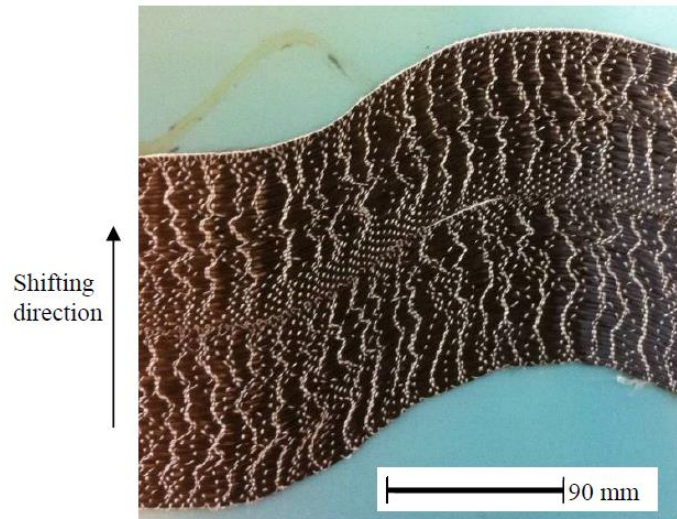


Figure 19: Unidirectional non crimped fabric steered by a CMTS head [40].

Another limitation is that paths are restricted by the maximum shear angle [39]. A shear angle of 90 degrees cannot be attained because the thickness would become infinite. The minimum radius of curvature of the fiber path using CTS was determined to be 30 mm which is significantly less than that of conventional AFP. With CMTS, the maximum shear angle is reduced [40]. The heavily sized NCF tows, which are atypical for dry tows, resulted in a stiffer material that created local fiber buckling and resin pockets when sheared. After breaking the sizing material, a more flexible material resulted that could be used to shear the fabric up to 45 degrees. Thus CMTS is more equipped for higher production with smaller angle variations and slightly lower laminate quality than CTS.

To better characterize the fidelity of CTS, Kim et al. used the CTS method to lay carbon fiber tow onto a white acrylic substrate [41] Paths of constant angle, non-linear angle, and linear

angle variations were analyzed to investigate layup accuracy. The constant angle variation reference path, or coded path, and actual tow path are shown in Figure 20. The reference path starts at a zero shear angle and transitions to a constant shear angle through a 50 mm radius arc. After 100 mm of a constant shear angle, the path transitions through the same radius back to a zero shear angle. The midpoints of the straight sections for each path were aligned at the same horizontal position.

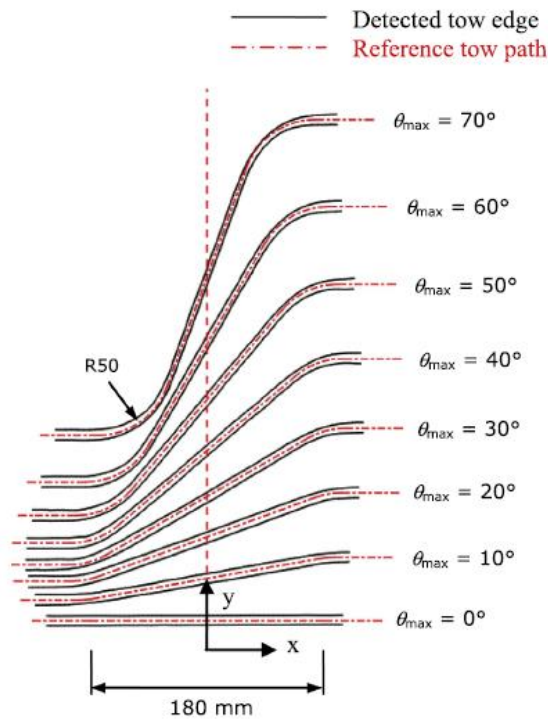


Figure 20: The reference tow paths and actual tow paths for a constant angle variation is shown [41].

Paths were scanned and converted to CAD data in order to calculate a number of different geometric features. These features are shown in Figure 21 with a description of each feature given in Table 2. Maximum path errors were found near the locations with the smallest steering radii. The non-linear angle variation paths had a radius arc as small as 25 mm. Error decreased from 3mm to 0.7 mm as it approached the inflection points in this path. In the

constant angle variation path, maximum error increased from 0 to 0.7 mm as the shear angle increased to 70°.

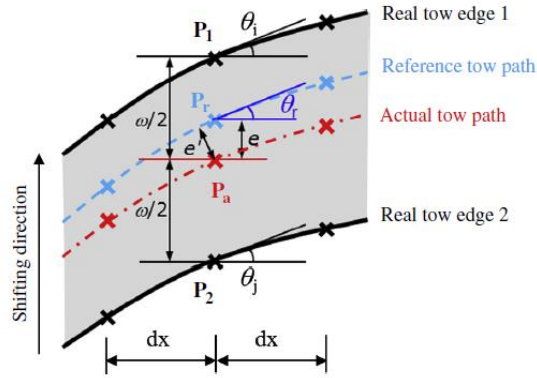


Figure 21: Geometric features determined in the study by Kim et al. [41].

Table 2: A description of the geometric features is shown.

| Symbol | Description |
|----------------------|---|
| dx | Imaginary lines created at every 1mm in the shifting direction |
| P_1, P_2 | Intersection points between the tow edge and these lines |
| P_r | Reference point (coded path point) |
| P_a | Midpoint of P_1, P_2 |
| w | Shift width (distance between P1 and P2) |
| θ_i, θ_j | Tangent angles |
| θ_r | Reference tangent angle |
| θ_{avg} | Tow shear angle |
| e | Positional error that is the distance from P_a to P_r |
| e' | Positional error that is the shortest distance from P_a to the reference tow path |

Characterization of manufacturing layup accuracy was further accomplished through the creation of shift width and average fiber angle charts as shown in Figure 22. In this work, shear angle and average fiber angle are synonymous. Shift width significantly increased above a shear angle of 50°. At high shear angles, fibers cannot easily exchange their transverse and vertical positions within a tow. The compaction shoe is applying pressure on the tow surface and the shearing is increasing the packing of the fibers. This results in in plane tow bending rather than

shearing; slight fiber wrinkles were evident continuously along the straight regions here. The angle error was usually in the range of $\pm 2^\circ$ with a maximum error of 5° near the inflection points.

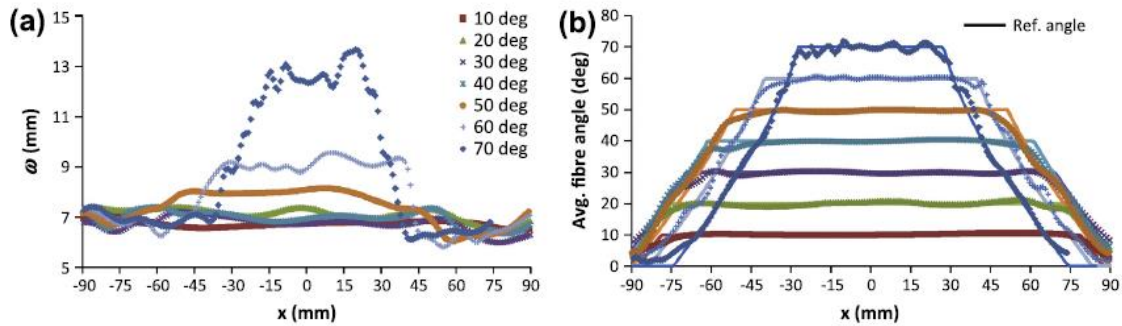


Figure 22: Shift width (a) and Average shear angle (b) graphs were made to characterize manufacturing layup accuracy [41].

1.6 Current Research

It is proposed that, through the use of commingled tow fiber reinforced thermoplastic, in conjunction with an FDM system integrated with a custom designed multi-axis filament winder, a continuous fiber reinforced composite with high reinforcement positional fidelity following complex reinforcement paths can be attained by the process of tow shearing. Due to the mixing inherent in the feedstock, commingled tow was chosen to be used. Wetout is occurring as the commingled tow is pulled through a heated FDM hot end in a pultrusion-like manner. Finally, consolidation is occurring at the point of contact on the mandrel by a custom nozzle.

2. MACHINE DEVELOPMENT

2.1 Requirements for Fabricating a High Quality Composite

Before a discussion of the machine development occurs, a high quality composite should be defined. A high quality composite is one with high volume fraction, uniform fiber distribution, low void content, and good wet out. In order to make a high quality composite, three variables need to be manipulated: time, temperature, and pressure. For load transfer to occur, the area surrounding the fiber, known as the interface, needs to be wet out with the matrix material. Uniform fiber distribution is essential for load transfer as local matrix rich areas are often sites of failure initiation. Time and temperature affects the viscosity of the matrix material, with higher viscosities requiring more pressure to distribute the matrix material and prevent porosity and voids. Higher fiber volume fractions reduce permeability making it more difficult for resin to flow to all fiber surfaces and achieve full wetout. The direction of resin flow has an effect as well; transverse flow to the fibers will require more pressure than flow along the fibers [18]. For prepreg tapes utilized in AFP, high pressures are not required and multiple studies have shown that pressure is the least important of the previously mentioned variables for interfacial bond strength, as the matrix is intimately mixed with the reinforcing fiber in the prepregging operation [23]. However, one study does show a correlation between pressure and reduced void content [23]. The qualities to make a good composite were considered in equipment design and materials chosen for the composites manufacturing machine described in this work.

2.1.1 Filament Winding 3D Printer Combination System

The temperature requirements are the most critical in achieving a good composite. The low cost and ease at incorporating custom nozzles resulted in a FDM hot end being selected as the method to heat the hybrid yarn prior to being placed on the deposition surface. To enable higher temperature thermoplastics like PEEK to be processed, a Gen1 Pico Hot End, shown in Figure 23, with temperature capability of 500°C was selected. The heated zone is restricted to the 20 mm section shown on the left in Figure 23 and the nozzle that is attached to the hot end. The section with cooling fins typically has air from a fan flowing through it during processing to prevent heat from causing buckling of the feedstock in an extrusion process. Since a pultrusion-like operation is being performed on the commingled tow, this is not as critical of a requirement but does help limit the heated zone.

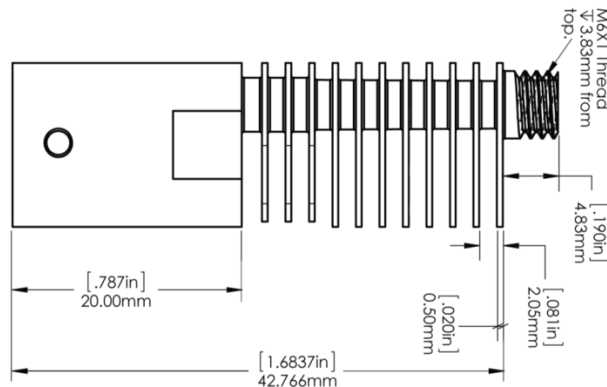


Figure 23: The Pico hot end utilized in controlling the temperature of the commingled tow.

During FDM of some plastics, warping will occur if the bed is not adequately heated. Initial adhesion of the filament to the bed on first layer deposition can become an issue with non-heated beds. For these reasons, a 2100 watt (W) Incoloy tubular heating element was implemented in this system to heat the cylindrical aluminum mandrel which has an outer diameter of 74.55 mm. This element, supplied by Hotwatt, is capable of a maximum outer

sheath temperature of 871°C and enables a mandrel surface temperature of at least 400 °C. Aluminum was chosen as the mandrel material due to faster cooling and heating rates. In addition, the difference in coefficient of thermal expansion between the composite and aluminum will allow for easier part removal.

To better attain the pressure requirements for a good composite a filament winding platform was chosen. This platform offers the potential of improved consolidation within a composite from the fiber tensioning inherent in the process. In addition, an indication of performance of a flatbed system can be attained from some fiber patterns. Like standard filament winders, the fiber placement system contains a fiber carriage complete with a tensioner. The tensioner utilizes a brushless DC gear motor with a slip clutch mechanism that allows for active tensioning and fiber retraction.

Concern of inadequate consolidation of longitudinal (0°) winds existed due to the absence of tension inherent in this path. For this reason, the hot end is equipped with a custom designed wire EDM nozzle that results in minimal abrasion of the fibers and ease in pulling them through the hot end. The design includes a smooth tapered interior geometry and edges with fillets as shown in Figure 24. The extruder hole size is just sufficient to thread the fiber tow through before a build process begins. Pressure is applied to consolidate the tow at the time of placement using displacement control of the flat end of the nozzle. Displacement control was chosen as alternative options would result in additional complexity that may not be needed.

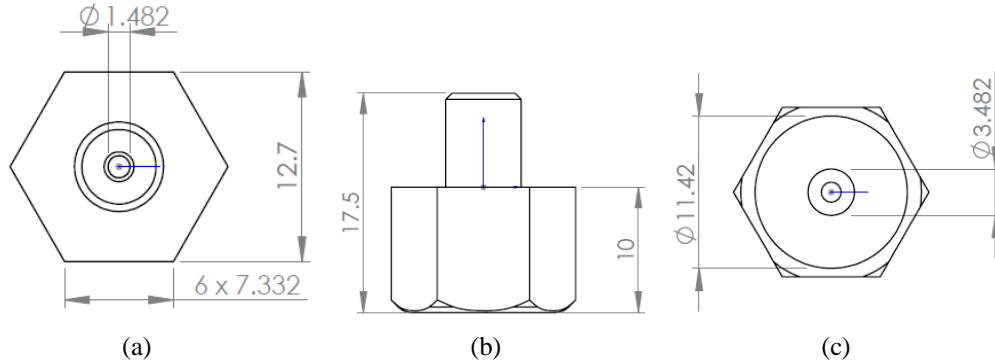


Figure 24: The tailored nozzle with (a) bottom, (b) front and (c) top views used to consolidate the composite.

The last variable this mechanical system must control is time. Time can be adjusted by the feed rate which is determined by the rate of movement of the system's axes. The movement of the fiber carriage parallel to the mandrel (v axis), perpendicular to the mandrel (w axis), and the rotation of the mandrel (u axis) itself affect the feed rate. These axis can be seen in Figure 25. A user written program in a numerical control programming language (g-code) determines the movement and feed rate. The chosen software, Repetier-host, will run the g-code program. The temperature of the hot end, temperature of the mandrel, axes homing, and many other functions can be performed in Repetier-host.

Two separate 3D printing gantries (x , y , z axis) incorporated into this system allow for localized adjustment of the fiber volume fraction and integration of plastic components like hard points, closeouts, and cores. FDM of plastic filament can be accomplished using Filastruder's standard E3D hot end with a 300°C capability. The fiber carriage axis, 3D printing axis, and two extrusion axes (e axes) totaling 11 axes of movement is shown in Figure 25. Two Azteeg X3 Pro controllers, with 8 stepper drivers to control stepper motors, were necessary to move all of these axes. Since the chosen firmware, Marlin, only allowed for simultaneous movement of four axes, a custom firmware was created that allowed for simultaneous movement of seven axes. The

modifications and additions to the original Marlin firmware can be seen in Section 9.1 of the appendices.

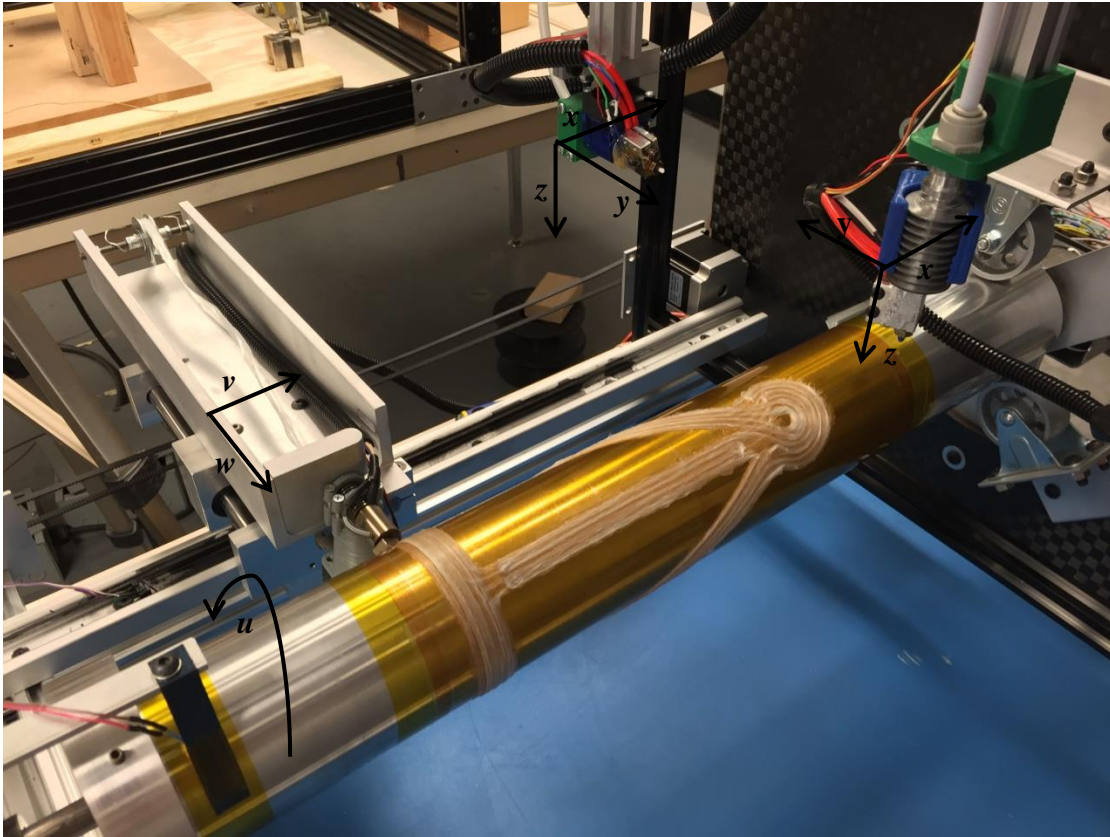


Figure 25: The developed machine with heated mandrel (u axis), fiber carriage (v , w) and two print head gantries (x , y , z).

A number of different requirements were considered when designing the tailstock. An aluminum Y bracket was fabricated to hold the tubular heating element in cantilever. High temperature casters were utilized to hold the mandrel while simultaneously allowing it to rotate. Additionally, slots were machined into the tailstock to allow for nominally three to four inch diameter mandrels to be held. Figure 26 depicts the tailstock without the carbon epoxy face sheets used to increase the stiffness. The components exposed to higher temperatures through conduction were thermally isolated from the carbon epoxy tailstock using alumina bisque ceramic washers.

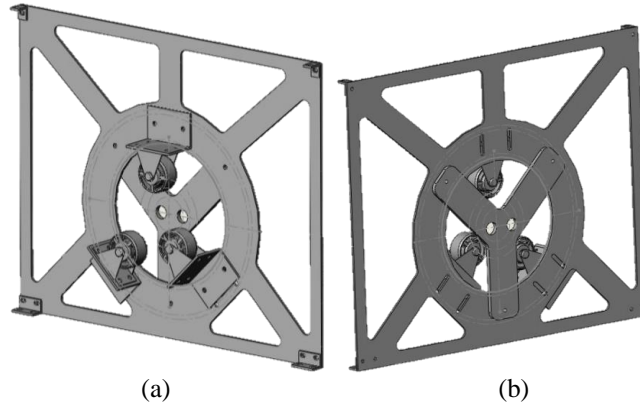


Figure 26: The tailstock shown from the (a) front and (b) back without carbon fiber reinforced face sheets demonstrates the ability to hold different diameter mandrels and an internal tubular heater.

All of the previously described elements were incorporated into developing the mechanical system shown in Figure 27. The commingled tow's path can be seen in Figure 25 and Figure 27. The tow is initially manually tacked onto the mandrel surface. Without having a change in cross section, the tow is pultruded through the hot end. The solidification of the thermoplastic matrix on the mandrel as the fiber carriage moves is the basis of the pulling force. From the PICO hot end, the tow goes around the pulley at the rear of the fiber carriage before being wrapped around the active tensioning system spool shown at the top of Figure 27. Finally the originating point of the tow, which is a large spool of the commingled tow inside a box, is reached.

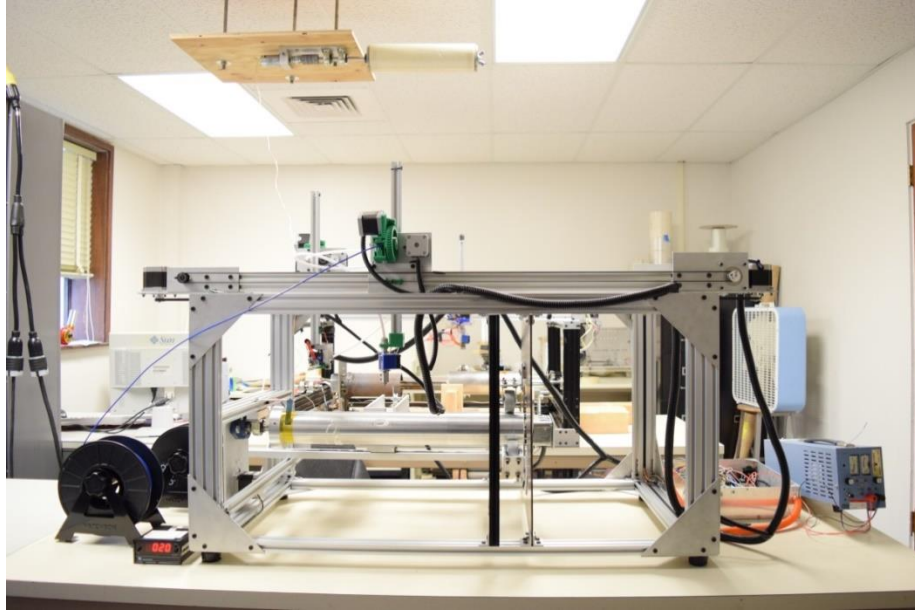


Figure 27: The designed mechanical system with all the previously described elements can be seen.

3. PRELIMINARY STUDIES

3.1 Materials Used

Fiberglass Industries Twintex tow designed for filament winding, with a nominal content of 60% by weight (28.5% by fiber volume) E-glass fibers commingled with polypropylene (PP) fibers, was used for this study. Off-white is the natural product color for this material. Processing of the commingled tow must occur above the flow temperature of the PP strands (180-230 °C). Internal neat plastic components were printed with white PP filament from Gizmodorks with a nominal diameter of 3mm [42]. The manufacturer recommended extrusion temperature for this filament is 230-260°C.

Polypropylene is one of the most commonly used thermoplastics due to its excellent chemical resistance, low density, and high tensile strength [43]. Polypropylene's desirable mechanical properties exist due to the strong bonding between its partially aligned chains. Polymers with chain alignment are termed semi-crystalline as 100% crystallinity is never achieved. Amorphous polymers with randomly oriented chains typically have reduced mechanical properties to that of semi-crystalline polymers. Processing, in terms of cooling rate and applied stress, will affect the resultant structure of a semi-crystalline polymer. Polymer chains are random above the melting temperature and will reorient themselves into a repeating structure between the melting and glass transition temperature. Below the glass transition temperature, only local movement of chains will occur. Polypropylene has a main melting peak at 168°C and other process-induced peaks at 163 and 78°C [43]. It has a glass transition temperature of 0°C. Even though polypropylene has such a low glass transition temperature, thermoplastics can be successfully used above its glass transition temperature if it possesses a

high degree of crystallinity. Due to the processing method and the presence of fibers, a relatively high degree of crystallinity is expected in the polypropylene used in this study. Fibers act as nucleation sites that allow for more favorable chain alignment.

A 0.0254 mm (0.001 in) thick Kapton film was used as the surface layer on the mandrel; this film served as a mold release from the aluminum mandrel. A 0.051 mm (0.002 in) thick PP, low-tack adhesive backed, film was placed on top of the Kapton film. The commingled tow adheres to this PP material much better than other plastic surfaces evaluated. At a mandrel temperature of 70°C, the PP film becomes soft and tends to rip during the placement of patterns with sharper curves.

3.2 Nongeodesic Trial Print

Once the system was operational, a nongeodesic trial print with a path shown in Figure 28 was conducted. Movements with the fiber carriage only, the mandrel only, and both the fiber carriage and mandrel were programmed. A 200 mm/min feed rate, 270°C hot end temperature, 21°C bed temperature, and the lowest allowable tension setting were the process parameters for this initial trial.

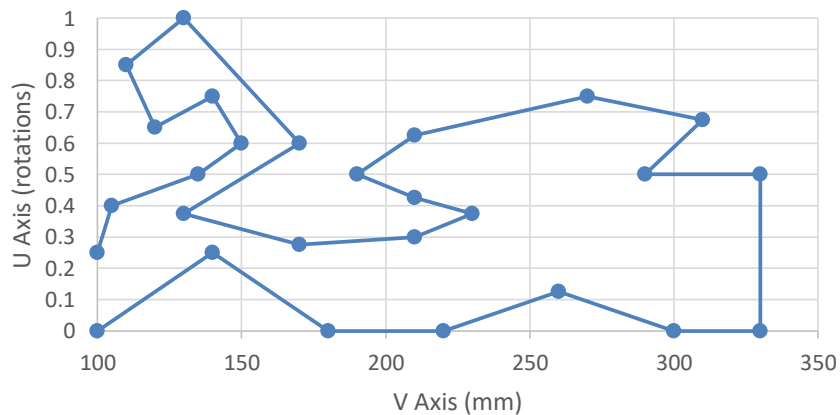


Figure 28: The coded path for a trial print incorporating nongeodesic features.

The encouraging results in which tow shearing enabled non-geodesic paths to be produced are shown in Figure 29. A notable result was the presence of radii on the sharp turns that were programmed. With machining, an inside corner of 90° cannot be produced due to the radius of the cutting tool. This process is analogous in which a 90° turn would result in tow buckling. A radius is necessary to allow the fibers to carry loads through a turn. The shearing of the tow resulted in the radius and prevented the fibers from buckling.

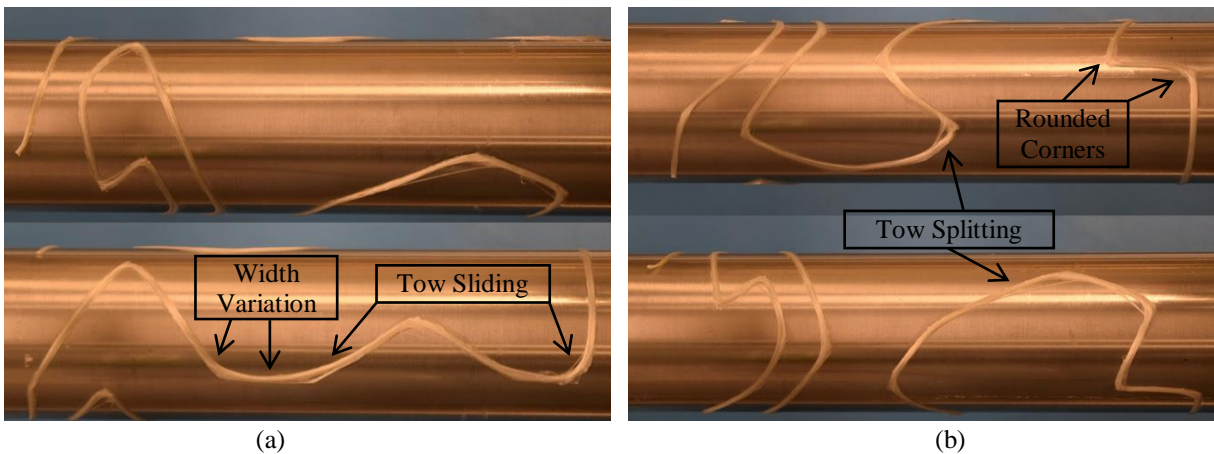


Figure 29: The actual path for the trial print with nongeodesic features; tow splitting, tow sliding, rounded corners and width variation are shown.

Some undesirable results were also obtained from this trial. Tow sliding, tow splitting, tow discreteness, and width variations were present throughout as shown in Figure 29. Tow sliding is defined as the movement or sliding of the entire tow away from its programmed path and occurs outside the profile of the nozzle. The thermoplastic matrix is not solidifying quick enough to maintain its placed path. Tow splitting is the division or splitting of the tow around turns and results from a gradient in tension that exists through the tow. The discreteness of the tow and variations in width throughout can be partially attributed to the lack of consolidation pressure. The initial layer height used was too far off the mandrel. In addition, the mandrel and fiber carriage are not parallel to each other. They are out of plane in three different axes (V, Y, & U). Alterations were made to the machine to help correct this issue; however, perfect

parallelism and alignment was not able to be achieved due to an inability to micro adjust the fiber carriage or mandrel.

Additional preliminary trials and resultant machine modifications were performed to increase the quality of the placed tow. Applying more consolidation pressure through decreasing the initial layer height prevented tow splitting from occurring. Tow sliding was significantly reduced through bypassing the active tensioning system. Even the lowest allowable settings in the active tensioner resulted in the tow being pulled away from its programmed path. Elevated mandrel temperatures contributed to tow sliding; the rate of solidification of the thermoplastic matrix is increased when a room temperature mandrel surface is used. Reducing the feed rate to 100mm/min and implementing dwell times on sharp curves helped to lower the deviations from the programmed path as well. Lastly, preliminary results showed the programmed layer height should be 0.4 mm. Determining a programmed band width would require a more in detailed study. In this work, band width is the width of the tow which is equivalent to the center to center distance of the tows. Figure 30 depicts this distance which will be used to code fiber paths.

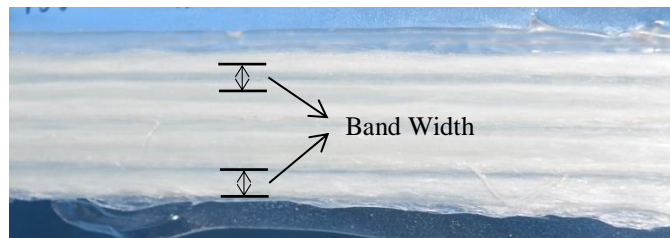


Figure 30: Band width, as shown above, is synonymous with the width of the tow and the center to center distance between adjacent tows.

3.3 Initial Study Assessing Composite Quality

In order to determine a programmed band width, assess composite quality, and better evaluate path limitations, hoop and longitudinal fiber paths were produced with band widths of 2.25, 2.5, and 2.75 mm. This experimental part consisted of three layers and was manufactured

from the inside radius to the outside radius as shown by the arrows in Figure 31. The outer radius edge is designated as the outside of the part. The paths were plotted in Excel with the different band widths. A Matlab program then converted the points into the g-code required for the software to read. The process parameters used for these samples are a layer height of 0.4 mm, feed rate of 100 mm/min, hot end temperature of 300°C, no tension, and a dwell time of 2 seconds on the curve. Completed parts were examined and qualitative observations were recorded. Areas of the experimental parts were sectioned and metallography was used as a preliminary measure of composite quality.

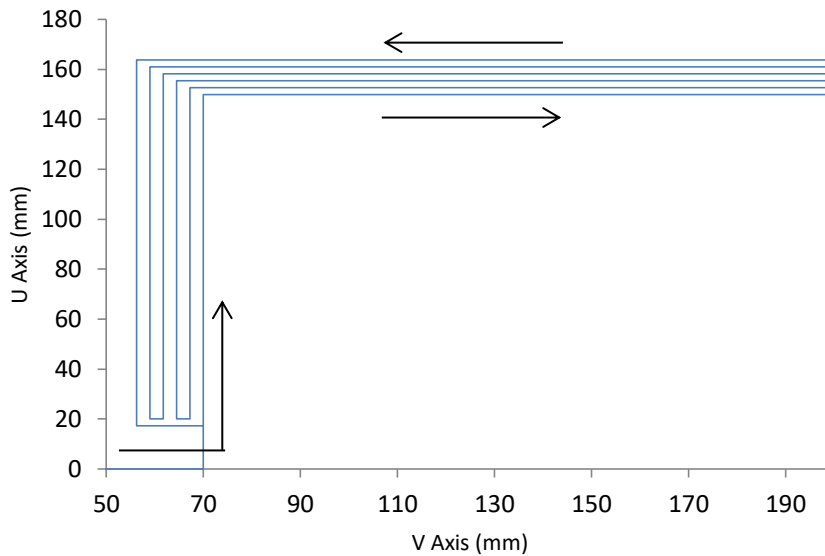


Figure 31: The experimental part shown was used to evaluate composite quality. The 3 layer part starts and finishes at the point crossing the V axis line.

3.3.1 Visual Evaluation Results

The part, with path transitions from a hoop (90°) to a longitudinal (0°), is shown as the manufacturing process progresses, in Figure 32. The arrow in Figure 32 (c) shows the initial tacking point to begin the build process. The first path change resulted in a very minimal radius as the fiber closely followed the preprogrammed path. Thickness increased slightly on the inside

of the tow due to tow shifting as each individual glass fiber tries to make that turn with the shortest distance possible. The lower line in Figure 32(a) marks the start of the curve from hoop to longitudinal wind; the upper line marks the start of the curve from longitudinal to radial wind. The transition from the hoop to the longitudinal path is better than the longitudinal to hoop transition. Each of these transitions occurs earlier than the preprogrammed path as a result of some fiber sliding. The radius of the transition areas increased on the 2nd and 3rd layer. This could be attributed to the polypropylene poor region present on the upper surface of each layer. Decreased tacking ability due to the larger surface area over which solidification between layers must occur coincides with trying to bond to a matrix poor region.

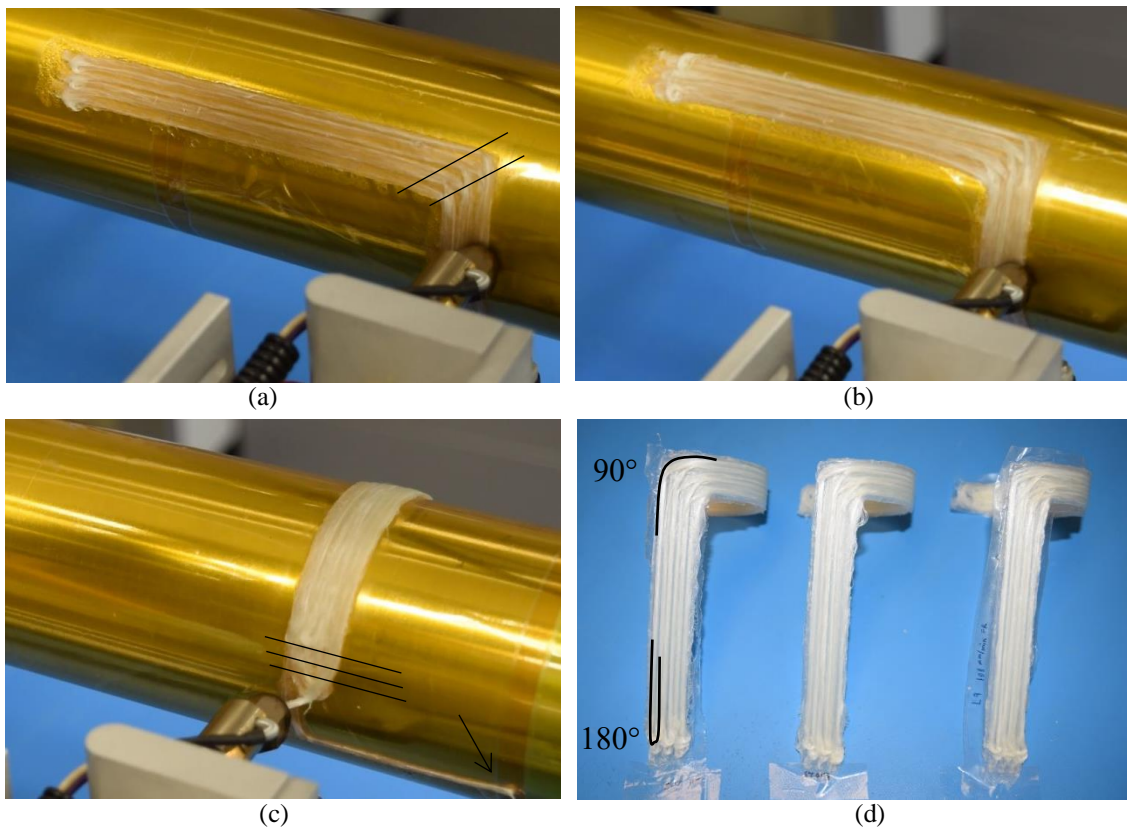


Figure 32: The hoop and longitudinal transition part as the build progresses: (a) placing the 1st layer; (b) placing the 2nd layer; (c) finishing the 3rd layer; (d) finished parts of 2.75, 2.5, and 2.25 mm.

The 180° turns on both the longitudinal and hoop winds resulted in thickness increases. The thickness increases grew with each layer as the adjacent tow was pulled slightly from its previously placed position. The sharp turning radius remaining under the heated nozzle prevented solidification of the thermoplastic. To prevent this pulling from occurring, manual mechanical fixation was sometimes used on this 180° turn to keep the 2nd and 3rd layers closer to the proper positions. The amount of tow sliding that occurred is evident in Figure 32(c) as the programmed tow positions would be adjacent to the longitudinal tow that was just placed. The three lines in Figure 32(c) mark the start of the 180° turn for each layer with the first layer experiencing the smallest amount of tow sliding.

The longitudinal tows are more discrete than the hoop winds. The top surface of the longitudinal placed tows appears corrugated in some respect whereas the thickness looks much more uniform across the hoop winds. The 2.25 mm hoop wind possesses a tapered thickness that increases toward the outside of the part. The polypropylene matrix is clearly flowing as small beads of neat thermoplastic are present on the outside edge of the part. Both of these phenomena can be attributed to the placement of fiber in the same direction for each layer. Excess matrix and some fiber are squeezed to the outside of the part by the consolidation nozzle. A previous trial in which build direction was reversed for each layer did not exhibit these symptoms.

3.3.2 Metallographic Evaluation Results

Photomicrographs of the cross section of the longitudinal fibers and hoop fibers are shown in Figure 33 and Figure 34. ImageJ was utilized to obtain thickness measurements throughout the cross section of each of the test parts. The results of these measurements are shown in Table 3. The polypropylene film is shown in black at the bottom of some of the photomicrographs. Small black spots are polishing debris associated with preparing samples

with such a soft thermoplastic matrix. Voids, which mostly appear at the top of the images, are emphasized with arrows. The location of these voids and the previous visual evaluation suggests they are dry spots on the upper surface of each composite.

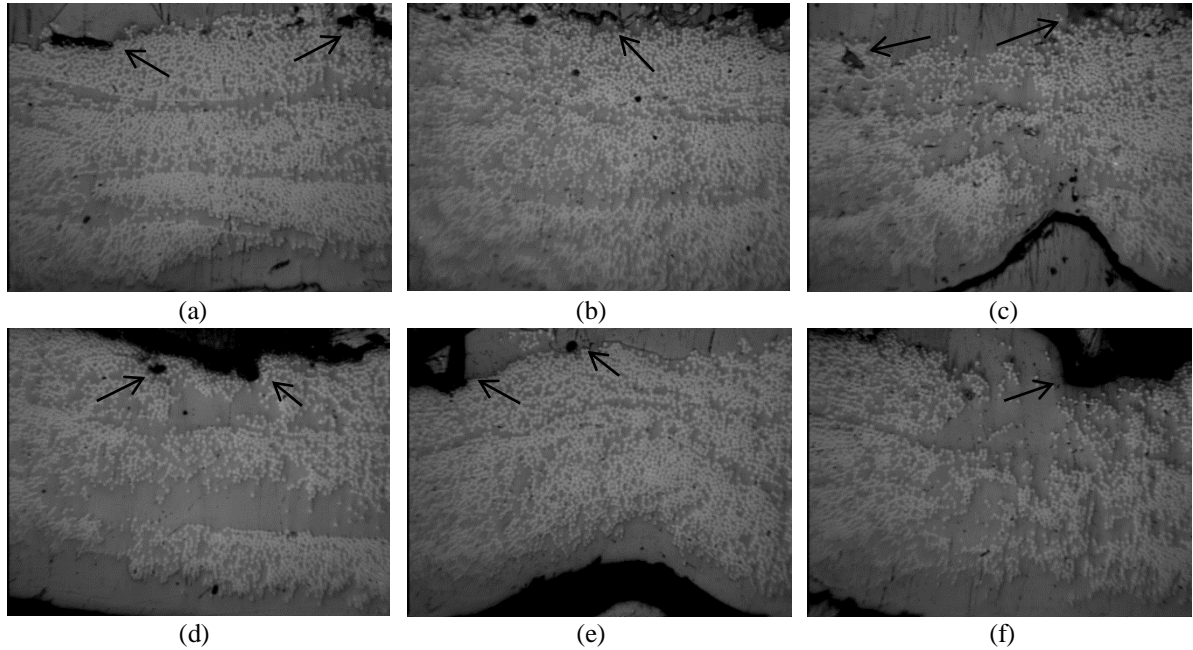


Figure 33: Photomicrographs of the cross section of (a) 2.25 mm hoop, (b) 2.5 mm hoop, (c) 2.75 mm hoop, (d,e) two views of 2.5 mm longitudinal and (f) 2.75 mm longitudinal samples taken at a magnification of 50X.

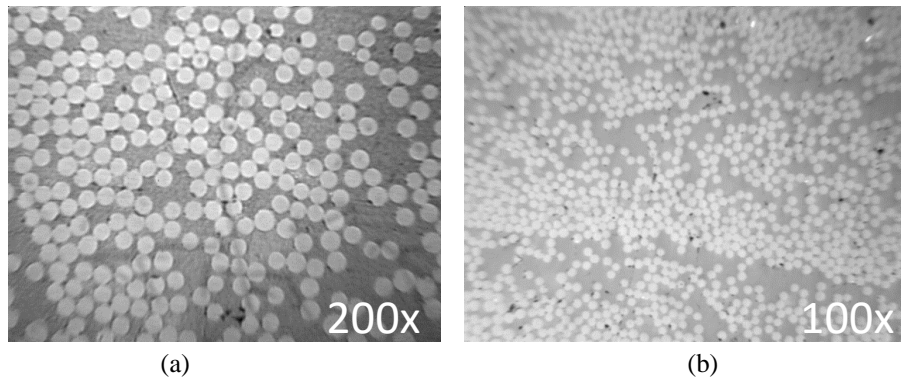


Figure 34: High magnification photomicrographs of the 2.5 mm hoop (a) and the 2.5 mm longitudinal (b) samples.

Table 3: Results of the sample thickness based on optical microscopy are shown.

| Fiber Spacing/Type (mm) | Minimum (mm) | Maximum (mm) | Mean (mm) | Standard Deviation |
|-------------------------|--------------|--------------|-----------|--------------------|
| 2.25—Hoop | 0.9144 | 1.245 | 1.149 | 0.122 |
| 2.25—Longitudinal | 0.864 | 1.27 | 1.118 | 0.133 |
| 2.5—Hoop | 1.143 | 1.295 | 1.207 | 0.051 |
| 2.5—Longitudinal | 1.112 | 1.295 | 1.207 | 0.060 |
| 2.75—Hoop | 1.041 | 1.245 | 1.067 | 0.125 |
| 2.75—Longitudinal | 0.711 | 1.194 | 1.058 | 0.118 |

Spacing between tows is more easily distinguished in the hoop winds than the longitudinal winds. The 2.25 mm sample, depicted in Figure 33(a), shows obvious overlapping tows; this phenomena was not present in the 2.5 mm samples (see Figure 33 (b)) or the 2.75 mm samples (see Figure 33 (c)). The 2.75 mm tow spacing sample did show evidence of gaps with lower volume fractions in between adjacent tows in the hoop and longitudinal samples (see Figure 33 (f)). The 2.5 mm samples exhibit different responses between longitudinally placed tows with more spacing and lower fiber volume evident in Figure 33 (d) while less spacing and higher fiber volume fraction in Figure 33 (e). Figure 33 (d) and Figure 33 (f) are the lowest representative fiber volume fraction areas found in the cross section of the respective samples. For the most part, a high fiber volume fraction is found within the composite.

Since the layer height was set to 0.4 mm, the theoretical thickness should be approximately 1.2 mm. The specimen with 2.5 mm tow spacing has an average thickness value of 1.207 mm for the hoop and longitudinal paths. Samples of the other two tow spacings showed much less consistent thickness values and average values that differed from the theoretical. Thickness measurements of the 2.25 mm sample confirm a taper exists in the hoop and longitudinal paths in the build direction.

3.3.3 Discussion

The test geometry was chosen to gain some quantitative understanding of the functionality of the new manufacturing system. Results from Sections 3.3.1 and 3.3.2 indicate that high volume fraction continuous fiber thermoplastic composites can be generated using this combination of fused deposition 3D printing technology with tow placement via filament winding.

The accurate placement of the first fiber tow in Section 3.3.1 could be attributed to the higher pressure that it receives. When a tow is placed next to another tow, the applied force, which is the parameter that is controlled, is distributed over a larger area since the diameter of the head of the nozzle is much larger than a single tow width. Therefore, when the head is pressed against multiple tows, side-by-side, the effective consolidation pressure drops. To improve the quality of the composite and the accuracy of tow placement, the viscous zone must be limited or solidified quicker.

The regions of discrete tows with resin rich regions in between that exist in the longitudinal paths could be attributed to a number of different sources. This characteristic could result from placing fiber on a curved surface in a direction creating a non-uniform pressure distribution. Another possibility is that the coded path is consistent from layer to layer despite the radius increasing. A small space in between the tows on the first applied layer grows as the layers and radius increase. This would explain why the same increase in tow spacing with increasing number of layers is not evident in the hoop winds. Lastly, the inherent tension present in the filament winding process could be a source; since minimal tension was purposely applied, any tension present in the process could have a significant impact.

Consolidation through the thickness is better in some areas than others. The inconsistency could be attributed to the amount of flexure that occurs in the PICO hot end mounting structure when paths are being placed. Due to different mounting systems stiffness in the vertical and horizontal directions, this flexure mostly occurs with the hoop winds, not the longitudinal winds. Determining the optimal thickness and tow spacing reduced the effect of this hot end structure deflection significantly.

The results shown in Sections 3.3.1 and 3.3.2 denote a number of successes in terms of demonstrating fabrication of a high quality composite. High fiber volume fractions were achieved that were significantly better than previous studies using the 3D printing platform to place continuous fiber. A minimal amount of voids were found within the composite. Thickness measurements and microscopy observations enabled an optimum tow spacing of 2.5 mm to be selected. Lastly, the placement of continuous fiber in nongeodesic paths was accomplished. The limitations observed through Sections 3.2 and 3.3 illustrate areas of needed improvement. Fiber tow spreading is not uniform as areas of differing fiber volume were detected within the longitudinal paths. Although thickness matched the theoretical thickness based on layer spacing for the 2.5 mm samples, it is not consistent throughout the entire cross sectional area of the composite. Dry fiber areas are present on the top surface and cause minor tow deviation from its preprogrammed path in all but the first layer. Lastly, poor consolidation of the transition regions, especially with small turning radii, is present.

3.4 Active Forced Air Cooling

The previous study made it apparent that faster solidification of the thermoplastic's viscous zone was needed to improve the accuracy of the tow and quality of the composite. Faster solidification would be implemented through the use of a forced air cooling (AC) system

that directs air in all directions of movement. If too much of this directed air hits the hot end, the temperature capabilities of the hot end would be reduced and the heating element could prematurely burnout. The manifold design, shown in Figure 35, consists of a lip that comes close to the nozzle to help prevent the forced air from deflecting back to the heating element. In addition, woven fiberglass was used to further reduce the gap between the lip and the nozzle and act as an insulator.

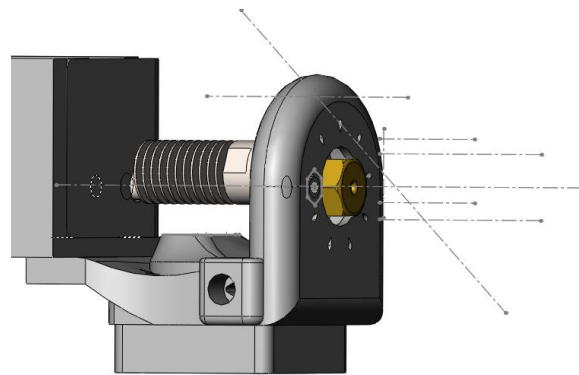


Figure 35: The designed cooling manifold that allows for forced air cooling in all directions.

The cooling manifold also must interface with the U channel's bottom holes that hold the PICO hot end bracket in place. Including a mount for a cooling fan that directs air just at the cooling fins and not the hot end's heated zone is needed as well. Both of these requirements allow a separate gantry to deposit filament much closer to the fiber placement nozzle; a higher probability of success in achieving a uniform microstructure while adjusting fiber volume fraction would occur.

Creation of this manifold out of aluminum or steel was considered. Meeting all of the requirements with metal would involve multiple parts, inclusion of an O-ring, and additional design simplifications. Furthermore, modifications after trialing a design could not occur in a cost and time efficient manner. For these reasons, ABS plastic was chosen as the cooling

manifold's material as it could be printed using FDM. Initial print trials involved using a dual extruder and HIPS filament as a support material in the inner cavities shown in Figure 36 (a) and (b). D-limonene could then be used to dissolve the HIPS material within the part. Unfortunately, ABS part warping occurred prior to the HIPS dissolving. The interior location and minimal surface area of exposure to the D-limonene prevented this method from being successful.

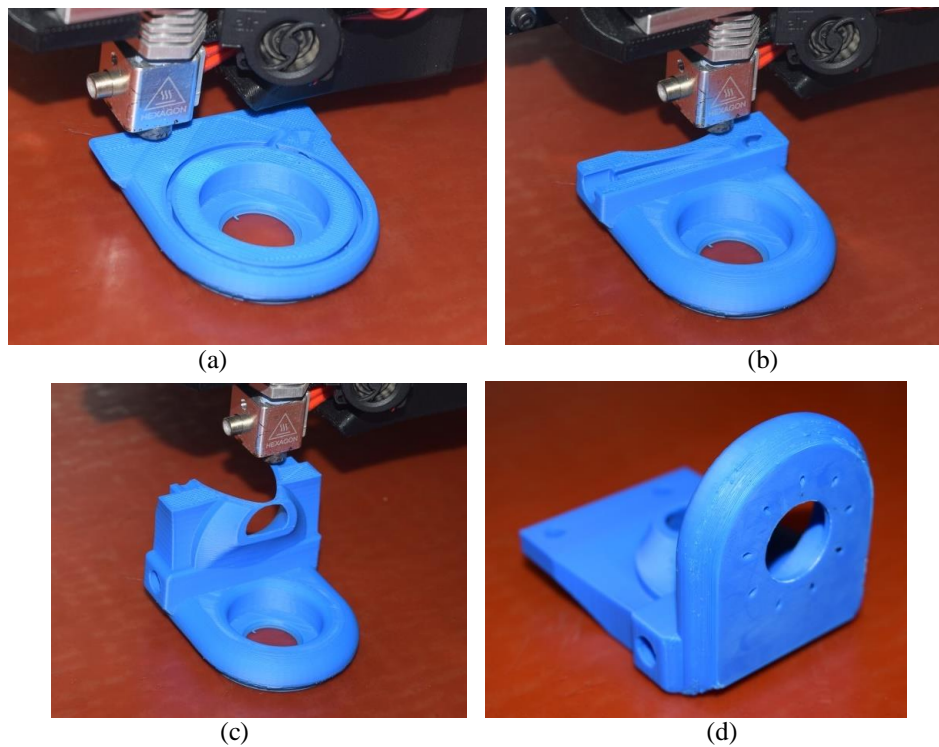


Figure 36: The forced air cooling manifold at different stages of the printing process; internal cavities can be seen in (a) and (b).

At this point, redesign of the component occurred so support material would not be needed. Holes and interior geometric features were changed to a teardrop shape with the point oriented up in the build direction. Overhangs were limited to higher angles as well. These modifications enabled a high-quality ABS manifold to be produced as shown in Figure 36.

A mini L bracket was produced to acquire a qualitative idea of the effect of AC. The three layer composite, shown in Figure 37 (b), was produced with a 100 mm/min feed rate, a 300°C hot end temperature, 55°C bed temperature, and a 25 psi AC rate. When compared to Figure 37 (a), AC resulted in improved consolidation, reduction in tow sliding, and reduced discreteness in the longitudinal tows. Gaps were present between the tows in the transition regions due to the sharp angled turns. A turn this sharp is not good design practice with continuous fiber reinforced composites; an increase in turning radius would eliminate the gaps present in the transition regions.

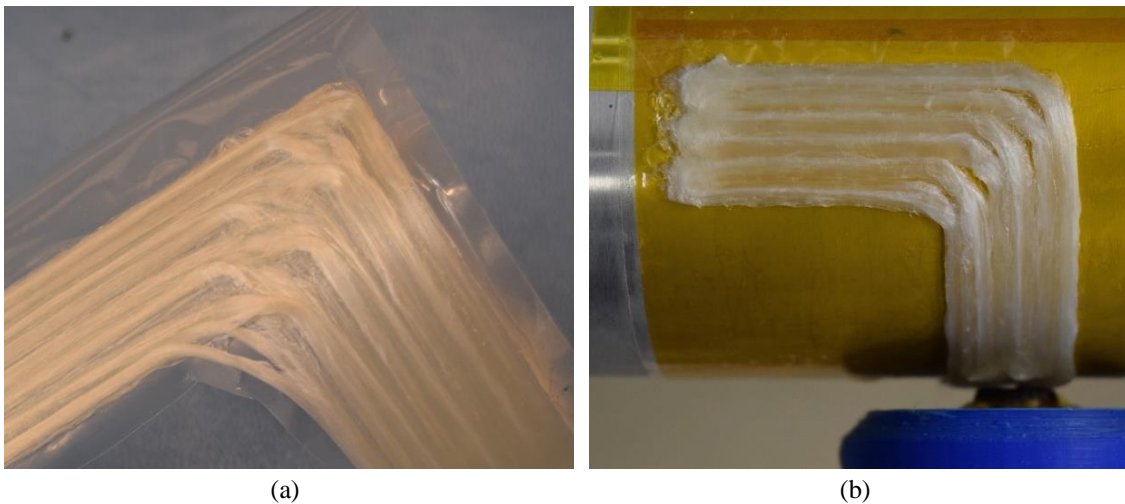


Figure 37: An L bracket produced without AC (a) and with AC (b) demonstrates the effectiveness of the cooling manifold.

4. EXPERIMENTAL

Although a qualitative idea of the effect of air cooling was obtained, characterizing the effect in a quantitative manner is desired to better understand its significance. In order to define different processing parameters that can produce similar composites, the effect of hot end temperature, feed rate, and deposition surface should be analyzed as well. In order to determine if greater positional fidelity causes a reduction in mechanical performance, both of these aspects will be quantified in this study.

As seen by the coded paths in Figure 38, tow fidelity will be analyzed in a similar manner used to the constant angle variation method used by Kim et al. in Section 1.5 [41]. Due to the restriction in size based on the circumference of the mandrel, a constant radius of 20 mm and a straight path (constant shear angle) of 100 mm will be used. A direct comparison between the obtained results and the results from Kim's study will not be made as these changes are expected to increase the amount of error. Therefore, comparisons between differently processed samples will be conducted.

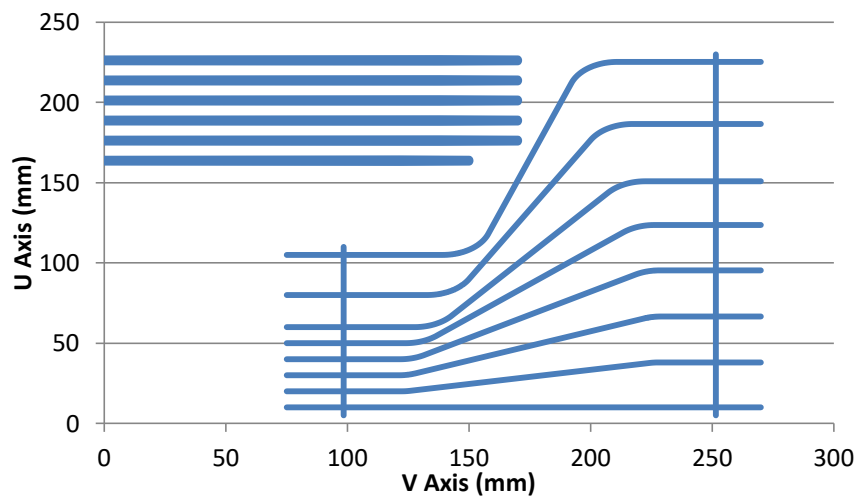


Figure 38: The coded path including the tow fidelity portion of the study and the samples for quantifying mechanical performance are shown.

An indication of mechanical performance will be obtained by the microstructure and peel strength. Voids, flash, and geometric dimensions will be quantified from micrographs of samples cross section. The peel strength will be obtained from a T-Peel Test in accordance with ASTM D1876. Although this standard is used to test the peel resistance of adhesives, this method is applicable as the intertow properties are expected to be the weakest point of the composites produced with this method. For FDM printed parts, interlayer properties are reduced as the polymer chains are not blended together between the layers. Since the composite specimens are made in a layer by layer fashion, a similar response is predicted. Additional details on the testing methods, including the manufacturing of specimens, will be given in the subsequent sections.

4.1 Manufacturing of Sample Specimens

The process for generating the g-code was not as simplistic as that used in the preliminary studies. Solidworks was employed to develop the paths in order to align the midpoints of the straight sections, create 100 mm straight paths, and incorporate a 20 mm constant radius. Points were created on these paths, exported to a text file, and then imported into Excel. A Matlab program read the excel file and converted it into the required g-code format. An example of one of the g-code programs created can be found in Section 9.2 of the appendix.

The first layer of the coded path for the first 18 samples with a PP deposition surface is shown in Figure 38. Note that the V axis is parallel to the mandrel while the U axis is the mandrel circumference. The hoop paths and the horizontal path will be used for locating purposes in post-processing. Only the specimens manufactured for peel strength and microscopy possess multiple layers. After the 2nd layer, Kapton tape is placed on top of the samples in one

location to create the unbonded ends for the T-peel samples. The placement of the 3rd glass PP layer on top of the Kapton tape is shown in shown in Figure 39. Within each variable set, five samples with a width of two tows and a thickness of four tows were manufactured for the T-Peel Test. A sixth shorter sample of similar cross section was manufactured for microscopy.

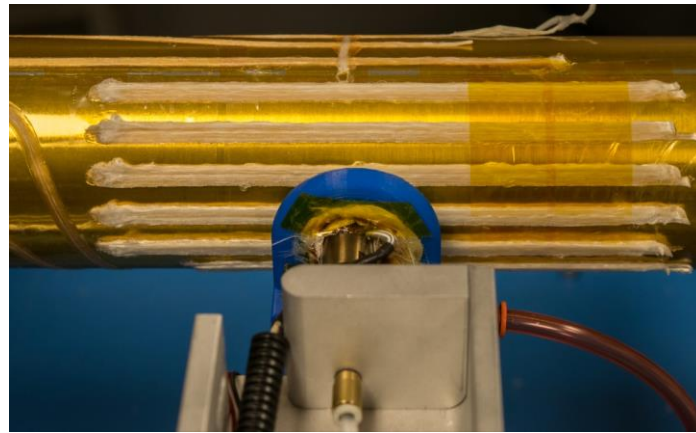
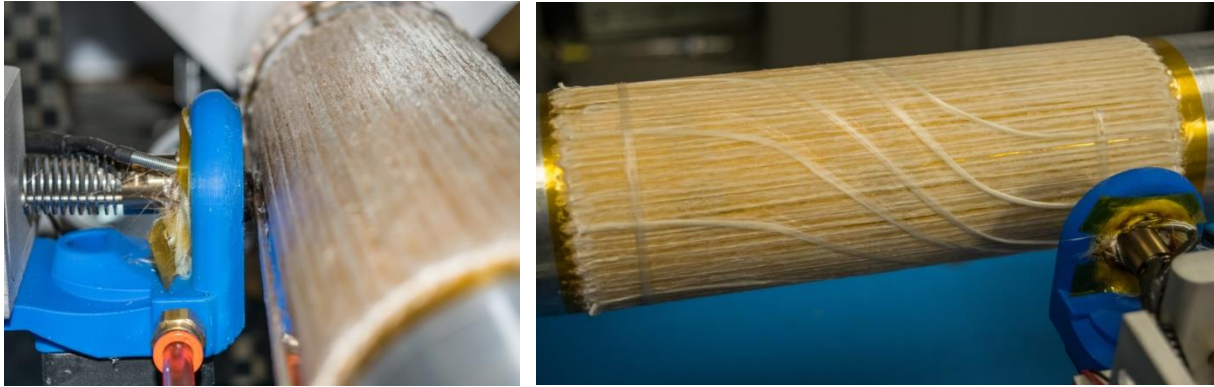


Figure 39: The placement of the 3rd glass PP layer of the specimens used for peel strength and microscopy is shown.

The last 18 samples consisted of a glass PP deposition surface as shown in Figure 40 (a). The misalignment between the mandrel and fiber carriage is evident in this base layer as larger gaps between the base layer tows exist on the initial side of the paths. Figure 40 (b) depicts the manufacturing of a non-AC sample; tow sliding was prominent with this sample. During processing, smoke, which suggested overheating of the PP, was coming from the nozzle with increasing amounts at the higher temperatures in the non-AC samples. Since the paths must sit flat during the scanning process, the base layer must consist of longitudinally placed tows instead of hoop placed tows.



(a)

(b)

Figure 40: Placement of the first deposition layer is shown in (a) while the large amount of tow sliding present in a sample without AC can be seen in (b).

Sample names were processed according to the values shown in Table 4. During processing, the hot end temperature output graphs were saved; the measurements in these graphs were taken from a thermistor inside the hot end. The min/max hot end temperature and the mean hot end temperature columns were estimated from the outputted graphs. At higher temperatures, the hot end set point varied significantly from what was measured in some of the samples. The addition of a much larger nozzle, which acts as a heat sink, and the active cooling system that continuously cools the nozzle clearly prevented the heating element from reaching its set temperature. Temperatures without AC were generally very close to the set point.

Table 4: The sample names along with the varying process parameters are shown.

| Sample Name | Dep. Surface | Set HE Temp (°C) | Min/Max HE Temp (°C) | Est. Mean HE Temp (°C) | Forced Air Cooling (PSI) | Feed Rate (mm/min) |
|-------------|--------------|------------------|----------------------|------------------------|--------------------------|--------------------|
| S1 | PP | 300 | 282-308 | 292 | 30 | 200 |
| S2 | PP | 300 | 288-309 | 300 | 0 | 200 |
| S3 | PP | 300 | 282-304 | 295 | 30 | 300 |
| S4 | PP | 300 | 286-307 | 297 | 0 | 300 |
| S5 | PP | 300 | 282-305 | 298 | 30 | 400 |
| S6 | PP | 300 | 286-308 | 299 | 0 | 400 |
| S7 | PP | 350 | 321-343 | 333 | 30 | 200 |
| S8 | PP | 350 | 338-357 | 348 | 0 | 200 |
| S9 | PP | 350 | 322-348 | 334 | 30 | 300 |
| S10 | PP | 350 | 332-358 | 346 | 0 | 300 |
| S11 | PP | 350 | 323-354 | 335 | 30 | 400 |
| S12 | PP | 350 | 330-356 | 347 | 0 | 400 |
| S13 | PP | 400 | 326-374 | 344 | 30 | 200 |
| S14 | PP | 400 | 367-398 | 387 | 0 | 200 |
| S15 | PP | 400 | 334-390 | 357 | 30 | 300 |
| S16 | PP | 400 | 376-404 | 394 | 0 | 300 |
| S17 | PP | 400 | 332-397 | 353 | 30 | 400 |
| S18 | PP | 400 | 378-403 | 394 | 0 | 400 |
| S19 | GF/PP | 300 | 278-308 | 295 | 30 | 200 |
| S20 | GF/PP | 300 | 288-309 | 298 | 0 | 200 |
| S21 | GF/PP | 300 | 283-306 | 298 | 30 | 300 |
| S22 | GF/PP | 300 | 289-309 | 300 | 0 | 300 |
| S23 | GF/PP | 300 | 281-308 | 297 | 30 | 400 |
| S24 | GF/PP | 300 | 289-309 | 300 | 0 | 400 |
| S25 | GF/PP | 350 | 330-352 | 340 | 30 | 200 |
| S26 | GF/PP | 350 | 333-354 | 347 | 0 | 200 |
| S27 | GF/PP | 350 | 321-352 | 338 | 30 | 300 |
| S28 | GF/PP | 350 | 330-354 | 345 | 0 | 300 |
| S29 | GF/PP | 350 | 326-357 | 339 | 30 | 400 |
| S30 | GF/PP | 350 | 337-353 | 346 | 0 | 400 |
| S31 | GF/PP | 400 | 360-397 | 373 | 30 | 200 |
| S32 | GF/PP | 400 | 383-404 | 396 | 0 | 200 |
| S33 | GF/PP | 400 | 360-400 | 375 | 30 | 300 |
| S34 | GF/PP | 400 | 384-404 | 397 | 0 | 300 |
| S35 | GF/PP | 400 | 370-394 | 378 | 30 | 400 |
| S36 | GF/PP | 400 | 383-405 | 396 | 0 | 400 |

4.2 Heat Transfer Analysis to Estimate Actual Deposition Temperature

In order to get a better idea of the temperature of the commingled tow as it is deposited onto the deposition surface, a time dependent conduction model was created. Prior to the implementation of the model, the number of PP filaments and glass fibers in the commingled tow must be determined.

Unprocessed commingled tow was mounted in acrylic, ground, and polished so that microscopic analysis could take place. Figure 41 depicts large diameter PP filaments and much smaller diameter glass fibers within the unprocessed commingled tow. Since the cross section of the unprocessed tow is not very homogeneous, counting the glass fibers and PP filaments within a localized area would not be a very accurate approach. To avoid counting fibers and filaments in a much larger area, an alternative method was used.

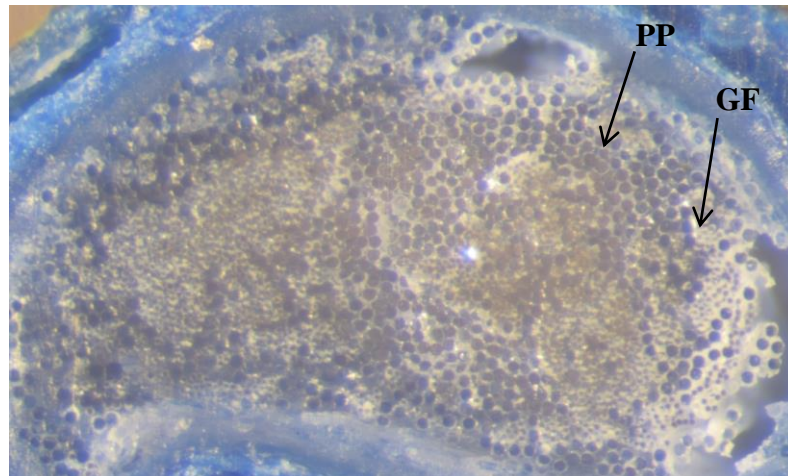


Figure 41: Unprocessed commingled tow with large PP filaments and small glass fibers is shown.

Section 4.4 details the process of conducting microscopic analysis of composite beams. Section 5.2.2 displays the results of the analysis including width and height measurements of all the samples. The average width and height measurements from every sample were multiplied to acquire a composite area of 11.996 mm^2 . Dividing this composite area by the number of tows

(8), results in an average area per tow of $A_c=1.4995 \text{ mm}^2$. This tow area was multiplied by a known fiber volume fraction of 28.47% to yield a fiber area and matrix area. The diameter of the glass fiber ($D_{GF} = 0.02 \text{ mm}$) and the diameter of the PP filaments ($D_{PP} = 0.04 \text{ mm}$) were measured from Figure 41. The fiber area and matrix area were divided by the area of one glass fiber and one PP filament to determine 427 glass fibers(N_{GF}) and 107 PP filaments(N_{PP}) were present in the tow. These values might be slightly high as the voids were included in the composite width and heights. Alternatively, an area without the voids could have been used; however, this would result in partial removal of glass fibers. Thus, the chosen approach was considered the most rational.

Table 5: The symbols, values, and units used for the time dependent conduction heat transfer model are shown.

| Symbol | Value | Units |
|------------------|-----------------------------|---------------------|
| A_c | $1.5*10^{-6}$ | m |
| l | 0.001 | m |
| N_{GF} | 427 | |
| N_{PP} | 107 | |
| D_{GF} | 0.00002 | m |
| D_{PP} | 0.00004 | m |
| h_{air} | 20 | $\frac{W}{m^2 * K}$ |
| $k_{E-glass}$ | 1.2 [44] | $\frac{W}{m * K}$ |
| $c_{E-glass}$ | 805 [44] | $\frac{J}{kg * K}$ |
| $\rho_{E-glass}$ | 2550 [44] | $\frac{kg}{m^3}$ |
| $k_{PP} =$ | 0.1 [45] | $\frac{W}{m * K}$ |
| c_{PP} | 1700 [45] | $\frac{J}{kg * K}$ |
| $\rho_{PP} =$ | 900 [45] | $\frac{kg}{m^3}$ |
| T_i | 298.15 | K |
| T_∞ | 573.15, 623.15, & 673.15 | K |
| t | 4.5, 6, & 9 | sec |

The values in Table 5 were inputted into the time dependent conduction heat transfer model. A length (l) of 1 mm was chosen. Room temperature was used as the initial temperature (T_i) while the temperature of the surroundings (T_∞) was considered the hot end temperature set point. The values used for time (t) were found using the feed rates and the distance at elevated temperature which was considered to be the length of the hot end plus the length of the nozzle.

The first step in the time dependent conduction model was to determine the Biot number (Bi). The characteristic length for the glass fiber and PP filament was found using Equation (1).

$$L_c = \frac{\text{volume}}{\text{surface area}} = \frac{A_c * l}{\pi * D_{GF} * l * N_{GF} + \pi * D_{PP} * l * N_{PP}} \quad (1)$$

The characteristic length along with the heat transfer coefficient and thermal conductivity were inserted into Equation (2) to determine a Biot number for glass fiber and PP.

$$Bi = \frac{h_{air} * L_c}{k} \quad (2)$$

Since both Biot numbers were found to be much less than 0.1, the validity of using the lumped capacitance method for this scenario was confirmed as the induced error is small. After some simple algebra, the temperature of the PP filament and glass fiber as it exits the nozzle and is deposited on the surface can be determined from Equation (3).

$$\theta = \theta_o * \exp(-Bi * Fo) \rightarrow (T - T_\infty) = (T_i - T_\infty) * \exp\left(-Bi * \frac{\alpha * t}{L_c^2}\right)$$

$$T = T_\infty + (T_i - T_\infty) * \exp\left(-Bi * \left(\frac{k}{\rho * c}\right) * \frac{t}{L_c^2}\right) \quad (3)$$

The resultant temperatures of the glass fiber and PP filaments determined from the time dependent conduction model are displayed in Table 6 and Table 7. Since the set hot end temperature didn't match the measured hot end temperature during processing, Figure 42 was created to better estimate the resultant temperature of each constituent as it leaves the nozzle. This will be referred to as the deposition temperature in future sections. It is important to note

from the figure and tables that the constituent temperature was actually between 11 and 77°C below the measured hot end temperature depending on the material and processing conditions.

Table 6: Resultant temperatures of the glass fiber at different processing conditions obtained through a time dependent conduction model.

| Hot End Set Temp. (K) | Time (s) | | | GF Resultant Temperature (K) |
|-----------------------|----------|--------|--------|------------------------------|
| | 4.5 | 6 | 9 | |
| 573.15 | 488.45 | 515.95 | 547.06 | GF Resultant Temperature (K) |
| 623.15 | 523.05 | 555.55 | 592.32 | |
| 673.15 | 557.65 | 595.15 | 637.57 | |

Table 7: Resultant temperatures of the PP filament at different processing conditions obtained through a time dependent conduction model.

| Hot End Set Temp. (K) | Time (s) | | | PP Resultant Temperature (K) |
|-----------------------|----------|--------|--------|------------------------------|
| | 4.5 | 6 | 9 | |
| 573.15 | 516.51 | 539.7 | 561.48 | PP Resultant Temperature (K) |
| 623.15 | 556.21 | 583.15 | 609.36 | |
| 673.15 | 595.91 | 627.53 | 657.24 | |

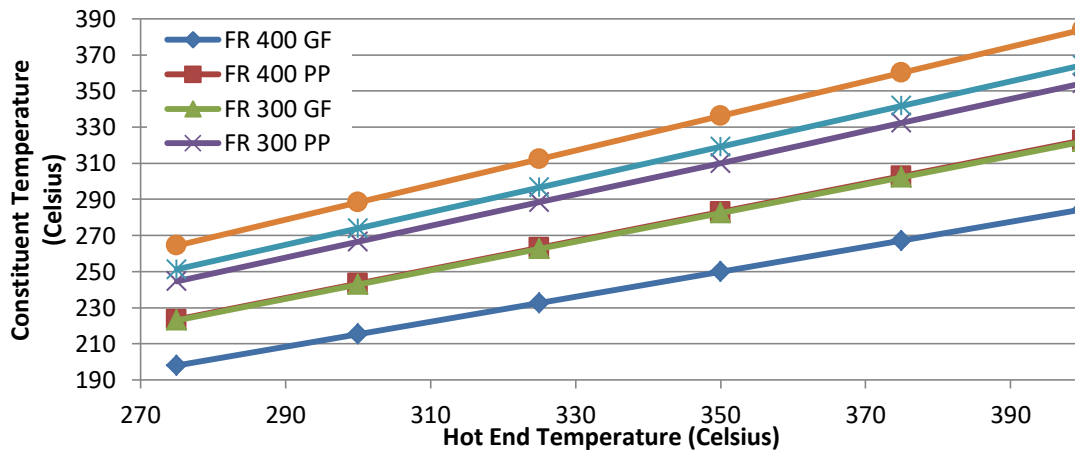


Figure 42: Temperatures of the constituents as it leaves the nozzle as a function of hot end temperature.

The time dependent conduction model will not be near as accurate on the AC samples. It doesn't include the effect of forced convection on the deposited tow in the forced air cooled samples. Figure 43 shows the direction of forced air flowing from the manifold and into the

heated zone. Air flows into the gap between the nozzle and the mandrel effectively hitting the tow as it is pultruded. In addition, a temperature gradient assuredly exists within the nozzle and hot end. Constantly cooling the nozzle as a result of air deflected off the mandrel will cause the nozzle to function as a heat sink for the hot end. With the high PSI of AC used in this study (30 psi), a significant temperature reduction of the values in the time dependent conduction model can be expected.

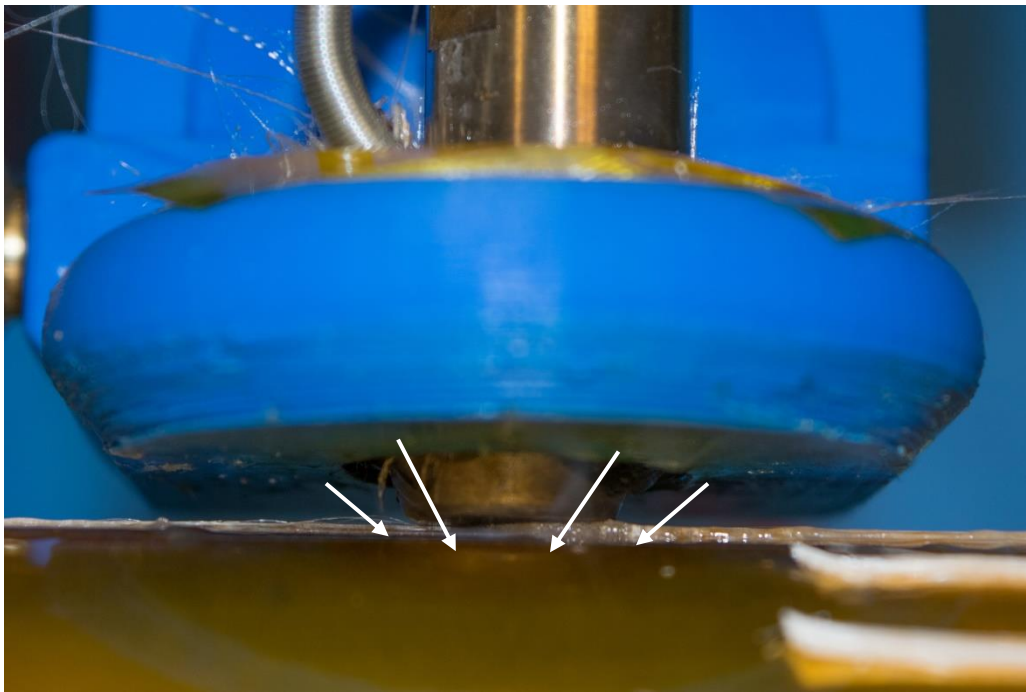


Figure 43: The manifold forces air in the direction of the arrows at the deposited tow in order to allow for rapid solidification.

4.3 Post-Processing for Positional Fidelity

After processing and cooling of the mandrel, the PP adhesive backed film with the tow paths on them was removed from the mandrel. To allow for the paths to lie flat during scanning, slits were cut into the hoop tow paths; the ends where the paths started and ended were cut off as well. Paths were then scanned using a high-resolution Epson flatbed scanner. In Adobe Lightroom, the image was mirrored and rotated to align the bottom tow path as horizontal as

possible and the radially placed tow path as vertical as possible. The images were then cropped to the inside edge of the vertical tows which was a known location.

In Adobe Photoshop, the background was removed, and the tows were painted one solid color. The process from a scanned image to this point is shown in Figure 44. The PP flash was included in the tow path for the base layer. This inclusion and the variability of tow width will decrease the layup accuracy as the midpoint of each shift-width is perturbed slightly. Each of the 8 tow paths were separated into 8 images in Photoshop. These images were opened in Inkscape so the bitmap images could be scanned, traced and saved as a scalable vector graphics (SVG) file. Next the SVG files were imported into Blender where the background layer was deleted. The individual tow path layer was converted to a mesh; it was then exported as a Stereolithography (STL) file. In Meshlab, the STL file was scaled to the correct size and then converted to a point cloud (XYZ) file. The point cloud paths were inputted into an excel spreadsheet where sort was used to arrange the data points by increasing x axis values. A Matlab script (called Tow_edge.m) was run to separate the points into two data sets, one for each edge of the tow. This program reduced the number of points so that one point every 0.1 mm in the x axis was created; these points were exported back into excel. After running the Tow_edge.m for each of the eight paths, a separate matlab script (Get_Results.m) was run. This program calculated the slope of the center of the bottom tow; all of the fiber paths were rotated to make this slope zero. Each path was then shifted in the y direction by the difference between the center of the bottom tow and the coded path. Positions, error, shift width, shear angle, and slope were calculated for all of the paths and then exported into excel for analysis. The scripts for Tow_edge.m and Get_Results.m can be found in Section 9.3 of the appendix.

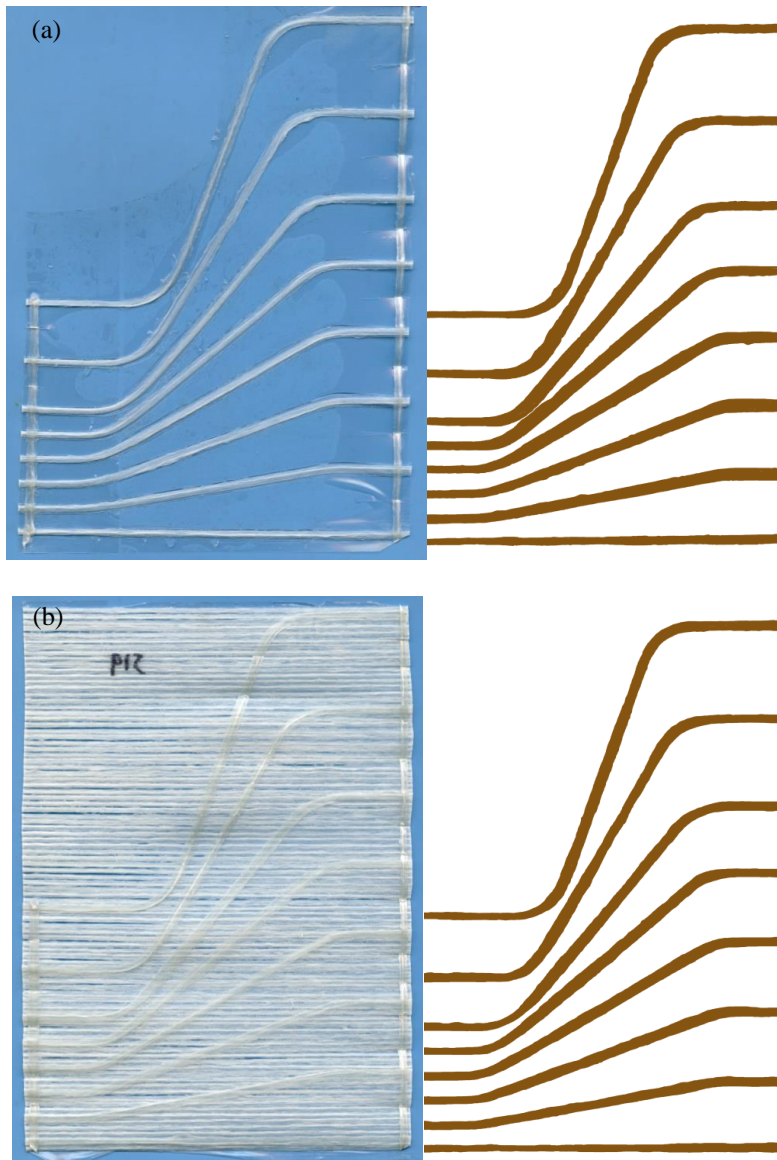


Figure 44: The process from a scanned image to an image with just the fiber paths is shown for a PP deposition surface (Sample 2) (a) and a glass fiber PP deposition surface (Sample 19) (b).

4.4 Post-Processing for Mechanical Performance

After the samples were manufactured, a soldering iron was used to bend the unbonded ends apart. These unbonded ends were inserted into the Instron mechanical testing machine as shown in Figure 45. A 10lb load cell and a crosshead speed of 10in/min were used as specified in ASTM D1876-08. This standard also recommends testing ten specimens over a bonded

distance of 9 inches. Due to the machine limitations, only five samples were tested over a minimum bonded distance of 4 inches.

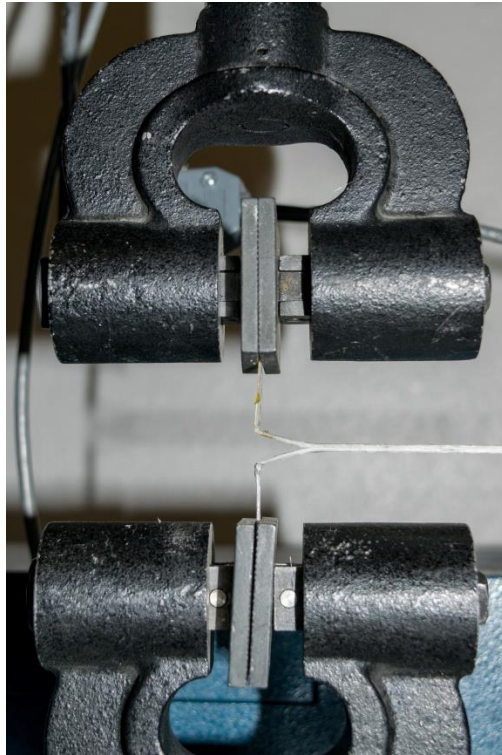


Figure 45: Instron mechanical testing machine setup for a t-peel specimen.

The sixth sample was sectioned in two different locations and prepared for metallographic analysis. Four different cross sections were imaged and then analyzed in Adobe Photoshop. After scaling the images, the composite, flash, intraply, and interply void areas were selected and quantified. An example of the selected areas is shown in Figure 46. Flash was considered the PP dominant region on the edges of the composite. If voids were present within this region, the void was considered part of the flash. Intraply voids were considered as those within a tow while interply voids were those between tows. Void percentages should be taken as conservative estimates as the area around a void often appears white as well due to the grinding

and polishing process. Photomicrograph images for all the other samples can be viewed in Section 9.4 of the appendix.

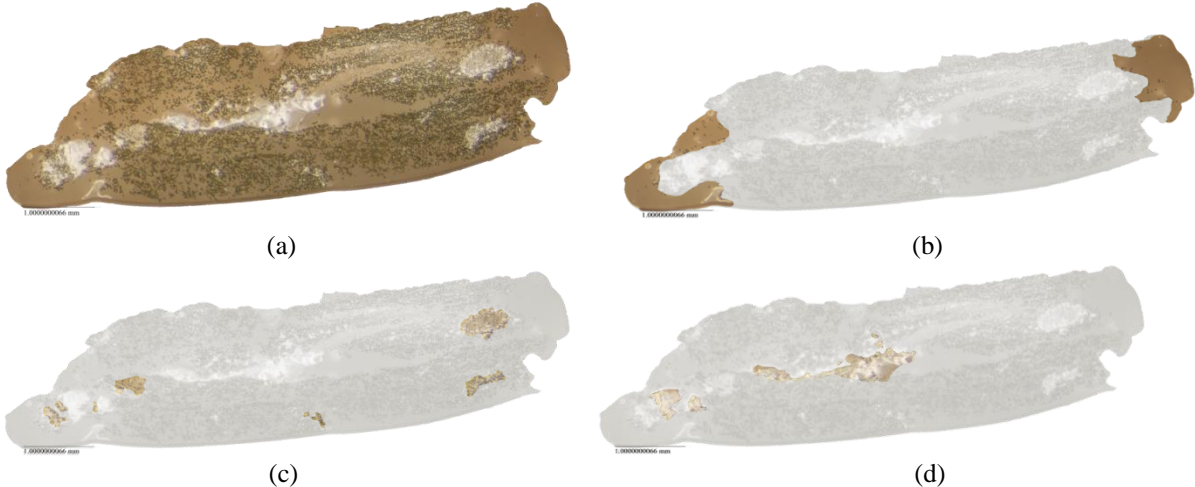


Figure 46: Adobe Photoshop was used to select and quantify the area of the composite (a), flash (b), intraply voids (c), and interply voids (d).

5. RESULTS

5.1 Tow Positional Fidelity Graphs

Thirty-six glass fiber polypropylene tows were produced and then processed using the previously described methods to analyze tow positional fidelity. Graphs similar to the study by Kim et al. were first produced. Comparisons will not be made to Kim's study as the material and machine head utilized to continuously shear the tow are completely different in this study. Instead, comparisons will be made to other samples manufactured.

The first graph produced compares the tow edges, shown by solid lines in Figure 47 and Figure 48, to the programmed tow path, shown by dotted lines in Figure 47 and Figure 48. This graph was generated for all thirty-six samples; the paths for Sample 33 and Sample 34 are shown as examples in Figure 47 and Figure 48. Sample 33 and 34 were processed with a glass fiber/ PP deposition surface, a feed rate of 300 mm/min, and an average measured hot end temperature of 375°C and 397°C. The major difference in processing was the presence of AC in Sample 33.

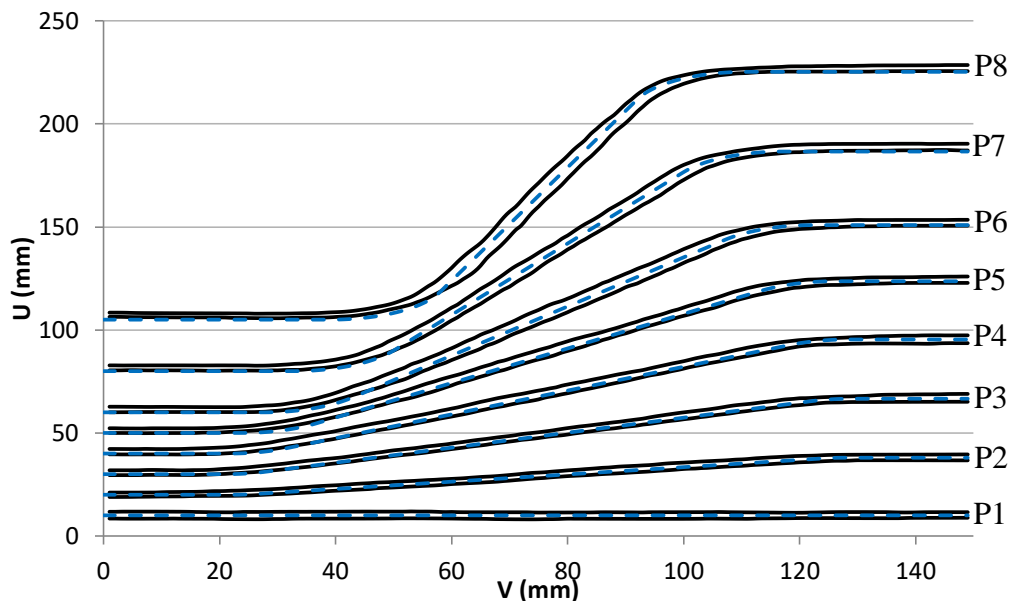


Figure 47: The tow edges (solid lines) and programmed tow path (dotted lines) for Sample 33 are shown.

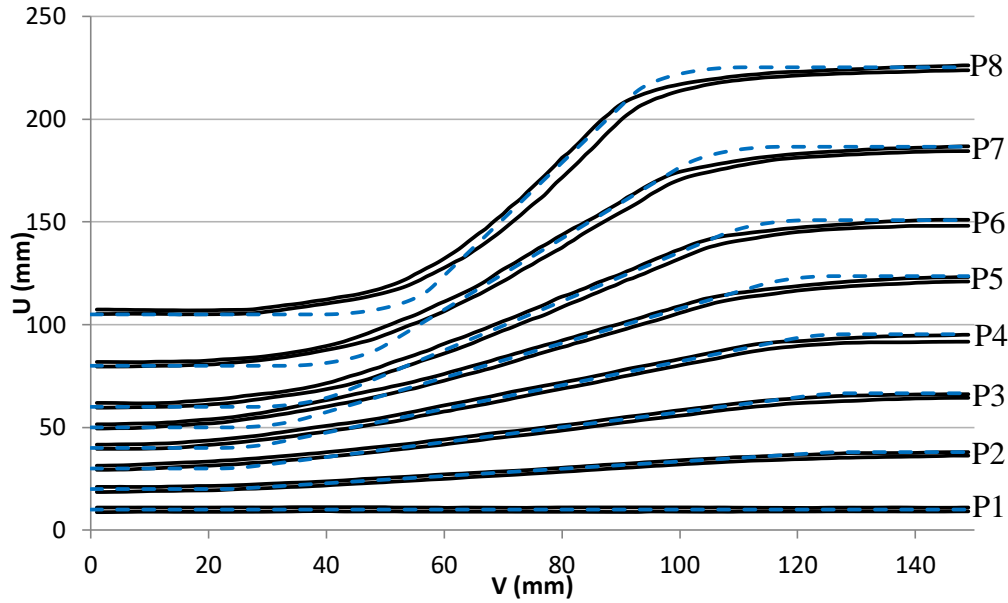


Figure 48: The tow edges (solid lines) and programmed tow path (dotted lines) for Sample 34 are shown.

In the figures, the band width changes throughout with the largest width taking place during the constant angle portions. Path 1 (P1), which was the first path placed, has good alignment with the programmed path while the last path placed, Path 8 (P8), performed much worse. It initially started off the programmed path position by a couple mm.

The main difference in positional fidelity between the two samples is the performance on the 20 mm radius turns. Even at a maximum shear angle as low as a 20° , Sample 34 leads the programmed path on the first turn; the leading effect increases as the maximum shear angle increases. This same effect can be observed on the turn back to the longitudinal path. The AC sample (S35) performed much better with only minor instances in which it is leading the programmed path.

Shift width was defined as the vertical difference between intersection points P_1 and P_2 shown in Figure 21. Figure 49 displays a five point moving average of the shift-width as it progresses along the mandrel axis for Samples 33 and 34. The moving average in this graph and

subsequent graphs will cause a slight lag behind the actual performance. Above a maximum shear angle of 40° , the shift width significantly increases. Sample 33 has larger shift widths with maximum points occurring earlier than Sample 34.

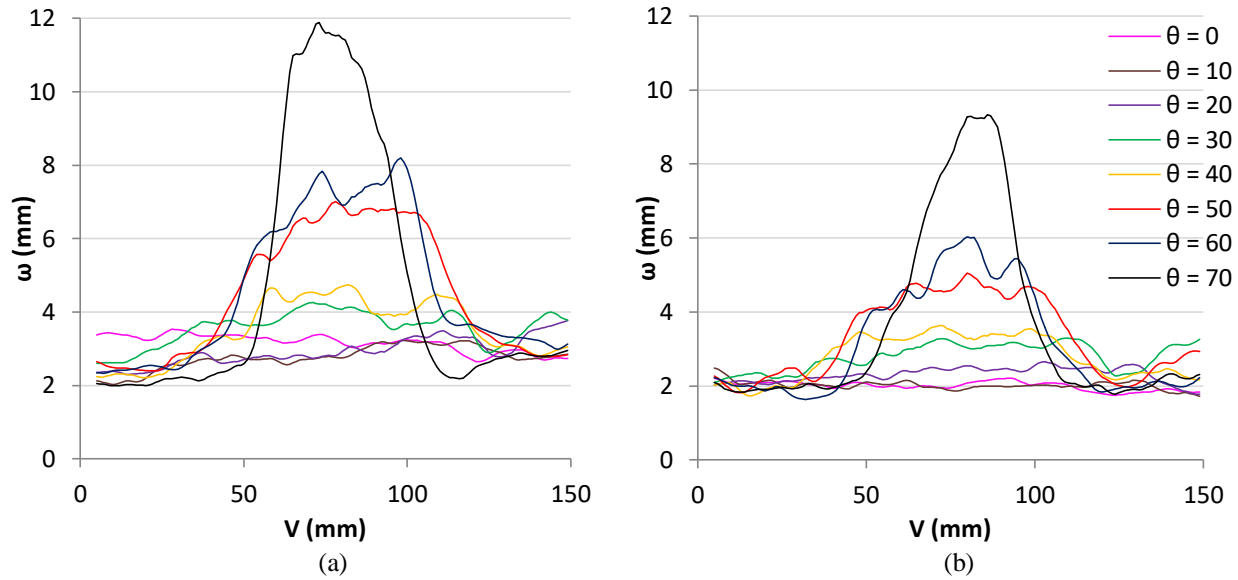


Figure 49: The shift-width for Sample 33 (a) and Sample 34 (b) as it progresses along the mandrel axis.

The tangent angles, θ_i and θ_j , were found from each edge of the tow. Averaging these fiber angles allows the shear angle to be determined. Figure 50 displays a five point moving average of the shear angle as it progresses along the mandrel axis for Samples 33 and 34. For each of the paths for Sample 34, the shear angle tapers to the maximum shear angle value. Much more abrupt transitions are present in Sample 33 as evident by the plateau that is observed in each of the paths.

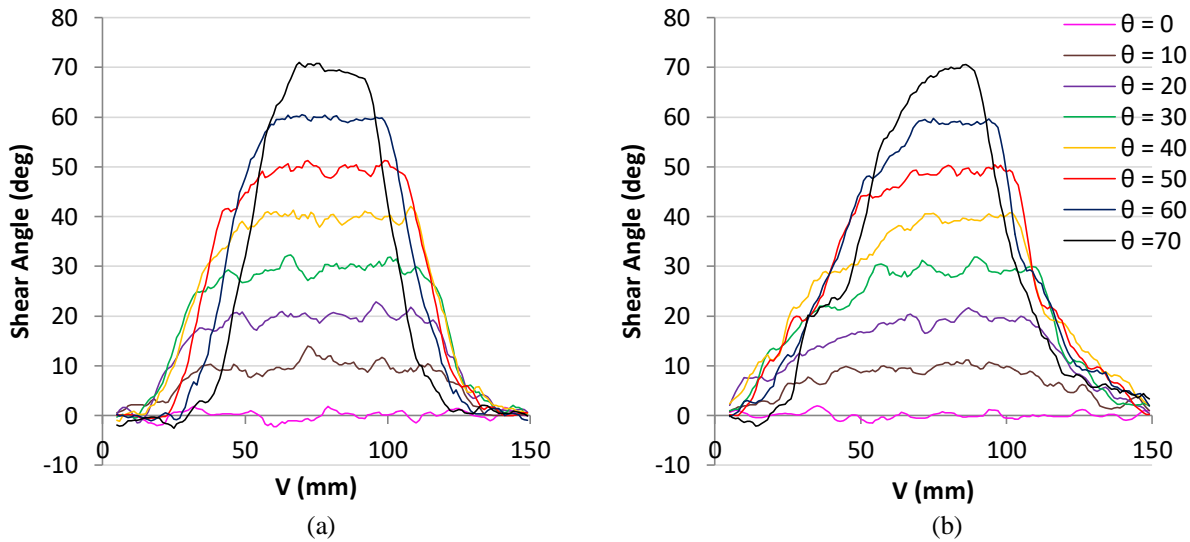


Figure 50: The shear angle for Sample 33 (a) and Sample 34 (b) as it progresses along the mandrel axis.

The above graphs, similar to those produced by Kim, are useful when comparing just one or two samples. In this study, with 36 different samples, it is more pertinent to compare one individual path between the samples. Paths with a maximum shear angle of 70° possess the most variation. For this reason, a 70° maximum shear angle path with each sample will be primarily analyzed with graphs of the shear angle, shift width, and error in the following sections.

5.1.1 Shear Angle

Figure 51 and Figure 52 depicts a three point moving average for the shear angle for samples with a PP deposition surface. The green, black, and red lines signify samples that were processed with a hot end temperature of 400°C , 350°C and 300°C . The solid, large dash and small dash lines correspond with feed rates of 400, 300 and 200 mm/min. Lastly, the solid blue line represents the programmed path.

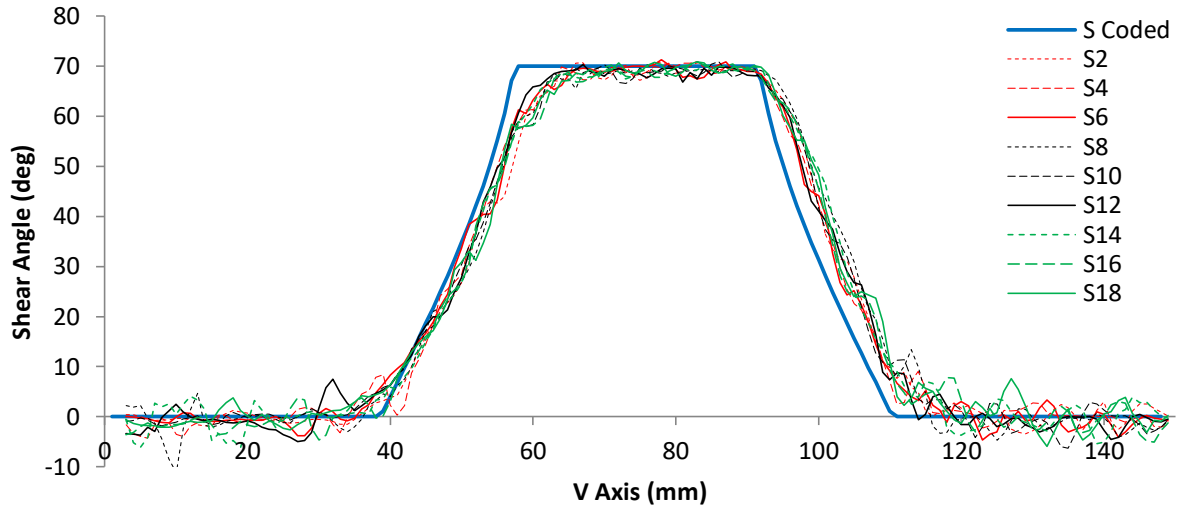


Figure 51: The shear angle as the path progresses along the mandrel axis for samples with no air cooling and a PP deposition surface.

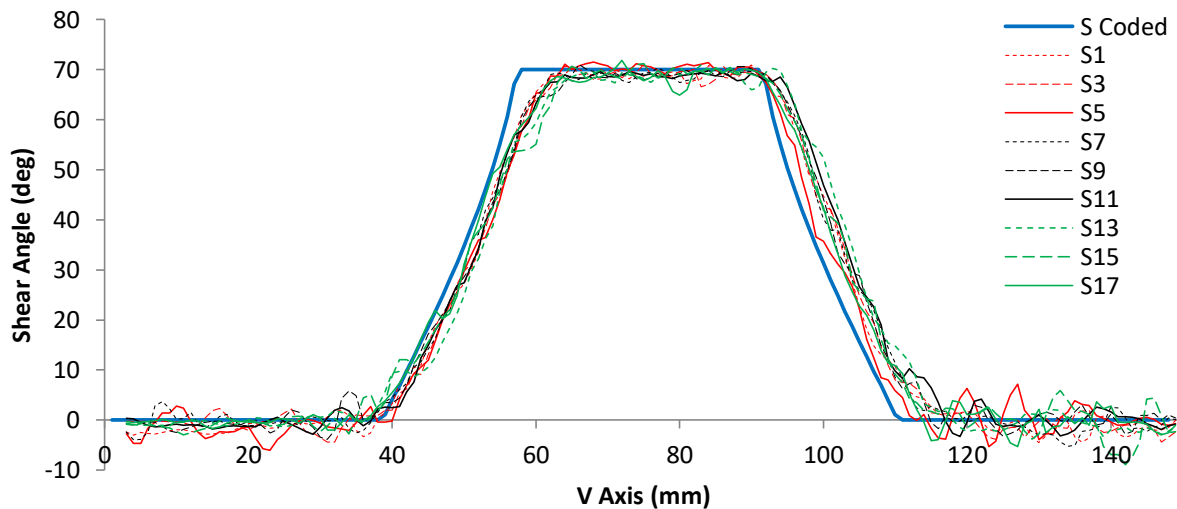


Figure 52: The shear angle as the path progresses along the mandrel axis for samples with air cooling and a PP deposition surface.

In both figures, the transition to the constant shear angle varies slightly more from the programmed path than the transition back to the longitudinal path. For the most part, there is little variation present between the samples. The AC samples have less variance and do not lag quite as much as the non-AC samples.

Figure 53 depicts a three point moving average of the shear angles for a feed rate of 400 mm/min (a) and 200 mm/min (b) on a PP/GF deposition surface. The red lines correspond to AC samples, while the black lines correspond to non-AC samples. The solid, large dash and small dash lines correspond with 400°C, 350°C, and 300°C hot end set point temperatures. The center solid blue line represents the coded path; the other solid blue lines represent a 5 mm lead and lag path. The diameter of the flat end of the nozzle used for consolidation is 11.42 mm (see Figure 24); therefore, the 5 mm lead and lag paths are a conservative estimate for the heat affected zone during fiber placement.

When compared to the PP deposition surface graphs, the PP/GF has considerably more variation from the coded paths. Feed rate has a huge effect on the fidelity of the non-AC samples especially during the transition to a constant shear angle. The higher temperature samples, 36 and 30, in Figure 53 deviate extremely from the heat affected zone area on this transition due to tow sliding. There is significantly less deviation on the transition back to longitudinal; feed rate is not as sensitive on this transition when you compare samples 36 and 30 to 32 and 26. As expected, lower temperatures (24 & 20) are less reactive to changes in feed rate. AC samples are minimally responsive to changes in feed rate and hot end temperature as they maintain alignment to a position within the heat affected zone.

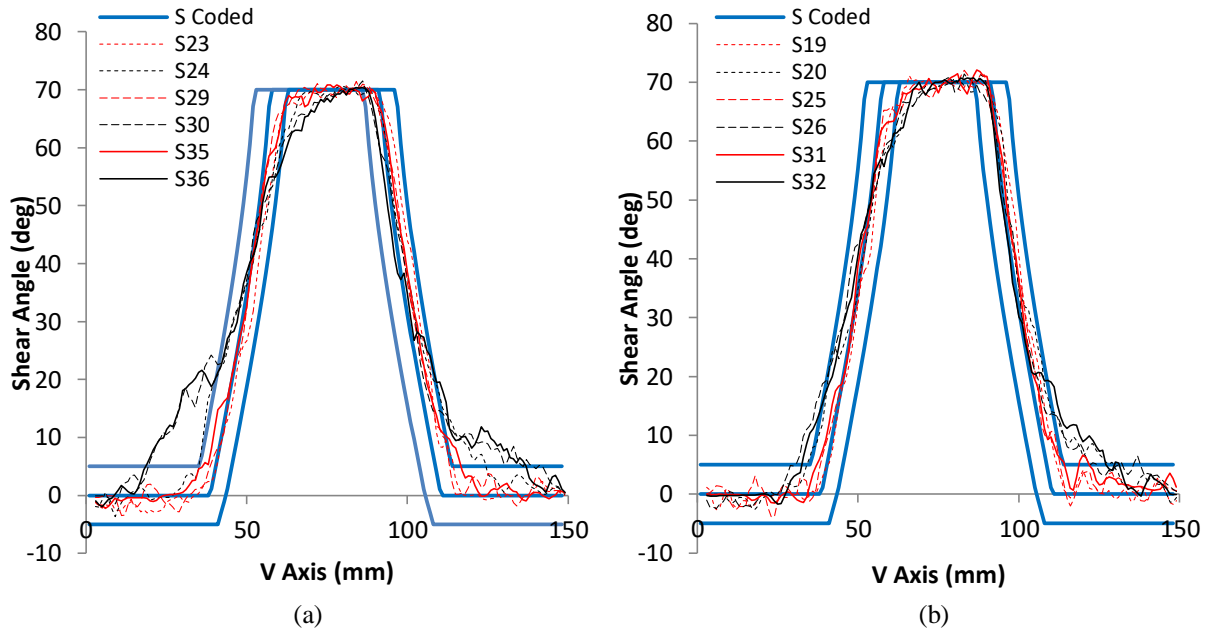


Figure 53: The shear angle as the path progresses along the mandrel axis for samples on a PP/GF deposition surface with a feedrate of 400 mm/min (a) and 200 mm/min (b).

Another perspective on the previously described trends can be observed through three point moving average graphs of the shear angles for a hot end set temperature of 400°C (a) and 300°C (b) as shown in Figure 54. In this graph, the solid, large dash and small dash lines correspond with feed rates of 400, 300 and 200 mm/min. Greater responsiveness is again observed on the transition to a constant shear angle at higher temperatures, at higher feed rates, and in the non-AC samples.

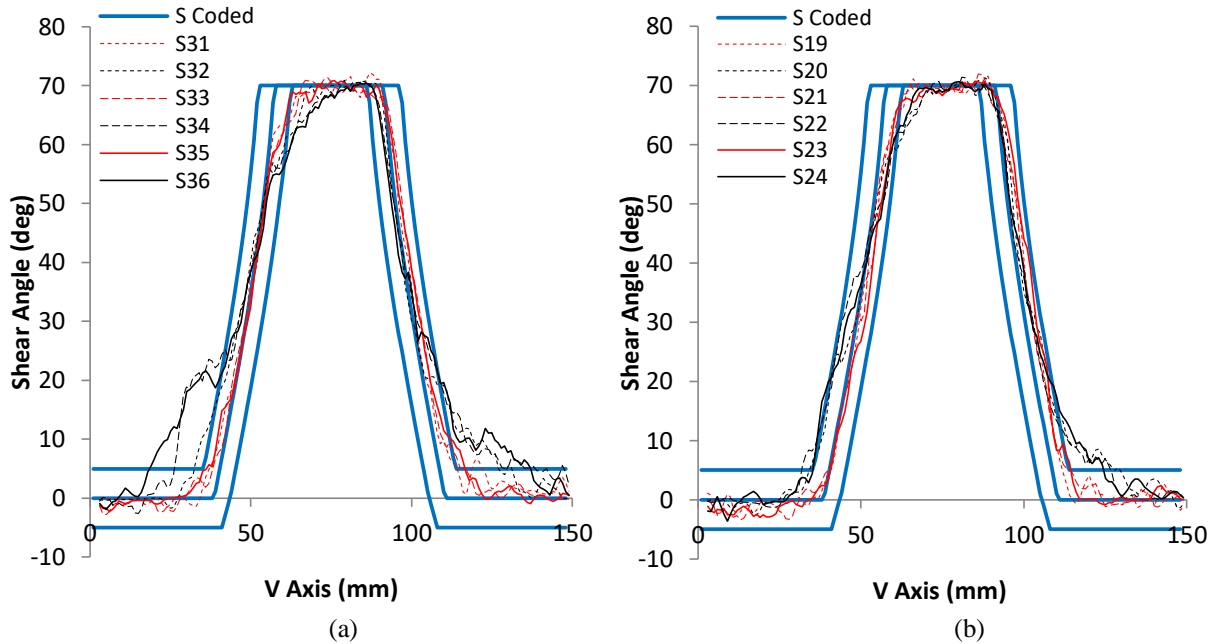


Figure 54: The shear angle as the path progresses along the mandrel axis for samples on a PP/GF deposition surface with a hot end set temperature of 400°C (a) and 300°C (b).

The effect of feed rate and temperature is evident even at a maximum shear angle of 10°. Figure 55 depicts the shear angles for a feed rate of 400 mm/min on a PP/GF deposition surface. The red lines correspond with AC, while the black lines correspond with no AC. The solid, large dash, and small dash lines correspond with 400°C, 350°C, and 300°C hot end set point temperatures. A five point moving average trend line was used. A plateau region is much more evident in the AC samples and Sample 24 which was processed at the lowest temperature. The non-AC samples processed at higher temperatures possess a taper which causes the shear angle curve to materialize as an upside-down parabola. This graph confirms the assumption that higher maximum shear angles will exacerbate the trends making them easier to interpret. Graphs of the shear angles for every path can be found in Section 9.6 of the appendix.

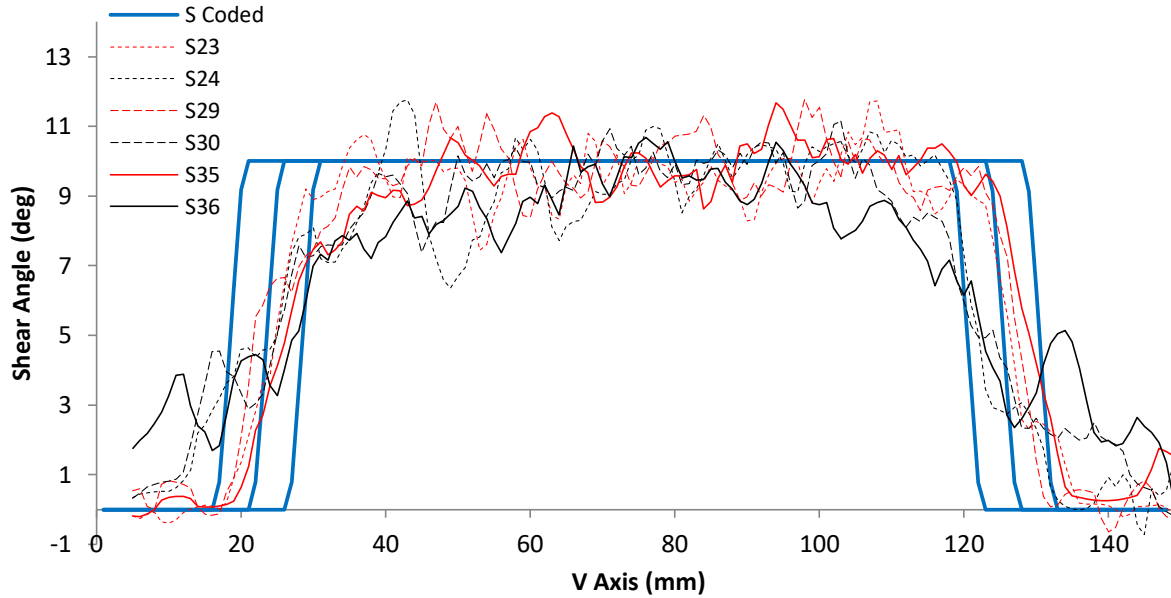


Figure 55: The shear angle as the path progresses along the mandrel axis for samples on a PP/GF deposition surface with a feed rate of 400 mm/min.

5.1.2 Shift Width Graphs

Figure 56 depicts a three point moving average shift width with and without AC on a PP deposition surface. In this graph, the solid, large dash, and small dash lines correspond with feed rates of 400, 300 and 200 mm/min. The green, black, and red lines signify samples that were processed with a hot end temperature of 400°C, 350°C, and 300°C. The solid blue line represents the path of the placed tow; it helps to evaluate when the changes in shift width are occurring. The shift widths at the end of the paths are slightly higher than the beginning when longitudinal paths should be equivalent.

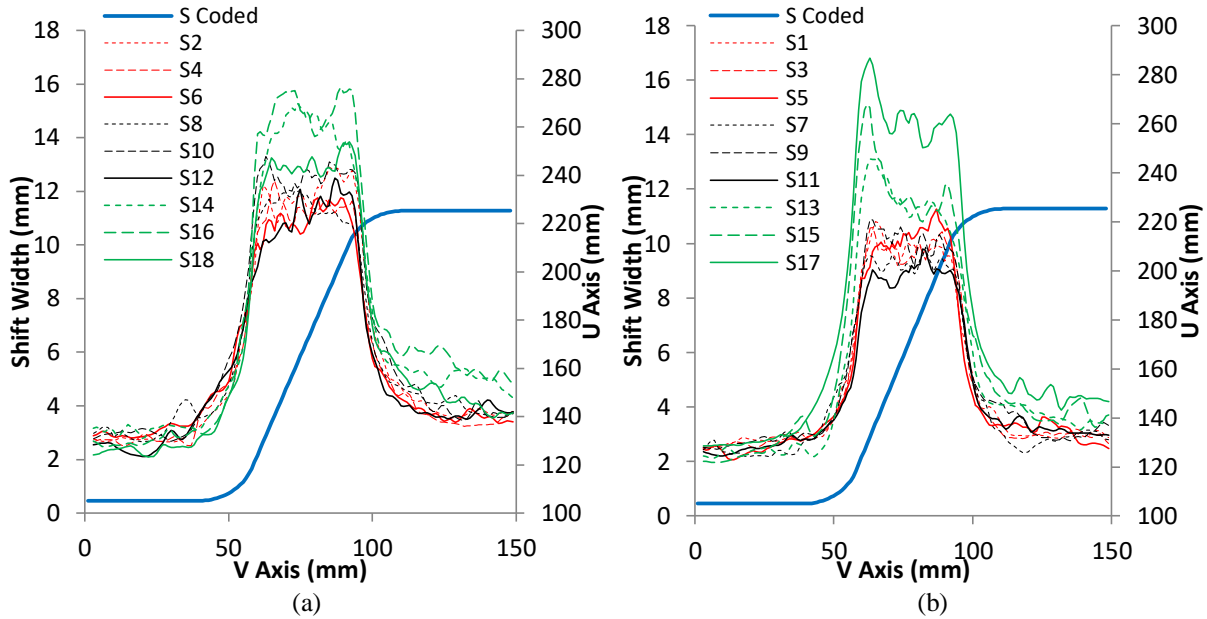


Figure 56: The shift width as the path progresses along the mandrel axis for samples on a PP deposition surface without AC (a) and with AC (b).

Higher hot end temperatures, regardless of AC, resulted in higher shift widths. There is much less variation at the two lower processing temperatures. At the highest processing temperature, the maximum shift width value occurred at the end of the initial transition to a constant shear angle in the AC samples; a clear maximum shift width is not present in the non-AC samples. When comparing AC to non-AC samples, higher shift width plateaus are found in the non-AC samples; S17 is the only exception.

Figure 57 depicts a three point moving average shift width with and without AC on a PP deposition surface. Line colors and types correspond with the previous figure analyzed. Shift width values are much higher with AC than without AC; in addition, the width of the plateau in shift width values is noticeably decreased (thinner) without AC than with AC. A true plateau isn't evident in many of the non-AC samples. Greater consistency is present in these samples as well. With both AC and non-AC samples, the highest temperatures resulted in the lowest shift widths values.

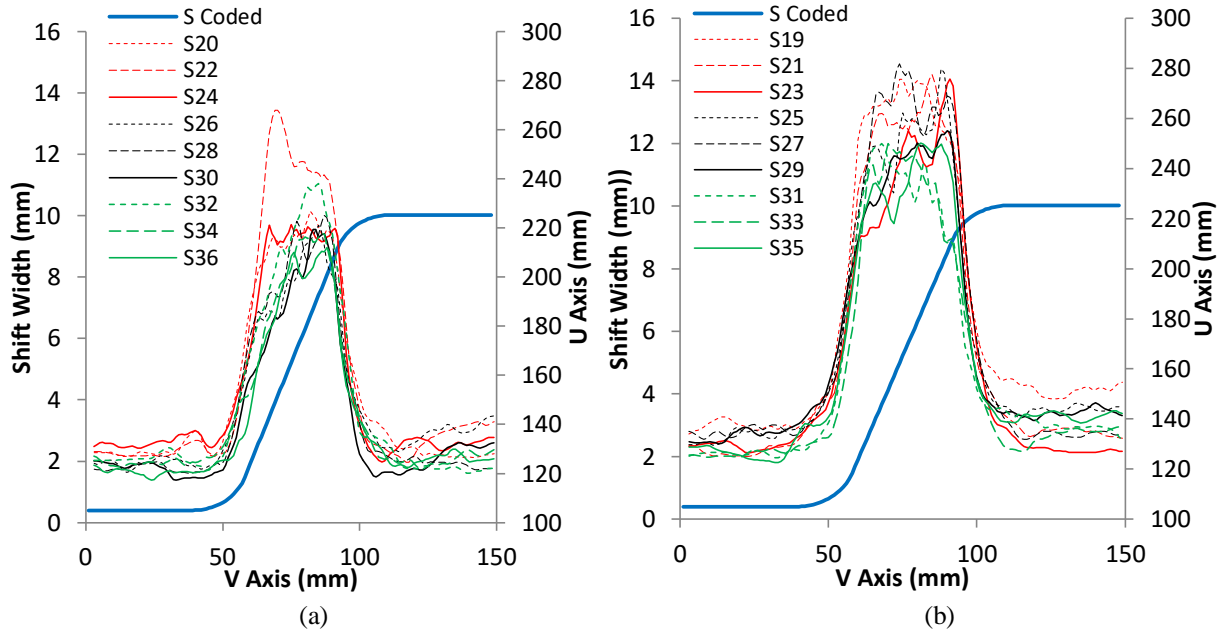


Figure 57: The shift width as the path progresses along the mandrel axis for samples on a PP/GF deposition surface without AC (a) and with AC (b).

The PP deposition surface shift width graphs have a much more prominent plateau region than the PP/GF deposition surface shift width graphs. The AC PP/GF deposition surface graphs have a comparable plateau region width to the PP deposition surface graphs. The major difference is the performance at the highest temperatures. On a PP deposition surface, the highest hot end set temperatures produced the highest shift width values. With the PP/GF deposition surface, the highest hot end set temperatures produced the lowest shift width values. Lastly, higher plateaus in shift width were present in the non-AC samples on the PP deposition surface, while the AC samples produced the higher plateaus on the PP/GF deposition surface.

The effect of some of the previously described trends is much more evident in Figure 58. In this graph, the solid, large dash and small dash lines correspond with feed rates of 400, 300 and 200 mm/min. The programmed path of the placed tow is represented by the solid blue line. A three point moving average trend line was used.

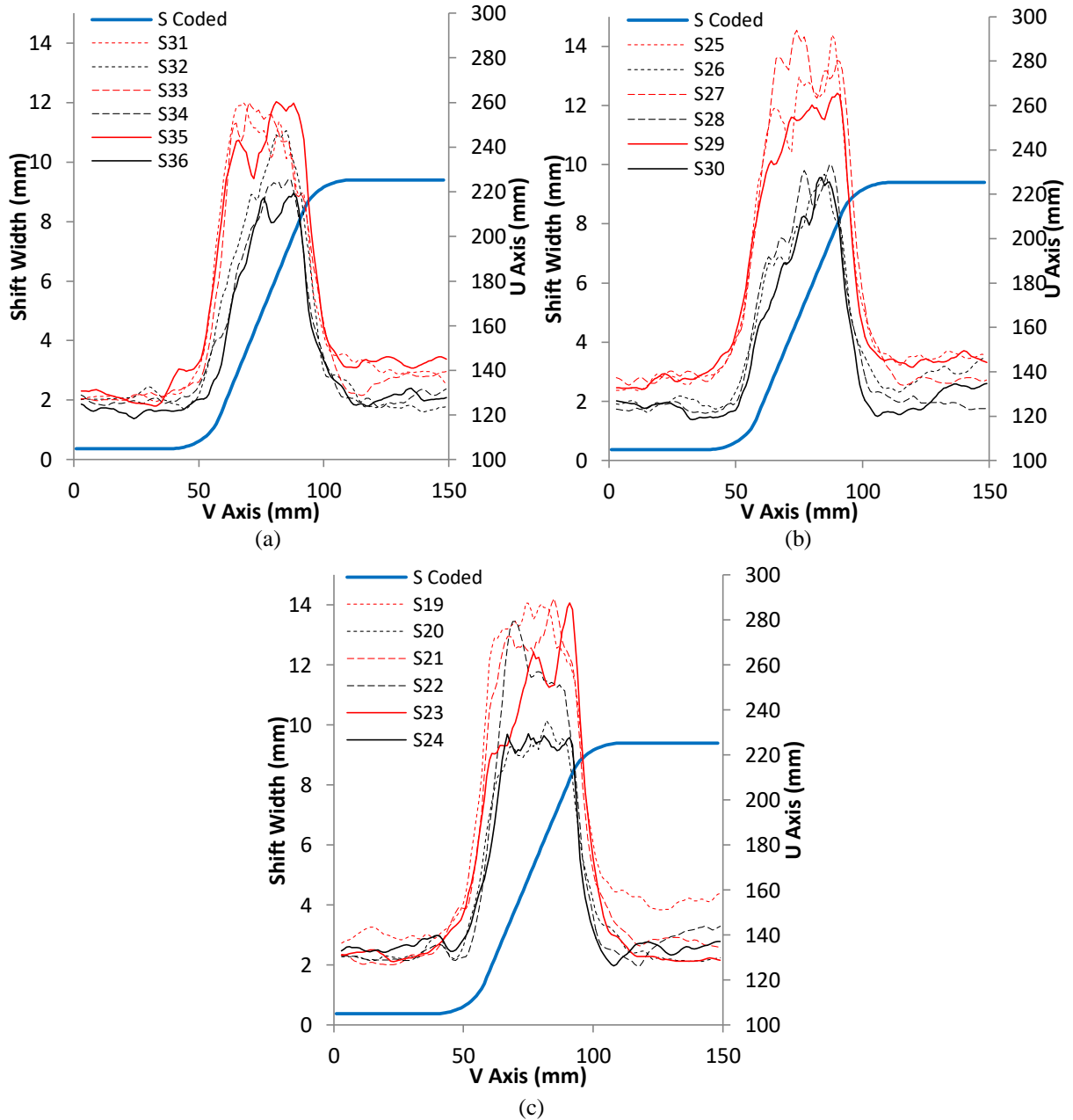


Figure 58: The shift width as the path progresses along the mandrel axis for samples on a PP/GF deposition surface with a hot end set temperature of 400°C (a), 350°C (b) and 300°C (c).

The absence of a plateau is clearly evident in the non-AC samples at the two higher temperatures. A delayed response to the 20 mm radius turn occurs in these samples. During the constant shear angle portion, a gradual taper ensues until a maximum point at the start of the

transition back to longitudinal. This taper is less distinct but still present in the highest feed rate samples with AC at each hot end temperature (S23, S29, & S35).

In order to better understand the changes in tow or band width occurring with fiber angle variation, the tow width as the path progresses along the mandrel axis is shown in Figure 59. Tow width was calculated from the shift width and the reference tangent angle θ_r . The same trends evident in the shift width graphs are present here. The actual increase in tow width during the transitions and 70° maximum shear angle are more apparent. During the constant shear angle portion of the path, tow width increased by greater than 50% over the initial width; the width even doubled in some samples. A similar width increase is present with the samples produced on a PP deposition surface (not shown). With both deposition surfaces, width values tend to gradually increase until a point within the transition region back to a longitudinal path. Width values are higher for the AC samples on the PP/GF deposition surface. Graphs of the shift widths for every path can be found in Section 9.7 of the appendix.

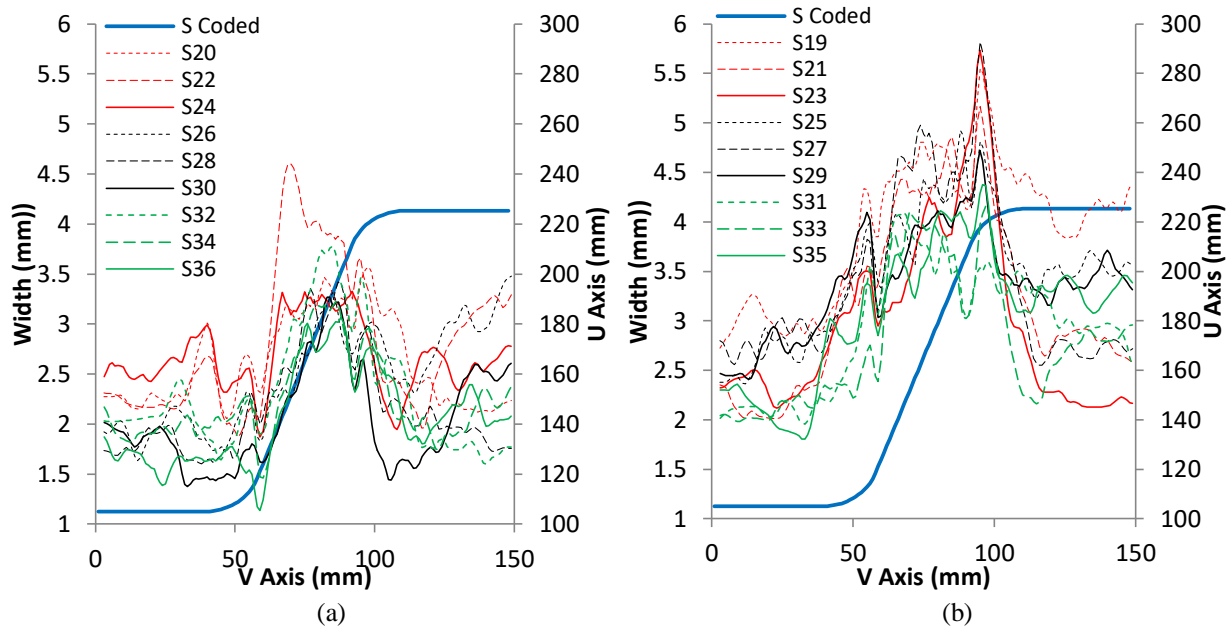


Figure 59: The tow width as the path progresses along the mandrel axis for samples on a PP/GF deposition surface without AC (a) and with AC (b).

5.1.3 Error Graphs

For the following graphs, error is defined as the coded value minus the average value of the tow edges. Therefore, a positive error value can be equated with lagging the programmed path for the initial turn, while a negative error value can be equated with leading the programmed path for the initial turn. The opposite is true for the final 20 mm radius turn. Since tow edge values are used in these calculations, error is referred to as the vertical positional error e .

Figure 60 depicts a three point moving average for error without (a) and with AC (b) on a PP deposition surface. The solid, large dash, and small dash lines correspond with feed rates of 400, 300, and 200 mm/min. The green, black, and red lines signify samples that were processed with a hot end temperature of 400°C, 350°C, and 300°C. The solid blue line represents the path of the placed tow

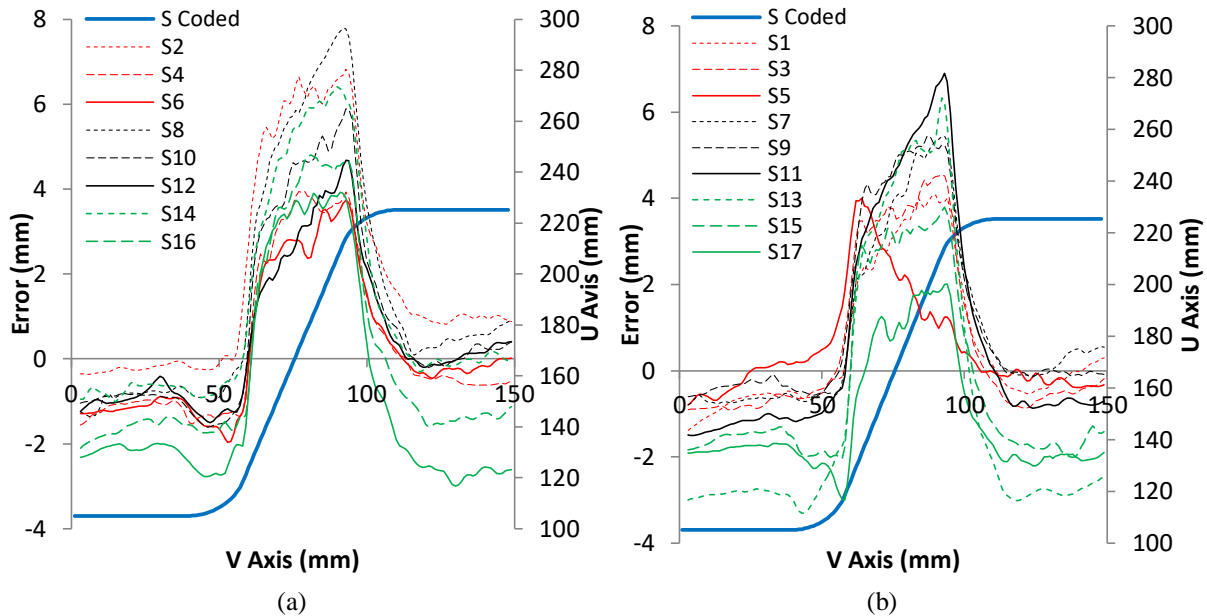


Figure 60: Error as the path progresses along the mandrel axis for samples on a PP deposition surface without AC (a) and with AC (b).

All the samples should start with an initial error of 0. Regardless, error stays consistent until the initial 20 mm radius turn. At this point, the error increases sharply as it begins lagging

the programmed path. At a constant shear angle, the error increases gradually to a maximum value as the actual shear angle is slightly less than the programmed shear angle. S5 is the only exception to this trend as the error decreased during the constant shear angle path; the actual shear angle must have been larger than the programmed shear angle. Once the 20 mm radius which turns back to a longitudinal path is reached, the error decreases sharply back to zero. Error then stays consistent throughout the longitudinal path.

Trends are not as discernable in Figure 60. There is a slight error reduction in the AC samples over the non-AC samples. In the non-AC samples, higher feed rates corresponded with lower error. With the exception of Sample 11, this trend holds true for the AC samples as well. No other trends associated with feed rates or hot end temperatures are evident.

The error on the PP/GF deposition surface shown in Figure 61 is much more counter-intuitive. The error in the samples without AC was consistent for a very short time; error started to gradually increase in the leading direction significantly before the 20 mm radius turn. Higher feed rates and hot end temperature combinations resulted in earlier commencement and higher magnitudes of this leading error that is attributed to tow sliding. At the constant shear angle, error spiked back past zero and into a slight lagging state. At some intermediate point during the constant shear angle path, the error became relatively constant. Error spiked again as the 20 mm radius turn was reached implying tow sliding is causing a leading error. It then gradually decreased back to zero during the turn and the longitudinal path. The higher feed rate and hot end temperature combinations took much longer to get to zero if they were able to even get to that point.

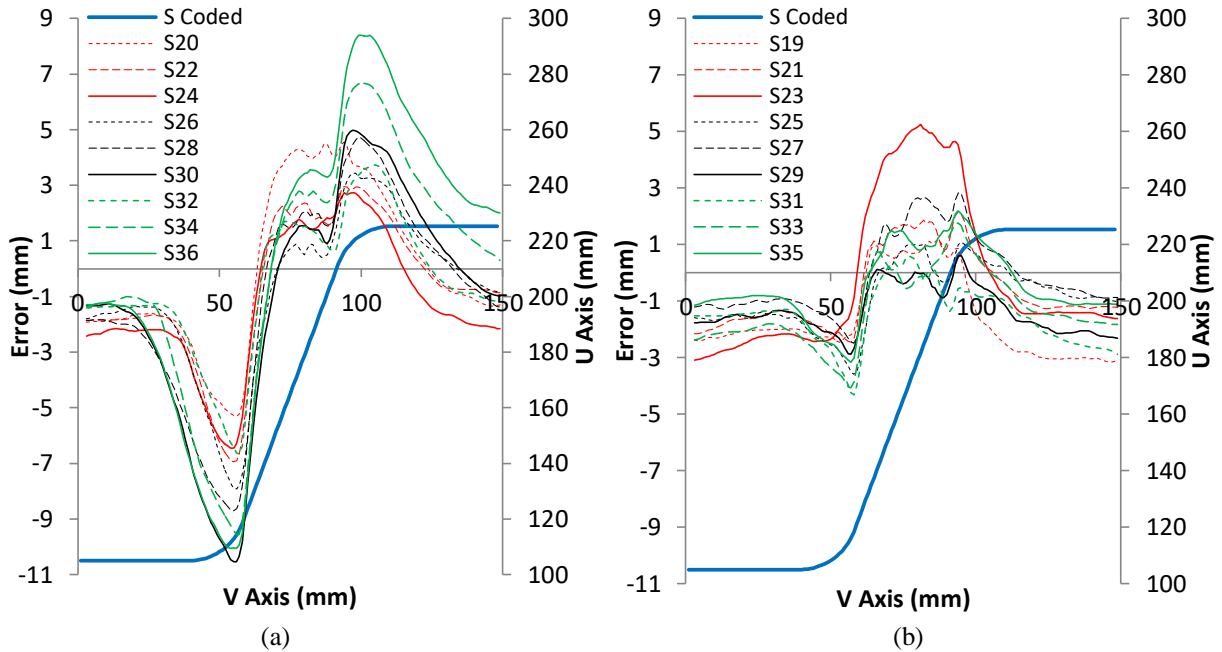


Figure 61: Error as the path progresses along the mandrel axis for samples on a PP/GF deposition surface without AC (a) and with AC (b).

Errors in the samples with AC were significantly diminished over those without AC. A similar error profile to the samples without AC was observed albeit in a reduced manner. The sensitivity to feed rate and hot end temperature that occurred in the non-AC samples was not clearly present in the AC samples. For the AC samples with a PP/GF deposition surface, the error profile was consistently less than 6 mm with a worst case sample of approximately 8mm. For the non-AC samples, the error profile fluctuated with a minimum profile of 10 mm and a worst case profile of 18mm. The 56% reduction in the error profile of the worst performing samples of each group shows the benefit of AC in achieving positional fidelity. When comparing the PP/GF deposition surface with the PP deposition surface, the error significantly increased for the non-AC samples whereas the error decreased for the AC samples. Graphs of the error for every path can be found in Section 9.8 of the appendix.

5.2 Composite Beam Analysis

Six four layer beams for the first 18 samples of Table 4 were manufactured at the same time as the positional fidelity samples. Five of these samples were prepped for T-Peel testing while the sixth sample was used for microscopy analysis. As shown in Figure 62, the manufactured specimens appeared noticeably different; they were classified into one of the following three different categories: 1.) discreet tows prominent completely within the sample; 2.) non-discrete tows that cannot be distinguished in the sample; 3.) in between tows that could partially be distinguished but were not prominent. All the non-AC samples fit within the discreet tow classification. Samples 7 and 13 were categorized as in between while the rest of the AC samples were classified as non-discrete. Photos of all the samples can be found Section 9.5 of the appendix.

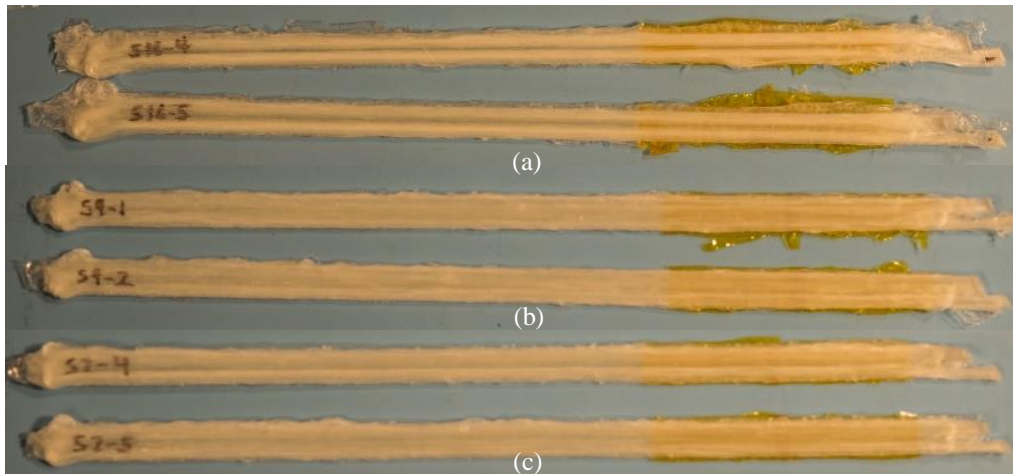


Figure 62: The manufactured specimens shown were classified based on their appearance as discreet (a), non-discreet (b) and in between (c).

5.2.1 T-Peel Results

In accordance with ASTM D1876-08, t-peel samples were tested until failure as shown in Figure 63. Adhesive failure was classified as one in which peeling occurred over the entire length of the sample which consisted of a minimum distance of 3.4 inches. Most of the samples

exhibiting this type of failure peeled between 4-4.5 inches. Adherend failure resulted in buckling of the tows in the top or bottom layer of the composite beam. Once this type of failure occurred, testing was stopped as the load increased significantly due to the tearing of fiber that was now occurring. Failures of this type manifested as early as 0.9 inches of peeling. Adherend failure was present in the following samples: S2 (2x), S4 (2x), S6 (5x), S9(1x), S10 (2x), S11 (1x), S12 (1x), S17 (1x) and S18 (1x).

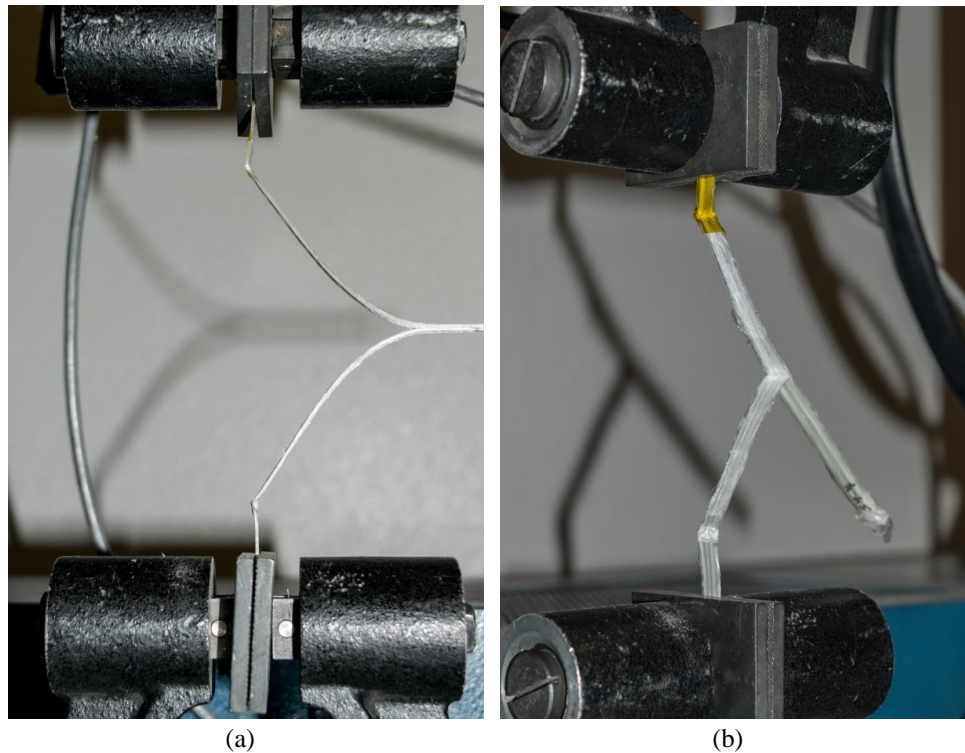


Figure 63: T-peel samples were tested in accordance with ASTM D1876-08. Failure was classified as adhesive (a) or adherend (b) failure.

Figure 64 depicts a failure surface as peeling is ongoing. Fibers pointing away from the failed surface were present in this sample and in most of the other samples tested.



Figure 64: Fiber pullout was evident in most of the adherend surfaces after peeling occurred.

After the completion of testing, load separation charts were produced as shown in Figure 65. Per the ASTM standard, the portion of the curve before the max point was removed and not included in any calculations. In addition, the sharp increase in the curve signifying adherend failure was removed as well. The missing portion of the curve is evident in Figure 65 by the premature stopping of the test prior to the load going to zero in Sample4 -3 and 4-4. Since these curves are incomplete, the data sets are not included in calculations dependent on average load. Other calculations were processed in a similar manner. For Sample 6, which had all five samples exhibit adherend failure, only the data sets with a load curve that decreased to a value below 1 lb were included in the calculations.

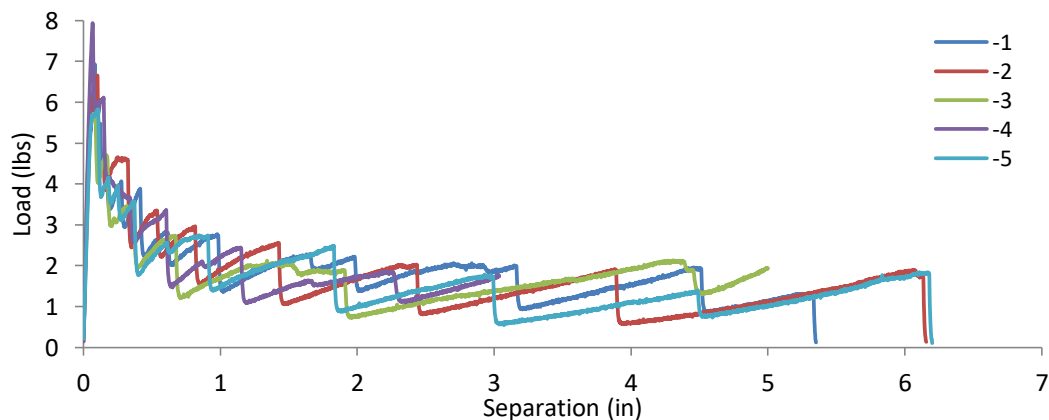


Figure 65: The load separation chart for all five of the beams tested for Sample 4.

The maximum loads from all five tests within a sample set were averaged to create an average maximum load. Similarly the average load for a sample set was found. The average load for each test was divided by the specimen's measured width in order to calculate the peel strength. The peel strength from each of the five tests within a sample set was averaged to create an average peel strength. The average maximum load and average peel strength results are shown in Figure 66. The samples were ordered from the lowest to highest deposition temperature by the resultant PP filament temperature found from the time dependent conduction model in Section 4.2. Since a reliable estimate of the resultant constituent temperatures cannot be made with the AC samples (odd numbered samples), they were grouped first in Figure 66 and the subsequent figures.

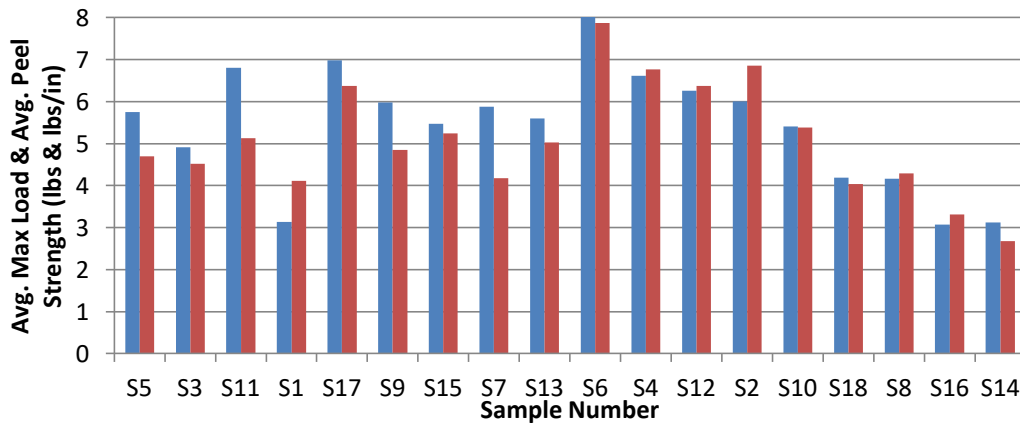


Figure 66: The average maximum load and average peel strength for each sample set are shown.

At each hot end temperature in the samples with AC and no AC, peel strength increased as feed rate increased. The highest feed rate, 400 mm/min, produced the highest peel strengths. For the 300°C and 350°C samples, no AC samples had higher peel strengths than non-AC samples. The samples processed at 400°C with no AC had much lower peel strengths and max loads than any of the other samples with the exception of Sample 1. Deposition temperature increases result in a reduction in peel strength in the non-AC samples. Sample 2 is an exception,

but its average max load is consistent with this trend. A similar trend is not evident with the AC samples. As one would expect, the samples exhibiting adherend failure seemed to possess higher average peel strengths than those samples that exhibited adhesive failure. Lastly, the average maximum loads for the AC samples were higher than the average peel strength values in all the samples except Sample 1. This trend is not evident in the non-AC samples.

5.2.2 Microstructure Results

As previously mentioned, four different cross sectional areas within a sample were analyzed to determine a number of different characteristics. Figure 67 depicts an average area for each of the samples. As the deposition temperature increased, area decreased in the non-AC samples. Sample 2 and 8 are an exception. Although it is not as evident, the AC samples generally show this trend as well.

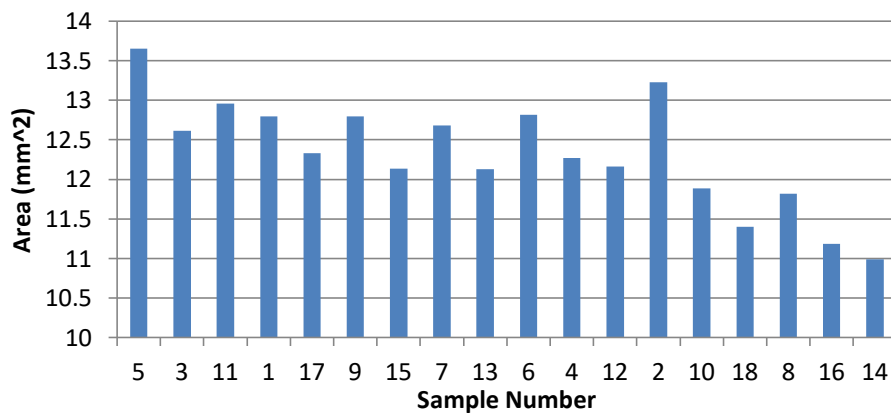


Figure 67: The average area for each of the samples analyzed was determined through microscopy.

Geometry was determined for each of the samples as shown in Figure 68. Theoretically, width should increase slightly as deposition temperature increases due to more flash being present in the sample. Within each hot end temperature set point in the non-AC samples, the slower feed rates, thus higher deposition temperatures, equated to more flash. Only the AC

samples processed at a hot end temperature of 350°C possessed this trend. The complete opposite trend existed in the 400°C AC samples, while the 300°C AC samples were consistent in width.

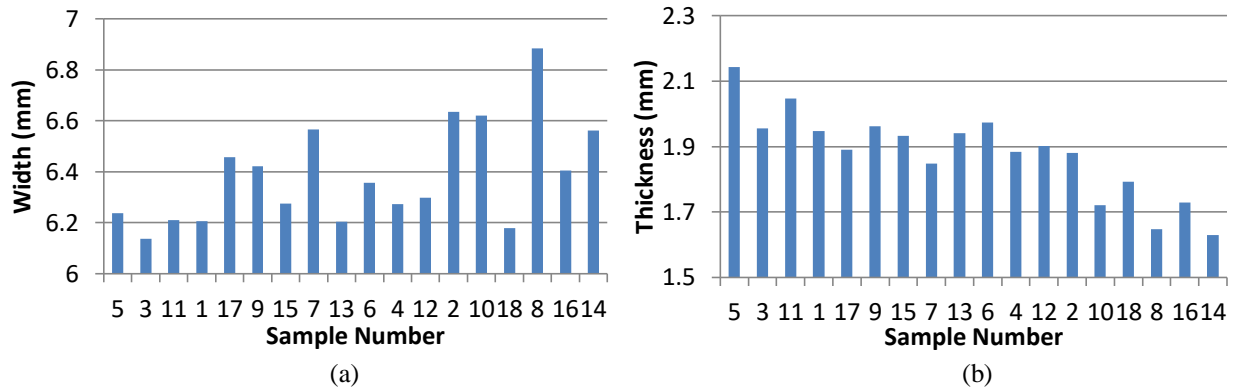


Figure 68: An average width (a) and thickness (b) were calculated via microscopy.

Thickness values should theoretically remain relatively constant around 1.6 mm for the four layer composite due to the programmed 0.4 mm layer height. Instead, the variability in all the samples was greater than the theoretical height of 1 layer. Other than the 400°C AC samples, thickness increased as the feed rate increased for each sample set processed at the same hot end set point. The increase in feed rate is associated with a lower deposition temperature. Lower deposition temperatures produce higher PP viscosity which causes elastic deformation of the system and results in a greater layer height.

In most composites manufacturing processes, flash is an inherent byproduct. After fabrication, trimming operations to remove the flash are typically conducted. Microscopy was utilized to determine flash in the samples. Results, which are displayed in Figure 69, are consistent with the width results in that slower feed rates equated to more flash within a hot end temperature set point for the non-AC samples. A trend with respect to flash amount and slow feed rates is not discernable in the AC samples.

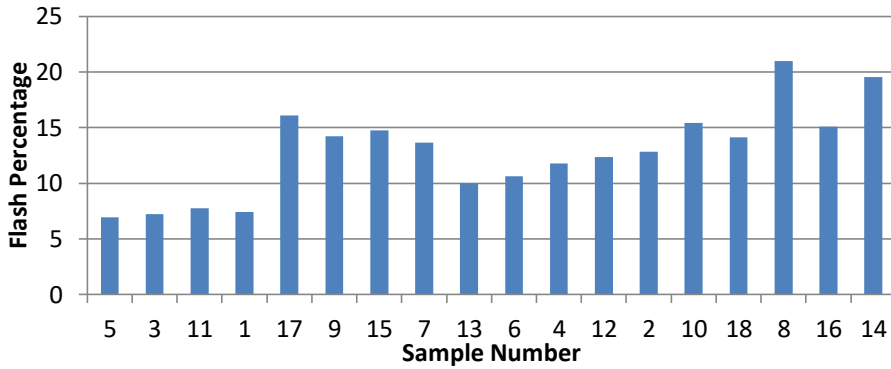


Figure 69: Average flash percentage was determined from each sample through microscopy.

The amount of voids is an important indicator of the quality of a composite. Figure 70 displays the total average void percentage for each sample along with the amount classified as intraply or interply voids. The AC samples possessed less variance in the amount of voids in the composite. The highest feed rate at each hot end temperature contained the most voids in the non-AC samples. Intraply voids are more prominent than interply voids. Low interply void percentages suggest good consolidation between layers. The higher concentration of intraply voids implies entrapped air is present within the tow. Too little consolidation pressure would increase both the interply and intraply voids.

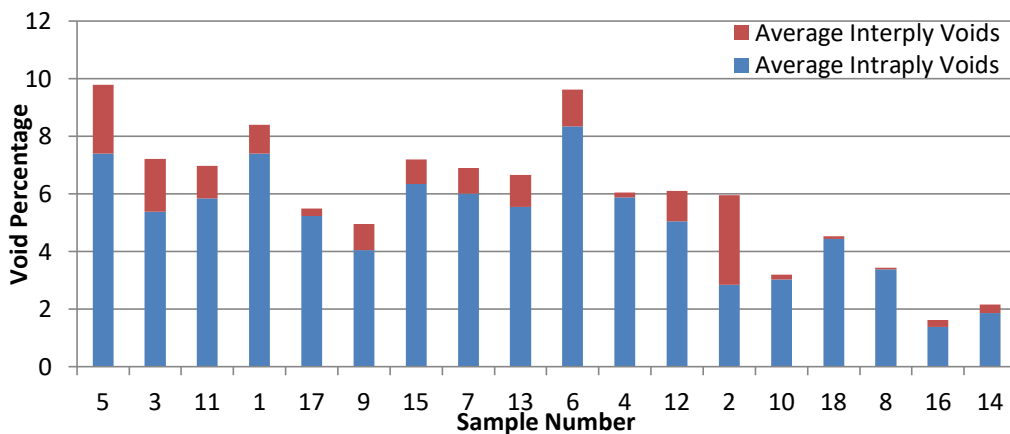


Figure 70: Average void percentage was determined from each sample through microscopy.

6. DISCUSSION

6.1 Effects of Tension on Tow Sliding and Tow Shifting

The results clearly showed that positional fidelity cannot be achieved without AC due to tow sliding. In Section 5.1, tow sliding can be visually seen in the tow edge graphs by the large amount of leading of the tow over the programmed path prior to the initial 20 mm radius turn. In Section 5.1.1, the shear angle increases almost instantaneously when it should be constant until the initial turn. Lastly, in Section 5.1.3, tow sliding is the cause of the excessive leading prior to the first error spike and after the second error spike present on the glass/PP deposition surface.

Tow sliding is completely different than tow shifting. As a tow passes through the hot end, it is pultruded out of the nozzle. Tow solidification on the mandrel is relied on to pull the tow through a hole in the nozzle with a 0.741 mm radius. This hole has a chamfer to a radius of 1.741 mm. During this transition region, filaments within the tow are tessellating or shifting to the substrate surface by shearing past one another with a bias to the shifting direction which is the same direction as the tension inherent to filament winding. The flat portion of the nozzle that extends 5.71 mm outside of the center of the pultrusion hole causes additional consolidation; it also allows adjacent tows to fuse together effectively eliminating the voids present in 3D printed plastics. Tow sliding occurs outside the profile of the nozzle. When the tow is under the nozzle, it is staying fixed due to the consolidation pressure. Imposing shear angle curves 5 mm before and 5 mm after was done Section 5.1.1 to give a better indication what is tow sliding outside the nozzle and what is tow shifting within the profile of the nozzle. Note that tow sliding is not occurring in the AC processed samples, while the non-AC samples exhibit greater tow sliding as feed rate and deposition temperature increase.

The magnitude of tow sliding that occurs is dependent on the forces involved in the tow placement process. The direction of these inherent forces is the reason the transition from a longitudinal path to constant shear angle is much worse than a transition back to the longitudinal. Tension inherent to filament winding (T_{FW}) is strongest on hoop winds; it will aid in consolidation the most with this angle wind. There is also a tension force attributed to the head movement (T_{HM}). Due to the pultrusion-like nature of the process, the origin of the tension forces is the point of tow solidification. Therefore these forces are lagging behind the head with one force in the direction of the current position of the head and the other force in the radial direction. The amount this point lags is dependent on feed rate and hot end temperature. This is why higher temperatures and higher feed rates showed greater responsiveness in the shear angle graphs.

A demonstration of how the tension forces interact with one another to influence the path fidelity is shown in Figure 71. Figure 71 (a) shows the transition from longitudinal path to a constant shear angle where Figure 71 (b) shows the transition back to a longitudinal path. In both figures, the point of solidification shown as the origin the forces is trailing the nozzle head shown as the circle. In Figure 71 (a), the vertical portion of each force is acting on the outside of the tow where the glass fibers are in tension. With a reduced viscosity, these fibers will slowly shift increasing the thickness on the inside radius and decreasing the width of the tow. The curvature of the mandrel allows this increase in thickness to occur even when the tow is still underneath the profile of the nozzle. This effect continues once the nozzle has passed as long as the viscosity is low enough. The decrease in surface area in contact with the previous layer, reduced tackiness from the rapidly increasing viscosity of the thermoplastic and the in plane bending the tow is now experiencing from the two tension forces all contribute to the sliding of

the tow. With significant tow sliding caused by a sharper angle transition, the tow doesn't even re-tack to the previous layer. In Figure 71 (b), the horizontal component of the lone force attributed to head movement must be the cause of tow sliding. The tension inherent to filament winding force actually helps maintain the programmed path.

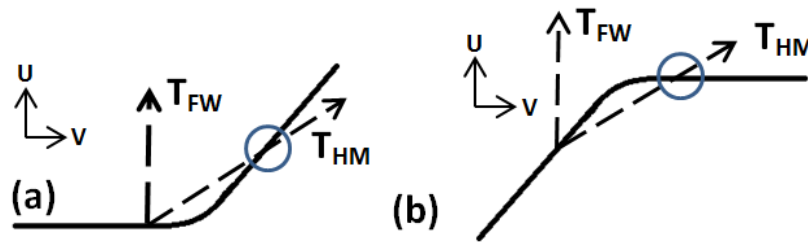


Figure 71: Tension inherent to filament winding and to head movement affect the transition from longitudinal to constant shear angle (a) differently than the transition from constant shear angle to longitudinal (b).

6.2 Effect of Consolidation Mechanisms

The fiber path has a strong influence on the consolidation mechanism being utilized. As a tow moves purely in the longitudinal direction as shown in Figure 72 (a), consolidation is occurring fully by the nozzle. The center part of the tow, shown by the darker blue box, is receiving more pressure than the edges of the tow shown by the lighter blue box. This pressure gradient within the tow exists due to the additional 2.5% area attributed to the mandrel radius. Although some fiber shifting can occur due to the radius of the mandrel, shifting of the glass fibers within the tow is largely restricted by the flat end of the nozzle and the lower pressure present at the tow edges. As a tow moves at a larger and larger angle, a lower percentage of the total consolidation is occurring from the nozzle because the contact area between the nozzle and tow is reduced due to the mandrel's curvature. This is shown in Figure 72 (b). At a shear angle of 70° , tension inherent to filament winding forms the majority of the force applying the consolidation pressure. Due to the much smaller area of the nozzle making contact with the tow,

the glass fibers have much more room to tessellate to the deposition surface. In addition, pressure is uniform within the tow. As a result, greater consolidation is achieved as the tow width and shift width expands which is evident in Section 5.1.2. The higher the temperature, the lower the PP viscosity becomes enabling the glass fibers to shift even more. This effect is observed by the higher hot end temperatures producing higher shift widths on the PP deposition surface.

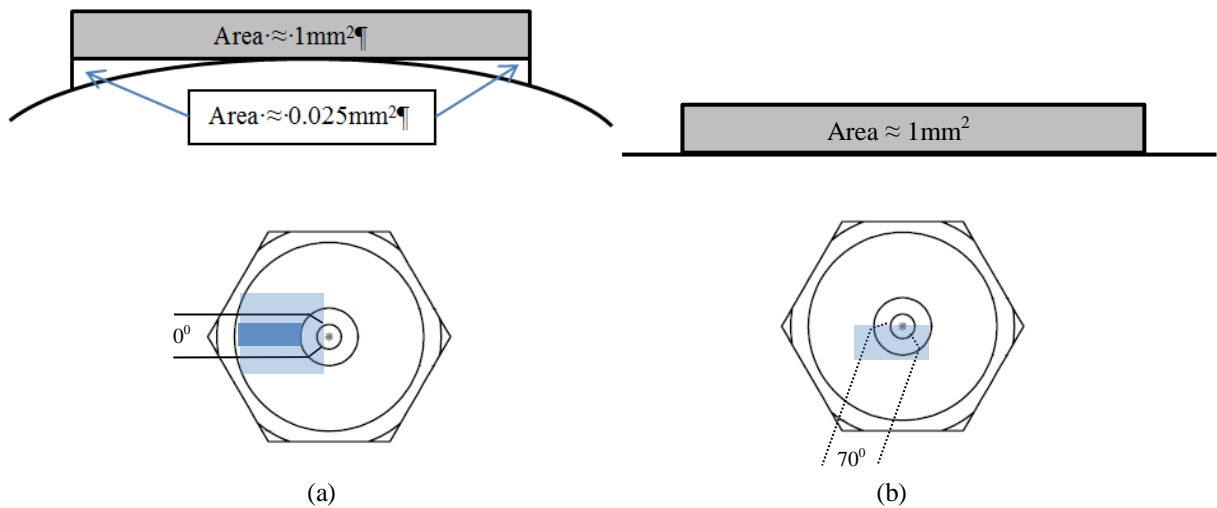


Figure 72: Consolidation of a longitudinal path (a) occurs fully by the nozzle while consolidation of a 70 degree path (b) occurs mostly by tension inherent to filament winding.

6.3 Effect of Forced Air Cooling and Deposition Surface

In order to determine the greatest amount of benefit in path fidelity possible with the current system, a high pressure of forced air was utilized in the AC samples. Once a portion of the tow is outside the 5.71 mm radius of the nozzle, the PP rapidly cools and freezes in place. Due to this freezing effect, the tension forces described in Section 6.1 have minimal effect on the accuracy of the placement in the AC samples. This reasoning is reinforced by the shear angles remaining inside the 5mm lead and lag paths in Section 5.1.1 and the error staying inside ± 5.71 mm for the PP/GF deposition surface in Section 5.1.3.

Surprisingly, performance in terms of error was reduced in the AC samples with the PP/GF deposition surface over the PP deposition surface. With the PP surface, the PP adheres very well even without AC; this is clear by the little variation between AC and non-AC samples in Sections 5.1.1 and 5.1.3. A stronger adherence is equated with more stability and more path lagging. Therefore, the tow is less responsive to head movement; it does not shift or position itself the full distance shown in Figure 72 (b) such that a 70° shear angle can be produced. Increasing the feed rate reduces the stability generating more shifting and more accurate shear angles with less error. Since the error in path placement remains largely less than the profile of the nozzle, AC has a minimal effect on this fairly stable system. With the PP/GF surface, the tow does not adhere to the previous layer quite as well; a more responsive system results with less lagging. In the case where AC is not used, higher feed rates and hot end temperatures induce a significant amount of error. With AC, the tow can be frozen much quicker so that there is less deviation from the programmed path. For this reason, the AC samples on the PP/GF deposition surface outperformed any of the other samples produced.

The use of AC and the deposition surface heavily influenced the amount of flash. Since flash could easily be detected on the PP deposition surface, it was included in defining the tow. It was not included in the PP/GF deposition surface. For this reason, higher shift widths were present in the PP deposition surface samples than the PP/GF deposition surface samples. Slower feed rates, higher processing temperatures, and consolidation through tension inherent to filament winding increased the amount of flash especially on the PP deposition surface samples. The use of AC restricts the amount of flash as shown by the lower plateaus in shift width in Figure 56. The maximum shift width in the AC samples on the PP deposition surface occurred just after the initial 20 mm radius turn because AC did not restrict the amount of flash as well in

that location. The glass fibers shifted in the shifting direction towards the inner radius while the PP continued to flow and produced a greater flash on the outside edge.

The shift widths trends on the glass/PP deposition surface were much different than the PP deposition surface. The more responsive system resulted in easier tow shifting and tow sliding. This is the reason behind a reduction in shift width being observed at higher temperatures and feed rates. With the use of AC, the tow shifting and tow sliding is reduced allowing higher shift widths to be maintained.

Improvement must occur in the 8 mm error profile that is best case for this system if widespread industry adoption of this technique is to occur. Optimization of nozzle size would reduce the error profile as the area in which tow shifting can occur would be limited. Maintaining functionality in terms of consolidation and adjoining of adjacent tows must still be achieved with a smaller nozzle. In FDM, greater resolution is achieved through the use of a smaller hole in the nozzle. With the method used in this study, the size of the hole in the nozzle is dependent on the size of the commingled tow. Therefore, the greatest increase in fidelity can occur through reducing the denier (linear mass density) of the commingled tow used with this method. From an initial characterization standpoint and when comparing to the samples without AC, the 8 mm error profile achieved is still fairly impressive.

6.4 Polypropylene Behavior at Elevated Temperatures

T-Peel testing and microscopy were conducted in order to gather insight on the mechanical performance of these samples. Before a discussion on the results occurs, the behavior of polypropylene at elevated temperatures should be explained.

Figure 73 details the melt viscosity of polypropylene at a heating rate of 2°C/min and a fixed shear rate of 5s⁻¹ or 10s⁻¹ [46]. Polypropylene #3 is similar to commercial PP while the

23K PP possesses a much lower molecular weight. The deposition temperature for most of the samples produced in this study fall within the viscosity curve in Figure 73.

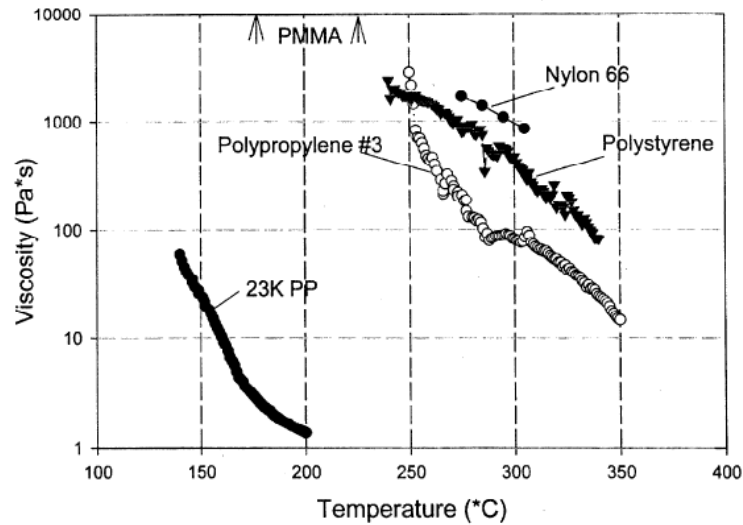


Figure 73: The melt viscosity as a function of temperature for polypropylene and other plastics is shown [46].

A study by Peterson et al. conducted thermogravimetric analysis (TGA) on PP beads received from Aldrich that were cut into thin oblong particles [47]. Using a flow rate of 100 ml/min for each gas and a heating rate of 9.1 and 8.2 K/min in the nitrogen and air environment, the samples were degraded completely until there was no noticeable residue as shown in Figure 74. The samples in this study were subjected to much higher temperatures than those that led to thermal degradation in Figure 74. However, the PP was only in the high temperature environment for a matter of seconds in this study compared to the significant amount of time for the TGA samples.

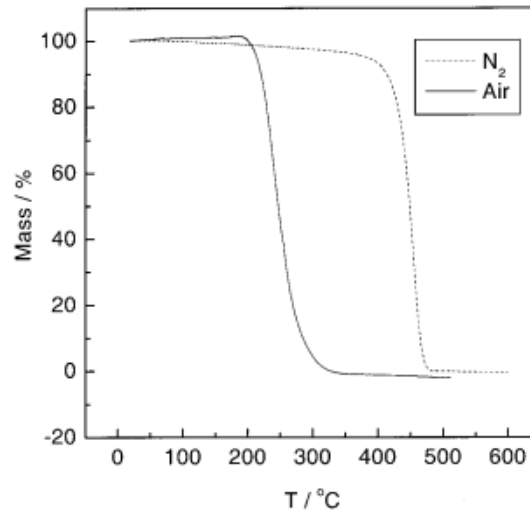


Figure 74: The thermal decomposition of PP in nitrogen and air is shown in the above TGA curves. A heating rate of 9.1 and 8.2 K/min was used for nitrogen and air [47].

The major products formed during decomposition of PP include pentane (24%), 2 methyl-1-pentene (15%) and 2-4 dimethyl-1-heptene (19%) [48]. Pentane is a type of alkane that oxidizes to form carbon dioxide and water with sufficient activation energy [49]. Since processing was occurring much higher than the boiling temperature of water, the smoke emanating from the nozzle during manufacturing was assuredly carbon dioxide and water vapor. Thermal degradation was likely occurring; a drop in mechanical performance would confirm that assumption.

6.5 Quality of Composite Beams

The t-peel test was selected for mechanical verification of composite properties for a number of different reasons. In the use of 3D printed plastics, loading in the build direction is discouraged due to weak interlayer bonding. Since the composites in this study are fabricated layer by layer as well, the interply properties were thought to be a source of weakness. Matrix rich areas and the presence of voids would be more likely to be found here than elsewhere in the composite. Varying manufacturing parameters would also have the greatest influence at this

location. By testing the quality of the bond between two layers of a composite, a quantitative comparison of the layer interfaces can be made as long as failure by peeling occurs in this region. If the adherend fails, this type of comparison cannot be conducted; however, the use of microscopy in parallel with this testing can create affirmation that the interply area is not the weak link and a quality composite in terms of interply properties was fabricated.

A number of specimens within an individual sample set exhibited failure at the adherend. Each of these specimens was among the better performers in terms of average maximum load or average peel strength. The three AC specimens exhibiting one adherend failure were the best AC performers in terms of average maximum load. Consistent adherend failure in all five specimens was only present in Sample 6 which was the best performing sample by the peel strength and maximum load categories. The peel strength for this specimen was calculated by the three samples whose load went below 1 pound. Since these loads did not go to zero like the other samples, the peel strength is artificially raised. Therefore, the peel strength for this sample can be considered relatively close to a best case estimate for this composite.

The composite cross section for Sample 6 is shown in Figure 75. Some large voids are present; however they are not located within the second and third layer which would affect the average peel strength. The area between the layers, shown by the line in Figure 75, is not well defined which potentially helped the average peel strength performance.

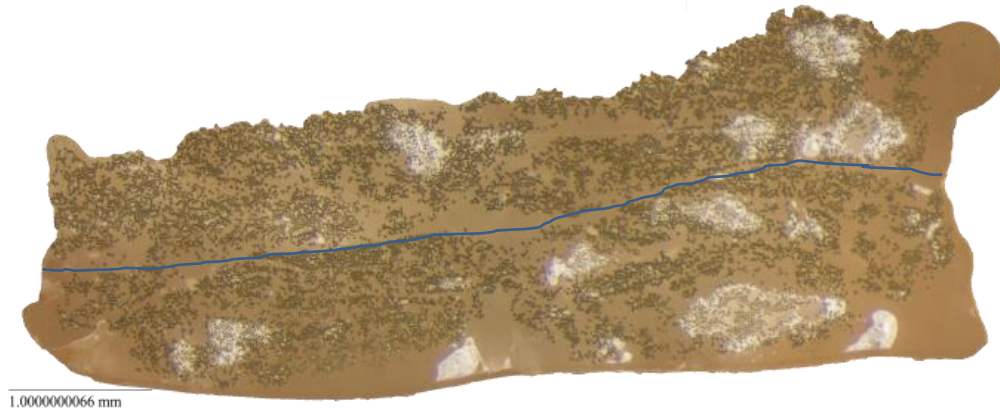


Figure 75: The composite cross section for Sample 6 Section 1.

Trends are not as obvious with the AC samples because they were processed between measured hot end temperatures of 292 and 357°C. This is a much narrower range of temperatures than the non-AC samples. The most evident trend in the T-Peel testing was the decrease in average peel strength as deposition temperature increased in the non-AC samples. The two samples processed with the highest deposition temperature (14 & 16) also possessed the lowest void percentage. The cross section of Sample 14, shown in Figure 76, shows a high quality composite with high fiber volume fraction, low voids, and good homogeneity in terms of fiber distribution throughout. The line drawn in the figure shows the area between the 2nd and 3rd layer that is visible but not too defined. The overall composite quality along with the area between the 2nd and 3rd layer actually looks superior to that of Sample 6. Surprisingly samples 14 and 16 yielded the lowest average max load and peel strength values; the only logical explanation based on the obtained evidence is that thermal degradation of the PP occurred. The low area values in samples 14 & 16 further support the idea that some of the PP left the system as carbon dioxide and water vapor. The same conclusion can be made for the samples processed at the next two highest deposition temperatures (8 & 18), albeit in a more reduced manner than samples 14 & 16.

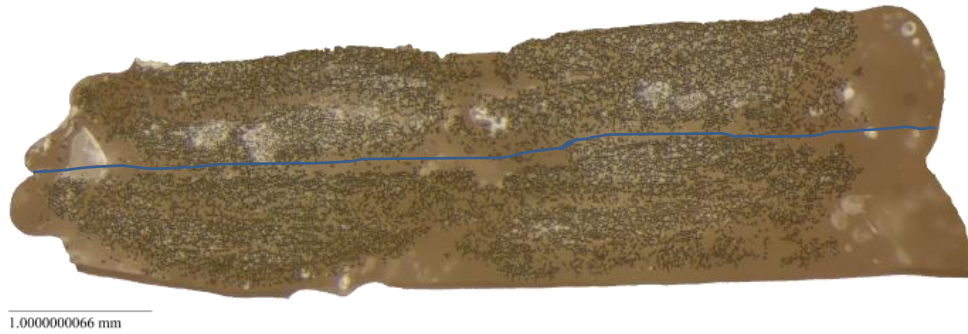


Figure 76: The cross section of Sample 14 section 1.

Unexpectedly, voids were not necessarily indicative of mechanical performance. As previously discussed, the samples with the lowest void content were the worst performing in terms of max load and peel strength. The opposite was found true in one case as well. The sample with the second highest void content (6) was the best performing in terms of max load and peel strength. In some cases, voids can have little to no effect on mechanical properties until a certain void percentage is reached [50]. The greater ductility thermoplastics possess over thermosets would suggest a higher void content can be tolerated without influencing the mechanical properties. As seen in Figure 70, intraply voids are more prominent than interply voids. If voids are not heavily located in the interply area between the second and third layers of the sample, they should not affect the peel strength. This reasoning can be confirmed in sample 6 (see Appendix 9.4). Deposition temperature and cooling rate will have an effect on the crystallinity of the PP matrix. Since sample 6 was processed at the lowest deposition temperature, it had the lowest cooling rate of all the samples analyzed. A low cooling rate will result in higher crystallinity. Higher levels of crystallinity in the semi-crystalline PP will result in better mechanical properties. This could be partially responsible for the high peel strength values sample 6 experienced. The effect would be fairly minimal as the highest cooling rates, which took place in the forced air cooling samples, produced peel strengths and maximum loads

roughly equivalent to the top half of the non-air cooled samples. These forced air cooled samples should possess a semi-crystalline structure that was more amorphous than the other samples.

A study of void percentages in out of autoclave composites suggested void contents between 2-4% are commonly produced [50]. Without considering the samples undergoing thermal degradation, void percentages in the current study were mostly in the range of 5-7%. This low void content is significant as thermoplastic composites possess much higher viscosities than thermosets making them much more difficult to manufacture.

With the high pressure of AC used to obtain positional fidelity in this study, a drop in mechanical performance through the thickness is possible. The results do not necessarily convey this drop in performance is occurring. Just behind the best performing sample, a group of four samples displayed similar performance in terms of average maximum load and average peel strength. One of these samples was the AC sample shown in Figure 77. The average maximum load for this sample was actually second best behind sample 6. Other than Sample 1, the values of the AC average maximum loads are comparable to the five best non-AC samples. In addition, void contents in AC samples were comparable to those non-AC samples not undergoing thermal degradation. When comparing average peel strength, performance is slightly reduced for the AC samples.

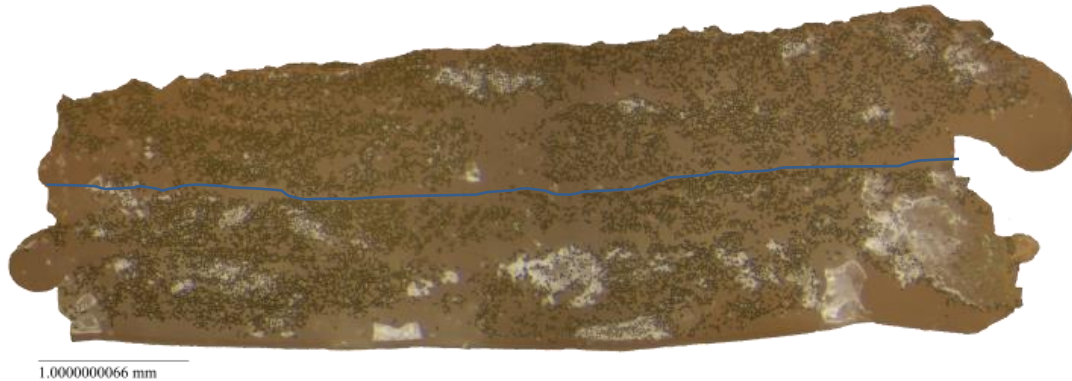


Figure 77: The cross section for Sample 17 section 2A.

Evaluating the mechanical performance through flexural testing like short beam shear would enable more conclusive evidence of whether or not greater positional fidelity results in a drop in mechanical performance. The peel testing utilized in this study is influenced by the processing of the plastic as voids were not heavily present in the interply area. It only determines interply strength which is a matrix dominated property. The peel testing does not give an indication of mechanical performance of the composite as a whole.

6.6 Irregularities

Although irregularities were present in the results, they were not so severe that conclusions could not be formulated from the data. In Section 5.1, the programmed path for Path 8 initially differed by a couple millimeters from the tow edges; this was also evident in Section 5.1.3 as the paths should have started with zero error. In Section 5.1.2, the longitudinal paths should have possessed the same shift width. The thickness of the composite samples varied significantly in Section 5.2.2. All of these described irregularities might be attributed to a couple different phenomenon. Inconsistency in the initial hand tacking operation by the user could have played a role in the accuracy of placement. Irregularity in axis homing, deflection or lack of

rigidity in the hot end mounting structure, and misalignment between the mandrel and fiber carriage are equipment imperfections that would contribute to additional variation.

7. VERIFICATION OF FUTURE POTENTIAL

Now that positional fidelity has been demonstrated with the current system, additional steps in achieving ultimate gains in structural performance can be discussed through verification of some of the design freedoms achieved through incorporating FDM and fiber placement.

7.1 Varying Fiber Orientations within a Layer

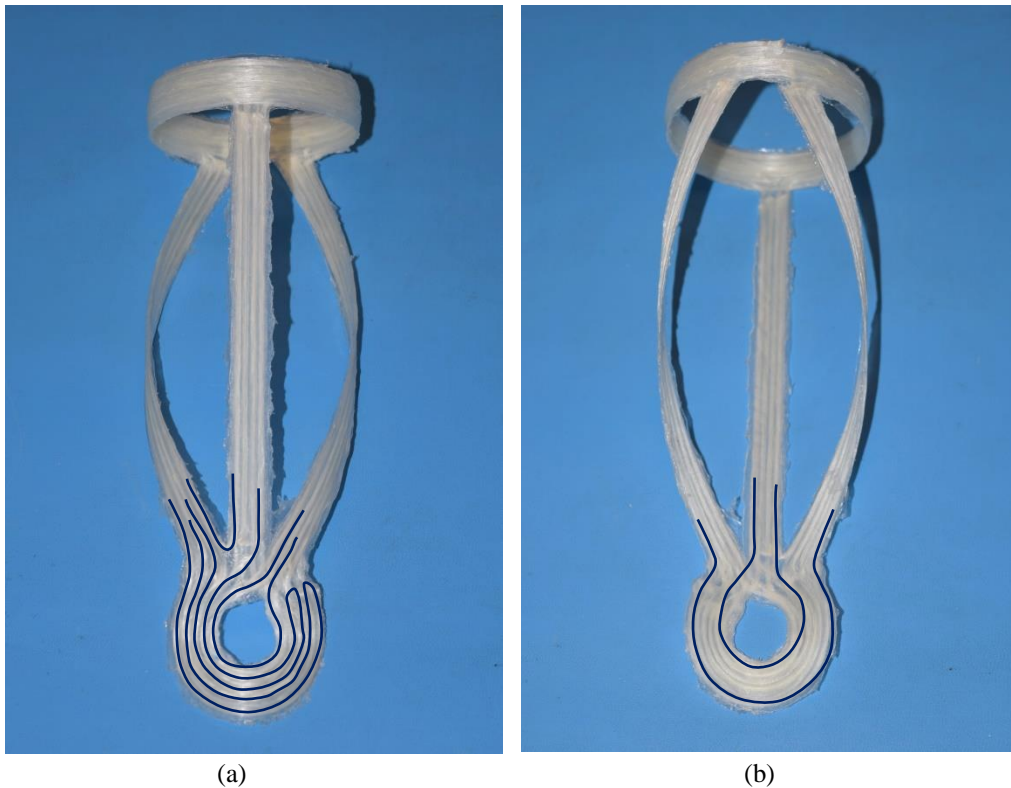


Figure 78: Outside and inside layer views of the fiber paths for a composite with a built in hole.

The fiber paths for the demonstration article, shown in Figure 78, were chosen to suggest discrete fiber positioning along complex load paths. Just as a three legged stool can support a person by distributing the load to each member, the three legs of the chosen part each have the ability to carry some of the load experienced around the hole. In the first layer, the reinforcement of the first leg encompasses a transition from a longitudinal path to form the inner

portion of the designed in hole. The second and third legs consist of a helical wind that transition into the outer portion of the hole. In the second layer, the inner portion of the hole transitions from one of the helical winds, while the reinforcement that forms the outer portion of the hole continues to form the other helical wind and the longitudinal wind. The goal of fiber placement along such paths is improved structural efficiency and one of the principal goals of this manufacturing system is to give the mechanical designer this opportunity.

Even with pins or a cone insert, the chosen path cannot be made by filament winding as that process is restricted to small diameter openings, since the fiber paths must remain close to their stable patterns [2]. Automated tape placement or automated fiber placement could not achieve the steering radii necessary to create this part. Using a preform and resin transfer molding within tailored fiber placement to make this part would also not be possible. No other studies using 3D printing technologies have demonstrated the fabrication of continuous fiber composite parts of this complexity.

7.2 Combining Conventional FDM with Fiber Placement

Through combining conventional FDM with fiber placement, greater structural efficiency can be achieved through use of less of the more expensive material, the fiber. Within composite materials, honeycomb structures are extremely stiff and lightweight. The thin composite face sheets carry the load while the core allows for shear transfer. Through standard fabrication methods, honeycomb structures incorporating edge closeouts, hard points, or beveled edges can be challenging to include. With the current system, no additional processing or complexity is added at all.

The manufacturing of a honeycomb composite structure through combining FDM and fiber placement can be seen in Figure 79. The bottom continuous fiber reinforced layer was

placed first; a honeycomb core with edge closeouts was printed on top of this base layer as shown in Figure 79 (a). Finally, the top continuous fiber reinforced layer was placed on top of the honeycomb as shown in Figure 79 (b).

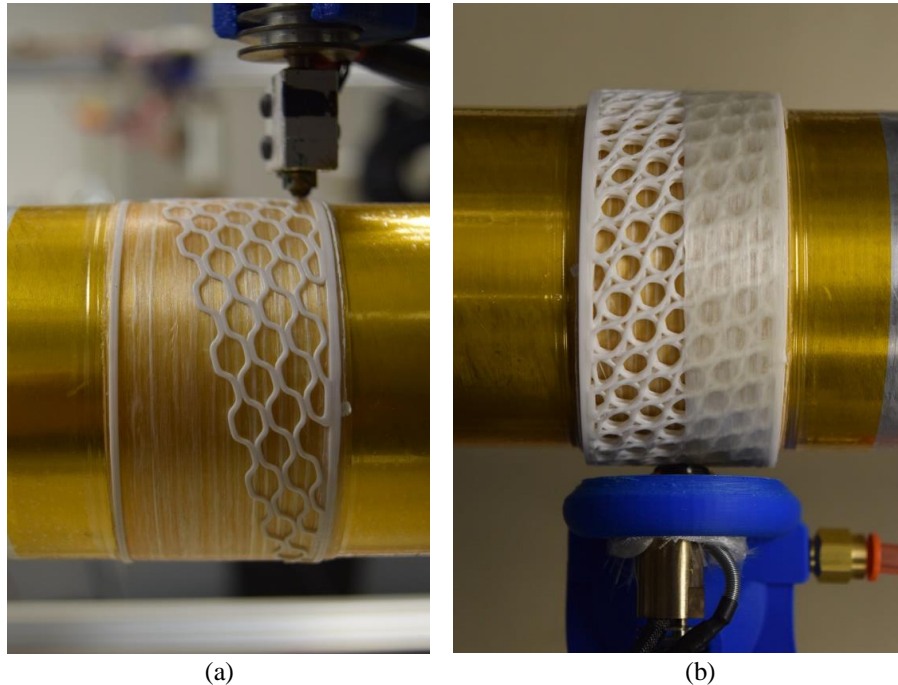


Figure 79: Honeycomb composites can be produced through combining conventional FDM with fiber placement. Printing of the plastic honeycomb on top of the base layer is shown in (a), while the placement of continuous reinforcement on top of the honeycomb is shown in (b).

The high quality completed honeycomb structure is shown in Figure 80. The top and bottom fiber reinforced layers have an excellent surface finish fostering the appearance of complete face sheets rather than a number of adjacently placed tows. A very minimal amount of flash is present on the edges; it can quickly be removed with some light sanding. Digital composites produced in this manner in which minimal or no post-processing is needed would eliminate one of the barriers preventing widespread use of composites within industry.



Figure 80: The de-tooled honeycomb composite with edge closeouts and a minimal amount of flash.

For a composite tube that is subject to bending loads, a hoop wind for the face sheets would not be as structural efficient as a longitudinal path. The current system possesses the ability to do so as shown in Figure 81. To ensure a high quality finished part is produced, 180° turns were included off of the part. Two separate scaffolds to support this turn were printed prior to the placement of the top face sheet. Like the honeycomb tube with hoop winds, this honeycomb tube with longitudinal winds was of high quality in terms of appearance after the excess material was removed.

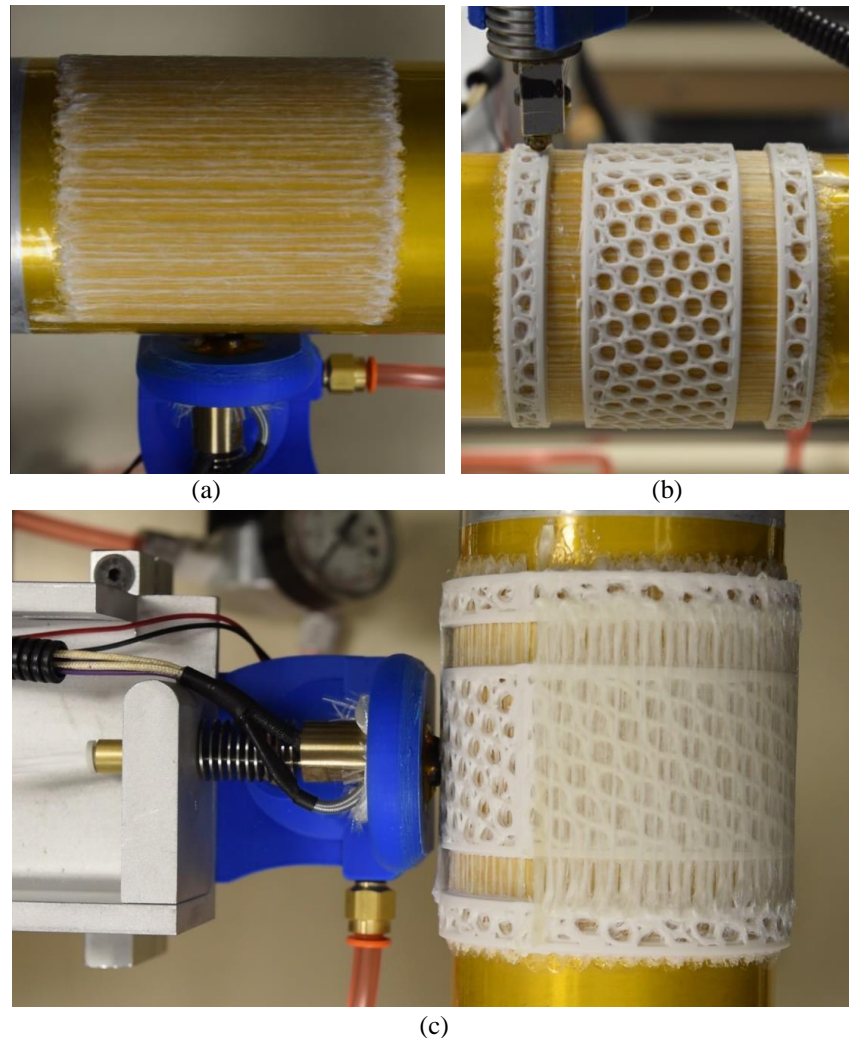


Figure 81: The manufacturing of the base layer (a), honeycomb core (b) and top face sheet (c) for a composite tube with longitudinal reinforcement is shown.

In the manufacturing of the longitudinal tube, commingled tow and neat PP was wasted in producing 180° turns and scaffolding. In addition, post processing is required to machine the part to its final dimensions. Both of these limitations can be avoided through implementation of a cut and retack or place mechanism. This added functionality would enhance design freedom in addition to allowing more efficient material use. Implementing this functionality into the system is beyond the scope of this research as complexity would significantly increase.

7.3 Out of Plane Fiber Placement and Fiber Volume Fraction Modification

In producing the top face sheet of the honeycomb tube shown in Figure 81, a fairly large gap was bridged. Due to the lack of consolidation in this area, the tow width decreased and thickness increased as depicted in Figure 81 (c). Application of subsequent layers could reduce the thickness and increase the width to potentially fill the gaps. The ability of this machine to bridge a large gap shows the potential for printing a base layer out of plane without tooling. Consolidation of the subsequent layers will be imperative in achieving the properties of a high quality composite. This cannot be accomplished with the current fiber carriage mandrel system due to lack of a servo controlled wrist mechanism. However, the lack of consolidation that occurs from the nozzle in high angle winds and hoop winds described in Section 6.2 could enable some out of plane paths to be produced with this system. Sub-par quality would likely be present in the transition regions between in-plane and out-of-plane paths.

Although the multiple gantries in the current system allow for varying fiber volume fraction to be produced, demonstration of this capability is quite challenging. The FDM gantry will have to lead the fiber carriage mandrel system. For this to occur on all types of paths, the FDM head must maintain a position perpendicular to the mandrel. Therefore, a servo controlled wrist mechanism will need to be implemented here as well. With the current system, conceptual verification of this method can be accomplished with longitudinal paths. Anticipated difficulty in maintaining a homogeneous microstructure will be faced with the addition of a matrix material. The tows will want to stay bundled close together in tension and close to the nozzle they are pultruded from. Increasing the thickness of a layer by adding additional matrix will very likely produce a microstructure that is fiber dominated close to the surface and matrix dominated increasingly as depth increases.

7.4 Barriers to making Digital Composites a Reality

Generating the g-code for complex fiber paths varying in plane and even out of plane is a barrier for widespread implementation of a mechanical system such as the one developed in this work. Although advanced slicing methods continue to be developed, the conventional slicing methods commonly used in 3d printing will not produce these paths. CAM software is currently the best platform to generate g-code for complicated paths. Instead of starting with a block of material and machining a finished product, one would start with a finished part and machine it until nothing exists. By running the resultant g-code in reverse, you could theoretically produce the g-code for a part with complicated fiber patterns.

Additional coding complexity will result from a system where tension inherent to filament winding will affect only some of the produced paths. The tow width on hoop paths will be larger than longitudinal paths. Being able to compensate for this change in width within the g-code will take more characterization. A flat plate system is not expected to have to deal with the issues of changes in tow width unless fiber placement is occurring on a pre-printed convex surface.

Flash is inherent to composite materials. If a uniform microstructure is desired throughout the entire part, the prospect of eliminating post-processing completely from composite materials fabrication is slim. Advances in technology in 3D scanners and increased widespread use of CNC machines through cost reductions will enable digital composites to be produced in the future. A composite part will be fabricated using additive manufacturing techniques slightly oversized from a CAD file. A 3D scan of the part will determine how much deviation from the CAD dimensions exists. Within the same platform, a milling machine will remove the flash and other out of dimension areas such that tolerance requirements can be met.

If a uniform microstructure throughout the entire part is not required, a more simplistic system can be developed. Fiber reinforcement can only be placed in the interior and neat plastic can be printed to cover the entire exterior surface. As previously described in Section 1.3.1, this is the approach Mark Forge is using to obtain dimensional tolerance requirements [7] [9].

8. CONCLUSIONS

It has been proven that a continuous fiber reinforced composites manufacturing platform, utilizing 3D printing hardware and the continuous tow shearing technique, has demonstrated that high quality composites with high reinforcement positional fidelity over complex paths can be manufactured. Preliminary studies verified high quality composites with and without the tension inherent in filament winding could be manufactured along with non-geodesic fiber paths. A characterization study established that forced air cooling is necessary for geometric fidelity and high quality in transition regions as tow sliding otherwise reduces fidelity and quality. Forced air cooling becomes imperative on an unstable system like that of a previously deposited composite layer.

Through the use of air cooling, a high quality composite could be produced through just using the nozzle as the consolidation mechanism. Although the void content was higher than conventional composite manufacturing techniques, the maximum void content measured wasn't so high that a clear reduction in mechanical performance was observed. The best performing air cooled and non-air cooled samples possessed comparable average max loads, while the air cooled average peel strength values were only slightly reduced from the non-air cooled. Void contents mostly between 5-7% were attained with all the samples. Through modification of manufacturing parameters, viscosity of the matrix was further reduced enabling a void content as low as 2% to be realized; however, thermal degradation of the polypropylene was present in these samples with lower void content. This was determined by low peel strengths, low areas, and the presence of smoke during manufacturing.

This study also established that tow shifting within the profile of the nozzle largely determines the shift width and tow width. During a longitudinal path where consolidation is primarily occurring from the nozzle, minimal tow shifting is taking place and a smaller tow width results. During a constant shear angle path where consolidation is occurring minimally from the nozzle and more so from tension inherent to filament winding, maximal tow shifting is taking place. This effect is observed in the results by the tow width increasing by approximately 50% during the constant shear angle portion of the path for most of the samples; the tow width even doubled in a few of the samples.

The composite demonstration article with the designed-in hole and with reinforcement along pre-planned load paths demonstrates that much more complex patterns can be generated. It helps form the basis of support for the potential for continuous fiber reinforced composites not based on layer-by-layer construction. Reinforcement placed in pre-planned directions for honeycomb structures demonstrates increased structural performance through minimization of the more expensive fiber material. In addition, FDM of scaffolding, interior elements, and even tooling are capable of being incorporated into fiber reinforced structures produced in this system allowing for enhanced design flexibility.

The combination of 3D printing, filament winding, and automated fiber placement technologies in this system has shown the potential to produce unique parts with fiber oriented along preplanned paths that cannot be manufactured via other methods. The advantages of reduced costs a similar system would offer through no necessary tooling, no investment in large manufacturing equipment, increased part complexity, reduction in time to market, and redesign at any time in the product life cycle would make it very attractive for low production quantity components. To achieve all these benefits, advancements in g-code generation, better

characterization of tow width with varying path profiles, and implementation of post-process CNC machining to remove flash must be made. Lastly, the research undertaken demonstrates that digital composites, in which parts are manufactured directly from a CAD file, are much closer to becoming a reality than previously perceived further enabling fiber reinforced composites to be manufactured that are much closer to possessing the ultimate gains in structural performance possible.

9. REFERENCES

- [1] H. Tekinalp, V. Kunc, G. Valez-Garcia, C. Duty, L. Love, A. Naskar, C. Blue and S. Ozcan, "Highly Oriented Carbon Fiber–Polymer Composites via Additive Manufacturing.," *Composites Science and Technology*, pp. 144-150, 2014.
- [2] H. Prub and T. Vietor, "Design for Fiber-Reinforced Additive Manufacturing," *Journal of Mechanical Design, Transactions of the ASME*, vol. 137, no. 11, 2015.
- [3] K. Rijswijk, W. Brouwer and A. Beukers, "Application of Natural Fibre Composites in the Development of Rural Societies," in *Food and Agriculture Organization of the United Nations*, Rome, 2003.
- [4] C. Hill, K. Rowe, R. Bedsole, J. Earle and V. Kunc, "Materials and Process Development for Direct Digital Manufacturing of Vehicles," in *SAMPE Long Beach 2016 Conference and Exhibition*, Long Beach, 2016.
- [5] S. Crump, "Direct Digital Manufacturing Part One: What is Direct Digital Manufacturing," Stratasy Ltd., 2009.
- [6] S. Crump, "Direct Digital Manufacturing Part Two: Advantages and Considerations," Stratasy Inc., 2009.
- [7] F. Van Der Klift, Y. Koga, A. Todoroki, M. Ueda, Y. Hirano and R. Matsuzaki, "3D Printing of Continuous Carbon Fibre Reinforced Thermoplastic (CFRTP) Tensile Test Specimens," *Open Journal of Composite Materials*, vol. 6, no. 1, pp. 18-27, 2016.
- [8] F. Van Der Klift, Y. Koga, A. Todoroki, Y. Hirano, M. Ueda and R. Matsuzaki, "Mechanical Properties of 3D Printed Continuous Carbon Fibre Reinforced Thermo-plastic Tensile Test Bars," in *SAMPE Long Beach 2016 Conference and Exhibition*, Long Beach, 2016.
- [9] G. Malenka, B. Cheung, J. Schofield, M. Dawson and J. Carey, "Evaluation and Prediction of the Tensile Properties of Continuous Fiber-reinforced 3D Printed Structures," *Composite Structures*, vol. 153, pp. 866-875, 2016.
- [10] S. Kumar and J. Kruth, "Composites by Rapid Prototyping Technology," *Materials and Design*, vol. 31, no. 2, pp. 850-856, 2010.
- [11] M. Namiki, M. Ueda, A. Todoroki, Y. Hirano and R. Matsuzaki, "3D Printing of Continuous Fiber Reinforced Plastic," in *SAMPE Tech Seattle 2014 Conference*, Seattle, 2014.
- [12] R. Matsuzaki, M. Ueda, M. Namiki, T. Jeong, H. Asahara, K. Horiguchi, T. Nakamura, A. Todoroki and Y. Hirano, "Three-dimensional Printing of Continuous Fiber Composites by in-nozzle Impregnation," *Scientific Reports*, vol. 6, no. 23058, 2016.
- [13] P. Bettini, G. Alitta, G. Sala and L. Landro, "Fused Deposition Technique for Continuous Fiber Reinforced Thermoplastic," *Journal of Materials Engineering and Performance*, vol. 26, no. 2, pp. 843-848, 2017.
- [14] C. Yang, X. Tian, T. Liu, Y. Cao and D. Li, "3D Printing for Continuous Fiber Reinforced Thermoplastic Composites: mechanism and performance," *Rapid Prototyping Journal*, vol. 23, no. 1, pp. 209-215, 2017.

- [15] N. Li, Y. Li and S. Liu, "Rapid Prototyping of Continuous Carbon Fiber Reinforced Poly(lactic Acid) Composites by 3D Printing," *Journal of Materials Processing Technology*, vol. 238, pp. 218-225, 2016.
- [16] X. Tian, T. Liu, C. Yang, Q. Wang and D. Li, "Interface and Performance of 3D Printed Continuous Carbon Fiber Reinforced PLA Composites," *Composites: Part A*, vol. 88, pp. 198-205, 2016.
- [17] M. Eichenhofer, J. Maldonado, F. Klunker and P. Ermanni, "Analysis of Processing Conditions for a Novel 3D-Composite Production Technique," in *20th International Conference on Composite Materials.*, Copenhagen, 2015.
- [18] A. Gibson and J. Manson, "Impregnation Technology for Thermoplastic Matrix Composites," *Composites Manufacturing*, vol. 3, no. 4, pp. 223-233, 1992.
- [19] D. Radford and K. Hedin, "Fused Deposition Technology Applied to Thermoplastic Matrix Placement and Wetout in Filament Winding," in *20th International Conference on Composite Materials*, Copenhagen, 2015.
- [20] V. Parady, "How to Reinforce Holes in Filament Wound Structures," *Materials in Design Engineering*, pp. 108-122, 1965.
- [21] M. Lamontia, "Remaining Developments Required for Commercializing In Situ Thermoplastic ATP.," in *2007 SAMPE Symposium and Exhibition*, Baltimore, 2007.
- [22] M. Lamontia, M. Gruber, B. Waibel, R. Cope, S. Funck and A. Hulcher, "Contoured Tape Laying and Fiber Placement Heads for Automated Fiber Placement of Large Composite Aerospace Structures," in *34th International SAMPE Technical Conference*, Baltimore, 2002.
- [23] Z. August, G. Ostrander, J. Michasiow and D. Hauber, "Recent Developments in Automated Fiber Placement of Thermoplastic Composites," in *SAMPE Tech 2013 Conference and Exhibition*, Wichita, 2013.
- [24] M. Lamontia, S. Funck, M. Gruber, R. Cope, B. Waibel and N. Gopez, "Manufacturing Flat and Cylindrical Laminates and Build Up Structure Using Automated Thermoplastic Tape Laying, Fiber Placement, and Filament Winding," *SAMPE Journal*, vol. 39, no. 2, pp. 30-38, 2003.
- [25] M. Wiehn and R. Hale, "Low Cost Robotic Fabrication Methods for Tow Placement," in *47th International SAMPE Symposium and Exhibition*, Long Beach, 2002.
- [26] D. Feltin and K. Gliesche, "Tailored Fiber Placement: Cost-Effective Preforms for High Loaded Composites," in *46th International SAMPE Symposium and Exhibition*, Long Beach, 2001.
- [27] K. Hazra, K. Potter and M. Wisnom, "Tow Steered CFRP Aircraft Parts –Preforming and Mechanical Properties," in *2009 SAMPE Fall Technical Conference and Exhibition – Global Material Technology: Soaring to New Horizons*, Wichita, 2009.
- [28] R. Li, D. Kelly, S. Arima, R. Willgoss and A. Crosky, "Fiber Steering Around a Cutout in a Shear Loaded Panel," in *47th International SAMPE Symposium and Exhibition*, Long Beach, 2002.
- [29] D. Kelly, R. Li, R. Willgoss and A. Crosky, "Improvement of Bearing Strength of Mechanically Fastened Composite Joints Using Fiber Steering," in *46th International SAMPE Symposium and Exhibition 2001 a Materials and Processes Odyssey*, Long Beach,

- 2001.
- [30] C. Lopes, Z. Gurdal and P. Camanho, "Variable-Stiffness Composite Panels: Buckling and First-Ply Failure Improvements Over Straight-Fibre Laminates," *Composites and Structures*, vol. 86, pp. 897-907, 2008.
- [31] S. IJsselmuiden, M. Abdalla, V. Pilaka and Z. Gurdal, "Design of Variable Stiffness Composite Structures For Advanced Fibre Placement Technology," in *SAMPE 2010 Conference and Exhibition: New Materials and Processes for a New Economy*, Seattle, 2010.
- [32] R. Klomp, "Development of Automated Dry Fiber Placement Material, Process and Design Technology," in *SAMPE Tech 2011 Conference and Exhibition: Developing Scalable Materials and Processes for Our Future*, Fort Worth, 2011.
- [33] D. Jegley, B. Tatting and Z. Gurdal, "Optimization of Elastically Tailored Tow-Placed Plates with Holes," in *AIAA/ASME/ASCE/AHS/ASC Structures, Structural Dynamics and Materials Conference*, Norfolk, 2003.
- [34] B. Tatting and Z. Guerdal, "Design and Manufacture of Elastically Tailored Tow Placed Plates," NASA Langley Research Center, Hampton, 2002.
- [35] K. Wu, B. Stanford, G. Hrinda, W. Zhuosong, R. Martin and H. Kim, "Structural Assessment of Advanced Composite Tow-Steered Shells," in *54th AIAA/ASME/ASCE/AHS/ASC Structures, Structural Dynamics and Materials Conference*, Palm Springs, 2013.
- [36] K. Wu, B. Tatting, B. Smith, R. Stevens, G. Occhipinti, J. Swift, D. Achary and R. Thornburgh, "Design and Manufacturing of Tow-Steered Composite Shells Using Fiber Placement," in *50th AIAA/ASME/ASCE/AHS/ASC Structures, Structural Dynamics and Materials Conference*, Palm Springs, 2009.
- [37] K. Wu, J. Turpin, B. Stanford and R. Martin, "Structural Performance of Advanced Composite Tow-Steered Shells with Cutouts," in *55th AIAA/ASME/ASCE/AHS/ASC Structures Structural Dynamics and Materials Conference*, National Harbor, 2014.
- [38] B. Kim, K. Hazra, P. Weaver and K. Potter, "Limitations of Fibre Placement Techniques for Variable Angle Tow Composites and Their Process-Induced Defects," in *The 18th International Conference on Composite Materials*, Jeju, Korea, 2011.
- [39] B. Kim, K. Potter and P. Weaver, "Continuous Tow Shearing for Manufacturing Variable Angle Tow Composites," *Composites: Part A*, vol. 43, pp. 1347-1356, 2012.
- [40] B. Kim, K. Potter and P. Weaver, "Multi-Tow Shearing Mechanism for High-Speed Manufacturing of Variable Angle Tow Composites," in *15th European Conference on Composite Materials*, Venice, 2012.
- [41] B. Kim, P. Weaver and K. Potter, "Manufacturing Characteristics of the Continuous Tow Shearing Method for Manufacturing Variable Angle Tow Composites," *Composites: Part A*, vol. 61, pp. 141-151, 2014.
- [42] "Polypropylene 3D Printer Filament," GiZMO DORKS, 2017. [Online]. Available: <http://gizmodorks.com/polypropylene-3d-printer-filament/>. [Accessed 4 3 2017].
- [43] W. Sichina, "Measurement of Tg of Polypropylene Using the PYRIS Power Compensation DSC," PerkinElmer instruments.
- [44] AZom, "AZO Materials: E-Glass Fibre," AZoNetwork, 30 8 2001. [Online]. Available:

- <http://www.azom.com/article.aspx?ArticleID=764>. [Accessed 21 3 2017].
- [45] "Polypropylene (PP) Material Information," Goodfellow, [Online]. Available: <http://www.goodfellow.com/E/Polypropylene.html>. [Accessed 21 3 2017].
- [46] T. Ohlemiller, J. Shields, K. Bulter, B. Collins and M. Seck, "Exploring the Role of Polymer Melt Viscosity in Melt Flow and Flammability Behavior," in *New Developments and Key Market Trends in Flame Retardancy: Fire Retardance Chemicals Association*, Ponte Vedra, 2000.
- [47] J. Peterson, S. Vyazovkin and C. Wight, "Kinetics of the Thermal and Thermo-Oxidative Degradation of Polystyrene, Polyethylene and Poly(propylene)," *Macromolecular Chemistry and Physics*, vol. 202, no. 6, pp. 775-784, 2001.
- [48] C. Beyler and M. Hirschler, "Thermal Decomposition of Polymers," in *SFPE Handbook of Fire Protection Engineering*, Quincy, MA, National Fire Protection Association, 2002, pp. 111-131.
- [49] W. Reusch, "Alkane Heats of Combustion," LibreTexts: Chemistry, 26 2 2017. [Online]. Available: https://chem.libretexts.org/Core/Organic_Chemistry/Alkanes/Reactivity_of_Alkanes/Alkane_Heats_of_Combustion. [Accessed 21 3 2017].
- [50] C. Wilson, E. Currens and J. Rakow, "Void Content in Out-of-Autoclave Manufacturing Processes," *Proceedings of Microscopy & Microanalysis 2016*, vol. 22, no. S3, pp. 1832-1833, 2016.

10. APPENDICES

10.1 Marlin Firmware Modifications

The firmware modifications made to each file of the marlin firmware are shown below.

Note that the edit abbreviations stand for addition (ADD) and modification (MOD).

File: CONFIGURATION_H

| Line # | Edit Type | Line of Code: |
|--------|-----------|---|
| 39 | MOD | #define BAUDRATE 250000 |
| 47 | MOD | #define MOTHERBOARD BOARD_AZTEEG_X3_PRO |
| 95 | ADD | // 65 is 500C thermistor for PICO Hot End |
| 107 | MOD | #define TEMP_SENSOR_0 65 #define TEMP_SENSOR_1 0 #define TEMP_SENSOR_2 0 #define TEMP_SENSOR_BED 1 |
| 132 | MOD | #define HEATER_0_MAXTEMP 495 // PICO Hot END MAX TEMP for Thermistor=500C |
| 135 | MOD | #define BED_MAXTEMP 300 //Thermistor on mandrel max temp = 300; HE max temp = 871C=1600F |
| 149 | MOD | #define BANG_MAX 255 // limits current to nozzle while in bang-bang mode; 255=full current |
| 154 | MOD | #define SLOW_PWM_HEATERS // PWM with very low frequency (roughly 0.125Hz=8s) and minimum state time of approximately 1s useful for heaters driven by a relay //initially commented #define PID_FUNCTIONAL_RANGE 50 // If the temperature difference between the target temperature and the actual temperature // is more then PID_FUNCTIONAL_RANGE then the PID will be shut off and the heater will be set to min/max. //Initially #define PID_FUNCTIONAL_RANGE 10 |
| 189 | MOD | #define PIDTEMPBED |
| 197 | MOD | #define MAX_BED_POWER 89.25 // limits duty cycle to bed; 255=full current |
| 202 | MOD | #define DEFAULT_bedKp 11.55 #define DEFAULT_bedKi 10 #define DEFAULT_bedKd 6.66 |
| 216 | MOD | //this prevents dangerous Extruder moves, i.e. if the temperature is under the limit //can be software-disabled for whatever purposes by //#define PREVENT_DANGEROUS_EXTRUDE //Will need to be commented since I will run this extruder on the opposite board //if PREVENT_DANGEROUS_EXTRUDE is on, you can still disable (uncomment) very long bits of extrusion separately. //#define PREVENT_LENGTHY_EXTRUDE #define EXTRUDE_MINTEMP 20 //Adjust this to allow for cold extrusion?? |
| 283 | ADD | #ifndef ENDSTOPPULLUPS #define ENDSTOPPULLUP_XMAX #define ENDSTOPPULLUP_YMAX #define ENDSTOPPULLUP_ZMAX #define ENDSTOPPULLUP_UMAX //Added #define ENDSTOPPULLUP_VMAX //Added #define ENDSTOPPULLUP_WMAX //Added #define ENDSTOPPULLUP_XMIN #define ENDSTOPPULLUP_YMIN |

| | | |
|-----|-----|---|
| | | <pre> #define ENDSTOPPULLUP_ZMIN #define ENDSTOPPULLUP_UMIN //Added #define ENDSTOPPULLUP_VMIN //Added #define ENDSTOPPULLUP_WMIN //Added #endif </pre> |
| 298 | ADD | <pre> // The pullups are needed if you directly connect a mechanical endswitch between the signal and ground pins. const bool X_MIN_ENDSTOP_INVERTING = true; // set to true to invert the logic of the endstop. const bool Y_MIN_ENDSTOP_INVERTING = true; // set to true to invert the logic of the endstop. const bool Z_MIN_ENDSTOP_INVERTING = true; // set to true to invert the logic of the endstop. const bool U_MIN_ENDSTOP_INVERTING = true; // Added const bool V_MIN_ENDSTOP_INVERTING = true; // Added const bool W_MIN_ENDSTOP_INVERTING = true; // Added const bool X_MAX_ENDSTOP_INVERTING = true; // set to true to invert the logic of the endstop. const bool Y_MAX_ENDSTOP_INVERTING = true; // set to true to invert the logic of the endstop. const bool Z_MAX_ENDSTOP_INVERTING = true; // set to true to invert the logic of the endstop. const bool U_MAX_ENDSTOP_INVERTING = true; // Added const bool V_MAX_ENDSTOP_INVERTING = true; // Added const bool W_MAX_ENDSTOP_INVERTING = true; // Added </pre> |
| 319 | ADD | <pre> // For Inverting Stepper Enable Pins (Active Low) use 0, Non Inverting (Active High) use 1 #define X_ENABLE_ON 0 #define Y_ENABLE_ON 0 #define Z_ENABLE_ON 0 #define E_ENABLE_ON 0 // For all extruders #define U_ENABLE_ON 0 //Added #define V_ENABLE_ON 0 //Added #define W_ENABLE_ON 0 //Added </pre> |
| 328 | ADD | <pre> // Disables axis when it's not being used. #define DISABLE_X false #define DISABLE_Y false #define DISABLE_Z false #define DISABLE_U false //Added #define DISABLE_V false //Added #define DISABLE_W false //Added </pre> |
| 338 | MOD | <pre> #define INVERT_X_DIR true // for Mendel set to false, for Orca set to true #define INVERT_Y_DIR false // for Mendel set to true, for Orca set to false #define INVERT_Z_DIR false // for Mendel set to false, for Orca set to true #define INVERT_U_DIR true //Added #define INVERT_V_DIR false //Added #define INVERT_W_DIR false //Added </pre> |
| 349 | ADD | <pre> // Sets direction of endstops when homing; 1=MAX, -1=MIN #define X_HOME_DIR -1 #define Y_HOME_DIR -1 #define Z_HOME_DIR -1 #define U_HOME_DIR -1 //Added #define V_HOME_DIR -1 //Added #define W_HOME_DIR -1 //Added </pre> |
| 360 | MOD | <pre> // Travel limits after homing #define X_MAX_POS 460 //475 #define X_MIN_POS 0 #define Y_MAX_POS 70 //200 #define Y_MIN_POS 0 #define Z_MAX_POS 202 //202 #define Z_MIN_POS 0 #define U_MAX_POS 200 //ADDED 460 #define U_MIN_POS 0 //ADDED </pre> |

| | | |
|-----|-----|---|
| | | #define V_MAX_POS 200 //ADDED 460 #define V_MIN_POS 0 //ADDED #define W_MAX_POS 202 //ADDED 70 #define W_MIN_POS 0 //ADDED |
| 374 | ADD | #define X_MAX_LENGTH (X_MAX_POS - X_MIN_POS) //Not needed?? #define Y_MAX_LENGTH (Y_MAX_POS - Y_MIN_POS) #define Z_MAX_LENGTH (Z_MAX_POS - Z_MIN_POS) #define U_MAX_LENGTH (U_MAX_POS - U_MIN_POS) //Added #define V_MAX_LENGTH (V_MAX_POS - V_MIN_POS) //Added #define W_MAX_LENGTH (W_MAX_POS - W_MIN_POS) //Added |
| 504 | ADD | #define MANUAL_X_HOME_POS 0 #define MANUAL_Y_HOME_POS 0 #define MANUAL_Z_HOME_POS 0 #define MANUAL_U_HOME_POS 0 //Added #define MANUAL_V_HOME_POS 0 //Added #define MANUAL_W_HOME_POS 0 //Added |
| 513 | MOD | #define NUM_AXIS 7 // The axis order in all axis related arrays is X, Y, Z, E0, U, V, W #define HOMING_FEEDRATE {75*60, 75*60, 0, 0, 75*60, 75*60, 75*60} // set the homing speeds (mm/min) {75*60, 75*60, 75*60, 0, 0, 75*60, 75*60} |
| 517 | MOD | #define DEFAULT_AXIS_STEPS_PER_UNIT {106.66, 1600, 30720, 1741, 106.66, 106.66, 214.52} //steps/mm #define DEFAULT_MAX_FEEDRATE {0.1, 30, 0.1, 3.33, 3.33, 3.33, 3.33} // (mm/sec) {3.33, 3.33, 3.33, 3.33, 0.1, 0.1, 30} #define DEFAULT_MAX_ACCELERATION {9000, 1000, 9000, 10000, 9000, 9000, 100} // X, Y, Z, E, U, V, W maximum start speed for accelerated moves. |
| 783 | MOD | #define NUM_SERVOS 2 // Servo index starts with 0 for M280 command |

File: CONFIGURATION_ADV.H

| Line # | Edit Type | Line of Code: |
|--------|-----------|--|
| 59 | COM | #define TEMP_SENSOR_AD595_GAIN 1.0 //Set to 2.0 is using K type thermocouples |
| 89 | MOD | //#define ENDSTOPS_ONLY_FOR_HOMING // If defined the endstops will only be used for homing |
| 138 | ADD | // U axis Added #if U_HOME_DIR == -1 //BED_CENTER_AT_0_0 not used #define U_HOME_POS U_MIN_POS #else #define U_HOME_POS U_MAX_POS #endif //U_HOME_DIR == -1 // V axis Added #if V_HOME_DIR == -1 //BED_CENTER_AT_0_0 not used #define V_HOME_POS V_MIN_POS #else #define V_HOME_POS V_MAX_POS #endif //V_HOME_DIR == -1 // W axis Added #if W_HOME_DIR == -1 //BED_CENTER_AT_0_0 not used #define W_HOME_POS Z_MIN_POS #else #define W_HOME_POS Z_MAX_POS #endif //W_HOME_DIR == -1 |
| 239 | ADD | //homing hits the endstop, then retracts by this distance, before it tries to slowly bump again: #define X_HOME_RETRACT_MM 10 |

| | | |
|-----|-----|---|
| | | #define Y_HOME_RETRACT_MM 10 #define Z_HOME_RETRACT_MM 10 #define U_HOME_RETRACT_MM 10 //Added #define V_HOME_RETRACT_MM 10 //Added #define W_HOME_RETRACT_MM 10 //Added |
| 249 | MOD | #define AXIS_RELATIVE_MODES {false, false, false, false, false, false, false} |
| 255 | ADD | //By default pololu step drivers require an active high signal. However, some high power drivers require an active low signal as step. #define INVERT_X_STEP_PIN false #define INVERT_Y_STEP_PIN false #define INVERT_Z_STEP_PIN false #define INVERT_E_STEP_PIN false #define INVERT_U_STEP_PIN false //Added #define INVERT_V_STEP_PIN false //Added #define INVERT_W_STEP_PIN false //Added |

File: CONFIGURATIONSTORE.CPP

| Line # | Edit Type | Line of Code: |
|--------|-----------|--|
| 46 | MOD | char ver[7]= "000"; //Initially 4 |
| 136 | ADD | SERIAL_ECHOPAIR(" M92 X",axis_steps_per_unit[X_AXIS]); SERIAL_ECHOPAIR(" Y",axis_steps_per_unit[Y_AXIS]); SERIAL_ECHOPAIR(" Z",axis_steps_per_unit[Z_AXIS]); SERIAL_ECHOPAIR(" U",axis_steps_per_unit[U_AXIS]); //Added SERIAL_ECHOPAIR(" V",axis_steps_per_unit[V_AXIS]); //Added SERIAL_ECHOPAIR(" W",axis_steps_per_unit[W_AXIS]); //Added SERIAL_ECHOPAIR(" E",axis_steps_per_unit[E_AXIS]); |
| 158 | ADD | SERIAL_ECHOPAIR(" M203 X", max_feedrate[X_AXIS]); SERIAL_ECHOPAIR(" Y", max_feedrate[Y_AXIS]); SERIAL_ECHOPAIR(" Z", max_feedrate[Z_AXIS]); SERIAL_ECHOPAIR(" U", max_feedrate[U_AXIS]); //Added SERIAL_ECHOPAIR(" V", max_feedrate[V_AXIS]); //Added SERIAL_ECHOPAIR(" W", max_feedrate[W_AXIS]); //Added SERIAL_ECHOPAIR(" E", max_feedrate[E_AXIS]); |
| 170 | ADD | SERIAL_ECHOPAIR(" M201 X",max_acceleration_units_per_sq_second[X_AXIS]); SERIAL_ECHOPAIR(" Y", max_acceleration_units_per_sq_second[Y_AXIS]); SERIAL_ECHOPAIR(" Z",max_acceleration_units_per_sq_second[Z_AXIS]); SERIAL_ECHOPAIR(" U",max_acceleration_units_per_sq_second[U_AXIS]); //Added SERIAL_ECHOPAIR(" V",max_acceleration_units_per_sq_second[V_AXIS]); //Added SERIAL_ECHOPAIR(" W",max_acceleration_units_per_sq_second[W_AXIS]); //Added SERIAL_ECHOPAIR(" E",max_acceleration_units_per_sq_second[E_AXIS]); |
| 202 | ADD | SERIAL_ECHOPAIR(" U",add_homing[U_AXIS]); //Added SERIAL_ECHOPAIR(" V",add_homing[V_AXIS]); //Added SERIAL_ECHOPAIR(" W",add_homing[W_AXIS]); //Added |
| 213 | ADD | SERIAL_ECHOPAIR(" U",endstop_adj[U_AXIS]); //Added SERIAL_ECHOPAIR(" V",endstop_adj[V_AXIS]); //Added SERIAL_ECHOPAIR(" W",endstop_adj[W_AXIS]); //Added |
| 390 | MOD | for (short i=0;i<7;i++) //Initially 4 |
| 411 | MOD | add_homing[X_AXIS] = add_homing[Y_AXIS] = add_homing[Z_AXIS] = add_homing[U_AXIS] = add_homing[V_AXIS] = add_homing[W_AXIS] = 0; |

File: MARLIN.H

| Line # | Edit Type | Line of Code: |
|--------|-----------|---------------|
|--------|-----------|---------------|

| | | |
|-----|-----|---|
| 157 | ADD | <pre> #if defined(U_ENABLE_PIN) && (U_ENABLE_PIN > -1) //Added #define enable_u() WRITE(U_ENABLE_PIN, U_ENABLE_ON) #define disable_u() WRITE(U_ENABLE_PIN,!U_ENABLE_ON) #else #define enable_u() /* nothing */ #define disable_u() /* nothing */ #endif #if defined(V_ENABLE_PIN) && (V_ENABLE_PIN > -1) //Added #define enable_v() WRITE(V_ENABLE_PIN, V_ENABLE_ON) #define disable_v() WRITE(V_ENABLE_PIN,!V_ENABLE_ON) #else #define enable_v() /* nothing */ #define disable_v() /* nothing */ #endif #if defined(W_ENABLE_PIN) && (W_ENABLE_PIN > -1) //Added #define enable_w() WRITE(W_ENABLE_PIN, W_ENABLE_ON) #define disable_w() WRITE(W_ENABLE_PIN,!W_ENABLE_ON) #else #define enable_w() /* nothing */ #define disable_w() /* nothing */ #endif </pre> |
| 198 | MOD | enum AxisEnum {X_AXIS=0, Y_AXIS=1, Z_AXIS=2, U_AXIS=3, V_AXIS=4, W_AXIS=5, E_AXIS=6}; |
| 244 | MOD | extern float add_homing[6]; //For x, y, z, u, v, w axis |
| 255 | MOD | extern float min_pos[6]; //Initially 3 extern float max_pos[6]; //Initially 3 extern bool axis_known_position[6]; //Initially 3 |

File: MARLIN_MAIN.CPP

| Line # | Edit Type | Line of Code: |
|----------|-----------|--|
| 23 5 | MOD | float current_position[NUM_AXIS] = { 0.0, 0.0, 0.0, 0.0, 0.0, 0.0, 0.0 }; float add_homing[6]={0,0,0,0,0,0}; |
| 24 1 | MOD | float min_pos[6] = { X_MIN_POS, Y_MIN_POS, Z_MIN_POS, U_MIN_POS, V_MIN_POS, W_MIN_POS }; float max_pos[6] = { X_MAX_POS, Y_MAX_POS, Z_MAX_POS, U_MAX_POS, V_MAX_POS, W_MAX_POS }; bool axis_known_position[7] = {false, false, false, false, false, false, false}; |
| 34 7 | MOD | const char axis_codes[NUM_AXIS] = {'X', 'Y', 'Z', 'U', 'V', 'W', 'E'};static float destination[NUM_AXIS] = { 0.0, 0.0, 0.0, 0.0, 0.0, 0.0, 0.0}; |
| 35 0 | MOD | #ifndef DELTA //TRUE static float delta[7] = {0.0, 0.0, 0.0, 0.0, 0.0, 0.0, 0.0}; //Initially 3 #endif |
| 86 8 | MOD | static const PROGMEM type array##_P[6] = \ { X_##CONFIG, Y_##CONFIG, Z_##CONFIG, U_##CONFIG, V_##CONFIG, W_##CONFIG }; \ |
| 11 84 | MOD | if (axis==X_AXIS ? HOMEAXIS_DO(X) : axis==Y_AXIS ? HOMEAXIS_DO(Y) : axis==Z_AXIS ? HOMEAXIS_DO(Z) : axis==U_AXIS ? HOMEAXIS_DO(U) : //Added axis==V_AXIS ? HOMEAXIS_DO(V) : //Added axis==W_AXIS ? HOMEAXIS_DO(W) : //Added |

| | | |
|----------|-----|--|
| | | 0) { |
| 11 97 | MOD | current_position[axis] = 0; plan_set_position(current_position[X_AXIS], current_position[Y_AXIS], current_position[Z_AXIS], current_position[U_AXIS], current_position[V_AXIS], current_position[W_AXIS], current_position[E_AXIS]); |
| 12 15 | MOD | // destination[axis] = 750 * -1; //this just works for v,w axis destination[axis] = 1.5 * max_length(axis) * axis_home_dir; //this does not work for some reason; not creating vectors like it is supposed to feedrate = homing_feedrate[axis]; plan_buffer_line(destination[X_AXIS], destination[Y_AXIS], destination[Z_AXIS], destination[U_AXIS], destination[V_AXIS], destination[W_AXIS], destination[E_AXIS], feedrate/60, active_extruder); st_synchronize(); current_position[axis] = 0; plan_set_position(current_position[X_AXIS], current_position[Y_AXIS], current_position[Z_AXIS], current_position[U_AXIS], current_position[V_AXIS], current_position[W_AXIS], current_position[E_AXIS]); destination[axis] = -home_retract_mm(axis) * axis_home_dir; plan_buffer_line(destination[X_AXIS], destination[Y_AXIS], destination[Z_AXIS], destination[U_AXIS], destination[V_AXIS], destination[W_AXIS], destination[E_AXIS], feedrate/60, active_extruder); st_synchronize(); destination[axis] = 2*home_retract_mm(axis) * axis_home_dir; |
| 12 33 | MOD | plan_buffer_line(destination[X_AXIS], destination[Y_AXIS], destination[Z_AXIS], destination[U_AXIS], destination[V_AXIS], destination[W_AXIS], destination[E_AXIS], feedrate/60, active_extruder); st_synchronize(); |
| 12 94 | MOD | plan_set_position(current_position[X_AXIS], current_position[Y_AXIS], current_position[Z_AXIS], current_position[U_AXIS], current_position[V_AXIS], current_position[W_AXIS], current_position[E_AXIS]); |
| 13 08 | MOD | plan_set_position(current_position[X_AXIS], current_position[Y_AXIS], current_position[Z_AXIS], current_position[U_AXIS], current_position[V_AXIS], current_position[W_AXIS], current_position[E_AXIS]); |
| 14 88 | MOD | home_all_axis = !((code_seen(axis_codes[X_AXIS])) (code_seen(axis_codes[Y_AXIS])) (code_seen(axis_codes[Z_AXIS])) (code_seen(axis_codes[U_AXIS])) (code_seen(axis_codes[V_AXIS])) (code_seen(axis_codes[W_AXIS]))); |
| 14 99 | ADD | current_position[X_AXIS] = 0; current_position[Y_AXIS] = 0; current_position[U_AXIS] = 0; current_position[V_AXIS] = 0; current_position[W_AXIS] = 0; //Added |
| 15 09 | MOD | plan_set_position(current_position[X_AXIS], current_position[Y_AXIS], current_position[Z_AXIS], current_position[U_AXIS], current_position[V_AXIS], current_position[W_AXIS], current_position[E_AXIS]); |
| 15 11 | ADD | destination[U_AXIS] = 1.5 * max_length(U_AXIS) * u_axis_home_dir; destination[V_AXIS] = 1.5 * max_length(V_AXIS) * v_axis_home_dir; destination[W_AXIS] = 1.5 * max_length(W_AXIS) * home_dir(W_AXIS); //Added |
| 15 20 | MOD | plan_buffer_line(destination[X_AXIS], destination[Y_AXIS], destination[Z_AXIS], destination[U_AXIS], destination[V_AXIS], destination[W_AXIS], destination[E_AXIS], feedrate/60, active_extruder); |
| 15 23 | MOD | axis_is_at_home(X_AXIS); axis_is_at_home(Y_AXIS); axis_is_at_home(U_AXIS); //Added axis_is_at_home(V_AXIS); //Added axis_is_at_home(W_AXIS); //Added |

| | | |
|----------|-----|--|
| | | <pre> plan_set_position(current_position[X_AXIS], current_position[Y_AXIS], current_position[Z_AXIS], current_position[U_AXIS], current_position[V_AXIS], current_position[W_AXIS], current_position[E_AXIS]); destination[X_AXIS] = current_position[X_AXIS]; destination[Y_AXIS] = current_position[Y_AXIS]; destination[V_AXIS] = current_position[V_AXIS]; //Added destination[W_AXIS] = current_position[W_AXIS]; //Added plan_buffer_line(destination[X_AXIS], destination[Y_AXIS], destination[Z_AXIS], destination[U_AXIS], destination[V_AXIS], destination[W_AXIS], destination[E_AXIS], feedrate/60, active_extruder); </pre> |
| 15 41 | ADD | <pre> current_position[U_AXIS] = destination[U_AXIS]; //Added current_position[V_AXIS] = destination[V_AXIS]; //Added current_position[W_AXIS] = destination[W_AXIS]; //Added </pre> |
| 15 72 | ADD | <pre> if((home_all_axis) (code_seen(axis_codes[W_AXIS]))) { //Added HOMEAXIS(W); } if((home_all_axis) (code_seen(axis_codes[V_AXIS]))) { //Added HOMEAXIS(V); } if((home_all_axis) (code_seen(axis_codes[U_AXIS]))) { //Added HOMEAXIS(U); } </pre> |
| 16 05 | ADD | <pre> if(code_seen(axis_codes[U_AXIS])) { if(code_value_long() != 0) { #ifdef SCARA //Not Defined/Enabled current_position[U_AXIS]=code_value(); #else //enabled current_position[U_AXIS]=code_value()+add_homing[U_AXIS]; #endif } } if(code_seen(axis_codes[V_AXIS])) { if(code_value_long() != 0) { #ifdef SCARA //Not Defined/Enabled current_position[V_AXIS]=code_value(); #else //enabled current_position[V_AXIS]=code_value()+add_homing[V_AXIS]; #endif } } if(code_seen(axis_codes[W_AXIS])) { if(code_value_long() != 0) { #ifdef SCARA //Not Defined/Enabled current_position[W_AXIS]=code_value(); #else //enabled current_position[W_AXIS]=code_value()+add_homing[W_AXIS]; #endif } } </pre> |
| 16 41 | MOD | <pre> plan_buffer_line(destination[X_AXIS], destination[Y_AXIS], destination[Z_AXIS], destination[U_AXIS], destination[V_AXIS], destination[W_AXIS], destination[E_AXIS], feedrate, </pre> |

| | | |
|----------|-----|--|
| | | active_extruder); |
| 17 03 | MOD | plan_set_position(current_position[X_AXIS], current_position[Y_AXIS], current_position[Z_AXIS], current_position[U_AXIS], current_position[V_AXIS], current_position[W_AXIS], current_position[E_AXIS]); |
| 19 29 | MOD | plan_set_position(current_position[X_AXIS], current_position[Y_AXIS], current_position[Z_AXIS], current_position[U_AXIS], current_position[V_AXIS], current_position[W_AXIS], current_position[E_AXIS]); |
| 19 94 | ADD | case 17: LCD_MESSAGEPGM(MSG_NO_MOVE); enable_x(); enable_y(); enable_z(); enable_u(); //Added enable_v(); //Added enable_w(); //Added |
| 27 32 | MOD | case 82: axis_relative_modes[7] = false; //Initially 3 break; case 83: axis_relative_modes[7] = true; //Initially 3 |
| 27 45 | MOD | bool all_axis = !((code_seen(axis_codes[X_AXIS])) (code_seen(axis_codes[Y_AXIS])) (code_seen(axis_codes[Z_AXIS])) (code_seen(axis_codes[U_AXIS])) (code_seen(axis_codes[V_AXIS])) (code_seen(axis_codes[W_AXIS])) (code_seen(axis_codes[E_AXIS]))); |
| 27 57 | ADD | if(code_seen('X')) disable_x(); if(code_seen('Y')) disable_y(); if(code_seen('Z')) disable_z(); if(code_seen('U')) disable_u(); //Added if(code_seen('V')) disable_v(); //Added if(code_seen('W')) disable_w(); //Added |
| 27 78 | MOD | case 92: // M92 //Change i=5 on line 2766 if need to change these values for v and w axis for(int8_t i=0; i < NUM_AXIS; i++) { if(code_seen(axis_codes[i])) { if(i == 5) { // E |
| 28 15 | ADD | SERIAL_PROTOCOLPGM(" U:"); //Added SERIAL_PROTOCOL(float(st_get_position(U_AXIS))/axis_steps_per_unit[U_AXIS]); //Added SERIAL_PROTOCOLPGM(" V:"); //Added SERIAL_PROTOCOL(float(st_get_position(V_AXIS))/axis_steps_per_unit[V_AXIS]); //Added SERIAL_PROTOCOLPGM(" W:"); //Added SERIAL_PROTOCOL(float(st_get_position(W_AXIS))/axis_steps_per_unit[W_AXIS]); //Added SERIAL_PROTOCOLPGM(" E:"); SERIAL_PROTOCOL(float(st_get_position(E_AXIS))/axis_steps_per_unit[E_AXIS]); |
| 28 30 | ADD | SERIAL_PROTOCOLPGM(" U:"); //Added SERIAL_PROTOCOL(float(st_get_position(U_AXIS))/axis_steps_per_unit[U_AXIS]); SERIAL_PROTOCOLPGM(" V:"); //Added SERIAL_PROTOCOL(float(st_get_position(V_AXIS))/axis_steps_per_unit[V_AXIS]); SERIAL_PROTOCOLPGM(" W:"); //Added SERIAL_PROTOCOL(float(st_get_position(W_AXIS))/axis_steps_per_unit[W_AXIS]); |
| 28 91 | ADD | #if defined(U_MIN_PIN) && U_MIN_PIN > -1 //Added SERIAL_PROTOCOLPGM(MSG_U_MIN); SERIAL_PROTOCOLLN(((READ(U_MIN_PIN)^U_MIN_ENDSTOP_INVERTING)?MSG_END STOP_HIT:MSG_ENDSTOP_OPEN)); |

| | | |
|----------|-----|--|
| | | <pre> #endif #if defined(U_MAX_PIN) && U_MAX_PIN > -1 //Added SERIAL_PROTOCOLPGM(MSG_U_MAX); SERIAL_PROTOCOLLN(((READ(U_MAX_PIN)^U_MAX_ENDSTOP_INVERTING)?MSG_EN DSTOP_HIT:MSG_ENDSTOP_OPEN)); #endif #if defined(V_MIN_PIN) && V_MIN_PIN > -1 //Added SERIAL_PROTOCOLPGM(MSG_V_MIN); SERIAL_PROTOCOLLN(((READ(V_MIN_PIN)^V_MIN_ENDSTOP_INVERTING)?MSG_EN DSTOP_HIT:MSG_ENDSTOP_OPEN)); #endif #if defined(V_MAX_PIN) && V_MAX_PIN > -1 //Added SERIAL_PROTOCOLPGM(MSG_V_MAX); SERIAL_PROTOCOLLN(((READ(V_MAX_PIN)^V_MAX_ENDSTOP_INVERTING)?MSG_EN DSTOP_HIT:MSG_ENDSTOP_OPEN)); #endif #if defined(W_MIN_PIN) && W_MIN_PIN > -1 //Added SERIAL_PROTOCOLPGM(MSG_W_MIN); SERIAL_PROTOCOLLN(((READ(W_MIN_PIN)^W_MIN_ENDSTOP_INVERTING)?MSG_EN DSTOP_HIT:MSG_ENDSTOP_OPEN)); #endif #if defined(W_MAX_PIN) && W_MAX_PIN > -1 //Added SERIAL_PROTOCOLPGM(MSG_W_MAX); SERIAL_PROTOCOLLN(((READ(W_MAX_PIN)^W_MAX_ENDSTOP_INVERTING)?MSG_EN DSTOP_HIT:MSG_ENDSTOP_OPEN)); #endif </pre> |
| 39 87 | MOD | <pre> plan_set_position(current_position[X_AXIS], current_position[Y_AXIS], current_position[Z_AXIS], current_position[U_AXIS], current_position[V_AXIS], current_position[W_AXIS], current_position[E_AXIS]); </pre> |
| 40 32 | MOD | <pre> void get_coordinates() { bool seen[7]={ false,false,false,false,false,false,false}; //Initially seen[4]=... </pre> |
| 40 74 | MOD | <pre> void clamp_to_software_endstops(float target[6]) { if (min_software_endstops) { if (target[X_AXIS] < min_pos[X_AXIS]) target[X_AXIS] = min_pos[X_AXIS]; if (target[Y_AXIS] < min_pos[Y_AXIS]) target[Y_AXIS] = min_pos[Y_AXIS]; if (target[U_AXIS] < min_pos[U_AXIS]) target[U_AXIS] = min_pos[U_AXIS]; //Added if (target[V_AXIS] < min_pos[V_AXIS]) target[V_AXIS] = min_pos[V_AXIS]; //Added if (target[W_AXIS] < min_pos[W_AXIS]) target[W_AXIS] = min_pos[W_AXIS]; //Added </pre> |
| 40 92 | ADD | <pre> if (max_software_endstops) { if (target[X_AXIS] > max_pos[X_AXIS]) target[X_AXIS] = max_pos[X_AXIS]; if (target[Y_AXIS] > max_pos[Y_AXIS]) target[Y_AXIS] = max_pos[Y_AXIS]; if (target[Z_AXIS] > max_pos[Z_AXIS]) target[Z_AXIS] = max_pos[Z_AXIS]; if (target[U_AXIS] > max_pos[U_AXIS]) target[U_AXIS] = max_pos[U_AXIS]; //Added if (target[V_AXIS] > max_pos[V_AXIS]) target[V_AXIS] = max_pos[V_AXIS]; //Added if (target[W_AXIS] > max_pos[W_AXIS]) target[W_AXIS] = max_pos[W_AXIS]; //Added </pre> |
| 41 40 | MOD | <pre> void prepare_move() //MODIFIED { // clamp_to_software_endstops(destination); previous_millis_cmd = millis(); </pre> |

| | | |
|----------|-----|--|
| | | <pre> #if ! (defined DELTA defined SCARA) //Enabled // Do not use feedmultiply for E or Z only moves if((current_position[X_AXIS] == destination [X_AXIS]) && (current_position[Y_AXIS] == destination [Y_AXIS])) { if((current_position[U_AXIS] != destination [U_AXIS]) (current_position[V_AXIS] != destination [V_AXIS]) (current_position[W_AXIS] != destination [W_AXIS])){ //Added plan_buffer_line(destination[X_AXIS], destination[Y_AXIS], destination[Z_AXIS], destination[U_AXIS], destination[V_AXIS], destination[W_AXIS], destination[E_AXIS], feedrate*feedmultiply/60/100.0, active_extruder); //Added } //Added else{ //Added plan_buffer_line(destination[X_AXIS], destination[Y_AXIS], destination[Z_AXIS], destination[U_AXIS], destination[V_AXIS], destination[W_AXIS], destination[E_AXIS], feedrate/60, active_extruder); } //Added } else { plan_buffer_line(destination[X_AXIS], destination[Y_AXIS], destination[Z_AXIS], destination[U_AXIS], destination[V_AXIS], destination[W_AXIS], destination[E_AXIS], feedrate*feedmultiply/60/100.0, active_extruder); } #endif // !(DELTA SCARA) for(int8_t i=0; i < NUM_AXIS; i++) { current_position[i] = destination[i]; } } </pre> |
| 44 74 | ADD | <pre> disable_u(); //Added disable_v(); //Added disable_w(); //Added </pre> |

File: LANGUAGE.H

| Line # | Edit Type | Line of Code: |
|--------|-----------|--|
| 124 | ADD | <pre> #define MSG_U_MIN "u_min: " //Added #define MSG_U_MAX "u_max: " //Added #define MSG_V_MIN "v_min: " //Added #define MSG_V_MAX "v_max: " //Added #define MSG_W_MIN "w_min: " //Added #define MSG_W_MAX "w_max: " //Added </pre> |

File: MOTION_CONTROL.CPP

| Line # | Edit Type | Line of Code: |
|--------|-----------|---|
| 137 | MOD | <pre> plan_buffer_line(arc_target[X_AXIS], arc_target[Y_AXIS], arc_target[Z_AXIS], arc_target[U_AXIS], arc_target[V_AXIS], arc_target[W_AXIS], arc_target[E_AXIS], feed_rate, extruder); </pre> |
| 141 | MOD | <pre> plan_buffer_line(target[X_AXIS], target[Y_AXIS], target[Z_AXIS], target[U_AXIS], target[V_AXIS], target[W_AXIS], target[E_AXIS], feed_rate, extruder); </pre> |

File: PLANNER.CPP

| Line # | Edit Type | Line of Code: |
|--------|-----------|---|
| 401 | ADD | <pre> previous_speed[4] = 0.0; //Added </pre> |

| | | |
|-----|-----|---|
| | | previous_speed[5] = 0.0; //Added previous_speed[6] = 0.0; //Added |
| 421 | MOD | while(block_index != block_buffer_head) { if((block_buffer[block_index].steps_x != 0) (block_buffer[block_index].steps_y != 0) (block_buffer[block_index].steps_z != 0) (block_buffer[block_index].steps_u != 0) //Added (block_buffer[block_index].steps_v != 0) //Added (block_buffer[block_index].steps_w != 0)) { //Added float se=(float(block_buffer[block_index].steps_e)/float(block_buffer[block_index].step_event_count))*block_buffer[block_index].nominal_speed; //se; mm/sec; if(se>high) { high=se; } } block_index = (block_index+1) & (BLOCK_BUFFER_SIZE - 1); } |
| 453 | ADD | void check_axes_activity() { unsigned char x_active = 0; unsigned char y_active = 0; unsigned char z_active = 0; unsigned char u_active = 0; //Added unsigned char v_active = 0; //Added unsigned char w_active = 0; //Added |
| 483 | ADD | if(block->steps_u != 0) u_active++; //Added if(block->steps_v != 0) v_active++; //Added if(block->steps_w != 0) w_active++; //Added |
| 493 | ADD | if((DISABLE_U) && (u_active == 0)) disable_u(); //Added if((DISABLE_V) && (v_active == 0)) disable_v(); //Added if((DISABLE_W) && (w_active == 0)) disable_w(); //Added |
| 546 | ADD | void plan_buffer_line(const float &x, const float &y, const float &z, const float &u, const float &v, const float &w, const float &e, float feed_rate, const uint8_t &extruder) |
| 568 | MOD | long target[NUM_AXIS]; //Initially 4 target[X_AXIS] = lround(x*axis_steps_per_unit[X_AXIS]); target[Y_AXIS] = lround(y*axis_steps_per_unit[Y_AXIS]); target[Z_AXIS] = lround(z*axis_steps_per_unit[Z_AXIS]); target[U_AXIS] = lround(u*axis_steps_per_unit[U_AXIS]); //Added target[V_AXIS] = lround(v*axis_steps_per_unit[V_AXIS]); //Added target[W_AXIS] = lround(w*axis_steps_per_unit[W_AXIS]); //Added target[E_AXIS] = lround(e*axis_steps_per_unit[E_AXIS]); |
| 617 | ADD | block->steps_z = labs(target[Z_AXIS]-position[Z_AXIS]); block->steps_u = labs(target[U_AXIS]-position[U_AXIS]); //Added block->steps_v = labs(target[V_AXIS]-position[V_AXIS]); //Added block->steps_w = labs(target[W_AXIS]-position[W_AXIS]); //Added block->steps_e = labs(target[E_AXIS]-position[E_AXIS]); |
| 623 | MOD | block->step_event_count = max(block->steps_x, max(block->steps_y, max(block->steps_z, max(block->steps_u, max(block->steps_v, max(block->steps_w, block->steps_e)))))); // Initially block->step_event_count = max(block->steps_x, max(block->steps_y, max(block->steps_z, block->steps_e))); |
| 663 | ADD | if (target[U_AXIS] < position[U_AXIS]) //Added { |

| | | |
|-----|-----|--|
| | | <pre> block->direction_bits = (1<<U_AXIS); } if (target[V_AXIS] < position[V_AXIS]) //Added { block->direction_bits = (1<<V_AXIS); } if (target[W_AXIS] < position[W_AXIS]) //Added { block->direction_bits = (1<<W_AXIS); } if (target[E_AXIS] < position[E_AXIS]) { block->direction_bits = (1<<E_AXIS); } </pre> |
| 697 | ADD | <pre> if(block->steps_u != 0) enable_u(); //Added if(block->steps_v != 0) enable_v(); //Added if(block->steps_w != 0) enable_w(); //Added </pre> |
| 760 | MOD | <pre> #ifndef COREXY //TRUE float delta_mm[7]; //Initially 4 </pre> |
| 772 | ADD | <pre> delta_mm[U_AXIS] = (target[U_AXIS]-position[U_AXIS])/axis_steps_per_unit[U_AXIS]; //Added delta_mm[V_AXIS] = (target[V_AXIS]-position[V_AXIS])/axis_steps_per_unit[V_AXIS]; //Added delta_mm[W_AXIS] = (target[W_AXIS]-position[W_AXIS])/axis_steps_per_unit[W_AXIS]; //Added </pre> |
| 776 | MOD | <pre> if (block->steps_x <=dropsegments && block->steps_y <=dropsegments && block->steps_z <=dropsegments && block->steps_u <=dropsegments && block->steps_v <=dropsegments && block->steps_w <=dropsegments) { block->millimeters = fabs(delta_mm[E_AXIS]); } else { #ifndef COREXY //Enabled block->millimeters = sqrt(square(delta_mm[X_AXIS]) + square(delta_mm[Y_AXIS]) + square(delta_mm[Z_AXIS]) + square(delta_mm[U_AXIS]) + square(delta_mm[V_AXIS]) + square(delta_mm[W_AXIS])); #else //Not Defined/Enabled block->millimeters = sqrt(square(delta_mm[X_HEAD]) + square(delta_mm[Y_HEAD]) + square(delta_mm[Z_AXIS])); #endif } </pre> |
| 782 | MOD | <pre> #ifndef COREXY //Enabled block->millimeters = sqrt(square(delta_mm[X_AXIS]) + square(delta_mm[Y_AXIS]) + square(delta_mm[Z_AXIS]) + square(delta_mm[U_AXIS]) + square(delta_mm[V_AXIS]) + square(delta_mm[W_AXIS])); #else //Not Defined/Enabled block->millimeters = sqrt(square(delta_mm[X_HEAD]) + square(delta_mm[Y_HEAD]) + square(delta_mm[Z_AXIS])); #endif </pre> |
| 864 | MOD | <pre> // Calculate and limit speed in mm/sec for each axis float current_speed[7]; //Initially 4 float speed_factor = 1.0; //factor <=1 do decrease speed for(int i=0; i < 7; i++) //initially i < 4 </pre> |
| 909 | MOD | <pre> // Correct the speed if(speed_factor < 1.0) { </pre> |

| | | |
|------|-----|---|
| | | <pre> for(unsigned char i=0; i < 7; i++) //Initially i < 4 { current_speed[i] *= speed_factor; } block->nominal_speed *= speed_factor; block->nominal_rate *= speed_factor; } </pre> |
| 920 | MOD | <pre> // Compute and limit the acceleration rate for the trapezoid generator. float steps_per_mm = block->step_event_count/block->millimeters; if(block->steps_x == 0 && block->steps_y == 0 && block->steps_z == 0 && block->steps_u == 0 && block->steps_v == 0 && block->steps_w == 0) // initially if(block->steps_x == 0 && block->steps_y == 0 && block->steps_z == 0) { block->acceleration_st = ceil(retract_acceleration * steps_per_mm); // convert to: acceleration steps/sec^2 </pre> |
| 930 | ADD | <pre> // Limit acceleration per axis if(((float)block->acceleration_st * (float)block->steps_x / (float)block->step_event_count) > axis_steps_per_sqr_second[X_AXIS]) block->acceleration_st = axis_steps_per_sqr_second[X_AXIS]; if(((float)block->acceleration_st * (float)block->steps_y / (float)block->step_event_count) > axis_steps_per_sqr_second[Y_AXIS]) block->acceleration_st = axis_steps_per_sqr_second[Y_AXIS]; if(((float)block->acceleration_st * (float)block->steps_z / (float)block->step_event_count) > axis_steps_per_sqr_second[Z_AXIS]) block->acceleration_st = axis_steps_per_sqr_second[Z_AXIS]; if(((float)block->acceleration_st * (float)block->steps_u / (float)block->step_event_count) > axis_steps_per_sqr_second[U_AXIS]) //Added block->acceleration_st = axis_steps_per_sqr_second[U_AXIS]; if(((float)block->acceleration_st * (float)block->steps_v / (float)block->step_event_count) > axis_steps_per_sqr_second[V_AXIS]) //Added block->acceleration_st = axis_steps_per_sqr_second[V_AXIS]; if(((float)block->acceleration_st * (float)block->steps_w / (float)block->step_event_count) > axis_steps_per_sqr_second[W_AXIS]) //Added block->acceleration_st = axis_steps_per_sqr_second[W_AXIS]; if(((float)block->acceleration_st * (float)block->steps_e / (float)block->step_event_count) > axis_steps_per_sqr_second[E_AXIS]) block->acceleration_st = axis_steps_per_sqr_second[E_AXIS]; </pre> |
| 1099 | MOD | <pre> void plan_set_position(const float &x, const float &y, const float &z, const float &u, const float &v, const float &w, const float &e) </pre> |
| 1107 | MOD | <pre> position[X_AXIS] = lround(x*axis_steps_per_unit[X_AXIS]); position[Y_AXIS] = lround(y*axis_steps_per_unit[Y_AXIS]); position[Z_AXIS] = lround(z*axis_steps_per_unit[Z_AXIS]); position[U_AXIS] = lround(u*axis_steps_per_unit[U_AXIS]); //Added position[V_AXIS] = lround(v*axis_steps_per_unit[V_AXIS]); //Added position[W_AXIS] = lround(w*axis_steps_per_unit[W_AXIS]); //Added position[E_AXIS] = lround(e*axis_steps_per_unit[E_AXIS]); st_set_position(position[X_AXIS], position[Y_AXIS], position[Z_AXIS], position[U_AXIS], position[V_AXIS], position[W_AXIS], position[E_AXIS]); </pre> |
| 1120 | ADD | <pre> previous_speed[4] = 0.0; //Added previous_speed[5] = 0.0; //Added previous_speed[6] = 0.0; //Added </pre> |

File: PLANNER.H

| Line | Edit | Line of Code: |
|------|------|---------------|
|------|------|---------------|

| # | Type | |
|----|------|--|
| 37 | MOD | long steps_x, steps_y, steps_z, steps_u, steps_v, steps_w, steps_e; // Step count along each axis |
| 91 | MOD | void plan_buffer_line(const float &x, const float &y, const float &z, const float &u, const float &v, const float &w, const float &e, float feed_rate, const uint8_t &extruder); |
| 98 | MOD | void plan_set_position(const float &x, const float &y, const float &z, const float &u, const float &v, const float &w, const float &e); |

File: STEPPER.CPP

| Line # | Edit Type | Line of Code: |
|--------|-----------|--|
| 50 | ADD | static long counter_x, // Counter variables for the bresenham line tracer counter_y, counter_z, counter_u, //Added counter_v, //Added counter_w, //Added counter_e; |
| 70 | MOD | volatile long endstops_trigsteps[6]={0,0,0,0,0,0}; //Initially 3 volatile long endstops_stepsTotal,endstops_stepsDone; static volatile bool endstop_x_hit=false; static volatile bool endstop_y_hit=false; static volatile bool endstop_z_hit=false; static volatile bool endstop_u_hit=false; //Added static volatile bool endstop_v_hit=false; //Added static volatile bool endstop_w_hit=false; //Added |
| 91 | ADD | static bool old_u_min_endstop=false; //Added static bool old_u_max_endstop=false; //Added static bool old_v_min_endstop=false; //Added static bool old_v_max_endstop=false; //Added static bool old_w_min_endstop=false; //Added static bool old_w_max_endstop=false; //Added |
| 100 | MOD | volatile long count_position[NUM_AXIS] = { 0, 0, 0, 0, 0, 0 }; //Initially 4 volatile signed char count_direction[NUM_AXIS] = { 1, 1, 1, 1, 1, 1 }; //Initially 4 |
| 185 | MOD | void checkHitEndstops() { if(endstop_x_hit endstop_y_hit endstop_z_hit endstop_u_hit endstop_v_hit endstop_w_hit) { SERIAL_ECHO_START; SERIAL_ECHOPGM(MSG_ENDSTOPS_HIT); if(endstop_x_hit) { SERIAL_ECHOPAIR(" X:",(float)endstops_trigsteps[X_AXIS]/axis_steps_per_unit[X_AXIS]); LCD_MESSAGEPGM(MSG_ENDSTOPS_HIT "X"); } if(endstop_y_hit) { SERIAL_ECHOPAIR(" Y:",(float)endstops_trigsteps[Y_AXIS]/axis_steps_per_unit[Y_AXIS]); LCD_MESSAGEPGM(MSG_ENDSTOPS_HIT "Y"); } if(endstop_z_hit) { SERIAL_ECHOPAIR(" Z:",(float)endstops_trigsteps[Z_AXIS]/axis_steps_per_unit[Z_AXIS]); LCD_MESSAGEPGM(MSG_ENDSTOPS_HIT "Z"); } if(endstop_u_hit) { //Added SERIAL_ECHOPAIR(" U:",(float)endstops_trigsteps[U_AXIS]/axis_steps_per_unit[U_AXIS]); LCD_MESSAGEPGM(MSG_ENDSTOPS_HIT "U"); } } |

| | | |
|-----|-----|--|
| | | <pre> if(endstop_v_hit) { //Added SERIAL_ECHOPAIR(" V:",(float)endstops_trigsteps[V_AXIS]/axis_steps_per_unit[V_AXIS]); LCD_MESSAGEPGM(MSG_ENDSTOPS_HIT "V"); } if(endstop_w_hit) { //Added SERIAL_ECHOPAIR(" W:",(float)endstops_trigsteps[W_AXIS]/axis_steps_per_unit[W_AXIS]); LCD_MESSAGEPGM(MSG_ENDSTOPS_HIT "W"); } SERIAL_ECHOLN(""); endstop_x_hit=false; endstop_y_hit=false; endstop_z_hit=false; endstop_u_hit=false; //Added endstop_v_hit=false; //Added endstop_w_hit=false; //Added </pre> |
| 235 | ADD | <pre> void endstops_hit_on_purpose() { endstop_x_hit=false; endstop_y_hit=false; endstop_z_hit=false; endstop_u_hit=false; //Added endstop_v_hit=false; //Added endstop_w_hit=false; //Added } </pre> |
| 357 | ADD | <pre> counter_u = counter_x; //Added counter_v = counter_x; //Added counter_w = counter_x; //Added counter_e = counter_x; </pre> |
| 563 | ADD | <pre> //Added U set direction and check endstops if ((out_bits & (1<<U_AXIS)) != 0) { // -direction WRITE(U_DIR_PIN,INVERT_U_DIR); count_direction[U_AXIS]=-1; CHECK_ENDSTOPS { #if defined(U_MIN_PIN) && U_MIN_PIN > -1 bool u_min_endstop=(READ(U_MIN_PIN) != U_MIN_ENDSTOP_INVERTING); if(u_min_endstop && old_u_min_endstop && (current_block->steps_u > 0)) { endstops_trigsteps[U_AXIS] = count_position[U_AXIS]; endstop_u_hit=true; step_events_completed = current_block->step_event_count; } old_u_min_endstop = u_min_endstop; #endif } } else { // +direction WRITE(U_DIR_PIN,!INVERT_U_DIR); count_direction[U_AXIS]=1; CHECK_ENDSTOPS { #if defined(U_MAX_PIN) && U_MAX_PIN > -1 bool u_max_endstop=(READ(U_MAX_PIN) != U_MAX_ENDSTOP_INVERTING); if(u_max_endstop && old_u_max_endstop && (current_block->steps_u > 0)) { </pre> |

```

endstops_trigsteps[U_AXIS] = count_position[U_AXIS];
endstop_u_hit=true;
step_events_completed = current_block->step_event_count;
}
old_u_max_endstop = u_max_endstop;
#endif
}
}

//Added V set direction and check endstops
if ((out_bits & (1<<V_AXIS)) != 0) { // -direction
WRITE(V_DIR_PIN,INVERT_V_DIR);

count_direction[V_AXIS]=-1;
CHECK_ENDSTOPS
{
#if defined(V_MIN_PIN) && V_MIN_PIN > -1
bool v_min_endstop=(READ(V_MIN_PIN) != V_MIN_ENDSTOP_INVERTING);
if(v_min_endstop && old_v_min_endstop && (current_block->steps_v > 0)) {
endstops_trigsteps[V_AXIS] = count_position[V_AXIS];
endstop_v_hit=true;
step_events_completed = current_block->step_event_count;
}
old_v_min_endstop = v_min_endstop;
#endif
}
}
else { // +direction
WRITE(V_DIR_PIN,!INVERT_V_DIR);

count_direction[V_AXIS]=1;
CHECK_ENDSTOPS
{
#if defined(V_MAX_PIN) && V_MAX_PIN > -1
bool v_max_endstop=(READ(V_MAX_PIN) != V_MAX_ENDSTOP_INVERTING);
if(v_max_endstop && old_v_max_endstop && (current_block->steps_v > 0)) {
endstops_trigsteps[V_AXIS] = count_position[V_AXIS];
endstop_v_hit=true;
step_events_completed = current_block->step_event_count;
}
old_v_max_endstop = v_max_endstop;
#endif
}
}

//Added W set direction and check endstops
if ((out_bits & (1<<W_AXIS)) != 0) { // -direction
WRITE(W_DIR_PIN,INVERT_W_DIR);

count_direction[W_AXIS]=-1;
CHECK_ENDSTOPS
{
#if defined(W_MIN_PIN) && W_MIN_PIN > -1
bool w_min_endstop=(READ(W_MIN_PIN) != W_MIN_ENDSTOP_INVERTING);
if(w_min_endstop && old_w_min_endstop && (current_block->steps_w > 0)) {
endstops_trigsteps[W_AXIS] = count_position[W_AXIS];

```

| | | |
|-----|-----|---|
| | | <pre> endstop_w_hit=true; step_events_completed = current_block->step_event_count; } old_w_min_endstop = w_min_endstop; #endif } } else { // +direction WRITE(W_DIR_PIN,!INVERT_W_DIR); count_direction[W_AXIS]=1; CHECK_ENDSTOPS { #if defined(W_MAX_PIN) && W_MAX_PIN > -1 bool w_max_endstop=(READ(W_MAX_PIN) != W_MAX_ENDSTOP_INVERTING); if(w_max_endstop && old_w_max_endstop && (current_block->steps_w > 0)) { endstops_trigsteps[W_AXIS] = count_position[W_AXIS]; endstop_w_hit=true; step_events_completed = current_block->step_event_count; } old_w_max_endstop = w_max_endstop; #endif } } </pre> |
| 721 | ADD | <pre> counter_u += current_block->steps_u; //Added but probably not used if (counter_u > 0) { WRITE(U_STEP_PIN, HIGH); } counter_v += current_block->steps_v; //Added but probably not used if (counter_v > 0) { WRITE(V_STEP_PIN, HIGH); } counter_w += current_block->steps_w; //Added but probably not used if (counter_w > 0) { WRITE(W_STEP_PIN, HIGH); } </pre> |
| 761 | ADD | <pre> if (counter_u > 0) { //Added but probably not used counter_u -= current_block->step_event_count; count_position[U_AXIS]+=count_direction[U_AXIS]; WRITE(U_STEP_PIN, LOW); } if (counter_v > 0) { //Added but probably not used counter_v -= current_block->step_event_count; count_position[V_AXIS]+=count_direction[V_AXIS]; WRITE(V_STEP_PIN, LOW); } if (counter_w > 0) { //Added but probably not used counter_w -= current_block->step_event_count; count_position[W_AXIS]+=count_direction[W_AXIS]; WRITE(W_STEP_PIN, LOW); } </pre> |
| 854 | ADD | <pre> counter_u += current_block->steps_u; //Added if (counter_u > 0) { </pre> |

| | | |
|------|-----|--|
| | | <pre> WRITE(U_STEP_PIN, !INVERT_U_STEP_PIN); counter_u -= current_block->step_event_count; count_position[U_AXIS]+=count_direction[U_AXIS]; WRITE(U_STEP_PIN, INVERT_U_STEP_PIN); } counter_v += current_block->steps_v; //Added if (counter_v > 0) { WRITE(V_STEP_PIN, !INVERT_V_STEP_PIN); counter_v -= current_block->step_event_count; count_position[V_AXIS]+=count_direction[V_AXIS]; WRITE(V_STEP_PIN, INVERT_V_STEP_PIN); } counter_w += current_block->steps_w; //Added if (counter_w > 0) { WRITE(W_STEP_PIN, !INVERT_W_STEP_PIN); counter_w -= current_block->step_event_count; count_position[W_AXIS]+=count_direction[W_AXIS]; WRITE(W_STEP_PIN, INVERT_W_STEP_PIN); } </pre> |
| 1046 | ADD | <pre> #if defined(U_DIR_PIN) && U_DIR_PIN > -1 //Added SET_OUTPUT(U_DIR_PIN); #endif #if defined(V_DIR_PIN) && V_DIR_PIN > -1 //Added SET_OUTPUT(V_DIR_PIN); #endif #if defined(W_DIR_PIN) && W_DIR_PIN > -1 //Added SET_OUTPUT(W_DIR_PIN); #endif </pre> |
| 1058 | MOD | <pre> // #if defined(E1_DIR_PIN) && (E1_DIR_PIN > -1) // SET_OUTPUT(E1_DIR_PIN); // #endif // #if defined(E2_DIR_PIN) && (E2_DIR_PIN > -1)F // SET_OUTPUT(E2_DIR_PIN); // #endif </pre> |
| 1093 | ADD | <pre> #if defined(U_ENABLE_PIN) && (U_ENABLE_PIN > -1) //Added SET_OUTPUT(U_ENABLE_PIN); if(!U_ENABLE_ON) WRITE(U_ENABLE_PIN,HIGH); #endif #if defined(V_ENABLE_PIN) && (V_ENABLE_PIN > -1) //Added SET_OUTPUT(V_ENABLE_PIN); if(!V_ENABLE_ON) WRITE(V_ENABLE_PIN,HIGH); #endif #if defined(W_ENABLE_PIN) && (W_ENABLE_PIN > -1) //Added SET_OUTPUT(W_ENABLE_PIN); if(!W_ENABLE_ON) WRITE(W_ENABLE_PIN,HIGH); #endif </pre> |
| 1109 | MOD | <pre> // #if defined(E1_ENABLE_PIN) && (E1_ENABLE_PIN > -1) // SET_OUTPUT(E1_ENABLE_PIN); // if(!E_ENABLE_ON) WRITE(E1_ENABLE_PIN,HIGH); // #endif // #if defined(E2_ENABLE_PIN) && (E2_ENABLE_PIN > -1) </pre> |

| | | |
|------|-----|---|
| | | <pre>// SET_OUTPUT(E2_ENABLE_PIN); // if(!E_ENABLE_ON) WRITE(E2_ENABLE_PIN,HIGH); // #endif</pre> |
| 1141 | ADD | <pre>#if defined(U_MIN_PIN) && U_MIN_PIN > -1 //Added SET_INPUT(U_MIN_PIN); #ifdef ENDSTOPPULLUP_UMIN WRITE(U_MIN_PIN,HIGH); #endif #endif #if defined(V_MIN_PIN) && V_MIN_PIN > -1 //Added SET_INPUT(V_MIN_PIN); #ifdef ENDSTOPPULLUP_VMIN WRITE(V_MIN_PIN,HIGH); #endif #endif #if defined(W_MIN_PIN) && W_MIN_PIN > -1 //Added SET_INPUT(W_MIN_PIN); #ifdef ENDSTOPPULLUP_WMIN WRITE(W_MIN_PIN,HIGH); #endif #endif</pre> |
| 1183 | ADD | <pre>#if defined(U_MAX_PIN) && U_MAX_PIN > -1 //Added SET_INPUT(U_MAX_PIN); #ifdef ENDSTOPPULLUP_UMAX WRITE(U_MAX_PIN,HIGH); #endif #endif #if defined(V_MAX_PIN) && V_MAX_PIN > -1 //Added SET_INPUT(V_MAX_PIN); #ifdef ENDSTOPPULLUP_VMAX WRITE(V_MAX_PIN,HIGH); #endif #endif #if defined(W_MAX_PIN) && W_MAX_PIN > -1 //Added SET_INPUT(W_MAX_PIN); #ifdef ENDSTOPPULLUP_WMAX WRITE(W_MAX_PIN,HIGH); #endif #endif</pre> |
| 1233 | ADD | <pre>#if defined(U_STEP_PIN) && (U_STEP_PIN > -1) //ADDED SET_OUTPUT(U_STEP_PIN); WRITE(U_STEP_PIN,INVERT_U_STEP_PIN); disable_u(); #endif #if defined(V_STEP_PIN) && (V_STEP_PIN > -1) //ADDED SET_OUTPUT(V_STEP_PIN); WRITE(V_STEP_PIN,INVERT_V_STEP_PIN); disable_v(); #endif #if defined(W_STEP_PIN) && (W_STEP_PIN > -1) //ADDED SET_OUTPUT(W_STEP_PIN); WRITE(W_STEP_PIN,INVERT_W_STEP_PIN);</pre> |

| | | |
|------|-----|--|
| | | <pre> disable_w(); #endif </pre> |
| 1253 | MOD | <pre> // #if defined(E1_STEP_PIN) && (E1_STEP_PIN > -1) // SET_OUTPUT(E1_STEP_PIN); // WRITE(E1_STEP_PIN,INVERT_E_STEP_PIN); // disable_e1(); // #endif // #if defined(E2_STEP_PIN) && (E2_STEP_PIN > -1) // SET_OUTPUT(E2_STEP_PIN); // WRITE(E2_STEP_PIN,INVERT_E_STEP_PIN); // disable_e2(); // #endif </pre> |
| 1264 | MOD | <pre> // waveform generation = 0100 = CTC //All Axis Don't Move when Uncommented TCCR1B &= ~(1<<WGM13); // <<Bitwise shift left ~bitwise NOT (flips bits from 0 to 1 or 1 to 0 TCCR1B = (1<<WGM12); // TCCR1B = TCCR1B (1<<WGM12) TCCR1A &= ~(1<<WGM11); // TCCR1A = TCCR1A & TCCR1A &= ~(1<<WGM10); // output mode = 00 (disconnected) TCCR1A &= ~(3<<COM1A0); TCCR1A &= ~(3<<COM1B0); // Set the timer pre-scaler // Generally we use a divider of 8, resulting in a 2MHz timer // frequency on a 16MHz MCU. If you are going to change this, be // sure to regenerate speed_lookuptable.h with // create_speed_lookuptable.py TCCR1B = (TCCR1B & ~(0x07<<CS10)) (2<<CS10); OCR1A = 0x4000; TCNT1 = 0; ENABLE_STEPPER_DRIVER_INTERRUPT(); </pre> |
| 1311 | MOD | <pre> void st_set_position(const long &x, const long &y, const long &z, const long &u, const long &v, const long &w, const long &e) { CRITICAL_SECTION_START; count_position[X_AXIS] = x; count_position[Y_AXIS] = y; count_position[Z_AXIS] = z; count_position[U_AXIS] = u; //Added count_position[V_AXIS] = v; //Added count_position[W_AXIS] = w; //Added count_position[E_AXIS] = e; CRITICAL_SECTION_END; } </pre> |
| 1348 | ADD | <pre> void finishAndDisableSteppers() { st_synchronize(); disable_x(); disable_y(); disable_z(); disable_u(); //Added disable_v(); //Added disable_w(); //Added disable_e0(); } </pre> |

| | | |
|--|--|--|
| | | <pre> disable_e1(); disable_e2(); } </pre> |
|--|--|--|

File: STEPPER.H

| Line # | Edit Type | Line of Code: |
|--------|-----------|--|
| 58 | MOD | void st_set_position(const long &x, const long &y, const long &z, const long &u, const long &v, const long &w, const long &e); |

File: PINS.H

| Line # | Edit Type | Line of Code: |
|--------|-----------|---|
| 596 | MOD | <pre> #define X_STEP_PIN 54 #define X_DIR_PIN 55 #define X_ENABLE_PIN 38 #define X_MIN_PIN 2 // 3 #define X_MAX_PIN -1 // Initially 2; turned off #define Y_STEP_PIN 60 #define Y_DIR_PIN 61 #define Y_ENABLE_PIN 56 #define Y_MIN_PIN 19 // 14 #define Y_MAX_PIN -1 //15 #define Z_STEP_PIN 46 #define Z_DIR_PIN 48 #define Z_ENABLE_PIN 62 #define Z_MIN_PIN -1 //18 #define Z_MAX_PIN -1 //Initially 19; turned off </pre> |
| 626 | MOD | <pre> #define U_STEP_PIN 36 //Initially #define E0_STEP_PIN 36 #define U_DIR_PIN 34 #define U_ENABLE_PIN 30 #define U_MIN_PIN 3 // #define U_MAX_PIN -1 // </pre> |
| 642 | MOD | <pre> #define V_STEP_PIN 23 //Initially #define E2_STEP_PIN 23 #define V_DIR_PIN 25 #define V_ENABLE_PIN 40 #define V_MIN_PIN 14 // was #define V_MAX_PIN 15 // Turned off #define W_STEP_PIN 27 //Initially #define E3_STEP_PIN 27 #define W_DIR_PIN 29 #define W_ENABLE_PIN 41 #define W_MIN_PIN 18 //Initially Z_MAX_PIN #define W_MAX_PIN -1 // Turned off </pre> |
| 715 | MOD | <pre> #define TEMP_1_PIN -1 // ANALOG NUMBERING //Initially 15 #if MB(AZTEEG_X3_PRO) #define TEMP_2_PIN -1 // ANALOG NUMBERING //Initially 12 #define TEMP_3_PIN -1 // ANALOG NUMBERING //Initially 11 #define TEMP_4_PIN -1 // ANALOG NUMBERING //Initially 10 </pre> |

File: THERMISTORTABLES.H

| Line | Edit | Line of Code: |
|------|------|---------------|
|------|------|---------------|

| # | Type | |
|------|------|--|
| 1029 | ADD | <pre> #if (THERMISTORHEATER_0 == 65) (THERMISTORHEATER_1 == 65) (THERMISTORHEATER_2 == 65) (THERMISTORHEATER_3 == 65) (THERMISTORBED == 65) // Contributed by Brandon Coates - May 2015 // B3 Innovations Pico 500c Thermistor // B150/250 = 5300 K +/- 3% // R 250 = 2.705k Ohms +/- 2.5% const short temptable_65[][2] PROGMEM = { { 9.36*OVERSAMPLNENR , 510 }, { 10.24*OVERSAMPLNENR , 505 }, { 11.07*OVERSAMPLNENR , 500 }, { 11.95*OVERSAMPLNENR , 495 }, { 12.72*OVERSAMPLNENR , 490 }, { 13.82*OVERSAMPLNENR , 485 }, { 14.60*OVERSAMPLNENR , 480 }, { 15.80*OVERSAMPLNENR , 475 }, { 16.76*OVERSAMPLNENR , 470 }, { 17.88*OVERSAMPLNENR , 465 }, { 19.20*OVERSAMPLNENR , 460 }, { 20.38*OVERSAMPLNENR , 455 }, { 21.92*OVERSAMPLNENR , 450 }, { 23.13*OVERSAMPLNENR , 445 }, { 24.76*OVERSAMPLNENR , 440 }, { 26.34*OVERSAMPLNENR , 435 }, { 27.96*OVERSAMPLNENR , 430 }, { 29.89*OVERSAMPLNENR , 425 }, { 31.52*OVERSAMPLNENR , 420 }, { 33.52*OVERSAMPLNENR , 415 }, { 35.90*OVERSAMPLNENR , 410 }, { 38.03*OVERSAMPLNENR , 405 }, { 40.73*OVERSAMPLNENR , 400 }, { 43.14*OVERSAMPLNENR , 395 }, { 46.31*OVERSAMPLNENR , 390 }, { 48.99*OVERSAMPLNENR , 385 }, { 52.44*OVERSAMPLNENR , 380 }, { 55.92*OVERSAMPLNENR , 375 }, { 59.88*OVERSAMPLNENR , 370 }, { 63.76*OVERSAMPLNENR , 365 }, { 68.21*OVERSAMPLNENR , 360 }, { 72.81*OVERSAMPLNENR , 355 }, { 77.65*OVERSAMPLNENR , 350 }, { 83.12*OVERSAMPLNENR , 345 }, { 88.75*OVERSAMPLNENR , 340 }, { 95.29*OVERSAMPLNENR , 335 }, { 101.95*OVERSAMPLNENR , 330 }, { 109.40*OVERSAMPLNENR , 325 }, { 117.50*OVERSAMPLNENR , 320 }, { 126.15*OVERSAMPLNENR , 315 }, { 135.38*OVERSAMPLNENR , 310 }, { 145.24*OVERSAMPLNENR , 305 }, { 155.84*OVERSAMPLNENR , 300 }, { 167.30*OVERSAMPLNENR , 295 }, { 179.91*OVERSAMPLNENR , 290 }, { 193.49*OVERSAMPLNENR , 285 }, { 207.96*OVERSAMPLNENR , 280 }, </pre> |

| | | |
|--|--|--|
| | | { 223.40*OVERSAMPLNR , 275 }, { 240.16*OVERSAMPLNR , 270 }, { 258.11*OVERSAMPLNR , 265 }, { 276.98*OVERSAMPLNR , 260 }, { 296.97*OVERSAMPLNR , 255 }, { 319.01*OVERSAMPLNR , 250 }, { 342.10*OVERSAMPLNR , 245 }, { 365.69*OVERSAMPLNR , 240 }, { 392.11*OVERSAMPLNR , 235 }, { 418.88*OVERSAMPLNR , 230 }, { 445.57*OVERSAMPLNR , 225 }, { 473.95*OVERSAMPLNR , 220 }, { 503.79*OVERSAMPLNR , 215 }, { 533.27*OVERSAMPLNR , 210 }, { 564.80*OVERSAMPLNR , 205 }, { 595.54*OVERSAMPLNR , 200 }, { 629.04*OVERSAMPLNR , 195 }, { 658.72*OVERSAMPLNR , 190 }, { 687.23*OVERSAMPLNR , 185 }, { 716.48*OVERSAMPLNR , 180 }, { 745.56*OVERSAMPLNR , 175 }, { 772.95*OVERSAMPLNR , 170 }, { 797.95*OVERSAMPLNR , 165 }, { 822.10*OVERSAMPLNR , 160 }, { 844.76*OVERSAMPLNR , 155 }, { 866.97*OVERSAMPLNR , 150 }, { 885.02*OVERSAMPLNR , 145 }, { 902.10*OVERSAMPLNR , 140 }, { 917.47*OVERSAMPLNR , 135 }, { 931.64*OVERSAMPLNR , 130 }, { 944.88*OVERSAMPLNR , 125 }, { 956.09*OVERSAMPLNR , 120 }, { 965.84*OVERSAMPLNR , 115 }, { 974.49*OVERSAMPLNR , 110 }, { 981.99*OVERSAMPLNR , 105 }, { 988.79*OVERSAMPLNR , 100 }, { 994.56*OVERSAMPLNR , 95 }, { 999.50*OVERSAMPLNR , 90 }, { 1003.87*OVERSAMPLNR , 85 }, { 1007.31*OVERSAMPLNR , 80 }, { 1010.30*OVERSAMPLNR , 75 }, { 1013.08*OVERSAMPLNR , 70 }, { 1015.08*OVERSAMPLNR , 65 }, { 1016.97*OVERSAMPLNR , 60 }, { 1018.17*OVERSAMPLNR , 55 }, { 1019.53*OVERSAMPLNR , 50 }, { 1020.48*OVERSAMPLNR , 45 }, { 1021.09*OVERSAMPLNR , 40 }, { 1021.18*OVERSAMPLNR , 35 }, { 1021.58*OVERSAMPLNR , 30 }, { 1021.91*OVERSAMPLNR , 25 }, { 1022.16*OVERSAMPLNR , 25 }, { 1022.36*OVERSAMPLNR , 25 }, { 1022.52*OVERSAMPLNR , 25 }, { 1022.64*OVERSAMPLNR , 25 }, { 1022.73*OVERSAMPLNR , 25 }, |
|--|--|--|

| | | |
|--|--|--------------|
| | | }; #endif |
|--|--|--------------|

10.2 Tow Positional Fidelity G-Code

An example g-code for the constant angle tow positional fidelity portion of the study is shown below. Note that this is for a feed rate of 200 mm/min and a PP base layer.

G1 V60
G92 V0
G1 V75
G1 W20.0 ;19.2 USED PREVIOUSLY
G92 U10 W18.5
G1 U 10.000 V 75.000 W18.500 F200
G1 U 10.000 V270.000 W18.500
G1 W5
G4 S15
G1 U 20.000 V 75.000 F1400
G4 S5
G1 U 20.000 V 75.000 W18.500 F200
G1 U 20.000 V122.287 W18.500
G1 U 20.007 V122.819 W18.500
G1 U 20.022 V123.216 W18.500
G1 U 20.042 V123.589 W18.500
G1 U 20.065 V123.895 W18.500
G1 U 20.094 V124.224 W18.500
G1 U 20.119 V124.468 W18.500
G1 U 20.149 V124.722 W18.500
G1 U 20.179 V124.960 W18.500
G1 U 20.208 V125.161 W18.500
G1 U 20.233 V125.327 W18.500
G1 U 20.266 V125.537 W18.500
G1 U 20.304 V125.760 W18.500
G1 U 37.669 V224.240 W18.500
G1 U 37.704 V224.448 W18.500
G1 U 37.738 V224.659 W18.500
G1 U 37.763 V224.829 W18.500
G1 U 37.788 V225.003 W18.500
G1 U 37.811 V225.180 W18.500
G1 U 37.834 V225.361 W18.500
G1 U 37.854 V225.543 W18.500
G1 U 37.881 V225.807 W18.500
G1 U 37.905 V226.073 W18.500
G1 U 37.920 V226.261 W18.500
G1 U 37.935 V226.492 W18.500
G1 U 37.949 V226.740 W18.500
G1 U 37.957 V226.934 W18.500
G1 U 37.965 V227.158 W18.500
G1 U 37.969 V227.351 W18.500
G1 U 37.971 V227.509 W18.500
G1 U 37.973 V227.713 W18.500
G1 U 37.973 V270.000 W18.500
G1 W5
G4 S15
G1 U 30.000 V 75.000 F1400
G4 S5
G1 U 30.000 V 75.000 W18.500 F200
G1 U 30.000 V121.175 W18.500

G1 U 30.000 V121.312 W18.500
G1 U 30.001 V121.419 W18.500
G1 U 30.003 V121.521 W18.500
G1 U 30.005 V121.614 W18.500
G1 U 30.008 V121.723 W18.500
G1 U 30.011 V121.829 W18.500
G1 U 30.014 V121.925 W18.500
G1 U 30.018 V122.021 W18.500
G1 U 30.022 V122.114 W18.500
G1 U 30.027 V122.215 W18.500
G1 U 30.032 V122.306 W18.500
G1 U 30.038 V122.407 W18.500
G1 U 30.044 V122.506 W18.500
G1 U 30.051 V122.602 W18.500
G1 U 30.059 V122.705 W18.500
G1 U 30.066 V122.802 W18.500
G1 U 30.073 V122.883 W18.500
G1 U 30.081 V122.974 W18.500
G1 U 30.089 V123.064 W18.500
G1 U 30.098 V123.156 W18.500
G1 U 30.107 V123.239 W18.500
G1 U 30.116 V123.328 W18.500
G1 U 30.125 V123.404 W18.500
G1 U 30.134 V123.489 W18.500
G1 U 30.144 V123.570 W18.500
G1 U 30.153 V123.647 W18.500
G1 U 30.165 V123.740 W18.500
G1 U 30.176 V123.823 W18.500
G1 U 30.188 V123.908 W18.500
G1 U 30.201 V124.002 W18.500
G1 U 30.216 V124.108 W18.500
G1 U 30.226 V124.176 W18.500
G1 U 30.236 V124.237 W18.500
G1 U 30.247 V124.307 W18.500
G1 U 30.257 V124.370 W18.500
G1 U 30.267 V124.432 W18.500
G1 U 30.277 V124.489 W18.500
G1 U 30.287 V124.551 W18.500
G1 U 30.297 V124.609 W18.500
G1 U 30.307 V124.666 W18.500
G1 U 30.316 V124.715 W18.500
G1 U 30.326 V124.770 W18.500
G1 U 30.334 V124.816 W18.500
G1 U 30.344 V124.867 W18.500
G1 U 30.352 V124.911 W18.500
G1 U 30.361 V124.959 W18.500
G1 U 30.371 V125.008 W18.500
G1 U 30.378 V125.044 W18.500
G1 U 30.389 V125.101 W18.500
G1 U 30.402 V125.164 W18.500

G1 U 30.416 V125.233 W18.500
G1 U 30.431 V125.306 W18.500
G1 U 30.444 V125.365 W18.500
G1 U 30.461 V125.443 W18.500
G1 U 30.480 V125.530 W18.500
G1 U 30.496 V125.600 W18.500
G1 U 30.517 V125.694 W18.500
G1 U 30.535 V125.768 W18.500
G1 U 30.551 V125.837 W18.500
G1 U 30.567 V125.902 W18.500
G1 U 30.586 V125.981 W18.500
G1 U 30.607 V126.063 W18.500
G1 U 30.623 V126.130 W18.500
G1 U 30.643 V126.206 W18.500
G1 U 30.663 V126.280 W18.500
G1 U 30.682 V126.352 W18.500
G1 U 30.702 V126.427 W18.500
G1 U 30.722 V126.500 W18.500
G1 U 30.740 V126.565 W18.500
G1 U 30.762 V126.642 W18.500
G1 U 30.782 V126.713 W18.500
G1 U 30.803 V126.784 W18.500
G1 U 30.822 V126.848 W18.500
G1 U 30.843 V126.919 W18.500
G1 U 30.863 V126.986 W18.500
G1 U 30.882 V127.049 W18.500
G1 U 30.905 V127.122 W18.500
G1 U 30.930 V127.202 W18.500
G1 U 30.950 V127.266 W18.500
G1 U 30.974 V127.341 W18.500
G1 U 30.999 V127.417 W18.500
G1 U 31.020 V127.482 W18.500
G1 U 31.047 V127.560 W18.500
G1 U 31.072 V127.634 W18.500
G1 U 31.097 V127.708 W18.500
G1 U 31.125 V127.789 W18.500
G1 U 31.154 V127.869 W18.500
G1 U 31.181 V127.944 W18.500
G1 U 31.206 V128.015 W18.500
G1 U 65.408 V221.985 W18.500
G1 U 65.432 V222.050 W18.500
G1 U 65.450 V222.102 W18.500
G1 U 65.466 V222.145 W18.500
G1 U 65.483 V222.193 W18.500
G1 U 65.498 V222.236 W18.500
G1 U 65.512 V222.278 W18.500
G1 U 65.526 V222.317 W18.500
G1 U 65.541 V222.361 W18.500
G1 U 65.553 V222.397 W18.500
G1 U 65.569 V222.443 W18.500
G1 U 65.584 V222.487 W18.500

G1 U 65.597 V222.529 W18.500
G1 U 65.613 V222.575 W18.500
G1 U 65.627 V222.618 W18.500
G1 U 65.642 V222.666 W18.500
G1 U 65.657 V222.710 W18.500
G1 U 65.669 V222.748 W18.500
G1 U 65.682 V222.790 W18.500
G1 U 65.695 V222.831 W18.500
G1 U 65.709 V222.875 W18.500
G1 U 65.724 V222.923 W18.500
G1 U 65.737 V222.966 W18.500
G1 U 65.750 V223.008 W18.500
G1 U 65.760 V223.044 W18.500
G1 U 65.772 V223.080 W18.500
G1 U 65.783 V223.118 W18.500
G1 U 65.793 V223.153 W18.500
G1 U 65.802 V223.185 W18.500
G1 U 65.812 V223.218 W18.500
G1 U 65.822 V223.252 W18.500
G1 U 65.833 V223.288 W18.500
G1 U 65.841 V223.318 W18.500
G1 U 65.851 V223.354 W18.500
G1 U 65.861 V223.387 W18.500
G1 U 65.872 V223.425 W18.500
G1 U 65.881 V223.460 W18.500
G1 U 65.891 V223.493 W18.500
G1 U 65.900 V223.528 W18.500
G1 U 65.911 V223.567 W18.500
G1 U 65.920 V223.600 W18.500
G1 U 65.929 V223.633 W18.500
G1 U 65.938 V223.668 W18.500
G1 U 65.948 V223.706 W18.500
G1 U 65.959 V223.745 W18.500
G1 U 65.970 V223.791 W18.500
G1 U 65.983 V223.838 W18.500
G1 U 65.994 V223.881 W18.500
G1 U 66.002 V223.913 W18.500
G1 U 66.011 V223.951 W18.500
G1 U 66.020 V223.986 W18.500
G1 U 66.029 V224.020 W18.500
G1 U 66.037 V224.056 W18.500
G1 U 66.047 V224.097 W18.500
G1 U 66.057 V224.136 W18.500
G1 U 66.066 V224.174 W18.500
G1 U 66.073 V224.203 W18.500
G1 U 66.079 V224.231 W18.500
G1 U 66.087 V224.265 W18.500
G1 U 66.095 V224.296 W18.500
G1 U 66.103 V224.333 W18.500
G1 U 66.111 V224.366 W18.500
G1 U 66.120 V224.408 W18.500

G1 U 66.128 V224.444 W18.500
G1 U 66.136 V224.478 W18.500
G1 U 66.143 V224.511 W18.500
G1 U 66.152 V224.548 W18.500
G1 U 66.160 V224.585 W18.500
G1 U 66.167 V224.620 W18.500
G1 U 66.177 V224.664 W18.500
G1 U 66.186 V224.707 W18.500
G1 U 66.194 V224.747 W18.500
G1 U 66.202 V224.784 W18.500
G1 U 66.210 V224.823 W18.500
G1 U 66.219 V224.866 W18.500
G1 U 66.227 V224.906 W18.500
G1 U 66.235 V224.949 W18.500
G1 U 66.244 V224.996 W18.500
G1 U 66.253 V225.038 W18.500
G1 U 66.259 V225.074 W18.500
G1 U 66.267 V225.115 W18.500
G1 U 66.276 V225.160 W18.500
G1 U 66.283 V225.202 W18.500
G1 U 66.292 V225.249 W18.500
G1 U 66.299 V225.287 W18.500
G1 U 66.306 V225.329 W18.500
G1 U 66.315 V225.377 W18.500
G1 U 66.322 V225.419 W18.500
G1 U 66.329 V225.461 W18.500
G1 U 66.337 V225.508 W18.500
G1 U 66.344 V225.546 W18.500
G1 U 66.350 V225.586 W18.500
G1 U 66.357 V225.630 W18.500
G1 U 66.364 V225.671 W18.500
G1 U 66.371 V225.714 W18.500
G1 U 66.378 V225.760 W18.500
G1 U 66.384 V225.800 W18.500
G1 U 66.390 V225.838 W18.500
G1 U 66.395 V225.872 W18.500
G1 U 66.400 V225.906 W18.500
G1 U 66.406 V225.947 W18.500
G1 U 66.412 V225.984 W18.500
G1 U 66.417 V226.020 W18.500
G1 U 66.422 V226.058 W18.500
G1 U 66.427 V226.094 W18.500
G1 U 66.432 V226.131 W18.500
G1 U 66.438 V226.173 W18.500
G1 U 66.443 V226.213 W18.500
G1 U 66.450 V226.265 W18.500
G1 U 66.455 V226.302 W18.500
G1 U 66.459 V226.335 W18.500
G1 U 66.463 V226.373 W18.500
G1 U 66.468 V226.408 W18.500
G1 U 66.473 V226.449 W18.500

G1 U 66.478 V226.493 W18.500
G1 U 66.482 V226.532 W18.500
G1 U 66.486 V226.566 W18.500
G1 U 66.489 V226.593 W18.500
G1 U 66.493 V226.626 W18.500
G1 U 66.496 V226.656 W18.500
G1 U 66.500 V226.689 W18.500
G1 U 66.504 V226.723 W18.500
G1 U 66.507 V226.759 W18.500
G1 U 66.511 V226.791 W18.500
G1 U 66.513 V226.819 W18.500
G1 U 66.518 V226.860 W18.500
G1 U 66.520 V226.885 W18.500
G1 U 66.523 V226.914 W18.500
G1 U 66.526 V226.949 W18.500
G1 U 66.529 V226.981 W18.500
G1 U 66.532 V227.013 W18.500
G1 U 66.535 V227.042 W18.500
G1 U 66.537 V227.073 W18.500
G1 U 66.540 V227.104 W18.500
G1 U 66.543 V227.137 W18.500
G1 U 66.546 V227.168 W18.500
G1 U 66.548 V227.199 W18.500
G1 U 66.551 V227.229 W18.500
G1 U 66.553 V227.259 W18.500
G1 U 66.556 V227.295 W18.500
G1 U 66.558 V227.328 W18.500
G1 U 66.561 V227.363 W18.500
G1 U 66.563 V227.400 W18.500
G1 U 66.566 V227.435 W18.500
G1 U 66.569 V227.473 W18.500
G1 U 66.571 V227.510 W18.500
G1 U 66.573 V227.543 W18.500
G1 U 66.575 V227.573 W18.500
G1 U 66.577 V227.611 W18.500
G1 U 66.580 V227.655 W18.500
G1 U 66.582 V227.695 W18.500
G1 U 66.585 V227.736 W18.500
G1 U 66.586 V227.769 W18.500
G1 U 66.588 V227.808 W18.500
G1 U 66.590 V227.845 W18.500
G1 U 66.592 V227.889 W18.500
G1 U 66.594 V227.927 W18.500
G1 U 66.596 V227.969 W18.500
G1 U 66.597 V228.004 W18.500
G1 U 66.599 V228.038 W18.500
G1 U 66.600 V228.077 W18.500
G1 U 66.602 V228.116 W18.500
G1 U 66.603 V228.156 W18.500
G1 U 66.604 V228.193 W18.500
G1 U 66.605 V228.230 W18.500

G1 U 66.606 V228.265 W18.500
G1 U 66.607 V228.302 W18.500
G1 U 66.608 V228.341 W18.500
G1 U 66.609 V228.378 W18.500
G1 U 66.610 V228.423 W18.500
G1 U 66.611 V228.463 W18.500
G1 U 66.612 V228.496 W18.500
G1 U 66.612 V228.536 W18.500
G1 U 66.613 V228.578 W18.500
G1 U 66.613 V228.618 W18.500
G1 U 66.614 V228.658 W18.500
G1 U 66.614 V228.688 W18.500
G1 U 66.614 V228.715 W18.500
G1 U 66.614 V228.739 W18.500
G1 U 66.614 V228.760 W18.500
G1 U 66.614 V228.784 W18.500
G1 U 66.614 V228.807 W18.500
G1 U 66.614 V228.825 W18.500
G1 U 66.614 V270.000 W18.500
G1 W5
G4 S15
G1 U 40.000 V 75.000 F1400
G4 S5
G1 U 40.000 V 75.000 W18.500 F200
G1 U 40.000 V121.699 W18.500
G1 U 40.003 V122.036 W18.500
G1 U 40.010 V122.328 W18.500
G1 U 40.018 V122.542 W18.500
G1 U 40.026 V122.710 W18.500
G1 U 40.036 V122.895 W18.500
G1 U 40.047 V123.066 W18.500
G1 U 40.059 V123.233 W18.500
G1 U 40.074 V123.413 W18.500
G1 U 40.089 V123.584 W18.500
G1 U 40.105 V123.747 W18.500
G1 U 40.120 V123.887 W18.500
G1 U 40.135 V124.017 W18.500
G1 U 40.150 V124.146 W18.500
G1 U 40.164 V124.256 W18.500
G1 U 40.179 V124.369 W18.500
G1 U 40.196 V124.491 W18.500
G1 U 40.212 V124.606 W18.500
G1 U 40.234 V124.751 W18.500
G1 U 40.258 V124.901 W18.500
G1 U 40.279 V125.029 W18.500
G1 U 40.298 V125.141 W18.500
G1 U 40.317 V125.244 W18.500
G1 U 40.335 V125.345 W18.500
G1 U 40.358 V125.465 W18.500
G1 U 40.378 V125.571 W18.500
G1 U 40.400 V125.680 W18.500

G1 U 40.420 V125.778 W18.500
G1 U 40.441 V125.877 W18.500
G1 U 40.466 V125.989 W18.500
G1 U 40.487 V126.086 W18.500
G1 U 40.508 V126.180 W18.500
G1 U 40.527 V126.260 W18.500
G1 U 40.548 V126.349 W18.500
G1 U 40.571 V126.442 W18.500
G1 U 40.596 V126.545 W18.500
G1 U 40.625 V126.661 W18.500
G1 U 40.651 V126.760 W18.500
G1 U 40.674 V126.847 W18.500
G1 U 40.696 V126.930 W18.500
G1 U 40.718 V127.010 W18.500
G1 U 40.741 V127.091 W18.500
G1 U 40.762 V127.167 W18.500
G1 U 40.787 V127.254 W18.500
G1 U 40.812 V127.338 W18.500
G1 U 40.834 V127.414 W18.500
G1 U 40.857 V127.491 W18.500
G1 U 40.883 V127.576 W18.500
G1 U 40.909 V127.660 W18.500
G1 U 40.937 V127.747 W18.500
G1 U 40.964 V127.833 W18.500
G1 U 40.989 V127.910 W18.500
G1 U 41.014 V127.986 W18.500
G1 U 41.053 V128.103 W18.500
G1 U 41.081 V128.186 W18.500
G1 U 41.116 V128.287 W18.500
G1 U 41.149 V128.380 W18.500
G1 U 41.184 V128.477 W18.500
G1 U 41.215 V128.564 W18.500
G1 U 41.245 V128.644 W18.500
G1 U 41.280 V128.739 W18.500
G1 U 41.315 V128.832 W18.500
G1 U 41.346 V128.912 W18.500
G1 U 41.382 V129.004 W18.500
G1 U 41.417 V129.092 W18.500
G1 U 41.450 V129.176 W18.500
G1 U 41.483 V129.258 W18.500
G1 U 41.518 V129.341 W18.500
G1 U 41.554 V129.428 W18.500
G1 U 41.586 V129.503 W18.500
G1 U 41.629 V129.604 W18.500
G1 U 41.668 V129.696 W18.500
G1 U 41.710 V129.790 W18.500
G1 U 41.751 V129.884 W18.500
G1 U 41.790 V129.969 W18.500
G1 U 41.832 V130.061 W18.500
G1 U 41.871 V130.145 W18.500
G1 U 41.911 V130.230 W18.500

G1 U 41.954 V130.322 W18.500
G1 U 41.996 V130.408 W18.500
G1 U 42.034 V130.486 W18.500
G1 U 42.078 V130.575 W18.500
G1 U 42.126 V130.671 W18.500
G1 U 42.172 V130.762 W18.500
G1 U 42.216 V130.849 W18.500
G1 U 42.263 V130.939 W18.500
G1 U 42.307 V131.025 W18.500
G1 U 42.355 V131.114 W18.500
G1 U 42.406 V131.209 W18.500
G1 U 42.454 V131.298 W18.500
G1 U 42.507 V131.394 W18.500
G1 U 42.557 V131.484 W18.500
G1 U 42.606 V131.571 W18.500
G1 U 42.679 V131.699 W18.500
G1 U 92.679 V218.301 W18.500
G1 U 92.818 V218.545 W18.500
G1 U 92.903 V218.699 W18.500
G1 U 92.994 V218.867 W18.500
G1 U 93.080 V219.029 W18.500
G1 U 93.159 V219.183 W18.500
G1 U 93.232 V219.327 W18.500
G1 U 93.304 V219.471 W18.500
G1 U 93.375 V219.616 W18.500
G1 U 93.440 V219.752 W18.500
G1 U 93.503 V219.886 W18.500
G1 U 93.564 V220.020 W18.500
G1 U 93.621 V220.147 W18.500
G1 U 93.681 V220.282 W18.500
G1 U 93.732 V220.399 W18.500
G1 U 93.788 V220.532 W18.500
G1 U 93.839 V220.653 W18.500
G1 U 93.898 V220.798 W18.500
G1 U 93.951 V220.930 W18.500
G1 U 94.003 V221.062 W18.500
G1 U 94.058 V221.205 W18.500
G1 U 94.105 V221.332 W18.500
G1 U 94.151 V221.456 W18.500
G1 U 94.188 V221.559 W18.500
G1 U 94.225 V221.663 W18.500
G1 U 94.258 V221.757 W18.500
G1 U 94.292 V221.855 W18.500
G1 U 94.331 V221.971 W18.500
G1 U 94.365 V222.076 W18.500
G1 U 94.398 V222.175 W18.500
G1 U 94.427 V222.269 W18.500
G1 U 94.457 V222.362 W18.500
G1 U 94.491 V222.473 W18.500
G1 U 94.518 V222.562 W18.500
G1 U 94.551 V222.675 W18.500

G1 U 94.578 V222.766 W18.500
G1 U 94.610 V222.878 W18.500
G1 U 94.638 V222.981 W18.500
G1 U 94.663 V223.072 W18.500
G1 U 94.684 V223.149 W18.500
G1 U 94.701 V223.215 W18.500
G1 U 94.718 V223.279 W18.500
G1 U 94.738 V223.355 W18.500
G1 U 94.766 V223.468 W18.500
G1 U 94.790 V223.566 W18.500
G1 U 94.809 V223.645 W18.500
G1 U 94.832 V223.742 W18.500
G1 U 94.851 V223.824 W18.500
G1 U 94.872 V223.916 W18.500
G1 U 94.891 V223.999 W18.500
G1 U 94.910 V224.087 W18.500
G1 U 94.927 V224.165 W18.500
G1 U 94.945 V224.252 W18.500
G1 U 94.962 V224.338 W18.500
G1 U 94.980 V224.429 W18.500
G1 U 94.994 V224.500 W18.500
G1 U 95.008 V224.570 W18.500
G1 U 95.022 V224.647 W18.500
G1 U 95.034 V224.711 W18.500
G1 U 95.046 V224.777 W18.500
G1 U 95.059 V224.852 W18.500
G1 U 95.071 V224.922 W18.500
G1 U 95.082 V224.984 W18.500
G1 U 95.094 V225.056 W18.500
G1 U 95.105 V225.125 W18.500
G1 U 95.116 V225.195 W18.500
G1 U 95.127 V225.266 W18.500
G1 U 95.138 V225.334 W18.500
G1 U 95.148 V225.403 W18.500
G1 U 95.157 V225.469 W18.500
G1 U 95.168 V225.542 W18.500
G1 U 95.178 V225.615 W18.500
G1 U 95.188 V225.688 W18.500
G1 U 95.195 V225.747 W18.500
G1 U 95.202 V225.799 W18.500
G1 U 95.209 V225.854 W18.500
G1 U 95.215 V225.902 W18.500
G1 U 95.220 V225.950 W18.500
G1 U 95.225 V225.994 W18.500
G1 U 95.230 V226.037 W18.500
G1 U 95.236 V226.084 W18.500
G1 U 95.240 V226.125 W18.500
G1 U 95.245 V226.166 W18.500
G1 U 95.250 V226.214 W18.500
G1 U 95.254 V226.253 W18.500
G1 U 95.258 V226.298 W18.500

G1 U 95.262 V226.334 W18.500
G1 U 95.267 V226.380 W18.500
G1 U 95.271 V226.425 W18.500
G1 U 95.275 V226.473 W18.500
G1 U 95.279 V226.512 W18.500
G1 U 95.282 V226.552 W18.500
G1 U 95.286 V226.597 W18.500
G1 U 95.290 V226.639 W18.500
G1 U 95.294 V226.684 W18.500
G1 U 95.297 V226.734 W18.500
G1 U 95.301 V226.778 W18.500
G1 U 95.305 V226.835 W18.500
G1 U 95.309 V226.883 W18.500
G1 U 95.312 V226.931 W18.500
G1 U 95.316 V226.997 W18.500
G1 U 95.320 V227.053 W18.500
G1 U 95.324 V227.118 W18.500
G1 U 95.328 V227.195 W18.500
G1 U 95.333 V227.279 W18.500
G1 U 95.337 V227.369 W18.500
G1 U 95.341 V227.455 W18.500
G1 U 95.344 V227.537 W18.500
G1 U 95.347 V227.609 W18.500
G1 U 95.349 V227.683 W18.500
G1 U 95.352 V227.763 W18.500
G1 U 95.354 V227.847 W18.500
G1 U 95.355 V227.921 W18.500
G1 U 95.357 V228.000 W18.500
G1 U 95.358 V228.079 W18.500
G1 U 95.358 V228.154 W18.500
G1 U 95.359 V228.224 W18.500
G1 U 95.359 V228.301 W18.500
G1 U 95.359 V270.000 W18.500
G1 W5
G4 S15
G1 U 50.000 V 75.000 F1400
G4 S5
G1 U 50.000 V 75.000 W18.500 F200
G1 U 50.000 V123.842 W18.500
G1 U 50.002 V124.103 W18.500
G1 U 50.007 V124.366 W18.500
G1 U 50.015 V124.614 W18.500
G1 U 50.025 V124.839 W18.500
G1 U 50.036 V125.038 W18.500
G1 U 50.049 V125.237 W18.500
G1 U 50.063 V125.423 W18.500
G1 U 50.079 V125.623 W18.500
G1 U 50.095 V125.784 W18.500
G1 U 50.112 V125.959 W18.500
G1 U 50.132 V126.134 W18.500
G1 U 50.153 V126.310 W18.500

G1 U 50.180 V126.518 W18.500
G1 U 50.210 V126.731 W18.500
G1 U 50.240 V126.929 W18.500
G1 U 50.270 V127.114 W18.500
G1 U 50.306 V127.328 W18.500
G1 U 50.348 V127.557 W18.500
G1 U 50.391 V127.779 W18.500
G1 U 50.434 V127.987 W18.500
G1 U 50.491 V128.247 W18.500
G1 U 50.554 V128.518 W18.500
G1 U 50.620 V128.785 W18.500
G1 U 50.691 V129.054 W18.500
G1 U 50.758 V129.294 W18.500
G1 U 50.837 V129.567 W18.500
G1 U 50.918 V129.833 W18.500
G1 U 50.996 V130.076 W18.500
G1 U 51.062 V130.274 W18.500
G1 U 51.144 V130.510 W18.500
G1 U 51.243 V130.784 W18.500
G1 U 51.311 V130.965 W18.500
G1 U 51.365 V131.105 W18.500
G1 U 51.418 V131.239 W18.500
G1 U 51.479 V131.390 W18.500
G1 U 51.550 V131.562 W18.500
G1 U 51.608 V131.699 W18.500
G1 U 51.671 V131.845 W18.500
G1 U 51.730 V131.978 W18.500
G1 U 51.785 V132.101 W18.500
G1 U 51.847 V132.237 W18.500
G1 U 51.904 V132.359 W18.500
G1 U 51.963 V132.483 W18.500
G1 U 52.029 V132.619 W18.500
G1 U 52.104 V132.772 W18.500
G1 U 52.182 V132.927 W18.500
G1 U 52.234 V133.027 W18.500
G1 U 52.291 V133.136 W18.500
G1 U 52.339 V133.227 W18.500
G1 U 52.395 V133.332 W18.500
G1 U 52.444 V133.422 W18.500
G1 U 52.498 V133.521 W18.500
G1 U 52.548 V133.612 W18.500
G1 U 52.603 V133.709 W18.500
G1 U 52.651 V133.793 W18.500
G1 U 52.702 V133.881 W18.500
G1 U 52.748 V133.959 W18.500
G1 U 52.788 V134.028 W18.500
G1 U 52.837 V134.110 W18.500
G1 U 52.888 V134.196 W18.500
G1 U 52.933 V134.268 W18.500
G1 U 52.981 V134.347 W18.500
G1 U 53.028 V134.424 W18.500

G1 U 53.074 V134.495 W18.500
G1 U 53.115 V134.562 W18.500
G1 U 53.168 V134.644 W18.500
G1 U 53.225 V134.732 W18.500
G1 U 53.283 V134.821 W18.500
G1 U 53.342 V134.910 W18.500
G1 U 53.398 V134.994 W18.500
G1 U 53.448 V135.068 W18.500
G1 U 53.493 V135.135 W18.500
G1 U 53.541 V135.205 W18.500
G1 U 53.590 V135.275 W18.500
G1 U 53.649 V135.359 W18.500
G1 U 53.696 V135.425 W18.500
G1 U 53.747 V135.497 W18.500
G1 U 53.809 V135.582 W18.500
G1 U 53.874 V135.672 W18.500
G1 U 53.935 V135.754 W18.500
G1 U 54.004 V135.848 W18.500
G1 U 54.061 V135.922 W18.500
G1 U 54.130 V136.013 W18.500
G1 U 54.196 V136.099 W18.500
G1 U 54.256 V136.176 W18.500
G1 U 54.313 V136.248 W18.500
G1 U 54.379 V136.331 W18.500
G1 U 54.447 V136.416 W18.500
G1 U 54.519 V136.504 W18.500
G1 U 54.593 V136.594 W18.500
G1 U 54.679 V136.698 W18.500
G1 U118.958 V213.302 W18.500
G1 U119.040 V213.401 W18.500
G1 U119.119 V213.497 W18.500
G1 U119.194 V213.589 W18.500
G1 U119.265 V213.677 W18.500
G1 U119.338 V213.769 W18.500
G1 U119.408 V213.859 W18.500
G1 U119.490 V213.964 W18.500
G1 U119.571 V214.070 W18.500
G1 U119.647 V214.172 W18.500
G1 U119.724 V214.275 W18.500
G1 U119.794 V214.370 W18.500
G1 U119.869 V214.474 W18.500
G1 U119.953 V214.591 W18.500
G1 U120.022 V214.689 W18.500
G1 U120.098 V214.799 W18.500
G1 U120.164 V214.894 W18.500
G1 U120.234 V214.999 W18.500
G1 U120.298 V215.094 W18.500
G1 U120.372 V215.206 W18.500
G1 U120.433 V215.300 W18.500
G1 U120.507 V215.415 W18.500
G1 U120.569 V215.513 W18.500

G1 U120.630 V215.611 W18.500
G1 U120.683 V215.697 W18.500
G1 U120.746 V215.800 W18.500
G1 U120.798 V215.886 W18.500
G1 U120.858 V215.987 W18.500
G1 U120.911 V216.078 W18.500
G1 U120.961 V216.164 W18.500
G1 U121.025 V216.275 W18.500
G1 U121.079 V216.371 W18.500
G1 U121.135 V216.472 W18.500
G1 U121.190 V216.571 W18.500
G1 U121.242 V216.667 W18.500
G1 U121.289 V216.755 W18.500
G1 U121.336 V216.844 W18.500
G1 U121.387 V216.942 W18.500
G1 U121.442 V217.049 W18.500
G1 U121.503 V217.170 W18.500
G1 U121.552 V217.267 W18.500
G1 U121.611 V217.387 W18.500
G1 U121.667 V217.502 W18.500
G1 U121.720 V217.615 W18.500
G1 U121.779 V217.740 W18.500
G1 U121.836 V217.863 W18.500
G1 U121.886 V217.975 W18.500
G1 U121.946 V218.109 W18.500
G1 U122.007 V218.249 W18.500
G1 U122.055 V218.363 W18.500
G1 U122.106 V218.483 W18.500
G1 U122.155 V218.602 W18.500
G1 U122.209 V218.736 W18.500
G1 U122.256 V218.855 W18.500
G1 U122.300 V218.968 W18.500
G1 U122.342 V219.077 W18.500
G1 U122.383 V219.187 W18.500
G1 U122.421 V219.291 W18.500
G1 U122.459 V219.394 W18.500
G1 U122.496 V219.500 W18.500
G1 U122.538 V219.620 W18.500
G1 U122.582 V219.749 W18.500
G1 U122.621 V219.866 W18.500
G1 U122.659 V219.982 W18.500
G1 U122.698 V220.103 W18.500
G1 U122.746 V220.255 W18.500
G1 U122.789 V220.397 W18.500
G1 U122.843 V220.579 W18.500
G1 U122.888 V220.736 W18.500
G1 U122.932 V220.895 W18.500
G1 U122.971 V221.040 W18.500
G1 U123.013 V221.199 W18.500
G1 U123.045 V221.326 W18.500
G1 U123.084 V221.488 W18.500

G1 U123.125 V221.660 W18.500
G1 U123.158 V221.806 W18.500
G1 U123.191 V221.959 W18.500
G1 U123.225 V222.118 W18.500
G1 U123.259 V222.289 W18.500
G1 U123.292 V222.459 W18.500
G1 U123.324 V222.632 W18.500
G1 U123.352 V222.796 W18.500
G1 U123.378 V222.950 W18.500
G1 U123.398 V223.076 W18.500
G1 U123.415 V223.185 W18.500
G1 U123.430 V223.285 W18.500
G1 U123.443 V223.376 W18.500
G1 U123.455 V223.466 W18.500
G1 U123.468 V223.564 W18.500
G1 U123.481 V223.663 W18.500
G1 U123.494 V223.768 W18.500
G1 U123.506 V223.872 W18.500
G1 U123.517 V223.970 W18.500
G1 U123.528 V224.070 W18.500
G1 U123.538 V224.167 W18.500
G1 U123.548 V224.275 W18.500
G1 U123.557 V224.366 W18.500
G1 U123.565 V224.466 W18.500
G1 U123.573 V224.561 W18.500
G1 U123.581 V224.667 W18.500
G1 U123.589 V224.771 W18.500
G1 U123.597 V224.888 W18.500
G1 U123.603 V224.986 W18.500
G1 U123.608 V225.078 W18.500
G1 U123.612 V225.163 W18.500
G1 U123.616 V225.251 W18.500
G1 U123.620 V225.327 W18.500
G1 U123.623 V225.415 W18.500
G1 U123.626 V225.494 W18.500
G1 U123.629 V225.580 W18.500
G1 U123.631 V225.670 W18.500
G1 U123.633 V225.753 W18.500
G1 U123.634 V225.841 W18.500
G1 U123.636 V225.925 W18.500
G1 U123.636 V226.012 W18.500
G1 U123.637 V226.084 W18.500
G1 U123.637 V226.158 W18.500
G1 U123.637 V270.000 W18.500
G1 W5
G4 S15
G1 U 60.000 V 75.000 F1400
G4 S5
G1 U 60.000 V 75.000 W18.500 F200
G1 U 60.000 V127.540 W18.500
G1 U 60.000 V127.677 W18.500

G1 U 60.002 V127.790 W18.500
G1 U 60.003 V127.884 W18.500
G1 U 60.004 V127.959 W18.500
G1 U 60.006 V128.048 W18.500
G1 U 60.009 V128.123 W18.500
G1 U 60.011 V128.215 W18.500
G1 U 60.014 V128.287 W18.500
G1 U 60.017 V128.374 W18.500
G1 U 60.021 V128.463 W18.500
G1 U 60.025 V128.546 W18.500
G1 U 60.030 V128.629 W18.500
G1 U 60.034 V128.705 W18.500
G1 U 60.040 V128.796 W18.500
G1 U 60.046 V128.890 W18.500
G1 U 60.052 V128.982 W18.500
G1 U 60.057 V129.054 W18.500
G1 U 60.063 V129.128 W18.500
G1 U 60.068 V129.189 W18.500
G1 U 60.074 V129.257 W18.500
G1 U 60.081 V129.337 W18.500
G1 U 60.088 V129.410 W18.500
G1 U 60.096 V129.496 W18.500
G1 U 60.104 V129.575 W18.500
G1 U 60.111 V129.646 W18.500
G1 U 60.119 V129.720 W18.500
G1 U 60.127 V129.794 W18.500
G1 U 60.135 V129.863 W18.500
G1 U 60.144 V129.939 W18.500
G1 U 60.153 V130.011 W18.500
G1 U 60.164 V130.096 W18.500
G1 U 60.174 V130.172 W18.500
G1 U 60.185 V130.256 W18.500
G1 U 60.196 V130.333 W18.500
G1 U 60.206 V130.403 W18.500
G1 U 60.215 V130.463 W18.500
G1 U 60.225 V130.531 W18.500
G1 U 60.234 V130.589 W18.500
G1 U 60.244 V130.657 W18.500
G1 U 60.255 V130.726 W18.500
G1 U 60.267 V130.797 W18.500
G1 U 60.279 V130.871 W18.500
G1 U 60.293 V130.948 W18.500
G1 U 60.307 V131.030 W18.500
G1 U 60.321 V131.106 W18.500
G1 U 60.336 V131.192 W18.500
G1 U 60.352 V131.276 W18.500
G1 U 60.368 V131.359 W18.500
G1 U 60.387 V131.454 W18.500
G1 U 60.405 V131.543 W18.500
G1 U 60.423 V131.633 W18.500
G1 U 60.444 V131.729 W18.500

G1 U 60.466 V131.831 W18.500
G1 U 60.489 V131.935 W18.500
G1 U 60.510 V132.027 W18.500
G1 U 60.529 V132.109 W18.500
G1 U 60.546 V132.183 W18.500
G1 U 60.569 V132.278 W18.500
G1 U 60.595 V132.383 W18.500
G1 U 60.617 V132.471 W18.500
G1 U 60.642 V132.566 W18.500
G1 U 60.667 V132.660 W18.500
G1 U 60.695 V132.767 W18.500
G1 U 60.720 V132.859 W18.500
G1 U 60.745 V132.949 W18.500
G1 U 60.775 V133.055 W18.500
G1 U 60.806 V133.161 W18.500
G1 U 60.831 V133.245 W18.500
G1 U 60.863 V133.350 W18.500
G1 U 60.891 V133.443 W18.500
G1 U 60.927 V133.558 W18.500
G1 U 60.955 V133.647 W18.500
G1 U 60.989 V133.752 W18.500
G1 U 61.019 V133.842 W18.500
G1 U 61.054 V133.946 W18.500
G1 U 61.088 V134.047 W18.500
G1 U 61.130 V134.167 W18.500
G1 U 61.165 V134.266 W18.500
G1 U 61.199 V134.362 W18.500
G1 U 61.234 V134.456 W18.500
G1 U 61.273 V134.561 W18.500
G1 U 61.309 V134.656 W18.500
G1 U 61.352 V134.768 W18.500
G1 U 61.392 V134.871 W18.500
G1 U 61.428 V134.961 W18.500
G1 U 61.468 V135.060 W18.500
G1 U 61.503 V135.147 W18.500
G1 U 61.538 V135.231 W18.500
G1 U 61.578 V135.326 W18.500
G1 U 61.617 V135.418 W18.500
G1 U 61.658 V135.514 W18.500
G1 U 61.705 V135.620 W18.500
G1 U 61.748 V135.716 W18.500
G1 U 61.784 V135.798 W18.500
G1 U 61.823 V135.883 W18.500
G1 U 61.862 V135.968 W18.500
G1 U 61.908 V136.065 W18.500
G1 U 61.947 V136.148 W18.500
G1 U 61.991 V136.240 W18.500
G1 U 62.035 V136.329 W18.500
G1 U 62.079 V136.418 W18.500
G1 U 62.121 V136.502 W18.500
G1 U 62.167 V136.594 W18.500

G1 U 62.210 V136.678 W18.500
G1 U 62.252 V136.759 W18.500
G1 U 62.290 V136.833 W18.500
G1 U 62.338 V136.924 W18.500
G1 U 62.391 V137.022 W18.500
G1 U 62.432 V137.098 W18.500
G1 U 62.470 V137.168 W18.500
G1 U 62.508 V137.237 W18.500
G1 U 62.547 V137.307 W18.500
G1 U 62.588 V137.380 W18.500
G1 U 62.627 V137.448 W18.500
G1 U 62.668 V137.520 W18.500
G1 U 62.713 V137.597 W18.500
G1 U 62.757 V137.672 W18.500
G1 U 62.803 V137.751 W18.500
G1 U 62.850 V137.829 W18.500
G1 U 62.892 V137.899 W18.500
G1 U 62.939 V137.976 W18.500
G1 U 62.998 V138.071 W18.500
G1 U 63.045 V138.148 W18.500
G1 U 63.095 V138.226 W18.500
G1 U 63.142 V138.302 W18.500
G1 U 63.197 V138.387 W18.500
G1 U 63.247 V138.464 W18.500
G1 U 63.297 V138.540 W18.500
G1 U 63.348 V138.618 W18.500
G1 U 63.407 V138.705 W18.500
G1 U 63.457 V138.779 W18.500
G1 U 63.512 V138.860 W18.500
G1 U 63.573 V138.948 W18.500
G1 U 63.625 V139.022 W18.500
G1 U 63.681 V139.102 W18.500
G1 U 63.729 V139.169 W18.500
G1 U 63.793 V139.258 W18.500
G1 U 63.861 V139.353 W18.500
G1 U 63.928 V139.443 W18.500
G1 U 63.995 V139.533 W18.500
G1 U 64.071 V139.634 W18.500
G1 U 64.145 V139.731 W18.500
G1 U 64.231 V139.842 W18.500
G1 U 64.312 V139.944 W18.500
G1 U 64.396 V140.051 W18.500
G1 U 64.494 V140.172 W18.500
G1 U 64.578 V140.274 W18.500
G1 U 64.677 V140.393 W18.500
G1 U 64.769 V140.502 W18.500
G1 U 64.864 V140.612 W18.500
G1 U 64.943 V140.703 W18.500
G1 U 65.035 V140.808 W18.500
G1 U 65.152 V140.938 W18.500
G1 U 65.256 V141.053 W18.500

G1 U 65.356 V141.161 W18.500
G1 U 65.471 V141.284 W18.500
G1 U 65.567 V141.385 W18.500
G1 U 65.668 V141.490 W18.500
G1 U 65.786 V141.610 W18.500
G1 U 65.901 V141.725 W18.500
G1 U 66.026 V141.848 W18.500
G1 U 66.142 V141.961 W18.500
G1 U 66.261 V142.074 W18.500
G1 U 66.384 V142.189 W18.500
G1 U 66.492 V142.289 W18.500
G1 U 66.606 V142.393 W18.500
G1 U 66.706 V142.482 W18.500
G1 U 66.834 V142.595 W18.500
G1 U 66.978 V142.720 W18.500
G1 U 67.144 V142.861 W18.500
G1 U143.749 V207.139 W18.500
G1 U143.814 V207.194 W18.500
G1 U143.890 V207.259 W18.500
G1 U143.971 V207.329 W18.500
G1 U144.055 V207.402 W18.500
G1 U144.139 V207.475 W18.500
G1 U144.216 V207.544 W18.500
G1 U144.298 V207.618 W18.500
G1 U144.386 V207.698 W18.500
G1 U144.465 V207.770 W18.500
G1 U144.540 V207.840 W18.500
G1 U144.618 V207.913 W18.500
G1 U144.687 V207.979 W18.500
G1 U144.764 V208.053 W18.500
G1 U144.841 V208.127 W18.500
G1 U144.926 V208.210 W18.500
G1 U145.010 V208.293 W18.500
G1 U145.096 V208.379 W18.500
G1 U145.181 V208.466 W18.500
G1 U145.277 V208.564 W18.500
G1 U145.363 V208.654 W18.500
G1 U145.449 V208.745 W18.500
G1 U145.526 V208.826 W18.500
G1 U145.618 V208.926 W18.500
G1 U145.700 V209.016 W18.500
G1 U145.789 V209.115 W18.500
G1 U145.879 V209.215 W18.500
G1 U145.978 V209.329 W18.500
G1 U146.082 V209.449 W18.500
G1 U146.188 V209.574 W18.500
G1 U146.276 V209.679 W18.500
G1 U146.365 V209.787 W18.500
G1 U146.460 V209.903 W18.500
G1 U146.584 V210.059 W18.500
G1 U146.673 V210.172 W18.500

G1 U146.769 V210.297 W18.500
G1 U146.867 V210.425 W18.500
G1 U146.956 V210.545 W18.500
G1 U147.050 V210.673 W18.500
G1 U147.150 V210.811 W18.500
G1 U147.240 V210.937 W18.500
G1 U147.336 V211.075 W18.500
G1 U147.427 V211.208 W18.500
G1 U147.516 V211.340 W18.500
G1 U147.585 V211.444 W18.500
G1 U147.650 V211.543 W18.500
G1 U147.728 V211.662 W18.500
G1 U147.811 V211.793 W18.500
G1 U147.884 V211.911 W18.500
G1 U147.964 V212.040 W18.500
G1 U148.036 V212.159 W18.500
G1 U148.100 V212.266 W18.500
G1 U148.174 V212.392 W18.500
G1 U148.249 V212.522 W18.500
G1 U148.322 V212.650 W18.500
G1 U148.393 V212.779 W18.500
G1 U148.464 V212.908 W18.500
G1 U148.531 V213.032 W18.500
G1 U148.601 V213.164 W18.500
G1 U148.674 V213.303 W18.500
G1 U148.737 V213.428 W18.500
G1 U148.806 V213.565 W18.500
G1 U148.871 V213.697 W18.500
G1 U148.929 V213.818 W18.500
G1 U148.994 V213.954 W18.500
G1 U149.068 V214.114 W18.500
G1 U149.126 V214.241 W18.500
G1 U149.192 V214.389 W18.500
G1 U149.255 V214.533 W18.500
G1 U149.314 V214.671 W18.500
G1 U149.362 V214.786 W18.500
G1 U149.426 V214.942 W18.500
G1 U149.496 V215.117 W18.500
G1 U149.556 V215.272 W18.500
G1 U149.626 V215.455 W18.500
G1 U149.690 V215.629 W18.500
G1 U149.759 V215.823 W18.500
G1 U149.818 V215.992 W18.500
G1 U149.877 V216.167 W18.500
G1 U149.927 V216.319 W18.500
G1 U149.984 V216.501 W18.500
G1 U150.033 V216.658 W18.500
G1 U150.085 V216.832 W18.500
G1 U150.134 V217.004 W18.500
G1 U150.179 V217.165 W18.500
G1 U150.221 V217.319 W18.500

G1 U150.263 V217.481 W18.500
G1 U150.300 V217.627 W18.500
G1 U150.336 V217.775 W18.500
G1 U150.374 V217.935 W18.500
G1 U150.408 V218.085 W18.500
G1 U150.445 V218.253 W18.500
G1 U150.481 V218.422 W18.500
G1 U150.515 V218.592 W18.500
G1 U150.544 V218.741 W18.500
G1 U150.576 V218.915 W18.500
G1 U150.608 V219.097 W18.500
G1 U150.635 V219.261 W18.500
G1 U150.661 V219.420 W18.500
G1 U150.685 V219.585 W18.500
G1 U150.712 V219.774 W18.500
G1 U150.732 V219.931 W18.500
G1 U150.751 V220.082 W18.500
G1 U150.768 V220.226 W18.500
G1 U150.783 V220.366 W18.500
G1 U150.798 V220.517 W18.500
G1 U150.813 V220.670 W18.500
G1 U150.826 V220.820 W18.500
G1 U150.836 V220.952 W18.500
G1 U150.845 V221.073 W18.500
G1 U150.854 V221.217 W18.500
G1 U150.862 V221.343 W18.500
G1 U150.870 V221.495 W18.500
G1 U150.877 V221.652 W18.500
G1 U150.882 V221.810 W18.500
G1 U150.887 V221.980 W18.500
G1 U150.890 V222.119 W18.500
G1 U150.892 V222.264 W18.500
G1 U150.893 V222.378 W18.500
G1 U150.893 V222.460 W18.500
G1 U150.893 V270.000 W18.500
G1 W5
G4 S15
G1 U 80.000 V 75.000 F1400
G4 S5
G1 U 80.000 V 75.000 W18.500 F200
G1 U 80.000 V132.679 W18.500
G1 U 80.002 V132.933 W18.500
G1 U 80.004 V133.095 W18.500
G1 U 80.007 V133.222 W18.500
G1 U 80.011 V133.334 W18.500
G1 U 80.014 V133.438 W18.500
G1 U 80.019 V133.542 W18.500
G1 U 80.023 V133.635 W18.500
G1 U 80.028 V133.732 W18.500
G1 U 80.033 V133.836 W18.500
G1 U 80.039 V133.921 W18.500

G1 U 80.045 V134.021 W18.500
G1 U 80.052 V134.122 W18.500
G1 U 80.059 V134.210 W18.500
G1 U 80.066 V134.307 W18.500
G1 U 80.075 V134.415 W18.500
G1 U 80.085 V134.527 W18.500
G1 U 80.094 V134.613 W18.500
G1 U 80.105 V134.727 W18.500
G1 U 80.114 V134.816 W18.500
G1 U 80.125 V134.913 W18.500
G1 U 80.138 V135.025 W18.500
G1 U 80.150 V135.122 W18.500
G1 U 80.162 V135.222 W18.500
G1 U 80.173 V135.303 W18.500
G1 U 80.182 V135.369 W18.500
G1 U 80.191 V135.438 W18.500
G1 U 80.202 V135.517 W18.500
G1 U 80.214 V135.595 W18.500
G1 U 80.226 V135.678 W18.500
G1 U 80.239 V135.762 W18.500
G1 U 80.250 V135.833 W18.500
G1 U 80.265 V135.926 W18.500
G1 U 80.279 V136.007 W18.500
G1 U 80.290 V136.075 W18.500
G1 U 80.301 V136.135 W18.500
G1 U 80.315 V136.215 W18.500
G1 U 80.327 V136.280 W18.500
G1 U 80.342 V136.363 W18.500
G1 U 80.353 V136.421 W18.500
G1 U 80.367 V136.495 W18.500
G1 U 80.384 V136.578 W18.500
G1 U 80.402 V136.670 W18.500
G1 U 80.420 V136.756 W18.500
G1 U 80.438 V136.841 W18.500
G1 U 80.455 V136.919 W18.500
G1 U 80.474 V137.006 W18.500
G1 U 80.494 V137.096 W18.500
G1 U 80.515 V137.188 W18.500
G1 U 80.537 V137.281 W18.500
G1 U 80.560 V137.379 W18.500
G1 U 80.577 V137.450 W18.500
G1 U 80.595 V137.522 W18.500
G1 U 80.615 V137.601 W18.500
G1 U 80.634 V137.674 W18.500
G1 U 80.649 V137.733 W18.500
G1 U 80.663 V137.788 W18.500
G1 U 80.678 V137.841 W18.500
G1 U 80.690 V137.888 W18.500
G1 U 80.704 V137.938 W18.500
G1 U 80.717 V137.988 W18.500
G1 U 80.731 V138.038 W18.500

G1 U 80.743 V138.081 W18.500
G1 U 80.757 V138.130 W18.500
G1 U 80.771 V138.177 W18.500
G1 U 80.784 V138.226 W18.500
G1 U 80.800 V138.279 W18.500
G1 U 80.812 V138.321 W18.500
G1 U 80.825 V138.365 W18.500
G1 U 80.837 V138.405 W18.500
G1 U 80.851 V138.452 W18.500
G1 U 80.870 V138.513 W18.500
G1 U 80.888 V138.571 W18.500
G1 U 80.908 V138.639 W18.500
G1 U 80.931 V138.711 W18.500
G1 U 80.954 V138.784 W18.500
G1 U 80.976 V138.852 W18.500
G1 U 81.002 V138.930 W18.500
G1 U 81.028 V139.009 W18.500
G1 U 81.052 V139.079 W18.500
G1 U 81.078 V139.157 W18.500
G1 U 81.104 V139.232 W18.500
G1 U 81.132 V139.313 W18.500
G1 U 81.157 V139.382 W18.500
G1 U 81.181 V139.451 W18.500
G1 U 81.211 V139.534 W18.500
G1 U 81.244 V139.624 W18.500
G1 U 81.273 V139.701 W18.500
G1 U 81.308 V139.792 W18.500
G1 U 81.335 V139.865 W18.500
G1 U 81.360 V139.929 W18.500
G1 U 81.384 V139.991 W18.500
G1 U 81.413 V140.063 W18.500
G1 U 81.442 V140.135 W18.500
G1 U 81.476 V140.219 W18.500
G1 U 81.509 V140.302 W18.500
G1 U 81.538 V140.371 W18.500
G1 U 81.573 V140.453 W18.500
G1 U 81.604 V140.526 W18.500
G1 U 81.638 V140.606 W18.500
G1 U 81.672 V140.686 W18.500
G1 U 81.705 V140.760 W18.500
G1 U 81.738 V140.834 W18.500
G1 U 81.760 V140.884 W18.500
G1 U 81.785 V140.939 W18.500
G1 U 81.808 V140.990 W18.500
G1 U 81.832 V141.041 W18.500
G1 U 81.854 V141.089 W18.500
G1 U 81.881 V141.147 W18.500
G1 U 81.903 V141.195 W18.500
G1 U 81.929 V141.249 W18.500
G1 U 81.954 V141.302 W18.500
G1 U 81.979 V141.355 W18.500

G1 U 82.011 V141.419 W18.500
G1 U 82.037 V141.473 W18.500
G1 U 82.070 V141.541 W18.500
G1 U 82.098 V141.598 W18.500
G1 U 82.127 V141.656 W18.500
G1 U 82.155 V141.709 W18.500
G1 U 82.181 V141.762 W18.500
G1 U 82.213 V141.824 W18.500
G1 U 82.239 V141.875 W18.500
G1 U 82.268 V141.930 W18.500
G1 U 82.298 V141.987 W18.500
G1 U 82.326 V142.041 W18.500
G1 U 82.361 V142.106 W18.500
G1 U 82.394 V142.168 W18.500
G1 U 82.426 V142.226 W18.500
G1 U 82.456 V142.282 W18.500
G1 U 82.485 V142.335 W18.500
G1 U 82.518 V142.394 W18.500
G1 U 82.551 V142.453 W18.500
G1 U 82.579 V142.503 W18.500
G1 U 82.607 V142.553 W18.500
G1 U 82.636 V142.604 W18.500
G1 U 82.663 V142.651 W18.500
G1 U 82.695 V142.706 W18.500
G1 U 82.720 V142.750 W18.500
G1 U 82.750 V142.800 W18.500
G1 U 82.783 V142.857 W18.500
G1 U 82.810 V142.903 W18.500
G1 U 82.839 V142.951 W18.500
G1 U 82.869 V143.001 W18.500
G1 U 82.902 V143.055 W18.500
G1 U 82.935 V143.110 W18.500
G1 U 82.969 V143.165 W18.500
G1 U 83.002 V143.219 W18.500
G1 U 83.031 V143.265 W18.500
G1 U 83.061 V143.312 W18.500
G1 U 83.094 V143.365 W18.500
G1 U 83.127 V143.417 W18.500
G1 U 83.160 V143.469 W18.500
G1 U 83.197 V143.527 W18.500
G1 U 83.228 V143.574 W18.500
G1 U 83.261 V143.626 W18.500
G1 U 83.294 V143.676 W18.500
G1 U 83.326 V143.724 W18.500
G1 U 83.365 V143.783 W18.500
G1 U 83.399 V143.834 W18.500
G1 U 83.430 V143.880 W18.500
G1 U 83.462 V143.927 W18.500
G1 U 83.503 V143.986 W18.500
G1 U 83.545 V144.047 W18.500
G1 U 83.593 V144.117 W18.500

G1 U 83.643 V144.189 W18.500
G1 U 83.682 V144.243 W18.500
G1 U 83.725 V144.304 W18.500
G1 U 83.763 V144.356 W18.500
G1 U 83.806 V144.417 W18.500
G1 U 83.850 V144.477 W18.500
G1 U 83.903 V144.548 W18.500
G1 U 83.958 V144.623 W18.500
G1 U 84.007 V144.689 W18.500
G1 U 84.065 V144.766 W18.500
G1 U 84.120 V144.838 W18.500
G1 U 84.176 V144.911 W18.500
G1 U 84.232 V144.983 W18.500
G1 U 84.275 V145.038 W18.500
G1 U 84.327 V145.104 W18.500
G1 U 84.378 V145.167 W18.500
G1 U 84.420 V145.220 W18.500
G1 U 84.469 V145.281 W18.500
G1 U 84.517 V145.339 W18.500
G1 U 84.561 V145.394 W18.500
G1 U 84.611 V145.454 W18.500
G1 U 84.662 V145.514 W18.500
G1 U 84.713 V145.575 W18.500
G1 U 84.769 V145.642 W18.500
G1 U 84.826 V145.708 W18.500
G1 U 84.869 V145.758 W18.500
G1 U 84.914 V145.810 W18.500
G1 U 84.960 V145.862 W18.500
G1 U 85.008 V145.917 W18.500
G1 U 85.053 V145.968 W18.500
G1 U 85.098 V146.019 W18.500
G1 U 85.147 V146.073 W18.500
G1 U 85.196 V146.127 W18.500
G1 U 85.253 V146.190 W18.500
G1 U 85.319 V146.262 W18.500
G1 U 85.379 V146.326 W18.500
G1 U 85.439 V146.390 W18.500
G1 U 85.494 V146.448 W18.500
G1 U 85.542 V146.499 W18.500
G1 U 85.601 V146.561 W18.500
G1 U 85.652 V146.612 W18.500
G1 U 85.700 V146.662 W18.500
G1 U 85.752 V146.715 W18.500
G1 U 85.811 V146.775 W18.500
G1 U 85.871 V146.835 W18.500
G1 U 85.924 V146.888 W18.500
G1 U 85.971 V146.934 W18.500
G1 U 86.021 V146.983 W18.500
G1 U 86.074 V147.035 W18.500
G1 U 86.121 V147.080 W18.500
G1 U 86.174 V147.130 W18.500

G1 U 86.217 V147.172 W18.500
G1 U 86.263 V147.215 W18.500
G1 U 86.301 V147.251 W18.500
G1 U 86.346 V147.294 W18.500
G1 U 86.385 V147.330 W18.500
G1 U 86.430 V147.371 W18.500
G1 U 86.481 V147.419 W18.500
G1 U 86.531 V147.464 W18.500
G1 U 86.569 V147.498 W18.500
G1 U 86.622 V147.546 W18.500
G1 U 86.679 V147.598 W18.500
G1 U 86.751 V147.661 W18.500
G1 U 86.808 V147.712 W18.500
G1 U 86.863 V147.760 W18.500
G1 U 86.917 V147.807 W18.500
G1 U 86.976 V147.858 W18.500
G1 U 87.033 V147.907 W18.500
G1 U 87.109 V147.971 W18.500
G1 U 87.190 V148.038 W18.500
G1 U 87.276 V148.110 W18.500
G1 U 87.376 V148.192 W18.500
G1 U 87.465 V148.264 W18.500
G1 U 87.545 V148.328 W18.500
G1 U 87.624 V148.390 W18.500
G1 U 87.705 V148.454 W18.500
G1 U 87.791 V148.520 W18.500
G1 U 87.881 V148.589 W18.500
G1 U 87.972 V148.658 W18.500
G1 U 88.064 V148.727 W18.500
G1 U 88.164 V148.801 W18.500
G1 U 88.264 V148.874 W18.500
G1 U 88.374 V148.953 W18.500
G1 U 88.498 V149.041 W18.500
G1 U 88.618 V149.125 W18.500
G1 U 88.741 V149.209 W18.500
G1 U 88.860 V149.290 W18.500
G1 U 88.987 V149.374 W18.500
G1 U 89.098 V149.447 W18.500
G1 U 89.232 V149.533 W18.500
G1 U 89.360 V149.615 W18.500
G1 U 89.498 V149.700 W18.500
G1 U 89.626 V149.779 W18.500
G1 U 89.754 V149.855 W18.500
G1 U 89.884 V149.933 W18.500
G1 U 90.000 V150.000 W18.500
G1 U176.603 V200.000 W18.500
G1 U176.696 V200.055 W18.500
G1 U176.802 V200.117 W18.500
G1 U176.956 V200.209 W18.500
G1 U177.131 V200.316 W18.500
G1 U177.252 V200.392 W18.500

G1 U177.372 V200.468 W18.500
G1 U177.500 V200.550 W18.500
G1 U177.629 V200.635 W18.500
G1 U177.748 V200.714 W18.500
G1 U177.869 V200.795 W18.500
G1 U177.982 V200.874 W18.500
G1 U178.079 V200.941 W18.500
G1 U178.194 V201.022 W18.500
G1 U178.326 V201.117 W18.500
G1 U178.447 V201.205 W18.500
G1 U178.568 V201.295 W18.500
G1 U178.689 V201.386 W18.500
G1 U178.810 V201.478 W18.500
G1 U178.940 V201.579 W18.500
G1 U179.086 V201.694 W18.500
G1 U179.214 V201.798 W18.500
G1 U179.349 V201.908 W18.500
G1 U179.470 V202.009 W18.500
G1 U179.593 V202.114 W18.500
G1 U179.703 V202.208 W18.500
G1 U179.824 V202.314 W18.500
G1 U179.938 V202.416 W18.500
G1 U180.043 V202.510 W18.500
G1 U180.171 V202.627 W18.500
G1 U180.285 V202.733 W18.500
G1 U180.390 V202.833 W18.500
G1 U180.500 V202.938 W18.500
G1 U180.615 V203.050 W18.500
G1 U180.738 V203.172 W18.500
G1 U180.862 V203.296 W18.500
G1 U180.960 V203.397 W18.500
G1 U181.043 V203.483 W18.500
G1 U181.129 V203.573 W18.500
G1 U181.228 V203.679 W18.500
G1 U181.320 V203.778 W18.500
G1 U181.409 V203.875 W18.500
G1 U181.511 V203.988 W18.500
G1 U181.615 V204.106 W18.500
G1 U181.722 V204.229 W18.500
G1 U181.813 V204.335 W18.500
G1 U181.953 V204.501 W18.500
G1 U182.089 V204.664 W18.500
G1 U182.225 V204.833 W18.500
G1 U182.348 V204.989 W18.500
G1 U182.457 V205.129 W18.500
G1 U182.543 V205.241 W18.500
G1 U182.652 V205.386 W18.500
G1 U182.757 V205.529 W18.500
G1 U182.868 V205.682 W18.500
G1 U182.987 V205.851 W18.500
G1 U183.096 V206.009 W18.500

G1 U183.213 V206.180 W18.500
G1 U183.333 V206.362 W18.500
G1 U183.448 V206.540 W18.500
G1 U183.543 V206.690 W18.500
G1 U183.622 V206.816 W18.500
G1 U183.685 V206.920 W18.500
G1 U183.750 V207.026 W18.500
G1 U183.805 V207.118 W18.500
G1 U183.871 V207.231 W18.500
G1 U183.923 V207.321 W18.500
G1 U183.982 V207.423 W18.500
G1 U184.040 V207.526 W18.500
G1 U184.091 V207.618 W18.500
G1 U184.146 V207.716 W18.500
G1 U184.201 V207.819 W18.500
G1 U184.259 V207.926 W18.500
G1 U184.315 V208.032 W18.500
G1 U184.383 V208.163 W18.500
G1 U184.445 V208.285 W18.500
G1 U184.501 V208.396 W18.500
G1 U184.564 V208.523 W18.500
G1 U184.615 V208.628 W18.500
G1 U184.670 V208.743 W18.500
G1 U184.727 V208.865 W18.500
G1 U184.778 V208.975 W18.500
G1 U184.825 V209.077 W18.500
G1 U184.880 V209.200 W18.500
G1 U184.927 V209.308 W18.500
G1 U184.978 V209.424 W18.500
G1 U185.025 V209.534 W18.500
G1 U185.072 V209.647 W18.500
G1 U185.124 V209.774 W18.500
G1 U185.170 V209.889 W18.500
G1 U185.218 V210.007 W18.500
G1 U185.267 V210.134 W18.500
G1 U185.314 V210.257 W18.500
G1 U185.361 V210.383 W18.500
G1 U185.410 V210.518 W18.500
G1 U185.457 V210.650 W18.500
G1 U185.504 V210.782 W18.500
G1 U185.547 V210.910 W18.500
G1 U185.578 V211.002 W18.500
G1 U185.620 V211.130 W18.500
G1 U185.669 V211.283 W18.500
G1 U185.712 V211.420 W18.500
G1 U185.756 V211.565 W18.500
G1 U185.793 V211.687 W18.500
G1 U185.827 V211.807 W18.500
G1 U185.868 V211.949 W18.500
G1 U185.910 V212.104 W18.500
G1 U185.946 V212.238 W18.500

G1 U185.990 V212.410 W18.500
G1 U186.025 V212.550 W18.500
G1 U186.061 V212.699 W18.500
G1 U186.092 V212.832 W18.500
G1 U186.136 V213.024 W18.500
G1 U186.172 V213.192 W18.500
G1 U186.200 V213.330 W18.500
G1 U186.224 V213.446 W18.500
G1 U186.246 V213.563 W18.500
G1 U186.269 V213.683 W18.500
G1 U186.291 V213.803 W18.500
G1 U186.311 V213.921 W18.500
G1 U186.332 V214.039 W18.500
G1 U186.350 V214.155 W18.500
G1 U186.369 V214.271 W18.500
G1 U186.391 V214.418 W18.500
G1 U186.409 V214.543 W18.500
G1 U186.430 V214.699 W18.500
G1 U186.446 V214.824 W18.500
G1 U186.466 V214.990 W18.500
G1 U186.482 V215.124 W18.500
G1 U186.498 V215.274 W18.500
G1 U186.511 V215.413 W18.500
G1 U186.525 V215.562 W18.500
G1 U186.537 V215.701 W18.500
G1 U186.548 V215.840 W18.500
G1 U186.557 V215.978 W18.500
G1 U186.567 V216.123 W18.500
G1 U186.575 V216.276 W18.500
G1 U186.581 V216.394 W18.500
G1 U186.586 V216.516 W18.500
G1 U186.593 V216.688 W18.500
G1 U186.597 V216.854 W18.500
G1 U186.600 V216.993 W18.500
G1 U186.602 V217.137 W18.500
G1 U186.602 V217.243 W18.500
G1 U186.603 V217.321 W18.500
G1 U186.603 V270.000 W18.500
G1 W5
G4 S15
G1 U105.000 V 75.000 F1400
G4 S5
G1 U105.000 V 75.000 W18.500 F200
G1 U105.000 V139.105 W18.500
G1 U105.000 V139.206 W18.500
G1 U105.001 V139.301 W18.500
G1 U105.002 V139.394 W18.500
G1 U105.004 V139.490 W18.500
G1 U105.006 V139.586 W18.500
G1 U105.008 V139.671 W18.500
G1 U105.011 V139.763 W18.500

G1 U105.014 V139.862 W18.500
G1 U105.018 V139.958 W18.500
G1 U105.022 V140.051 W18.500
G1 U105.027 V140.138 W18.500
G1 U105.031 V140.225 W18.500
G1 U105.037 V140.324 W18.500
G1 U105.043 V140.420 W18.500
G1 U105.049 V140.501 W18.500
G1 U105.055 V140.589 W18.500
G1 U105.062 V140.684 W18.500
G1 U105.070 V140.778 W18.500
G1 U105.079 V140.882 W18.500
G1 U105.087 V140.966 W18.500
G1 U105.095 V141.047 W18.500
G1 U105.104 V141.143 W18.500
G1 U105.115 V141.247 W18.500
G1 U105.125 V141.340 W18.500
G1 U105.137 V141.438 W18.500
G1 U105.149 V141.539 W18.500
G1 U105.160 V141.632 W18.500
G1 U105.172 V141.719 W18.500
G1 U105.183 V141.807 W18.500
G1 U105.196 V141.896 W18.500
G1 U105.207 V141.974 W18.500
G1 U105.220 V142.063 W18.500
G1 U105.233 V142.152 W18.500
G1 U105.247 V142.239 W18.500
G1 U105.260 V142.319 W18.500
G1 U105.273 V142.401 W18.500
G1 U105.289 V142.494 W18.500
G1 U105.302 V142.569 W18.500
G1 U105.317 V142.651 W18.500
G1 U105.333 V142.741 W18.500
G1 U105.349 V142.824 W18.500
G1 U105.363 V142.897 W18.500
G1 U105.378 V142.978 W18.500
G1 U105.394 V143.054 W18.500
G1 U105.409 V143.127 W18.500
G1 U105.425 V143.209 W18.500
G1 U105.441 V143.284 W18.500
G1 U105.461 V143.375 W18.500
G1 U105.483 V143.472 W18.500
G1 U105.504 V143.568 W18.500
G1 U105.525 V143.656 W18.500
G1 U105.542 V143.730 W18.500
G1 U105.560 V143.803 W18.500
G1 U105.581 V143.893 W18.500
G1 U105.603 V143.981 W18.500
G1 U105.626 V144.071 W18.500
G1 U105.646 V144.149 W18.500
G1 U105.666 V144.222 W18.500

G1 U105.686 V144.299 W18.500
G1 U105.704 V144.364 W18.500
G1 U105.721 V144.426 W18.500
G1 U105.739 V144.493 W18.500
G1 U105.759 V144.561 W18.500
G1 U105.772 V144.608 W18.500
G1 U105.787 V144.662 W18.500
G1 U105.801 V144.709 W18.500
G1 U105.817 V144.764 W18.500
G1 U105.835 V144.824 W18.500
G1 U105.853 V144.884 W18.500
G1 U105.871 V144.944 W18.500
G1 U105.890 V145.004 W18.500
G1 U105.909 V145.066 W18.500
G1 U105.928 V145.125 W18.500
G1 U105.946 V145.183 W18.500
G1 U105.962 V145.235 W18.500
G1 U105.978 V145.283 W18.500
G1 U105.998 V145.343 W18.500
G1 U106.015 V145.396 W18.500
G1 U106.032 V145.445 W18.500
G1 U106.046 V145.488 W18.500
G1 U106.061 V145.532 W18.500
G1 U106.075 V145.574 W18.500
G1 U106.089 V145.616 W18.500
G1 U106.105 V145.660 W18.500
G1 U106.118 V145.697 W18.500
G1 U106.132 V145.737 W18.500
G1 U106.145 V145.775 W18.500
G1 U106.158 V145.812 W18.500
G1 U106.169 V145.844 W18.500
G1 U106.184 V145.885 W18.500
G1 U106.199 V145.927 W18.500
G1 U106.218 V145.977 W18.500
G1 U106.238 V146.033 W18.500
G1 U106.260 V146.090 W18.500
G1 U106.278 V146.140 W18.500
G1 U106.297 V146.191 W18.500
G1 U106.315 V146.239 W18.500
G1 U106.337 V146.295 W18.500
G1 U106.358 V146.349 W18.500
G1 U106.375 V146.394 W18.500
G1 U106.396 V146.447 W18.500
G1 U106.417 V146.499 W18.500
G1 U106.438 V146.552 W18.500
G1 U106.458 V146.602 W18.500
G1 U106.479 V146.652 W18.500
G1 U106.502 V146.708 W18.500
G1 U106.522 V146.759 W18.500
G1 U106.543 V146.809 W18.500
G1 U106.564 V146.858 W18.500

G1 U106.587 V146.914 W18.500
G1 U106.611 V146.969 W18.500
G1 U106.637 V147.030 W18.500
G1 U106.662 V147.087 W18.500
G1 U106.688 V147.148 W18.500
G1 U106.714 V147.206 W18.500
G1 U106.738 V147.260 W18.500
G1 U106.765 V147.319 W18.500
G1 U106.790 V147.375 W18.500
G1 U106.816 V147.432 W18.500
G1 U106.839 V147.482 W18.500
G1 U106.864 V147.535 W18.500
G1 U106.890 V147.591 W18.500
G1 U106.916 V147.647 W18.500
G1 U106.946 V147.710 W18.500
G1 U106.974 V147.768 W18.500
G1 U107.001 V147.824 W18.500
G1 U107.023 V147.871 W18.500
G1 U107.047 V147.920 W18.500
G1 U107.066 V147.958 W18.500
G1 U107.087 V148.001 W18.500
G1 U107.114 V148.055 W18.500
G1 U107.144 V148.114 W18.500
G1 U107.176 V148.177 W18.500
G1 U107.206 V148.236 W18.500
G1 U107.242 V148.307 W18.500
G1 U107.275 V148.369 W18.500
G1 U107.305 V148.427 W18.500
G1 U107.341 V148.495 W18.500
G1 U107.374 V148.556 W18.500
G1 U107.408 V148.619 W18.500
G1 U107.442 V148.682 W18.500
G1 U107.482 V148.755 W18.500
G1 U107.520 V148.823 W18.500
G1 U107.557 V148.889 W18.500
G1 U107.594 V148.955 W18.500
G1 U107.632 V149.022 W18.500
G1 U107.674 V149.096 W18.500
G1 U107.714 V149.165 W18.500
G1 U107.754 V149.233 W18.500
G1 U107.801 V149.313 W18.500
G1 U107.852 V149.399 W18.500
G1 U107.910 V149.494 W18.500
G1 U107.960 V149.576 W18.500
G1 U108.014 V149.663 W18.500
G1 U108.072 V149.755 W18.500
G1 U108.129 V149.847 W18.500
G1 U108.189 V149.940 W18.500
G1 U108.248 V150.031 W18.500
G1 U108.303 V150.115 W18.500
G1 U108.353 V150.190 W18.500

G1 U108.398 V150.257 W18.500
G1 U108.453 V150.339 W18.500
G1 U108.511 V150.424 W18.500
G1 U108.565 V150.503 W18.500
G1 U108.617 V150.577 W18.500
G1 U108.671 V150.653 W18.500
G1 U108.731 V150.738 W18.500
G1 U108.784 V150.811 W18.500
G1 U108.846 V150.897 W18.500
G1 U108.911 V150.986 W18.500
G1 U108.978 V151.076 W18.500
G1 U109.039 V151.158 W18.500
G1 U109.107 V151.246 W18.500
G1 U109.169 V151.327 W18.500
G1 U109.233 V151.410 W18.500
G1 U109.299 V151.493 W18.500
G1 U109.362 V151.574 W18.500
G1 U109.425 V151.651 W18.500
G1 U109.498 V151.742 W18.500
G1 U109.572 V151.832 W18.500
G1 U109.637 V151.911 W18.500
G1 U109.704 V151.990 W18.500
G1 U109.777 V152.076 W18.500
G1 U109.839 V152.150 W18.500
G1 U109.914 V152.235 W18.500
G1 U109.992 V152.325 W18.500
G1 U110.077 V152.421 W18.500
G1 U110.165 V152.519 W18.500
G1 U110.235 V152.596 W18.500
G1 U110.305 V152.672 W18.500
G1 U110.375 V152.747 W18.500
G1 U110.446 V152.823 W18.500
G1 U110.528 V152.909 W18.500
G1 U110.595 V152.979 W18.500
G1 U110.662 V153.048 W18.500
G1 U110.732 V153.120 W18.500
G1 U110.802 V153.192 W18.500
G1 U110.869 V153.259 W18.500
G1 U110.939 V153.328 W18.500
G1 U111.006 V153.393 W18.500
G1 U111.077 V153.463 W18.500
G1 U111.144 V153.528 W18.500
G1 U111.205 V153.586 W18.500
G1 U111.279 V153.657 W18.500
G1 U111.334 V153.708 W18.500
G1 U111.407 V153.776 W18.500
G1 U111.480 V153.843 W18.500
G1 U111.556 V153.913 W18.500
G1 U111.635 V153.984 W18.500
G1 U111.712 V154.052 W18.500
G1 U111.794 V154.125 W18.500

G1 U111.877 V154.197 W18.500
G1 U111.966 V154.275 W18.500
G1 U112.066 V154.360 W18.500
G1 U112.167 V154.445 W18.500
G1 U112.251 V154.515 W18.500
G1 U112.338 V154.586 W18.500
G1 U112.411 V154.646 W18.500
G1 U112.507 V154.723 W18.500
G1 U112.612 V154.807 W18.500
G1 U112.727 V154.896 W18.500
G1 U112.842 V154.985 W18.500
G1 U112.943 V155.062 W18.500
G1 U113.057 V155.148 W18.500
G1 U113.189 V155.245 W18.500
G1 U113.298 V155.324 W18.500
G1 U113.427 V155.417 W18.500
G1 U113.563 V155.513 W18.500
G1 U113.728 V155.626 W18.500
G1 U113.884 V155.732 W18.500
G1 U114.043 V155.837 W18.500
G1 U114.201 V155.939 W18.500
G1 U114.364 V156.042 W18.500
G1 U114.540 V156.152 W18.500
G1 U114.708 V156.254 W18.500
G1 U114.871 V156.351 W18.500
G1 U115.044 V156.451 W18.500
G1 U115.211 V156.546 W18.500
G1 U115.390 V156.645 W18.500
G1 U115.528 V156.720 W18.500
G1 U115.698 V156.810 W18.500
G1 U115.893 V156.911 W18.500
G1 U116.066 V156.999 W18.500
G1 U116.214 V157.072 W18.500
G1 U116.410 V157.167 W18.500
G1 U116.590 V157.251 W18.500
G1 U116.791 V157.343 W18.500
G1 U116.954 V157.415 W18.500
G1 U117.115 V157.485 W18.500
G1 U117.284 V157.557 W18.500
G1 U117.451 V157.626 W18.500
G1 U117.641 V157.702 W18.500
G1 U117.818 V157.771 W18.500
G1 U117.983 V157.834 W18.500
G1 U118.160 V157.899 W18.500
G1 U212.129 V192.101 W18.500
G1 U212.189 V192.123 W18.500
G1 U212.255 V192.147 W18.500
G1 U212.348 V192.182 W18.500
G1 U212.449 V192.221 W18.500
G1 U212.560 V192.263 W18.500
G1 U212.680 V192.311 W18.500

G1 U212.817 V192.366 W18.500
G1 U212.987 V192.436 W18.500
G1 U213.146 V192.503 W18.500
G1 U213.340 V192.587 W18.500
G1 U213.543 V192.678 W18.500
G1 U213.719 V192.758 W18.500
G1 U213.903 V192.845 W18.500
G1 U214.091 V192.936 W18.500
G1 U214.279 V193.030 W18.500
G1 U214.452 V193.117 W18.500
G1 U214.619 V193.205 W18.500
G1 U214.811 V193.307 W18.500
G1 U214.996 V193.409 W18.500
G1 U215.183 V193.514 W18.500
G1 U215.394 V193.636 W18.500
G1 U215.580 V193.746 W18.500
G1 U215.752 V193.850 W18.500
G1 U215.902 V193.943 W18.500
G1 U216.056 V194.041 W18.500
G1 U216.264 V194.176 W18.500
G1 U216.461 V194.306 W18.500
G1 U216.600 V194.401 W18.500
G1 U216.748 V194.504 W18.500
G1 U216.893 V194.605 W18.500
G1 U217.009 V194.689 W18.500
G1 U217.136 V194.782 W18.500
G1 U217.269 V194.880 W18.500
G1 U217.389 V194.970 W18.500
G1 U217.532 V195.080 W18.500
G1 U217.647 V195.170 W18.500
G1 U217.750 V195.252 W18.500
G1 U217.862 V195.341 W18.500
G1 U217.964 V195.424 W18.500
G1 U218.062 V195.505 W18.500
G1 U218.170 V195.596 W18.500
G1 U218.266 V195.677 W18.500
G1 U218.373 V195.769 W18.500
G1 U218.483 V195.864 W18.500
G1 U218.559 V195.932 W18.500
G1 U218.649 V196.012 W18.500
G1 U218.745 V196.099 W18.500
G1 U218.825 V196.172 W18.500
G1 U218.905 V196.246 W18.500
G1 U218.988 V196.323 W18.500
G1 U219.065 V196.396 W18.500
G1 U219.139 V196.467 W18.500
G1 U219.236 V196.561 W18.500
G1 U219.312 V196.635 W18.500
G1 U219.393 V196.715 W18.500
G1 U219.467 V196.789 W18.500
G1 U219.537 V196.860 W18.500

G1 U219.617 V196.941 W18.500
G1 U219.709 V197.036 W18.500
G1 U219.800 V197.132 W18.500
G1 U219.871 V197.208 W18.500
G1 U219.956 V197.298 W18.500
G1 U220.052 V197.402 W18.500
G1 U220.133 V197.492 W18.500
G1 U220.210 V197.578 W18.500
G1 U220.282 V197.658 W18.500
G1 U220.362 V197.750 W18.500
G1 U220.437 V197.837 W18.500
G1 U220.508 V197.920 W18.500
G1 U220.589 V198.014 W18.500
G1 U220.662 V198.102 W18.500
G1 U220.730 V198.184 W18.500
G1 U220.811 V198.283 W18.500
G1 U220.900 V198.394 W18.500
G1 U220.996 V198.515 W18.500
G1 U221.078 V198.620 W18.500
G1 U221.153 V198.717 W18.500
G1 U221.238 V198.828 W18.500
G1 U221.313 V198.927 W18.500
G1 U221.383 V199.021 W18.500
G1 U221.446 V199.108 W18.500
G1 U221.501 V199.183 W18.500
G1 U221.563 V199.269 W18.500
G1 U221.617 V199.345 W18.500
G1 U221.671 V199.423 W18.500
G1 U221.726 V199.501 W18.500
G1 U221.775 V199.573 W18.500
G1 U221.831 V199.654 W18.500
G1 U221.882 V199.730 W18.500
G1 U221.945 V199.824 W18.500
G1 U221.994 V199.898 W18.500
G1 U222.051 V199.985 W18.500
G1 U222.101 V200.063 W18.500
G1 U222.157 V200.151 W18.500
G1 U222.204 V200.225 W18.500
G1 U222.255 V200.306 W18.500
G1 U222.311 V200.395 W18.500
G1 U222.355 V200.467 W18.500
G1 U222.403 V200.547 W18.500
G1 U222.451 V200.626 W18.500
G1 U222.494 V200.699 W18.500
G1 U222.547 V200.788 W18.500
G1 U222.600 V200.879 W18.500
G1 U222.654 V200.973 W18.500
G1 U222.709 V201.071 W18.500
G1 U222.757 V201.155 W18.500
G1 U222.791 V201.216 W18.500
G1 U222.830 V201.287 W18.500

G1 U222.871 V201.364 W18.500
G1 U222.915 V201.445 W18.500
G1 U222.959 V201.527 W18.500
G1 U223.005 V201.614 W18.500
G1 U223.040 V201.682 W18.500
G1 U223.078 V201.755 W18.500
G1 U223.122 V201.842 W18.500
G1 U223.168 V201.933 W18.500
G1 U223.211 V202.019 W18.500
G1 U223.251 V202.101 W18.500
G1 U223.297 V202.194 W18.500
G1 U223.334 V202.271 W18.500
G1 U223.370 V202.348 W18.500
G1 U223.406 V202.425 W18.500
G1 U223.451 V202.521 W18.500
G1 U223.486 V202.598 W18.500
G1 U223.521 V202.674 W18.500
G1 U223.557 V202.755 W18.500
G1 U223.588 V202.826 W18.500
G1 U223.619 V202.895 W18.500
G1 U223.646 V202.957 W18.500
G1 U223.674 V203.023 W18.500
G1 U223.705 V203.095 W18.500
G1 U223.733 V203.163 W18.500
G1 U223.762 V203.232 W18.500
G1 U223.791 V203.301 W18.500
G1 U223.819 V203.371 W18.500
G1 U223.847 V203.439 W18.500
G1 U223.878 V203.518 W18.500
G1 U223.911 V203.601 W18.500
G1 U223.948 V203.695 W18.500
G1 U223.980 V203.779 W18.500
G1 U224.013 V203.868 W18.500
G1 U224.042 V203.946 W18.500
G1 U224.076 V204.037 W18.500
G1 U224.106 V204.120 W18.500
G1 U224.136 V204.204 W18.500
G1 U224.171 V204.304 W18.500
G1 U224.204 V204.398 W18.500
G1 U224.236 V204.492 W18.500
G1 U224.267 V204.585 W18.500
G1 U224.293 V204.665 W18.500
G1 U224.316 V204.736 W18.500
G1 U224.348 V204.834 W18.500
G1 U224.375 V204.921 W18.500
G1 U224.402 V205.006 W18.500
G1 U224.421 V205.070 W18.500
G1 U224.446 V205.150 W18.500
G1 U224.469 V205.229 W18.500
G1 U224.493 V205.311 W18.500
G1 U224.515 V205.388 W18.500

G1 U224.534 V205.453 W18.500
G1 U224.552 V205.518 W18.500
G1 U224.572 V205.589 W18.500
G1 U224.592 V205.662 W18.500
G1 U224.611 V205.732 W18.500
G1 U224.631 V205.808 W18.500
G1 U224.653 V205.894 W18.500
G1 U224.671 V205.962 W18.500
G1 U224.691 V206.042 W18.500
G1 U224.709 V206.115 W18.500
G1 U224.729 V206.199 W18.500
G1 U224.746 V206.269 W18.500
G1 U224.762 V206.338 W18.500
G1 U224.778 V206.406 W18.500
G1 U224.795 V206.480 W18.500
G1 U224.812 V206.554 W18.500
G1 U224.829 V206.631 W18.500
G1 U224.843 V206.698 W18.500
G1 U224.858 V206.768 W18.500
G1 U224.876 V206.852 W18.500
G1 U224.891 V206.926 W18.500
G1 U224.905 V206.997 W18.500
G1 U224.919 V207.068 W18.500
G1 U224.934 V207.145 W18.500
G1 U224.947 V207.214 W18.500
G1 U224.958 V207.275 W18.500
G1 U224.973 V207.354 W18.500
G1 U224.988 V207.439 W18.500
G1 U225.000 V207.508 W18.500
G1 U225.013 V207.588 W18.500
G1 U225.027 V207.672 W18.500
G1 U225.041 V207.757 W18.500
G1 U225.052 V207.831 W18.500
G1 U225.062 V207.895 W18.500
G1 U225.073 V207.970 W18.500
G1 U225.084 V208.044 W18.500
G1 U225.096 V208.127 W18.500
G1 U225.108 V208.213 W18.500
G1 U225.120 V208.302 W18.500
G1 U225.130 V208.386 W18.500
G1 U225.140 V208.465 W18.500
G1 U225.149 V208.537 W18.500
G1 U225.160 V208.632 W18.500
G1 U225.169 V208.712 W18.500
G1 U225.178 V208.799 W18.500
G1 U225.187 V208.888 W18.500
G1 U225.198 V208.995 W18.500
G1 U225.209 V209.119 W18.500
G1 U225.220 V209.247 W18.500
G1 U225.231 V209.374 W18.500
G1 U225.241 V209.512 W18.500

G1 U225.250 V209.656 W18.500
G1 U225.256 V209.760 W18.500
G1 U225.261 V209.843 W18.500
G1 U225.265 V209.932 W18.500
G1 U225.270 V210.026 W18.500
G1 U225.274 V210.133 W18.500
G1 U225.277 V210.226 W18.500
G1 U225.281 V210.340 W18.500
G1 U225.283 V210.432 W18.500
G1 U225.285 V210.550 W18.500
G1 U225.287 V210.646 W18.500
G1 U225.288 V210.770 W18.500
G1 U225.288 V210.895 W18.500
G1 U225.288 V270.000 W18.500
G1 W5
G4 S15

;Hoop Winds For locating

G1 U220 V251.5 F350
G4 S5
G1 W18.4
G1 U5
G1 W5
G4 S15
G1 V98.4
G4 S5
G1 W18.4
G1 U110
G1 W5
G4 S15

;1st and 2nd layer of 4 layer composite

G1 U162.50 V0.00 F1400
G4 S5
G1 U162.50 V0.00 W18.5 F200
G1 U162.50 V150.00 W18.5
G1 U165.00 V150.00 W18.5
G1 U165.00 V0.00 W18.5
G1 U162.50 V0.00 W18.1
G1 U162.50 V150.00 W18.1
G1 U165.00 V150.00 W18.1
G1 U165.00 V0.00 W18.1
G1 W5
G4 S15
G1 U175.00 V0.00
G4 S5
G1 U175.00 V0.00 W18.5
G1 U175.00 V175.00 W18.5
G1 U177.50 V175.00 W18.5
G1 U177.50 V0.00 W18.5
G1 U177.50 V0.00 W18.1

G1 U175.00 V0.00 W18.1
G1 U175.00 V175.00 W18.1
G1 U177.50 V175.00 W18.1
G1 U177.50 V0.00 W18.1
G1 W5
G4 S15
G1 U187.50 V0.00
G4 S5
G1 U187.50 V0.00 W18.5
G1 U187.50 V175.00 W18.5
G1 U190.00 V175.00 W18.5
G1 U190.00 V0.00 W18.5
G1 U190.00 V0.00 W18.1
G1 U187.50 V0.00 W18.1
G1 U187.50 V175.00 W18.1
G1 U190.00 V175.00 W18.1
G1 U190.00 V0.00 W18.1
G1 W5
G4 S15
G1 U200.00 V0.00
G4 S5
G1 U200.00 V0.00 W18.5
G1 U200.00 V175.00 W18.5
G1 U202.50 V175.00 W18.5
G1 U202.50 V0.00 W18.5
G1 U202.50 V0.00 W18.1
G1 U200.00 V0.00 W18.1
G1 U200.00 V175.00 W18.1
G1 U202.50 V175.00 W18.1
G1 U202.50 V0.00 W18.1
G1 W5
G4 S15
G1 U212.50 V0.00
G4 S5
G1 U212.50 V0.00 W18.5
G1 U212.50 V175.00 W18.5
G1 U215.00 V175.00 W18.5
G1 U215.00 V0.00 W18.5
G1 U215.00 V0.00 W18.1
G1 U212.50 V0.00 W18.1
G1 U212.50 V175.00 W18.1
G1 U215.00 V175.00 W18.1
G1 U215.00 V0.00 W18.1
G1 W5
G4 S15
G1 U225.00 V0.00
G4 S5
G1 U225.00 V0.00 W18.5
G1 U225.00 V175.00 W18.5
G1 U227.50 V175.00 W18.5
G1 U227.50 V0.00 W18.5

G1 U227.50 V0.00 W18.1
G1 U225.00 V0.00 W18.1
G1 U225.00 V175.00 W18.1
G1 U227.50 V175.00 W18.1
G1 U227.50 V0.00 W18.1
G1 W5
G4 S15
//3rd + 4th Layer
G1 U162.50 V-20 F1400
G4 S30
G1 V0.00
G4 S5
G1 U162.50 V0.00 W17.7 F200
G1 U162.50 V150.00 W17.7
G1 U165.00 V150.00 W17.7
G1 U165.00 V0.00 W17.7
G1 U165.00 V0.00 W17.3
G1 U162.50 V0.00 W17.3
G1 U162.50 V150.00 W17.3
G1 U165.00 V150.00 W17.3
G1 U165.00 V0.00 W17.3
G1 W5
G4 S15
G1 U175.00 V0.00
G4 S5
G1 U175.00 V0.00 W17.7
G1 U175.00 V175.00 W17.7
G1 U177.50 V175.00 W17.7
G1 U177.50 V0.00 W17.7
G1 U177.50 V0.00 W17.3
G1 U175.00 V0.00 W17.3
G1 U175.00 V175.00 W17.3
G1 U177.50 V175.00 W17.3
G1 U177.50 V0.00 W17.3
G1 W5
G4 S15
G1 U187.50 V0.00
G4 S5
G1 U187.50 V0.00 W17.7
G1 U187.50 V175.00 W17.7
G1 U190.00 V175.00 W17.7
G1 U190.00 V0.00 W17.7
G1 U190.00 V0.00 W17.3
G1 U187.50 V0.00 W17.3
G1 U187.50 V175.00 W17.3
G1 U190.00 V175.00 W17.3
G1 U190.00 V0.00 W17.3
G1 W5
G4 S15
G1 U200.00 V0.00
G4 S5

G1 U200.00 V0.00 W17.7
G1 U200.00 V175.00 W17.7
G1 U202.50 V175.00 W17.7
G1 U202.50 V0.00 W17.7
G1 U202.50 V0.00 W17.3
G1 U200.00 V0.00 W17.3
G1 U200.00 V175.00 W17.3
G1 U202.50 V175.00 W17.3
G1 U202.50 V0.00 W17.3
G1 W5
G4 S15
G1 U212.50 V0.00
G4 S5
G1 U212.50 V0.00 W17.7
G1 U212.50 V175.00 W17.7
G1 U215.00 V175.00 W17.7
G1 U215.00 V0.00 W17.7
G1 U215.00 V0.00 W17.3
G1 U212.50 V0.00 W17.3
G1 U212.50 V175.00 W17.3
G1 U215.00 V175.00 W17.3
G1 U215.00 V0.00 W17.3
G1 W5
G4 S15
G1 U225.00 V0.00
G4 S5
G1 U225.00 V0.00 W17.7
G1 U225.00 V175.00 W17.7
G1 U227.50 V175.00 W17.7
G1 U227.50 V0.00 W17.7
G1 U227.50 V0.00 W17.3
G1 U225.00 V0.00 W17.3
G1 U225.00 V175.00 W17.3
G1 U227.50 V175.00 W17.3
G1 U227.50 V0.00 W17.3
G1 W5

10.3 Matlab Programs for Processing

The Matlab programs for postprocessing data for the tow positional fidelity study are shown in the subsequent sections. Details of each program are given in the comments.

10.3.1 Tow_edge.m Program:

```
%Tow Edge Finder
%Takes a Point Cloud File in excel and divides it into two data sets, one
%for each edge of the tow. It then simplifies the vector so that 1 point
%every so many mm in the x axis is created. It averages the y values for
%whatever the range is. This does all the output for all 8 paths. If you
%get an error stating Attempted to access Y_1(0), the first data point is
%not less than x_start. Create a data point less than that.

clc, clear all
%Read excel file
Tab=8; %Tab to read from: increase from 1-8; Tab_wt=Tab+1 excel tab to write
into
X_1=xlsread('Constant_Angle_Points_Raw.xlsx',Tab,'A1:A10000');
Y_1=xlsread('Constant_Angle_Points_Raw.xlsx',Tab,'B1:B10000');
% X_RP=xlsread('Constant_Angle_Points_Summary.xlsx',10,'A2:A255');
% Y_RP=xlsread('Constant_Angle_Points_Summary.xlsx',10,'I2:I255');
% Y1=B Y2=C Y3=D Y4=E Y5=F Y6=G Y7=H Y8=I

%Separates Values into 2 data sets and only the data that will be analyzed
x_start = 0.2; x_end = 149.8; %Start and end x values utilized for data
x_it = 0.1; %creates a data point at this iteration of numbers
Tol=1; %number tolerance to separate data If noisy, use 2 as max

i=1; j=1; k=1; %counters
while i<length(X_1)

    if X_1(i)>x_start && X_1(i)<x_end %take data point if between this bound
        if j==1 && k==1; %sets the initial bound based on a close value
            Y_bound_b=Y_1(i-1)+Tol;
            Y_bound_t=Y_1(i-1)-Tol;
        end
        if Y_1(i)<Y_bound_b && Y_1(i)>Y_bound_t %if meets this criteria
            create 1 data set
                Y_T_1(j)=Y_1(i);
                X_T_1(j)=X_1(i);
                Y_bound_b= Y_T_1(j)+Tol; %modified the bound so that it is a
            close value
                Y_bound_t= Y_T_1(j)-Tol;
                j=j+1;
        else %create this data set if it doesnt meet that criteria
            Y_B_1(k)=Y_1(i);
            X_B_1(k)=X_1(i);
            k=k+1;
        end
    end
    i=i+1;
end
```

```

%Now that 2 separate data sets are created, we want to create 1 data point
%every 0.1 mm in the x axis with both sets of data. The interp1 function does
%this as long as there are not repeated values in the cells. The loops
%below delete the repeated values.
i=1; j=1;
X_Ta_1(i)=X_T_1(i); Y_Ta_1(i)=Y_T_1(i);
while i<length(X_T_1)
    if X_T_1(i)~=X_T_1(i+1) && Y_T_1(i)~=Y_T_1(i+1)
        X_Ta_1(j+1)=X_T_1(i+1); Y_Ta_1(j+1)=Y_T_1(i+1);
        i=i+1; j=j+1;
    else
        i=i+1;
    end
end
i=1; j=1;
X_Ba_1(i)=X_B_1(i); Y_Ba_1(i)=Y_B_1(i);
while i<length(X_B_1)
    if X_B_1(i)~=X_B_1(i+1) && Y_B_1(i)~=Y_B_1(i+1)
        X_Ba_1(j+1)=X_B_1(i+1); Y_Ba_1(j+1)=Y_B_1(i+1);
        i=i+1; j=j+1;
    else
        i=i+1;
    end
end
end

X_S_1=[x_start:x_it:x_end];
Y_ST_1=interp1(X_Ta_1,Y_Ta_1,X_S_1);
Y_SB_1=interp1(X_Ba_1,Y_Ba_1,X_S_1);

%Fills the last few cells in if it is NaN
Lgth=length(X_S_1);
i=Lgth;
for k=1:1:Lgth;
    if isnan(Y_ST_1(i))==1;
    else
        first_real_val3=i;
        while i<=Lgth;
            Y_ST_1(i)=Y_ST_1(first_real_val3);
            i=i+1;
        end
        break
    end
    i=i-1;
end
i=Lgth;
for k=1:1:Lgth;
    if isnan(Y_SB_1(i))==1;
    else
        first_real_val4=i;
        while i<=Lgth;
            Y_SB_1(i)=Y_SB_1(first_real_val4);
            i=i+1;
        end
        break
    end
end
end

```

```

        i=i-1;
    end

    %Fills the first couple cells in if it is NaN
    i=1;
    for k=1:1:length(X_S_1);
        if isnan(Y_ST_1(i))==1;
            else
                first_real_val=i;
                while i>=1;
                    Y_ST_1(i)=Y_ST_1(first_real_val);
                    i=i-1;
                end
                break
            end
        end
        i=i+1;
    end
    i=1;
    for k=1:1:length(X_S_1);
        if isnan(Y_SB_1(i))==1;

            else
                first_real_val2=i;
                while i>=1;
                    Y_SB_1(i)=Y_SB_1(first_real_val2);
                    i=i-1;
                end
                break
            end
        end
        i=i+1;
    end

    Y_avg=(Y_ST_1+Y_SB_1)/2;

    %Plot
    figure
    hold on
    plot(X_T_1,Y_T_1,':') %Dotted Line
    plot(X_B_1,Y_B_1,':')
    plot(X_S_1,Y_ST_1,'--') %Dashed Line
    plot(X_S_1,Y_SB_1,'--')
    title('Raw Data and Simplified Data');
    hold off

    %Write data to excel
    %Path 1=2... Path 8=9;
    Tab_wt=Tab+1; %Tab in excel to print to
    fileID='Constant_Angle_Points_Untransformed.xlsx';
    P_data=[X_S_1',Y_ST_1',Y_SB_1',Y_avg'];
    xlswrite(fileID,P_data,Tab_wt,'A2')

```

10.3.2 Get_Results.m Program:

```

%Get Results
%This rotates, shifts the y axis, reduces the data points to 149, and then

```

```

%calculates the desired values.
clc, clear all

%%
%%Inputs:
fileID='Constant_Angle_Points_Untransformed.xlsx';

%Measured Values
[P_1_data,txt,row]=xlsread(fileID,2,'A2:D1500');
X_1_m=P_1_data(:,1);    Y_1_m=P_1_data(:,4);    Y_1_T=P_1_data(:,2);
Y_1_B=P_1_data(:,3);
[P_2_data,txt,row]=xlsread(fileID,3,'A2:D1500');
X_2_m=P_2_data(:,1);    Y_2_m=P_2_data(:,4);    Y_2_T=P_2_data(:,2);
Y_2_B=P_2_data(:,3);
[P_3_data,txt,row]=xlsread(fileID,4,'A2:D1500');
X_3_m=P_3_data(:,1);    Y_3_m=P_3_data(:,4);    Y_3_T=P_3_data(:,2);
Y_3_B=P_3_data(:,3);
[P_4_data,txt,row]=xlsread(fileID,5,'A2:D1500');
X_4_m=P_4_data(:,1);    Y_4_m=P_4_data(:,4);    Y_4_T=P_4_data(:,2);
Y_4_B=P_4_data(:,3);
[P_5_data,txt,row]=xlsread(fileID,6,'A2:D1500');
X_5_m=P_5_data(:,1);    Y_5_m=P_5_data(:,4);    Y_5_T=P_5_data(:,2);
Y_5_B=P_5_data(:,3);
[P_6_data,txt,row]=xlsread(fileID,7,'A2:D1500');
X_6_m=P_6_data(:,1);    Y_6_m=P_6_data(:,4);    Y_6_T=P_6_data(:,2);
Y_6_B=P_6_data(:,3);
[P_7_data,txt,row]=xlsread(fileID,8,'A2:D1500');
X_7_m=P_7_data(:,1);    Y_7_m=P_7_data(:,4);    Y_7_T=P_7_data(:,2);
Y_7_B=P_7_data(:,3);
[P_8_data,txt,row]=xlsread(fileID,9,'A2:D1500');
X_8_m=P_8_data(:,1);    Y_8_m=P_8_data(:,4);    Y_8_T=P_8_data(:,2);
Y_8_B=P_8_data(:,3);

%Coded Values
P_code=xlsread(fileID,10,'A2:I500');
X_code=P_code(:,1);
Y_1_code=P_code(:,2);    Y_2_code=P_code(:,3);    Y_3_code=P_code(:,4);
Y_4_code=P_code(:,5);
Y_5_code=P_code(:,6);    Y_6_code=P_code(:,7);    Y_7_code=P_code(:,8);
Y_8_code=P_code(:,9);

%%
%%%%% Rotates the bottom line to make it have a slope of zero %%%%%
P=polyfit(X_1_m,Y_1_m,1); %finds of coefficients of a polynomial of 1st
degree
slope=P(1);
Measured_data=[X_1_m,Y_1_m];
angle=atan(slope);
Rotation=rotz(angle);
Measured_data=Measured_data*Rotation;

%%
%%%%% corrects the Y Axis for the bottom line %%%%%
%Assumes measured line is above coded
%X Values are no longer spaced 1 coordinate per mm because of the rotation;
%this corrects that as well:

```



```

%X_1_cor=floor(Measured_data(:,1));
X_1_cor=[1:1:149]';
X_1_cor_lgth=length(X_1_cor);
Y_1_cor=interp1(Measured_data(:,1),Measured_data(:,2),X_1_cor);
Y_1_cor(1)=Y_1_cor(2);Y_1_cor(X_1_cor_lgth)=Y_1_cor(X_1_cor_lgth-1);
%%Correcting the Y Axis
Shift_y=(sum(Y_1_code)-sum(Y_1_cor))/length(Y_1_code);

%%
%%%%% Applying Rotation and Transformations to other Data Sets
Shift_x=0;
%Finish Path 1:
%X_1_f,Y_1_f] = transform_data(X_1_m,Y_1_m,Rotation,Shift_x,Shift_y);
[X_1_f,Y_1_Tf] = transform_data(X_1_m,Y_1_T,Rotation,Shift_x,Shift_y);
[X_1_f,Y_1_Bf] = transform_data(X_1_m,Y_1_B,Rotation,Shift_x,Shift_y);
%Path 2:
[X_2_f,Y_2_f] = transform_data(X_2_m,Y_2_m,Rotation,Shift_x,Shift_y);
[X_2_f,Y_2_Tf] = transform_data(X_2_m,Y_2_T,Rotation,Shift_x,Shift_y);
[X_2_f,Y_2_Bf] = transform_data(X_2_m,Y_2_B,Rotation,Shift_x,Shift_y);
%Path 3:
[X_3_f,Y_3_f] = transform_data(X_3_m,Y_3_m,Rotation,Shift_x,Shift_y);
[X_3_f,Y_3_Tf] = transform_data(X_3_m,Y_3_T,Rotation,Shift_x,Shift_y);
[X_3_f,Y_3_Bf] = transform_data(X_3_m,Y_3_B,Rotation,Shift_x,Shift_y);
%Path 4:
[X_4_f,Y_4_f] = transform_data(X_4_m,Y_4_m,Rotation,Shift_x,Shift_y);
[X_4_f,Y_4_Tf] = transform_data(X_4_m,Y_4_T,Rotation,Shift_x,Shift_y);
[X_4_f,Y_4_Bf] = transform_data(X_4_m,Y_4_B,Rotation,Shift_x,Shift_y);
%Path 5:
[X_5_f,Y_5_f] = transform_data(X_5_m,Y_5_m,Rotation,Shift_x,Shift_y);
[X_5_f,Y_5_Tf] = transform_data(X_5_m,Y_5_T,Rotation,Shift_x,Shift_y);
[X_5_f,Y_5_Bf] = transform_data(X_5_m,Y_5_B,Rotation,Shift_x,Shift_y);
%Path 6:
[X_6_f,Y_6_f] = transform_data(X_6_m,Y_6_m,Rotation,Shift_x,Shift_y);
[X_6_f,Y_6_Tf] = transform_data(X_6_m,Y_6_T,Rotation,Shift_x,Shift_y);
[X_6_f,Y_6_Bf] = transform_data(X_6_m,Y_6_B,Rotation,Shift_x,Shift_y);
%Path 7:
[X_7_f,Y_7_f] = transform_data(X_7_m,Y_7_m,Rotation,Shift_x,Shift_y);
[X_7_f,Y_7_Tf] = transform_data(X_7_m,Y_7_T,Rotation,Shift_x,Shift_y);
[X_7_f,Y_7_Bf] = transform_data(X_7_m,Y_7_B,Rotation,Shift_x,Shift_y);
%Finish Path 8:
[X_8_f,Y_8_f] = transform_data(X_8_m,Y_8_m,Rotation,Shift_x,Shift_y);
[X_8_f,Y_8_Tf] = transform_data(X_8_m,Y_8_T,Rotation,Shift_x,Shift_y);
[X_8_f,Y_8_Bf] = transform_data(X_8_m,Y_8_B,Rotation,Shift_x,Shift_y);

X_f=X_1_f;
%%
%Putting a Value into the last cell so calculations can be made
lgth=length(X_1_f);
Y_1_Tf(lgth)=Y_1_Tf(lgth-1);   Y_1_Bf(lgth)=Y_1_Bf(lgth-1);
Y_2_Tf(lgth)=Y_2_Tf(lgth-1);   Y_2_Bf(lgth)=Y_2_Bf(lgth-1);
Y_3_Tf(lgth)=Y_3_Tf(lgth-1);   Y_3_Bf(lgth)=Y_3_Bf(lgth-1);
Y_4_Tf(lgth)=Y_4_Tf(lgth-1);   Y_4_Bf(lgth)=Y_4_Bf(lgth-1);
Y_5_Tf(lgth)=Y_5_Tf(lgth-1);   Y_5_Bf(lgth)=Y_5_Bf(lgth-1);
Y_6_Tf(lgth)=Y_6_Tf(lgth-1);   Y_6_Bf(lgth)=Y_6_Bf(lgth-1);
Y_7_Tf(lgth)=Y_7_Tf(lgth-1);   Y_7_Bf(lgth)=Y_7_Bf(lgth-1);
Y_8_Tf(lgth)=Y_8_Tf(lgth-1);   Y_8_Bf(lgth)=Y_8_Bf(lgth-1);

```

```

%%
%Calculating Mean Values for Y Pts
Y_1_f=(Y_1_Tf+Y_1_Bf)/2;
Y_2_f=(Y_2_Tf+Y_2_Bf)/2;
Y_3_f=(Y_3_Tf+Y_3_Bf)/2;
Y_4_f=(Y_4_Tf+Y_4_Bf)/2;
Y_5_f=(Y_5_Tf+Y_5_Bf)/2;
Y_6_f=(Y_6_Tf+Y_6_Bf)/2;
Y_7_f=(Y_7_Tf+Y_7_Bf)/2;
Y_8_f=(Y_8_Tf+Y_8_Bf)/2;

%%
%Calculation for Error
Error_1=Y_1_code-Y_1_f;
Error_2=Y_2_code-Y_2_f;
Error_3=Y_3_code-Y_3_f;
Error_4=Y_4_code-Y_4_f;
Error_5=Y_5_code-Y_5_f;
Error_6=Y_6_code-Y_6_f;
Error_7=Y_7_code-Y_7_f;
Error_8=Y_8_code-Y_8_f;
%Shift Width Calculation
Shift_width_1 = abs(Y_1_Tf-Y_1_Bf);
Shift_width_2 = abs(Y_2_Tf-Y_2_Bf);
Shift_width_3 = abs(Y_3_Tf-Y_3_Bf);
Shift_width_4 = abs(Y_4_Tf-Y_4_Bf);
Shift_width_5 = abs(Y_5_Tf-Y_5_Bf);
Shift_width_6 = abs(Y_6_Tf-Y_6_Bf);
Shift_width_7 = abs(Y_7_Tf-Y_7_Bf);
Shift_width_8 = abs(Y_8_Tf-Y_8_Bf);
%Average Fiber Angle:
i=1;
theta_1T = zeros(length(Y_1_Tf),1); theta_1B = zeros(length(Y_1_Bf),1);
theta_2T = zeros(length(Y_2_Tf),1); theta_2B = zeros(length(Y_2_Bf),1);
theta_3T = zeros(length(Y_3_Tf),1); theta_3B = zeros(length(Y_3_Bf),1);
theta_4T = zeros(length(Y_4_Tf),1); theta_4B = zeros(length(Y_4_Bf),1);
theta_5T = zeros(length(Y_5_Tf),1); theta_5B = zeros(length(Y_5_Bf),1);
theta_6T = zeros(length(Y_6_Tf),1); theta_6B = zeros(length(Y_6_Bf),1);
theta_7T = zeros(length(Y_7_Tf),1); theta_7B = zeros(length(Y_7_Bf),1);
theta_8T = zeros(length(Y_8_Tf),1); theta_8B = zeros(length(Y_8_Bf),1);
while i<length(Y_8_Tf) %calculates tangent angles at tow edge points
    ratio_T_1 = (Y_1_Tf(i+1)-Y_1_Tf(i))/1; ratio_B_1 = (Y_1_Bf(i+1)-
Y_1_Bf(i))/1;
    theta_1T(i) = atan(ratio_T_1)*180/pi; theta_1B(i) =
atan(ratio_B_1)*180/pi;
    ratio_T_2 = (Y_2_Tf(i+1)-Y_2_Tf(i))/1; ratio_B_2 = (Y_2_Bf(i+1)-
Y_2_Bf(i))/1;
    theta_2T(i) = atan(ratio_T_2)*180/pi; theta_2B(i) =
atan(ratio_B_2)*180/pi;
    ratio_T_3 = (Y_3_Tf(i+1)-Y_3_Tf(i))/1; ratio_B_3 = (Y_3_Bf(i+1)-
Y_3_Bf(i))/1;
    theta_3T(i) = atan(ratio_T_3)*180/pi; theta_3B(i) =
atan(ratio_B_3)*180/pi;
    ratio_T_4 = (Y_4_Tf(i+1)-Y_4_Tf(i))/1; ratio_B_4 = (Y_4_Bf(i+1)-
Y_4_Bf(i))/1;

```

```

        theta_4T(i) = atan(ratio_T_4)*180/pi;      theta_4B(i) =
atan(ratio_B_4)*180/pi;
        ratio_T_5 = (Y_5_Tf(i+1)-Y_5_Tf(i))/1;    ratio_B_5 = (Y_5_Bf(i+1)-
Y_5_Bf(i))/1;
        theta_5T(i) = atan(ratio_T_5)*180/pi;      theta_5B(i) =
atan(ratio_B_5)*180/pi;
        ratio_T_6 = (Y_6_Tf(i+1)-Y_6_Tf(i))/1;    ratio_B_6 = (Y_6_Bf(i+1)-
Y_6_Bf(i))/1;
        theta_6T(i) = atan(ratio_T_6)*180/pi;      theta_6B(i) =
atan(ratio_B_6)*180/pi;
        ratio_T_7 = (Y_7_Tf(i+1)-Y_7_Tf(i))/1;    ratio_B_7 = (Y_7_Bf(i+1)-
Y_7_Bf(i))/1;
        theta_7T(i) = atan(ratio_T_7)*180/pi;      theta_7B(i) =
atan(ratio_B_7)*180/pi;
        ratio_T_8 = (Y_8_Tf(i+1)-Y_8_Tf(i))/1;    ratio_B_8 = (Y_8_Bf(i+1)-
Y_8_Bf(i))/1;
        theta_8T(i) = atan(ratio_T_8)*180/pi;      theta_8B(i) =
atan(ratio_B_8)*180/pi;
        i=i+1;
end
theta_avg_1 = (theta_1T + theta_1B)./2;
theta_avg_2 = (theta_2T + theta_2B)./2;
theta_avg_3 = (theta_3T + theta_3B)./2;
theta_avg_4 = (theta_4T + theta_4B)./2;
theta_avg_5 = (theta_5T + theta_5B)./2;
theta_avg_6 = (theta_6T + theta_6B)./2;
theta_avg_7 = (theta_7T + theta_7B)./2;
theta_avg_8 = (theta_8T + theta_8B)./2;
%Calculates Integral to determine Area between the curves:
Area_1_Tf=trapz(X_1_f,Y_1_Tf); Area_1_Bf=trapz(X_1_f,Y_1_Bf);
Area_1=abs(Area_1_Tf-Area_1_Bf);
Area_2_Tf=trapz(X_2_f,Y_2_Tf); Area_2_Bf=trapz(X_2_f,Y_2_Bf);
Area_2=abs(Area_2_Tf-Area_2_Bf);
Area_3_Tf=trapz(X_3_f,Y_3_Tf); Area_3_Bf=trapz(X_3_f,Y_3_Bf);
Area_3=abs(Area_3_Tf-Area_3_Bf);
Area_4_Tf=trapz(X_4_f,Y_4_Tf); Area_4_Bf=trapz(X_4_f,Y_4_Bf);
Area_4=abs(Area_4_Tf-Area_4_Bf);
Area_5_Tf=trapz(X_5_f,Y_5_Tf); Area_5_Bf=trapz(X_5_f,Y_5_Bf);
Area_5=abs(Area_5_Tf-Area_5_Bf);
Area_6_Tf=trapz(X_6_f,Y_6_Tf); Area_6_Bf=trapz(X_6_f,Y_6_Bf);
Area_6=abs(Area_6_Tf-Area_6_Bf);
Area_7_Tf=trapz(X_7_f,Y_7_Tf); Area_7_Bf=trapz(X_7_f,Y_7_Bf);
Area_7=abs(Area_7_Tf-Area_7_Bf);
Area_8_Tf=trapz(X_8_f,Y_8_Tf); Area_8_Bf=trapz(X_8_f,Y_8_Bf);
Area_8=abs(Area_8_Tf-Area_8_Bf);
%Calculating slope (dy/dx) and curvature (d^2y/d^2x)
Slope_1=diff(Y_1_f); Curve_1=diff(Y_1_f,2);
Slope_2=diff(Y_2_f); Curve_2=diff(Y_2_f,2);
Slope_3=diff(Y_3_f); Curve_3=diff(Y_3_f,2);
Slope_4=diff(Y_4_f); Curve_4=diff(Y_4_f,2);
Slope_5=diff(Y_5_f); Curve_5=diff(Y_5_f,2);
Slope_6=diff(Y_6_f); Curve_6=diff(Y_6_f,2);
Slope_7=diff(Y_7_f); Curve_7=diff(Y_7_f,2);
Slope_8=diff(Y_8_f); % Same as diff(Y_8_f)./diff(X_8_f) since denominator
always =1
Curve_8=diff(Y_8_f,2); %can't differentiate the denominator because curvature
values = infinity

```

```

%Making vector length 149 so I can use the same xlswrite below
Slope_1(lngth)=Slope_1(lngth-1); Curve_1(lngth-1)=Curve_1(lngth-2);
Curve_1(lngth)=Curve_1(lngth-1);
Slope_2(lngth)=Slope_2(lngth-1); Curve_2(lngth-1)=Curve_2(lngth-2);
Curve_2(lngth)=Curve_2(lngth-1);
Slope_3(lngth)=Slope_3(lngth-1); Curve_3(lngth-1)=Curve_3(lngth-2);
Curve_3(lngth)=Curve_3(lngth-1);
Slope_4(lngth)=Slope_4(lngth-1); Curve_4(lngth-1)=Curve_4(lngth-2);
Curve_4(lngth)=Curve_4(lngth-1);
Slope_5(lngth)=Slope_5(lngth-1); Curve_5(lngth-1)=Curve_5(lngth-2);
Curve_5(lngth)=Curve_5(lngth-1);
Slope_6(lngth)=Slope_6(lngth-1); Curve_6(lngth-1)=Curve_6(lngth-2);
Curve_6(lngth)=Curve_6(lngth-1);
Slope_7(lngth)=Slope_7(lngth-1); Curve_7(lngth-1)=Curve_7(lngth-2);
Curve_7(lngth)=Curve_7(lngth-1);
Slope_8(lngth)=Slope_8(lngth-1); Curve_8(lngth-1)=Curve_8(lngth-2);
Curve_8(lngth)=Curve_8(lngth-1);

%%
%%%%%% Plot to Check Everything %%%%%%
hold on
plot(X_code,Y_1_code,':') %dotted line
plot(X_f,Y_1_f,'--') %Dashed line
plot(X_f,Y_1_Tf,'-') %Solid Line
plot(X_f,Y_1_Bf,'-') %Solid Line
plot(X_code,Y_2_code,':')
plot(X_f,Y_2_f,'--')
plot(X_f,Y_2_Tf,'-')
plot(X_f,Y_2_Bf,'-')
plot(X_code,Y_3_code,':')
plot(X_f,Y_3_f,'--')
plot(X_f,Y_3_Tf,'-')
plot(X_f,Y_3_Bf,'-')
plot(X_code,Y_4_code,':')
plot(X_f,Y_4_f,'--')
plot(X_f,Y_4_Tf,'-')
plot(X_f,Y_4_Bf,'-')
plot(X_code,Y_5_code,':')
plot(X_f,Y_5_f,'--')
plot(X_f,Y_5_Tf,'-')
plot(X_f,Y_5_Bf,'-')
plot(X_code,Y_6_code,':')
plot(X_f,Y_6_f,'--')
plot(X_f,Y_6_Tf,'-')
plot(X_f,Y_6_Bf,'-')
plot(X_code,Y_7_code,':')
plot(X_f,Y_7_f,'--')
plot(X_f,Y_7_Tf,'-')
plot(X_f,Y_7_Bf,'-')
plot(X_code,Y_8_code,':')
plot(X_f,Y_8_f,'--')
plot(X_f,Y_8_Tf,'-')
plot(X_f,Y_8_Bf,'-')
hold off

%%

```

```

%%%%%%%% Writing Data to Excel %%%%%%%%%
%Path 1=2... Path 8=9;
%Tab in excel to print to
fileID='Constant_Angle_Points_Summary.xlsx';
%Path 1:
P1_f=[X_f,Y_1_Tf,Y_1_Bf,Y_1_f,Error_1,Shift_width_1,theta_avg_1,Slope_1,Curve
_1];
xlswrite(fileID,P1_f,2,'A2')
xlswrite(fileID,Area_1,2,'K3')
%Path 2:
P2_f=[X_f,Y_2_Tf,Y_2_Bf,Y_2_f,Error_2,Shift_width_2,theta_avg_2,Slope_2,Curve
_2];
xlswrite(fileID,P2_f,3,'A2')
xlswrite(fileID,Area_2,3,'K3')
%Path 3:
P3_f=[X_f,Y_3_Tf,Y_3_Bf,Y_3_f,Error_3,Shift_width_3,theta_avg_3,Slope_3,Curve
_3];
xlswrite(fileID,P3_f,4,'A2')
xlswrite(fileID,Area_3,4,'K3')
%Path 4:
P4_f=[X_f,Y_4_Tf,Y_4_Bf,Y_4_f,Error_4,Shift_width_4,theta_avg_4,Slope_4,Curve
_4];
xlswrite(fileID,P4_f,5,'A2')
xlswrite(fileID,Area_4,5,'K3')
%Path 5:
P5_f=[X_f,Y_5_Tf,Y_5_Bf,Y_5_f,Error_5,Shift_width_5,theta_avg_5,Slope_5,Curve
_5];
xlswrite(fileID,P5_f,6,'A2')
xlswrite(fileID,Area_5,6,'K3')
%Path 6:
P6_f=[X_f,Y_6_Tf,Y_6_Bf,Y_6_f,Error_6,Shift_width_6,theta_avg_6,Slope_6,Curve
_6];
xlswrite(fileID,P6_f,7,'A2')
xlswrite(fileID,Area_6,7,'K3')
%Path 7:
P7_f=[X_f,Y_7_Tf,Y_7_Bf,Y_7_f,Error_7,Shift_width_7,theta_avg_7,Slope_7,Curve
_7];
xlswrite(fileID,P7_f,8,'A2')
xlswrite(fileID,Area_7,8,'K3')
%Path 8:
P8_f=[X_f,Y_8_Tf,Y_8_Bf,Y_8_f,Error_8,Shift_width_8,theta_avg_8,Slope_8,Curve
_8];
xlswrite(fileID,P8_f,9,'A2')
xlswrite(fileID,Area_8,9,'K3')

```

10.3.3 transform_data.m User Written Function:

```

function [X_f,Y_f] = transform_data(X_pt,Y_pt,Rotation,Shift_x,Shift_y)
%Transform Data takes an x,y data set rotates it a desired amount, and then
%does a linear transformation in the x and y directions. The output is x
%and y pts with x's at integers of every 1 mm.
% [X_f,Y_f] = transform_data(X_pt,Y_pt,Rotation,Shift_x,Shift_y)

Measured_data=[X_pt,Y_pt];
%Measured_data=Measured_data*Rotation; %Applies Rotation to data set
X_cor=[1:1:149]'; %This reduces data to 1 pt every 1 mm

```

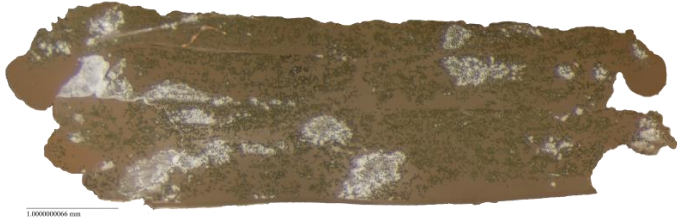



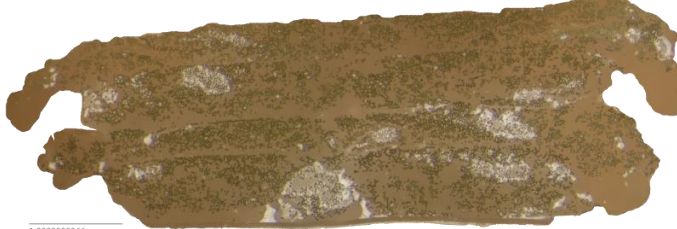



```

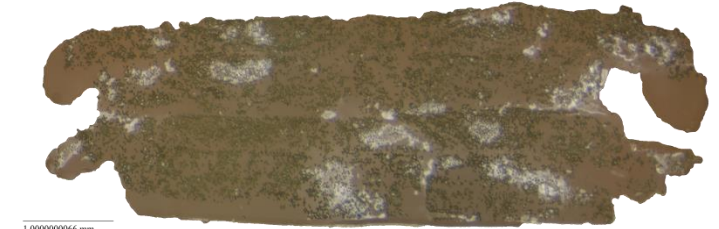



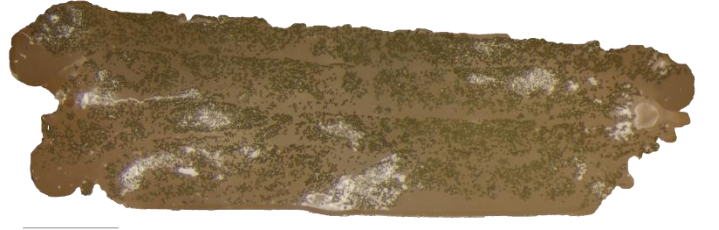



%X_cor=floor(Measured_data(:,1)); %rounds x to an integer %if get error
change round to floor
Y_cor=interp1(Measured_data(:,1),Measured_data(:,2),X_cor); %gets y value for
the rounded x
X_cor(1)=X_cor(2)-1; Y_cor(1)=Y_cor(2); %deletes NaN that exists in cell 1
for new x,y
Y_cor1=Y_cor+Shift_y; X_cor1=X_cor+Shift_x; %Shifts x and y by determined
amounts
X_f=X_cor1; Y_f=Y_cor1;
%%%This is only needed if shifting x and y; we aren't doing so in this
program
%X_f=floor(X_cor1); %rounds x to an integer
%Y_f=interp1(X_cor1,Y_cor1,X_f); %gets y value for the rounded x
%X_f(1)=X_f(2)-1; Y_f(1)=Y_f(2); %deletes NaN that exists in cell 1
end

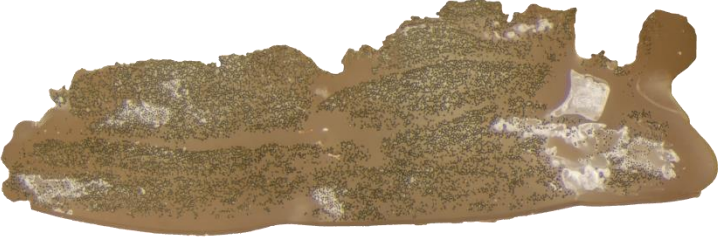



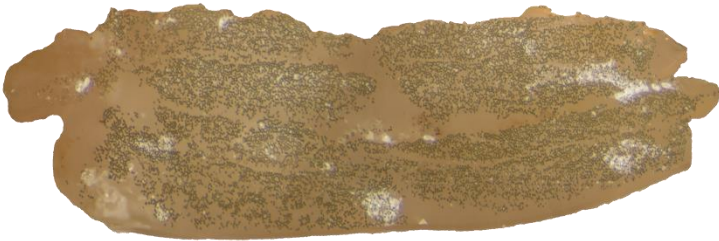



```

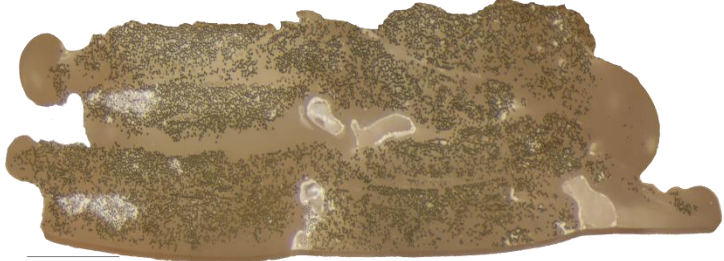

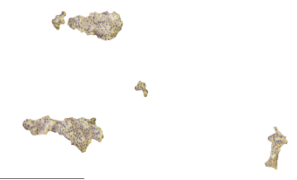





10.4 Microstructure Analysis Photomicrographs

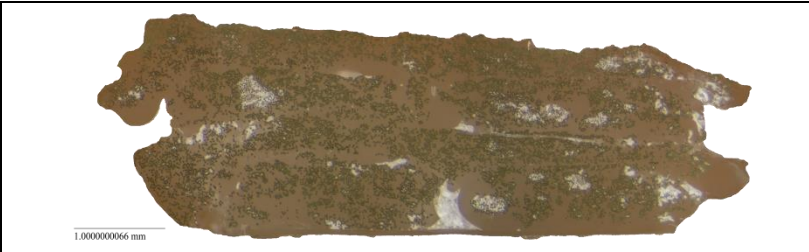
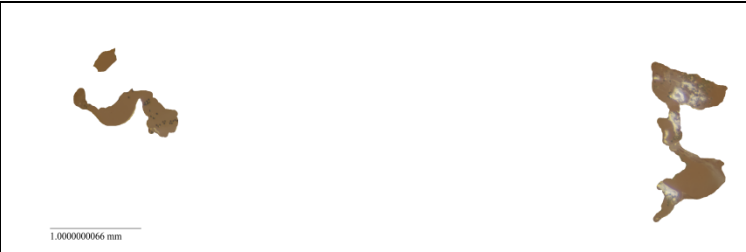


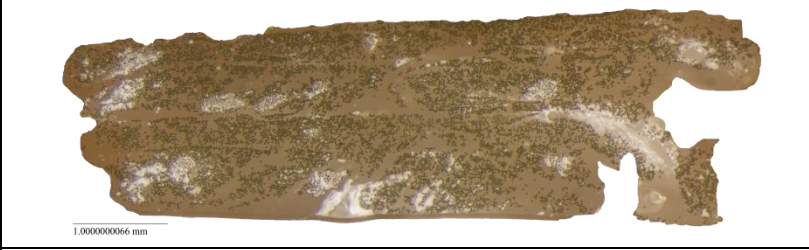



The following table displays the areas considered part of the composite, flash, intraply voids and interply voids. Note the void areas are considered conservative estimates as the area around a void often becomes a similar color as the void due to the ability to pick up polishing debris.

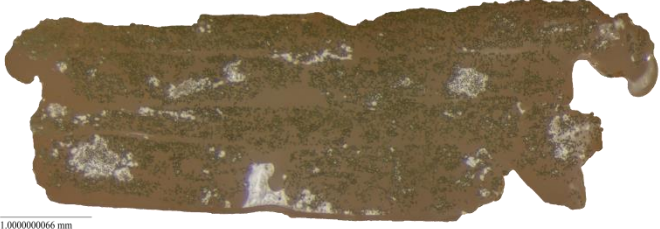



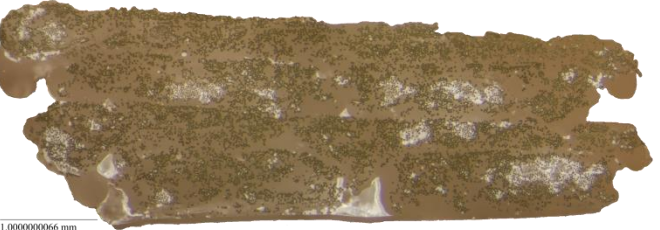



| Sample # & Section # | Composite and Intraply Void Picture | Composite Flash and Interply Void Pictures |
|------------------------|--|---|
| Sample 1 Section 1 |  |  |
| |  |  |
| Sample 1 Section 1A |  |  |
| |  |  |

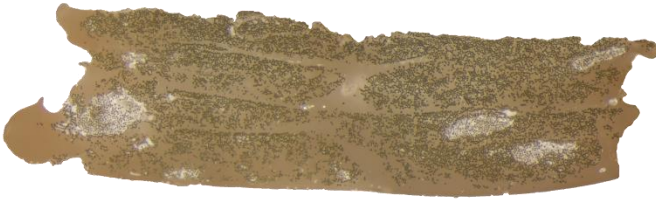



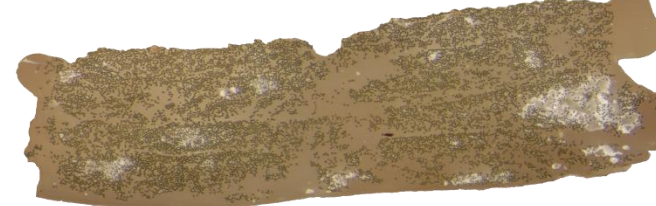



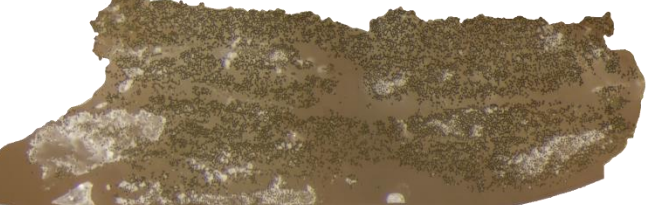

| | | |
|--------------------------------|---|--|
| <p>Sample 1 Section 2</p> |  |  |
| |  |  |
| <p>Sample 1 Section 2A</p> |  |  |
| |  |  |



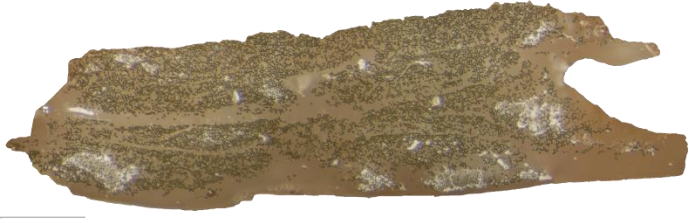


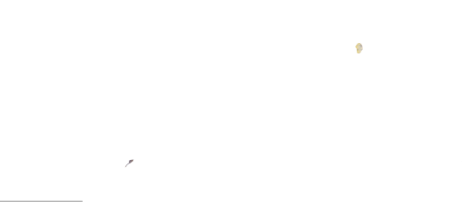
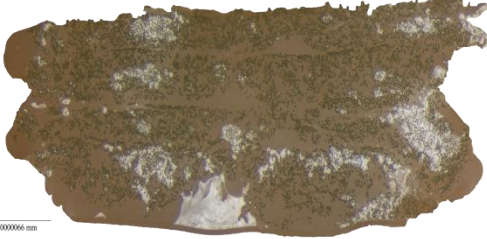

| | | |
|------------------------|--|---|
| Sample 2 Section 1 |  |  |
| |  |  |
| Sample 2 Section 1A |  |  |
| |  |  |

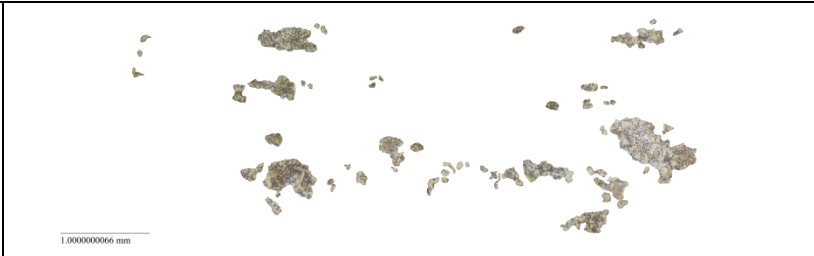

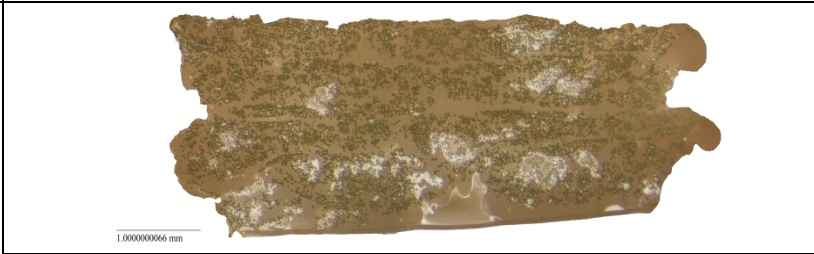
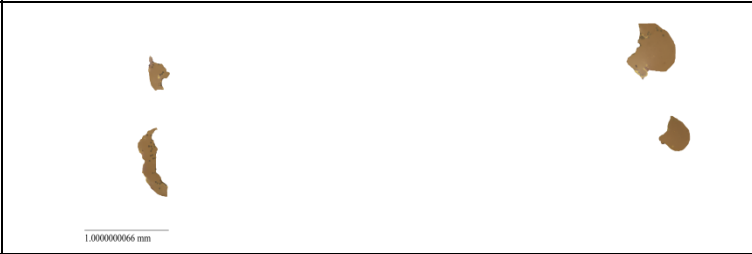

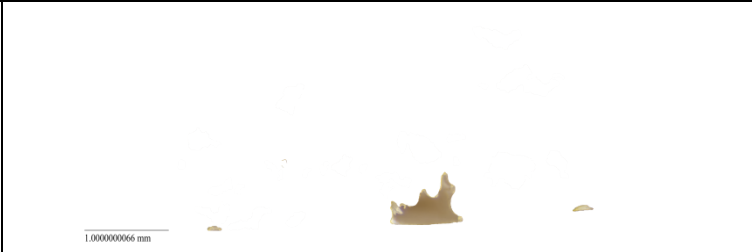
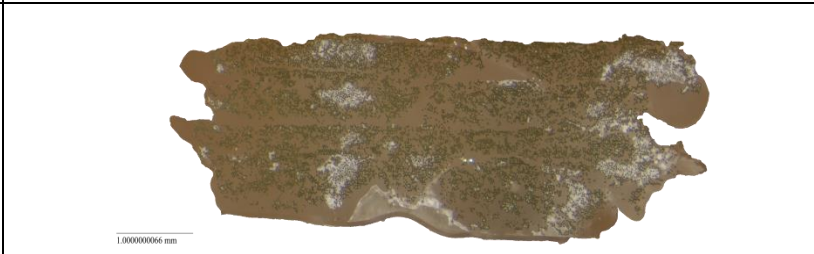

| | | |
|--------------------------------|--|---|
| <p>Sample 2 Section 2</p> |  |  |
| |  |  |
| <p>Sample 2 Section 2A</p> |  |  |
| |  |  |



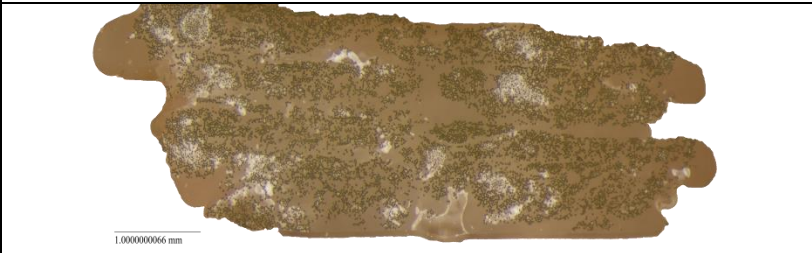

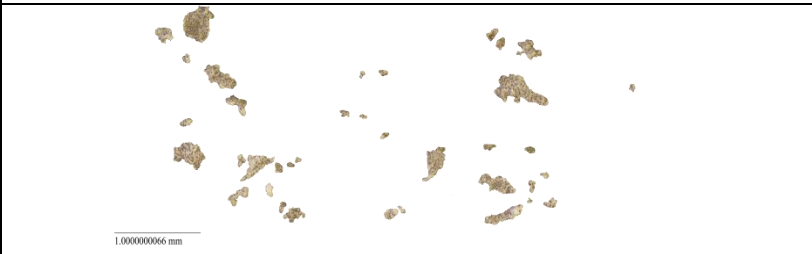

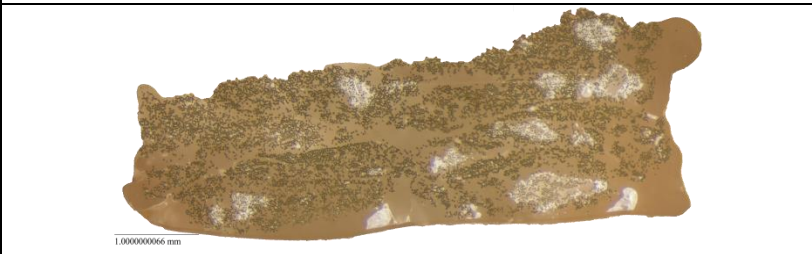

| | | |
|------------------------|---|--|
| Sample 3 Section 1 |  |  |
| |  |  |
| Sample 3 Section 1A |  |  |
| |  |  |



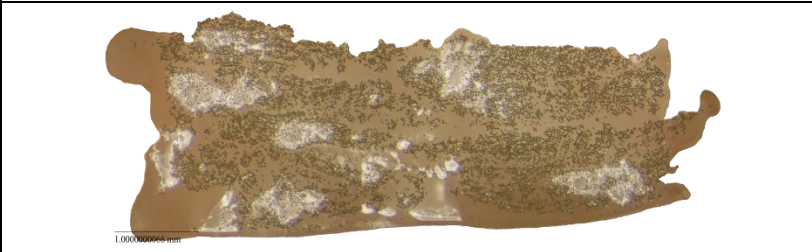
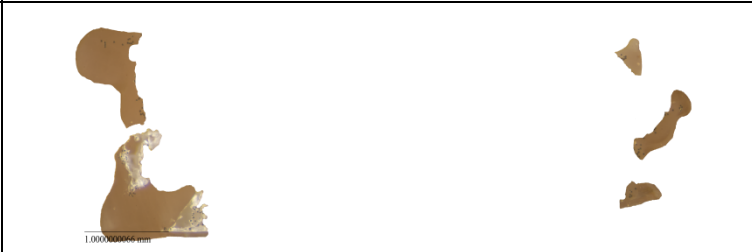


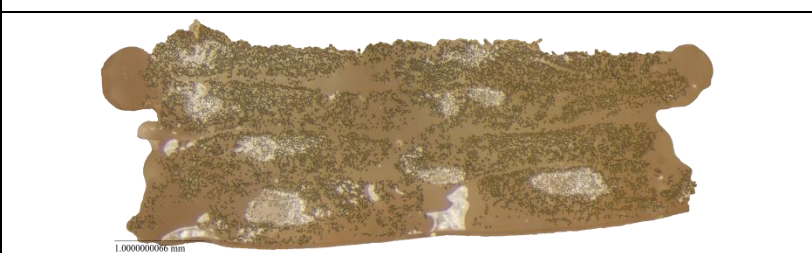

| | | |
|--------------------------------|---|--|
| <p>Sample 3 Section 2</p> |  |  |
| |  |  |
| <p>Sample 3 Section 2A</p> |  |  |
| |  |  |

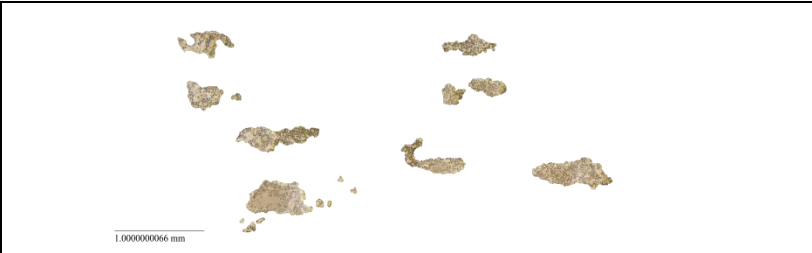

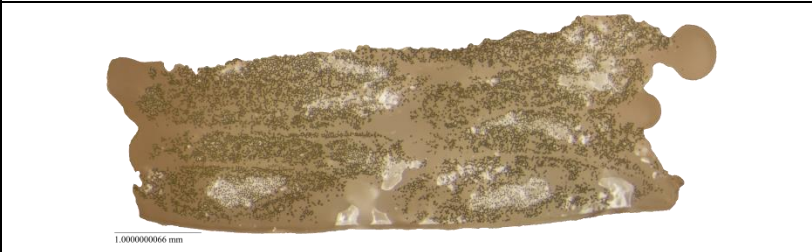
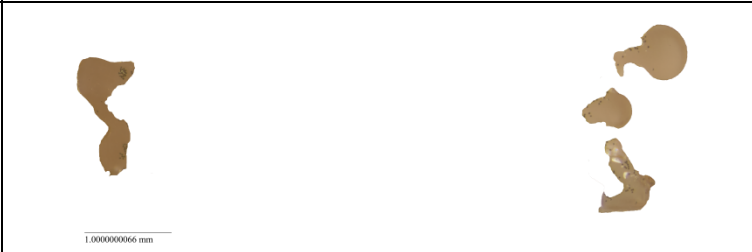


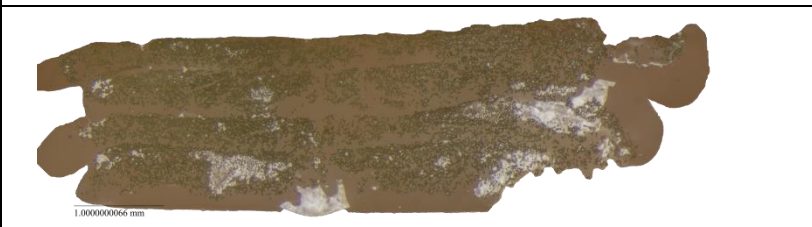



| | | |
|--------------------------------|--|---|
| <p>Sample 4 Section 1</p> |  |  |
| |  |  |
| <p>Sample 4 Section 1A</p> |  |  |
| |  |  |
| <p>Sample 4 Section 2</p> |  |  |

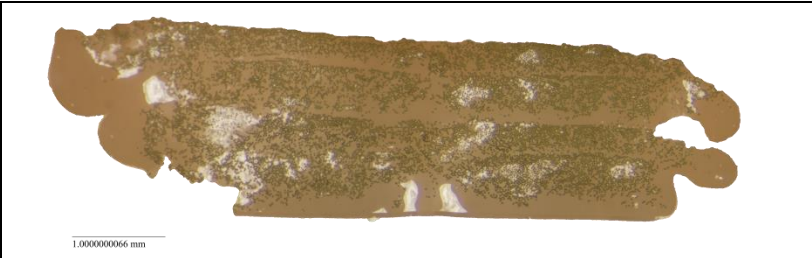
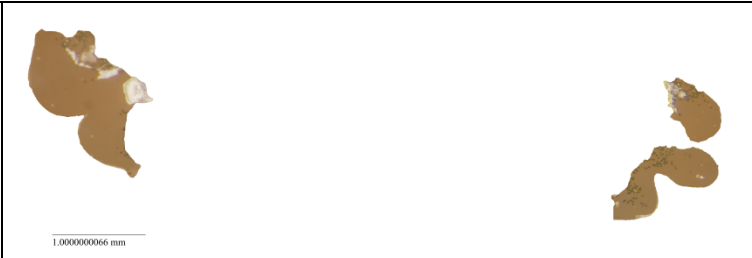


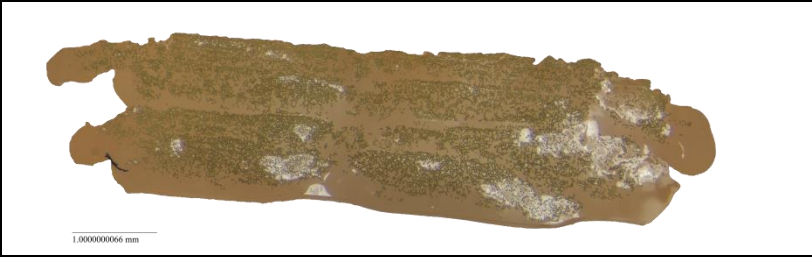
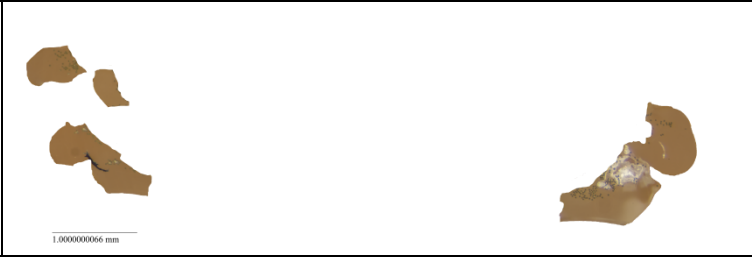


| | | |
|--------------------------------|--|--|
| |  <p>1.000000066 mm</p> |  <p>1.000000066 mm</p> |
| <p>Sample 4 Section 2A</p> |  |  |
| |  |  |
| <p>Sample 5 Section 1</p> |  <p>1.000000066 mm</p> |  <p>1.000000066 mm</p> |

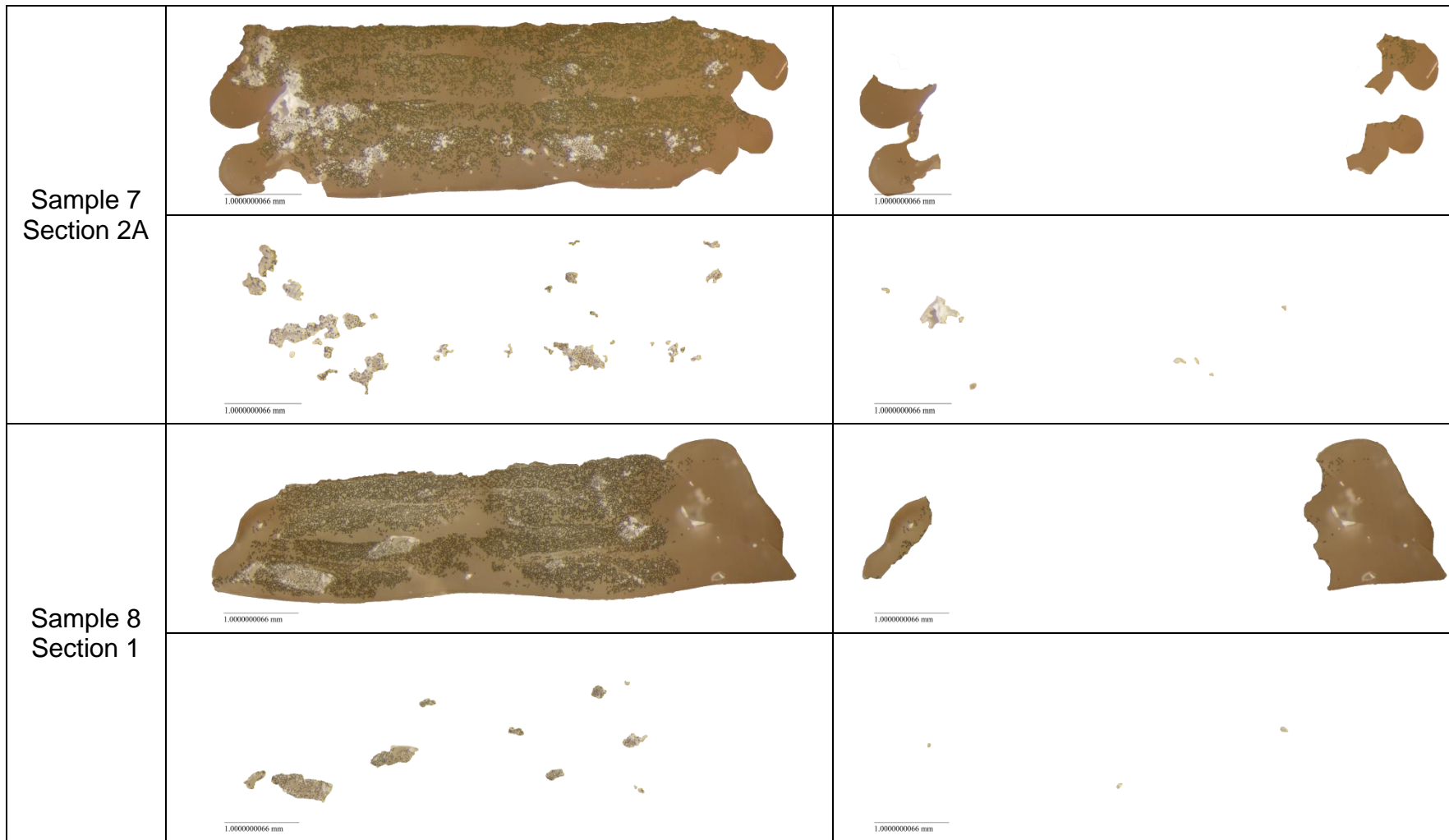
| | | |
|--------------------------------|---|--|
| |  |  |
| <p>Sample 5 Section 1A</p> |  |  |
| |  |  |
| <p>Sample 5 Section 2</p> |  |  |





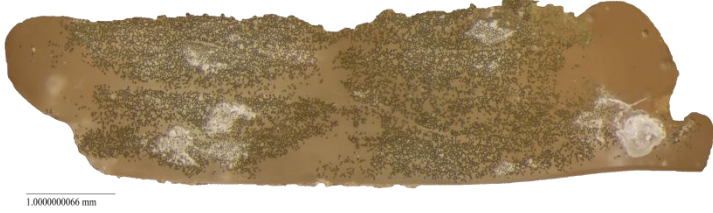


| | | |
|------------------------|---|--|
| |  |  |
| Sample 5 Section 2A |  |  |
| |  |  |
| Sample 6 Section 1 |  |  |

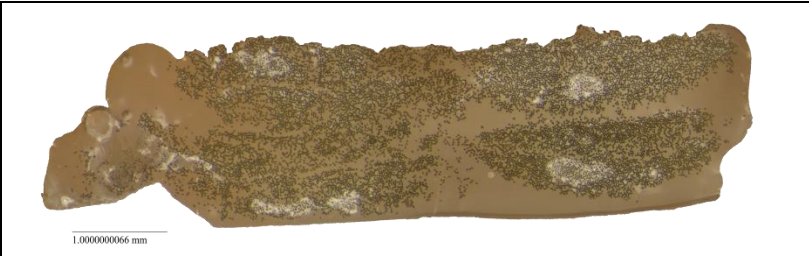
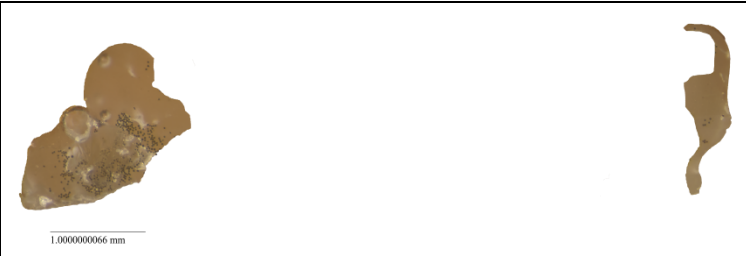

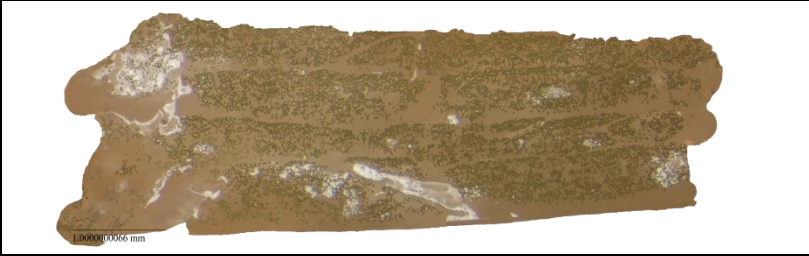
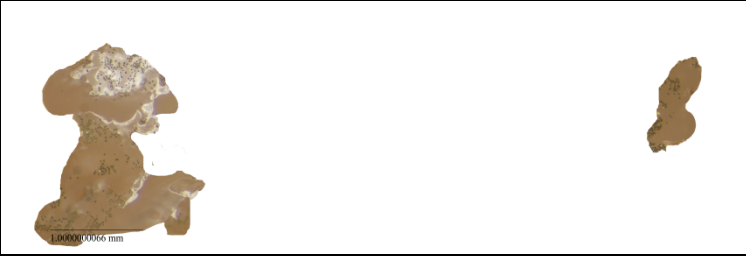


| | | |
|------------------------|---|--|
| |  |  |
| Sample 6 Section 1A |  |  |
| |  |  |
| Sample 6 Section 2 |  |  |

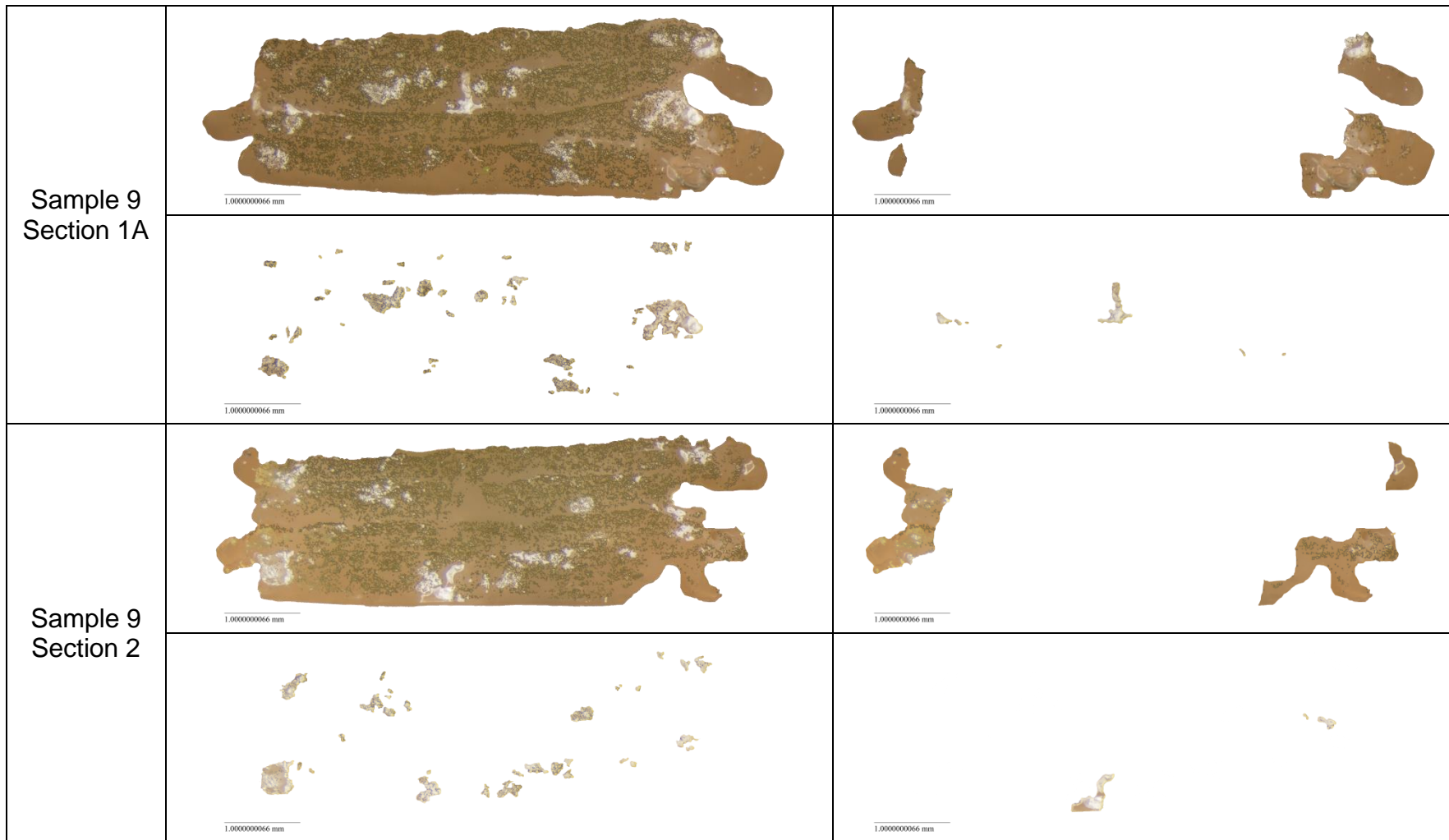
| | | |
|------------------------|--|---|
| |  |  |
| Sample 6 Section 2A |  |  |
| |  |  |
| Sample 7 Section 1 |  |  |
| |  |  |

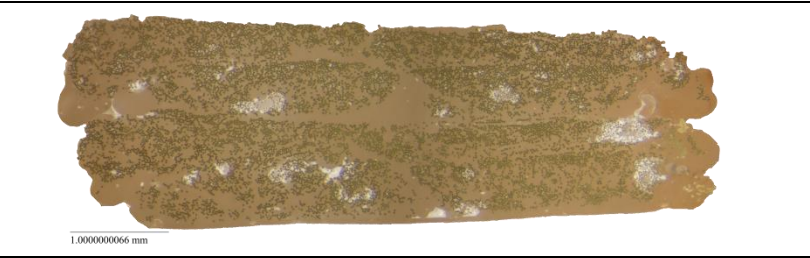
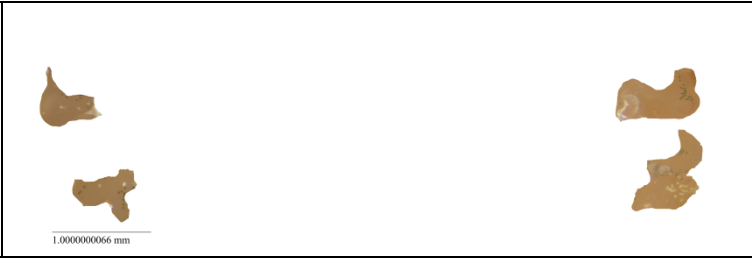


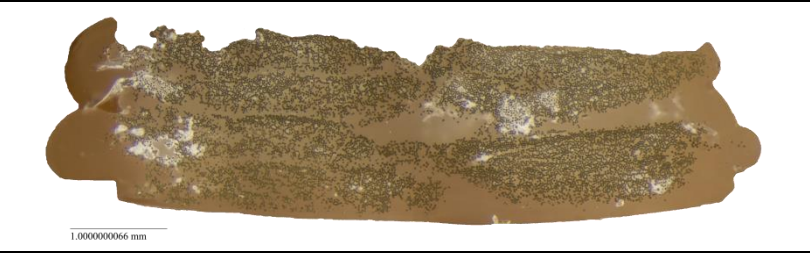
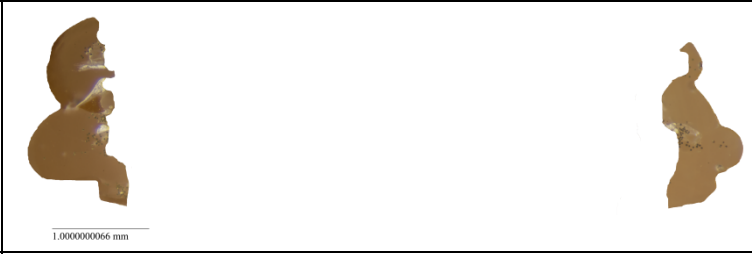


| | | |
|------------------------|---|--|
| Sample 7 Section 1A |  |  |
| |  |  |
| Sample 7 Section 2 |  |  |
| |  |  |

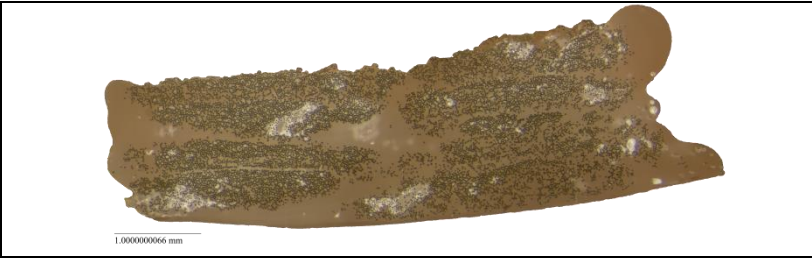
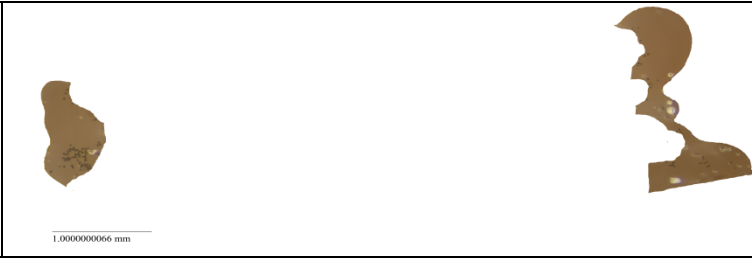



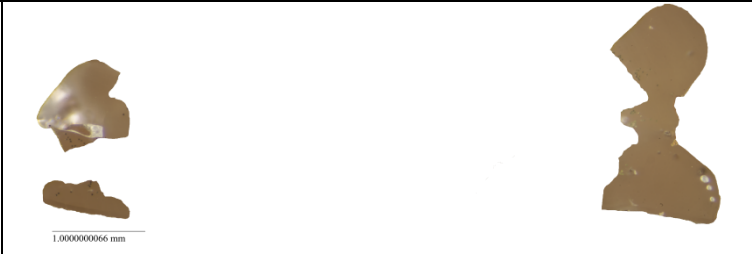



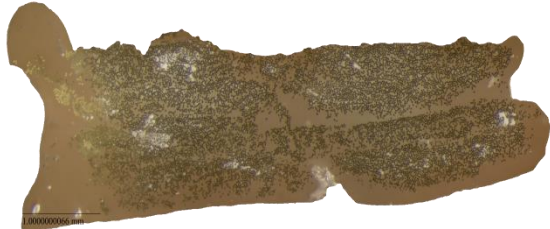



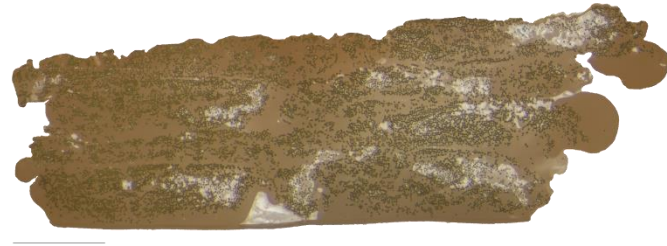



| | | |
|------------------------|--|---|
| Sample 8 Section 1A |  |  |
| |  |  |
| Sample 8 Section 2 |  |  |
| |  | N/A |

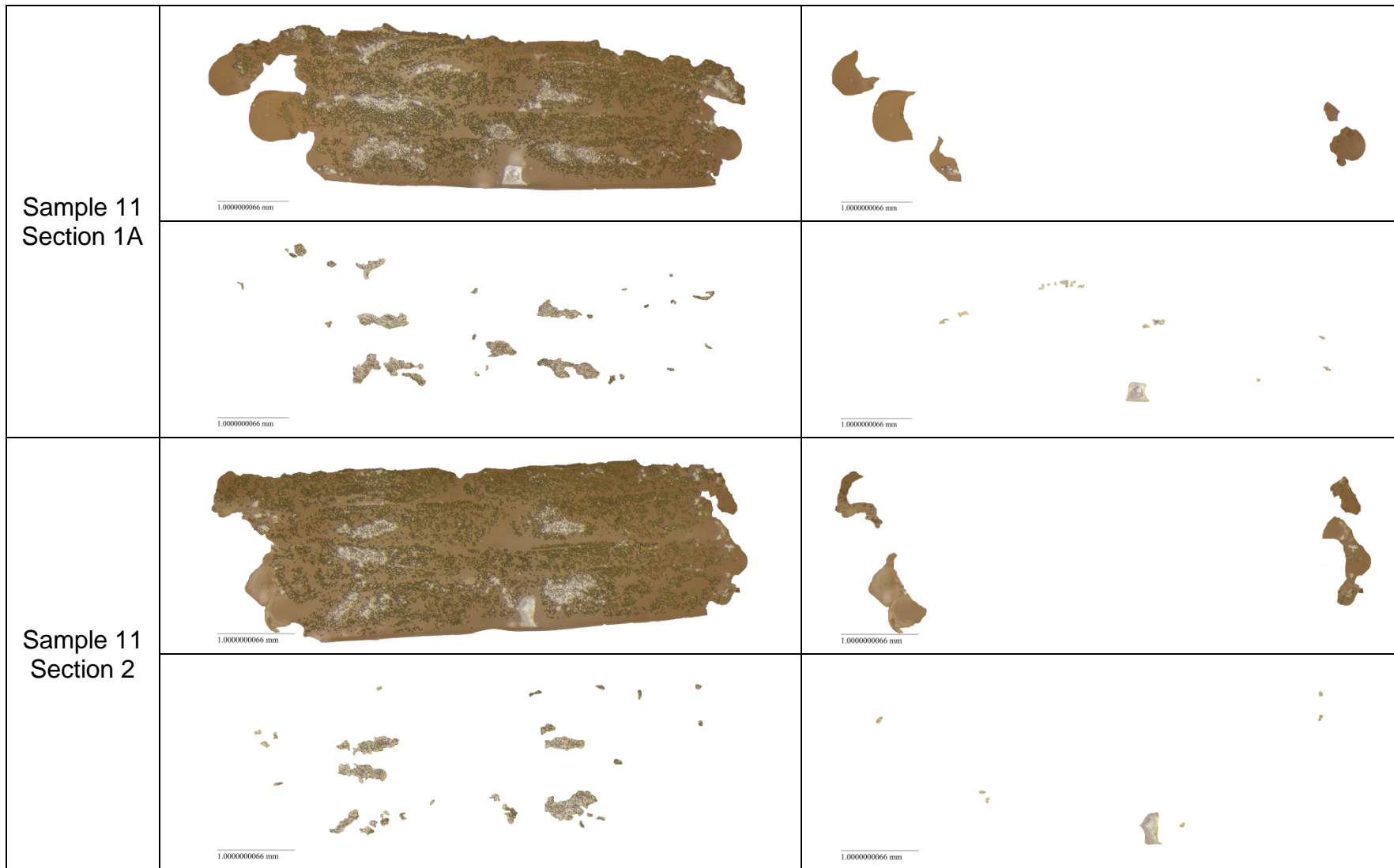
| | | |
|------------------------|---|--|
| Sample 8 Section 2A |  |  |
| |  | N/A |
| Sample 9 Section 1 |  |  |
| |  |  |

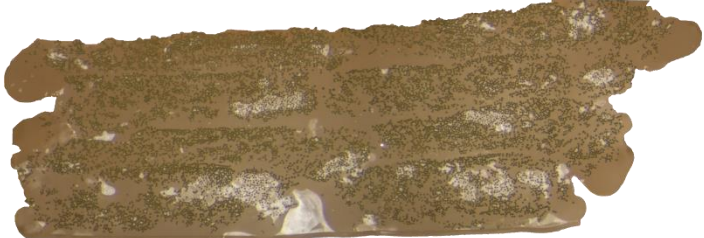



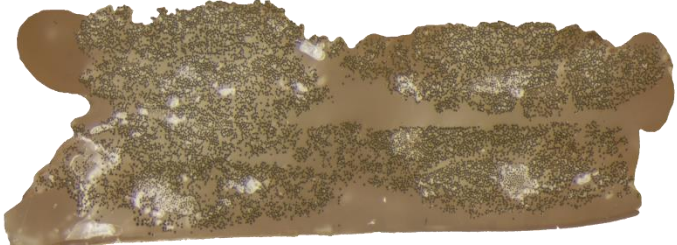





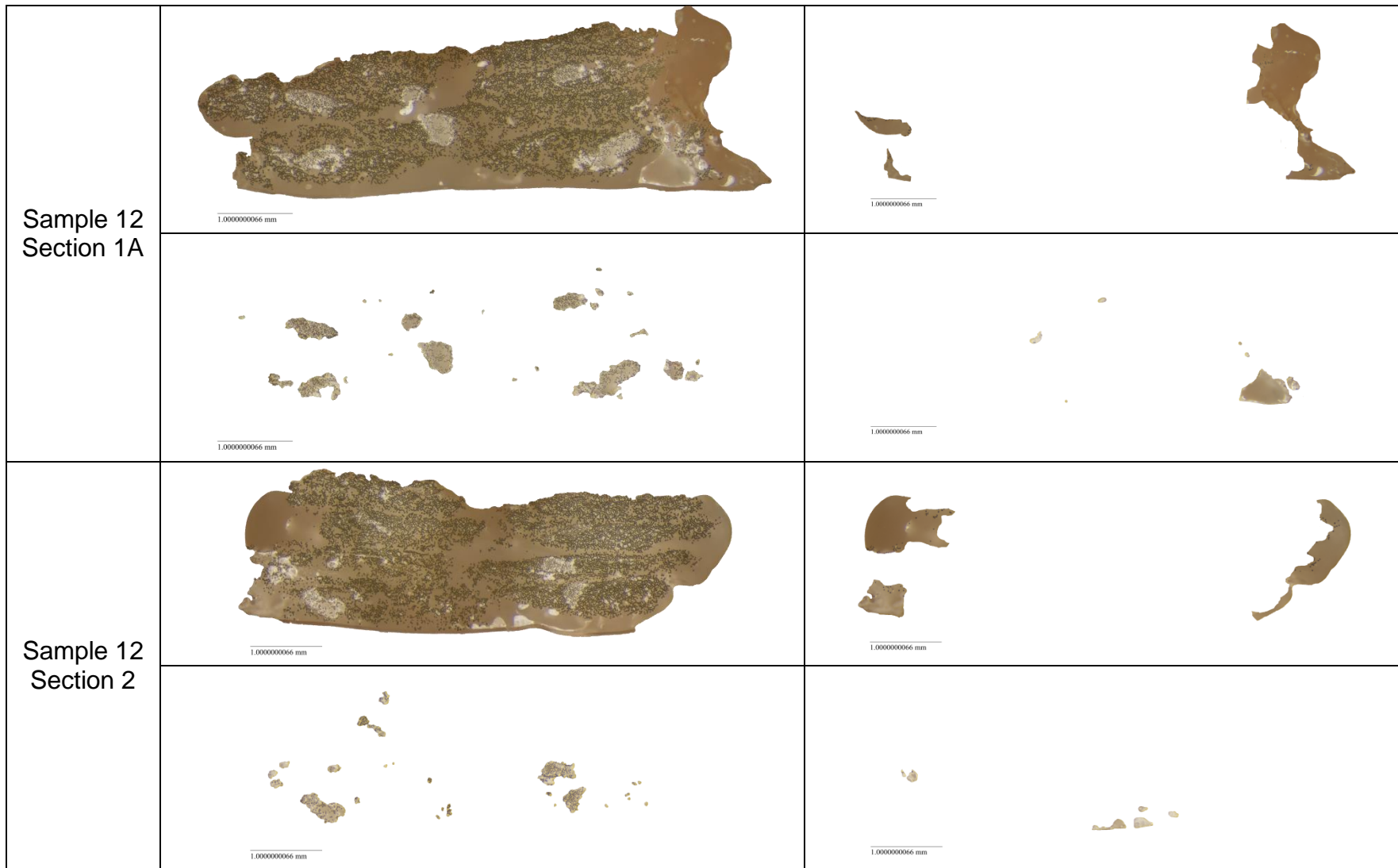
| | | |
|------------------------|---|--|
| Sample 9 Section 2A |  |  |
| |  |  |
| Sample 10 Section 1 |  |  |
| |  |  |

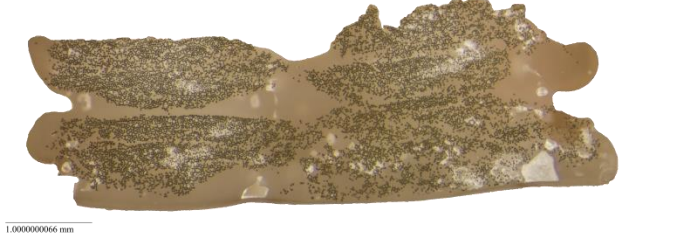



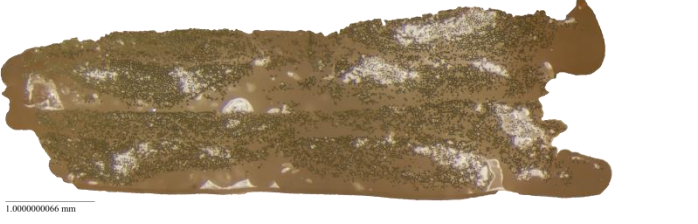



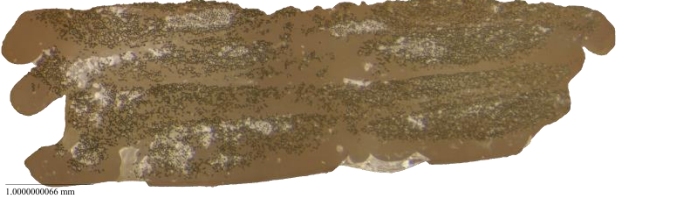

| | | |
|-------------------------|---|---|
| Sample 10 Section 1A |  |  |
| |  |  |
| Sample 10 Section 2 |  |  |
| |  | N/A |



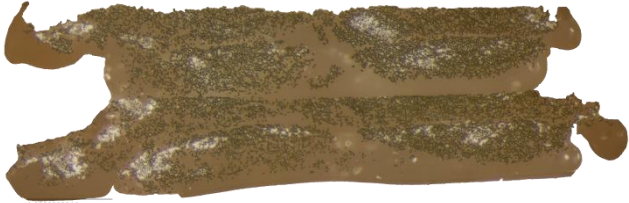


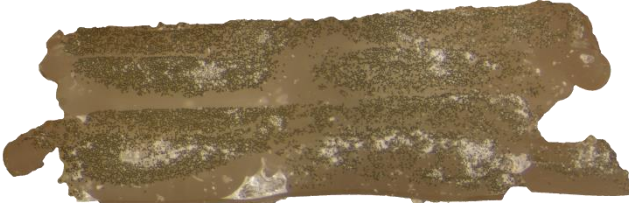



| | | |
|---------------------------------|---|---|
| <p>Sample 10 Section 2A</p> |  |  |
| |  |  |
| <p>Sample 11 Section 1</p> |  |  |
| |  |  |








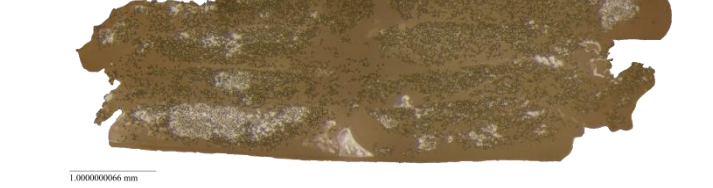



| | | |
|---------------------------------|--|---|
| <p>Sample 11 Section 2A</p> |  |  |
| |  |  |
| <p>Sample 12 Section 1</p> |  |  |
| |  |  |

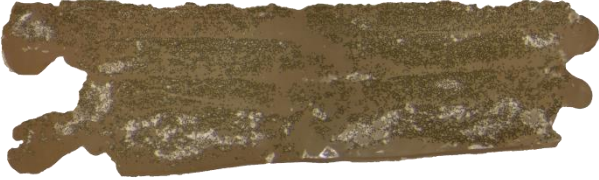



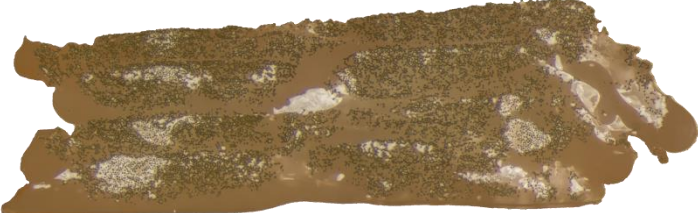





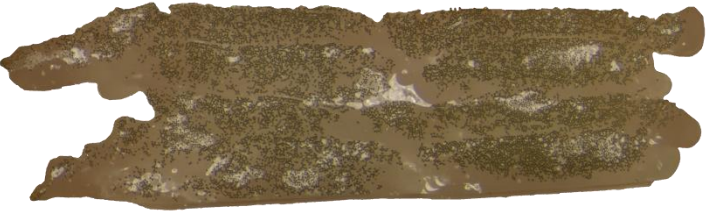



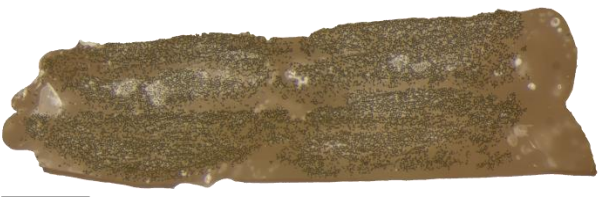



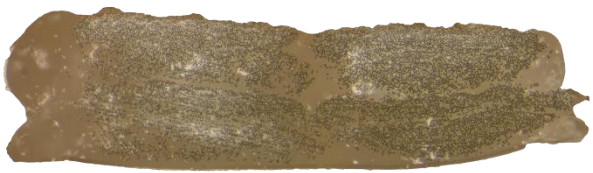

| | | |
|---------------------------------|--|---|
| <p>Sample 12 Section 2A</p> |  |  |
| |  |  |
| <p>Sample 13 Section 1</p> |  |  |
| |  |  |
| <p>Sample 13 Section 1A</p> |  |  |

| | | |
|---------------------------------|--|---|
| |  |  |
| <p>Sample 13 Section 2</p> |  |  |
| |  | <p>N/A</p> |
| <p>Sample 13 Section 2A</p> |  |  |
| |  |  |

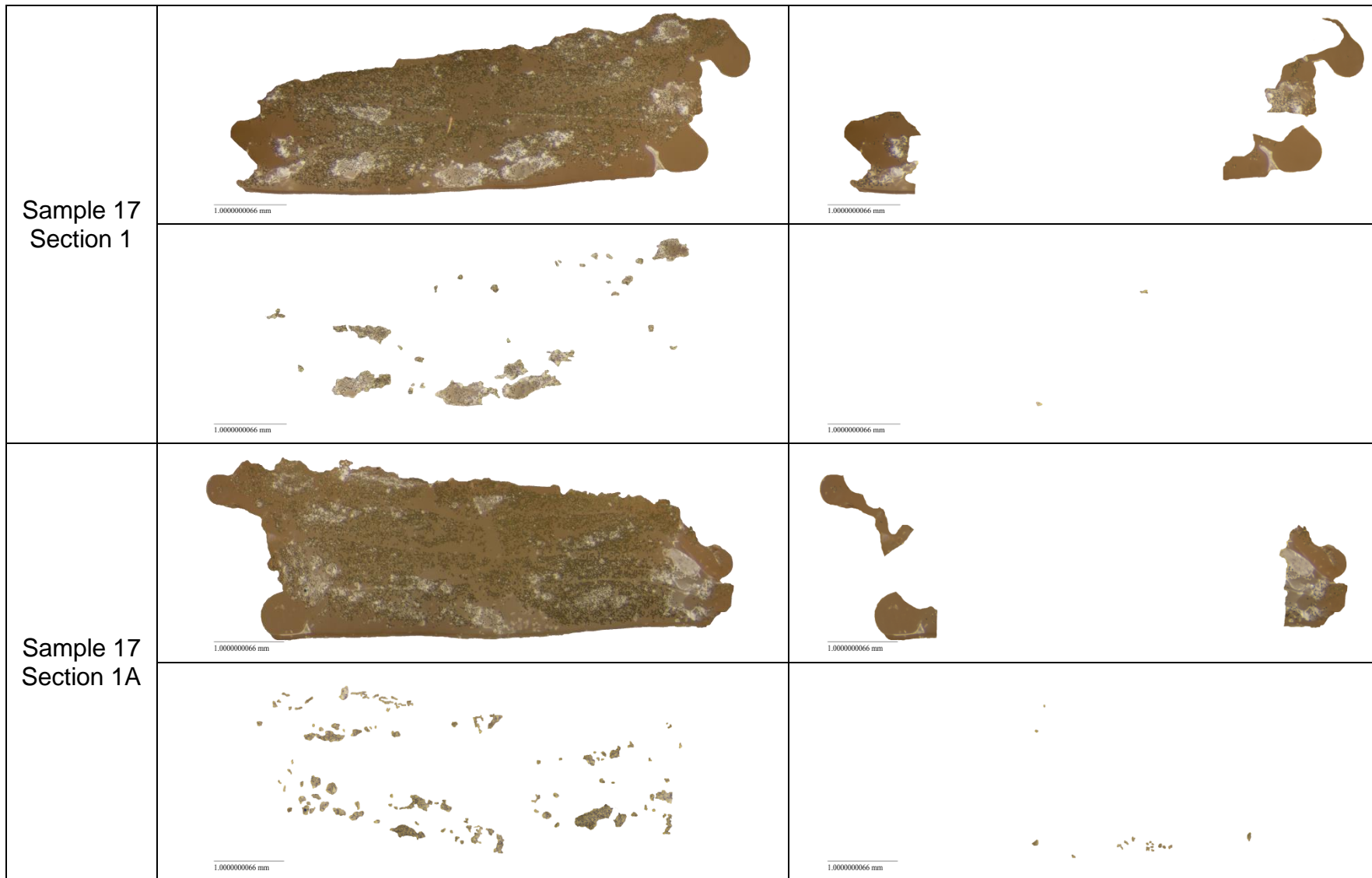
| | | |
|---------------------------------|--|---|
| <p>Sample 14 Section 1</p> |  |  |
| |  |  |
| <p>Sample 14 Section 1A</p> |  |  |
| |  |  |
| <p>Sample 14 Section 2</p> |  |  |

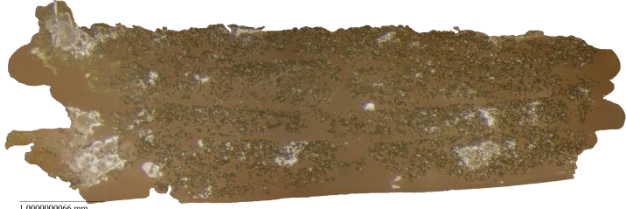



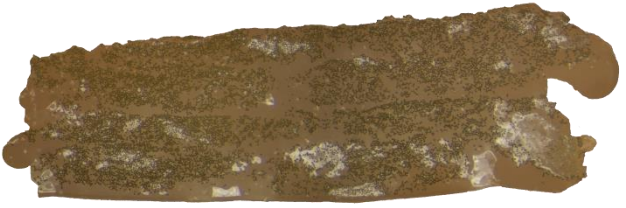



| | | |
|---------------------------------|--|---|
| |  | <p>N/A</p> |
| <p>Sample 14 Section 2A</p> |  |  |
| |  |  |
| <p>Sample 15 Section 1</p> |  |  |
| |  |  |

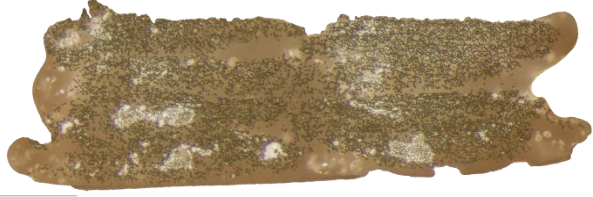



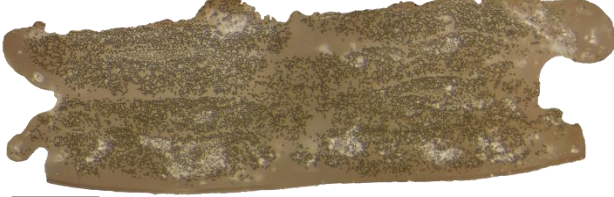



| | | |
|-------------------------|---|--|
| Sample 15 Section 1A |  |  |
| |  |  |
| Sample 15 Section 2 |  1.000000066 mm |  1.000000066 mm |
| |  1.000000066 mm |  1.000000066 mm |

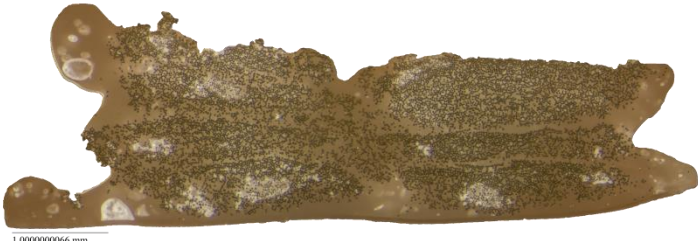







| | | |
|---------------------------------|--|---|
| <p>Sample 15 Section 2A</p> |  |  |
| |  |  |
| <p>Sample 16 Section 1</p> |  <p>1.000000066 mm</p> |  <p>1.000000066 mm</p> |
| |  <p>1.000000066 mm</p> |  <p>1.000000066 mm</p> |
| <p>Sample 16 Section 1A</p> |  <p>1.000000066 mm</p> |  <p>1.000000066 mm</p> |

| | | |
|-------------------------|--|---|
| |  |  |
| Sample 16 Section 2 |  |  |
| |  |  |
| Sample 16 Section 2A |  |  |
| |  |  |



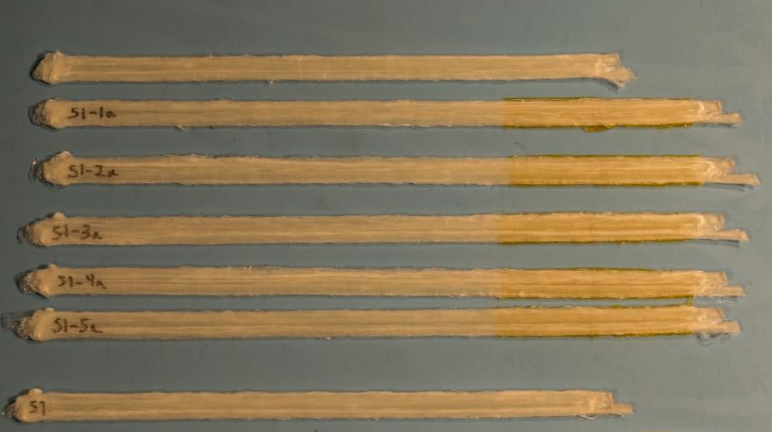
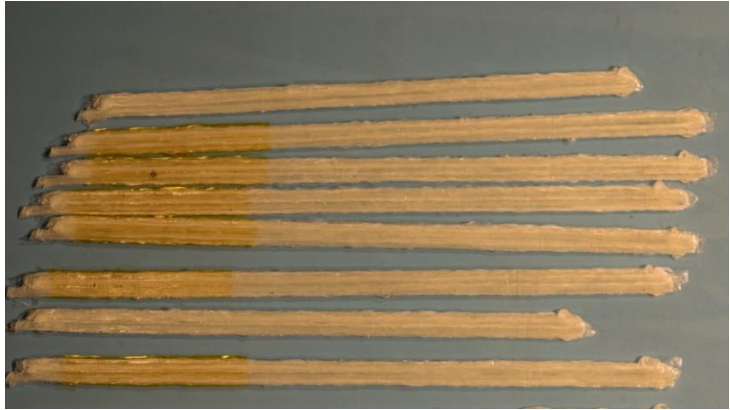
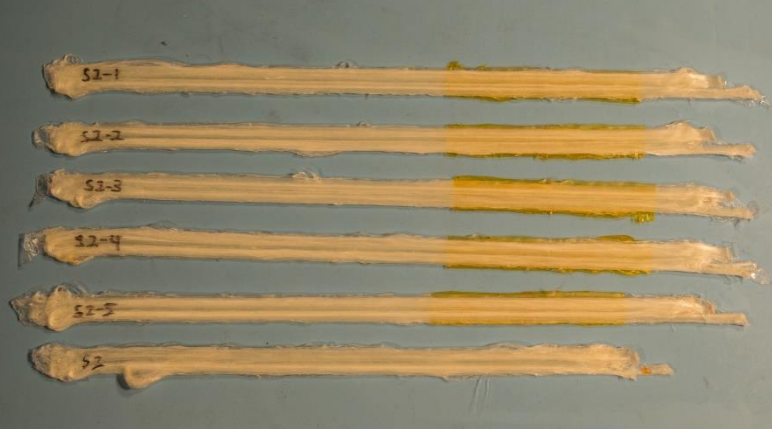

| | | |
|---------------------------------|--|---|
| <p>Sample 17 Section 2</p> |  |  |
| |  |  |
| <p>Sample 17 Section 2A</p> |  |  |
| |  |  |

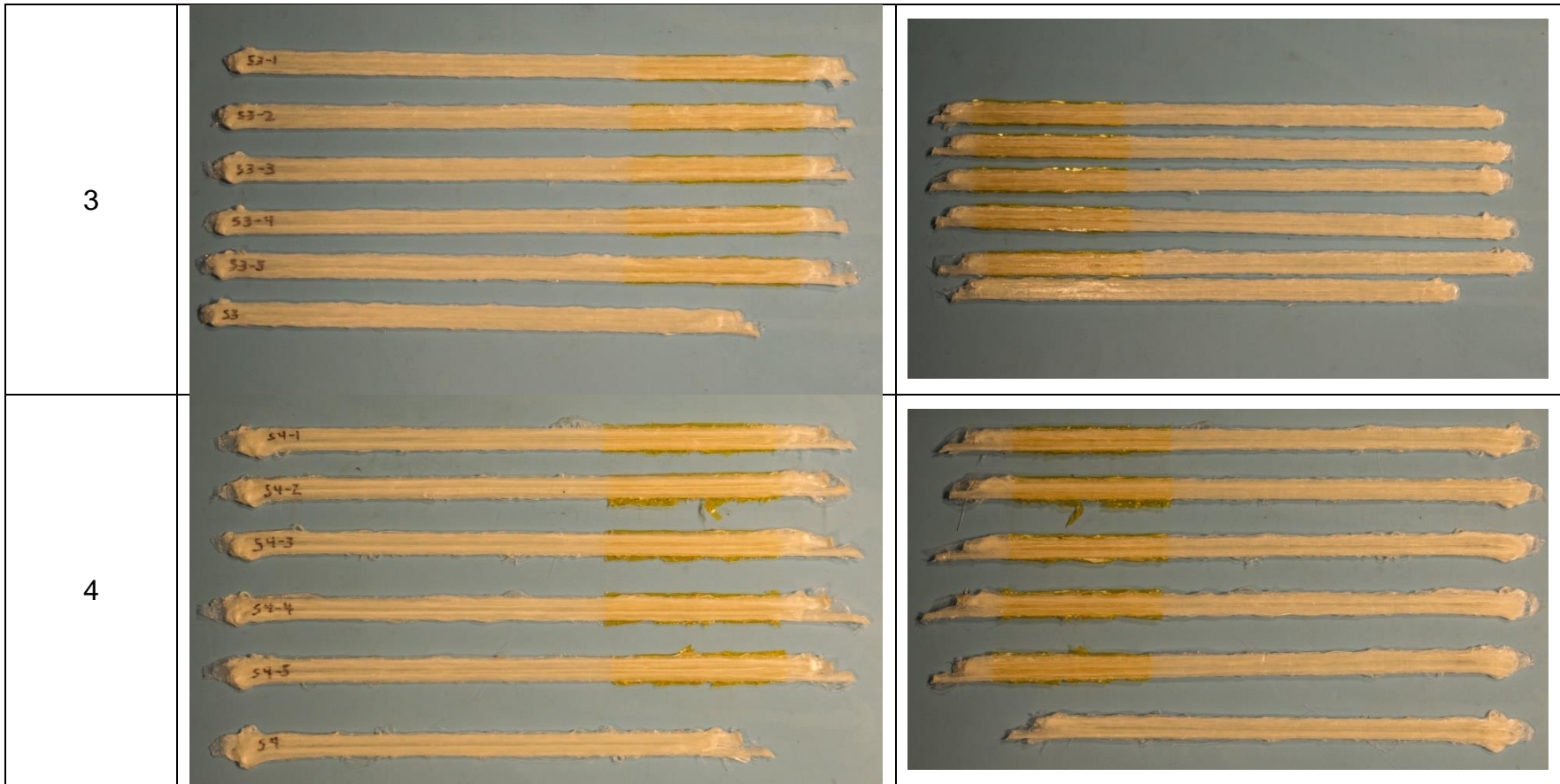
| | | |
|---------------------------------|--|---|
| <p>Sample 18 Section 1</p> |  |  |
| |  |  |
| <p>Sample 18 Section 1A</p> |  |  |
| |  |  |

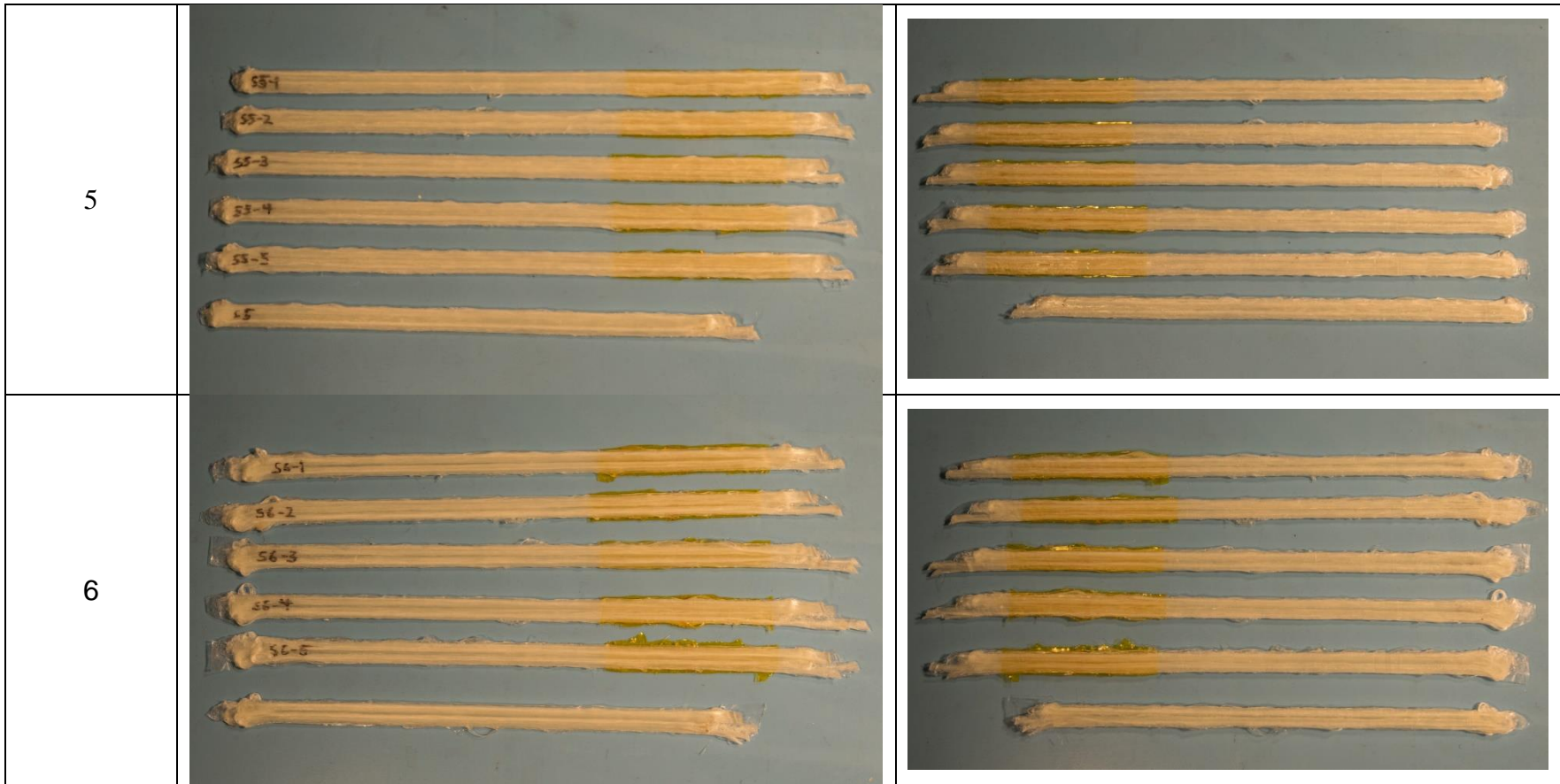
| | | |
|---------------------------------|--|---|
| <p>Sample 18 Section 2</p> |  |  |
| |  |  |
| <p>Sample 18 Section 2A</p> |  |  |
| |  |  |

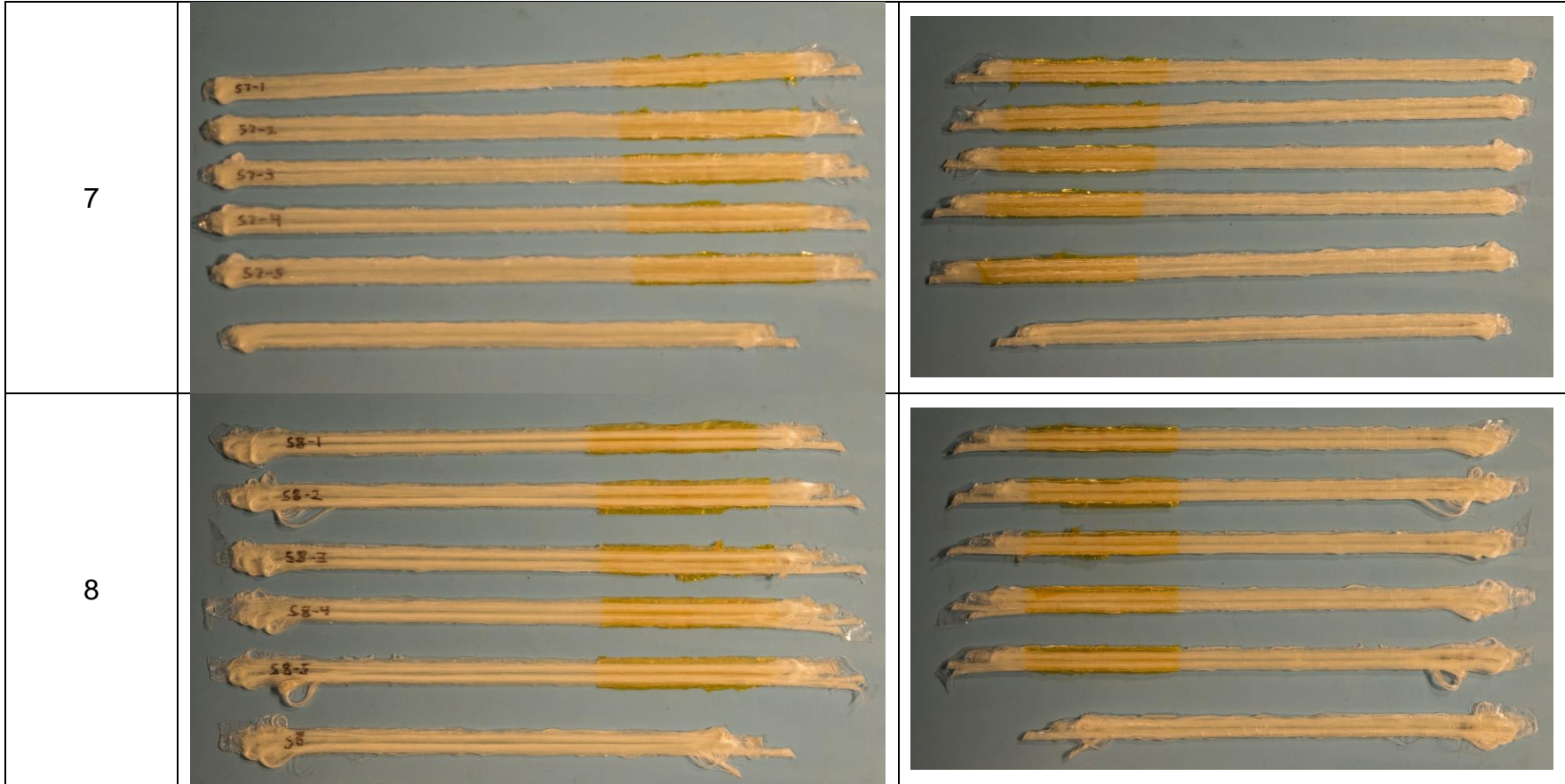
10.5 Composite Beam Specimen Pictures


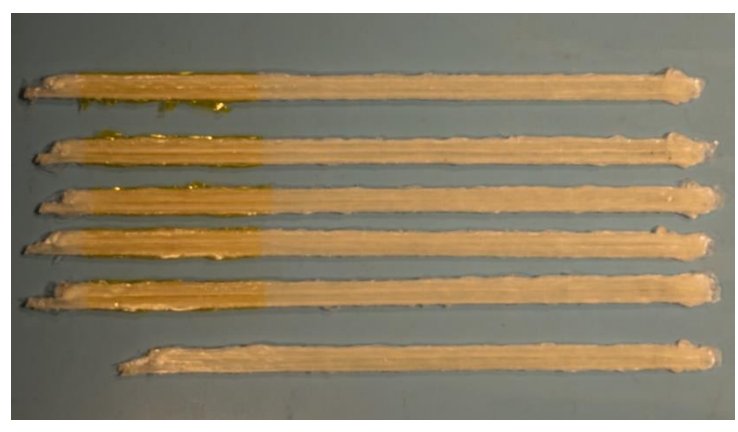
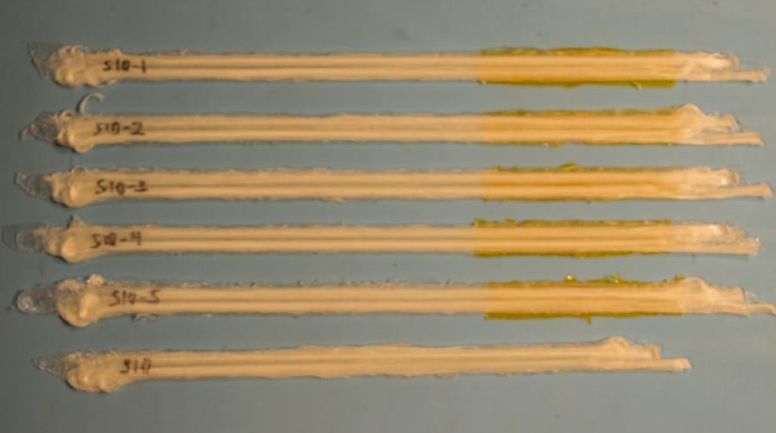
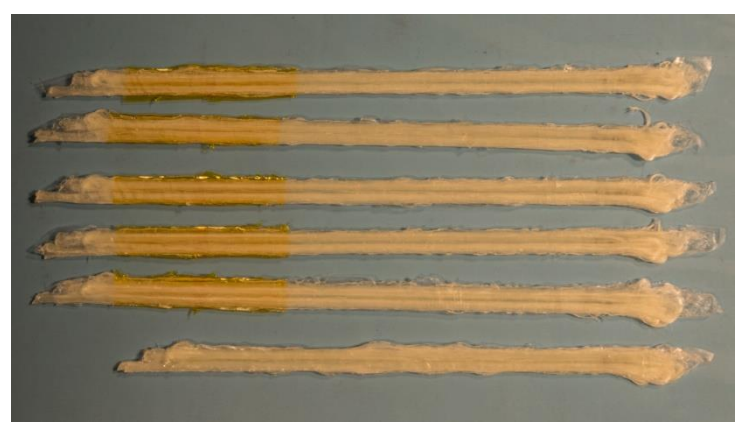
The following table displays all the composite beam specimens manufactured and used for either t-peel testing or microscopy analysis.

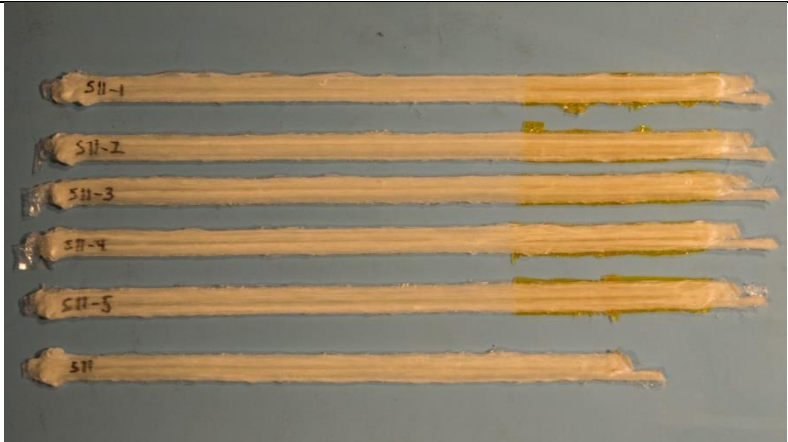
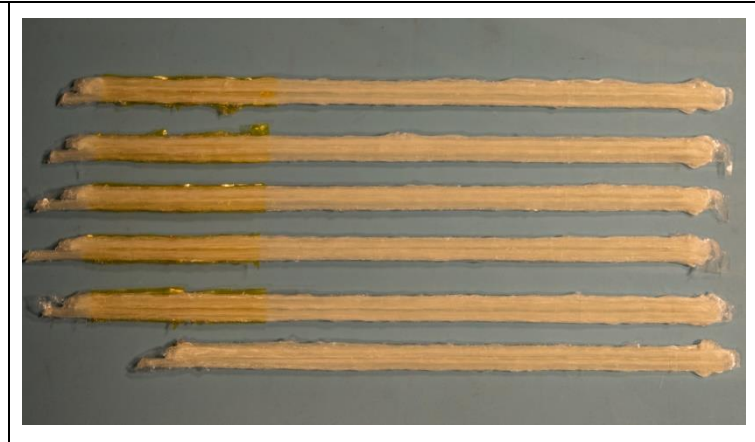
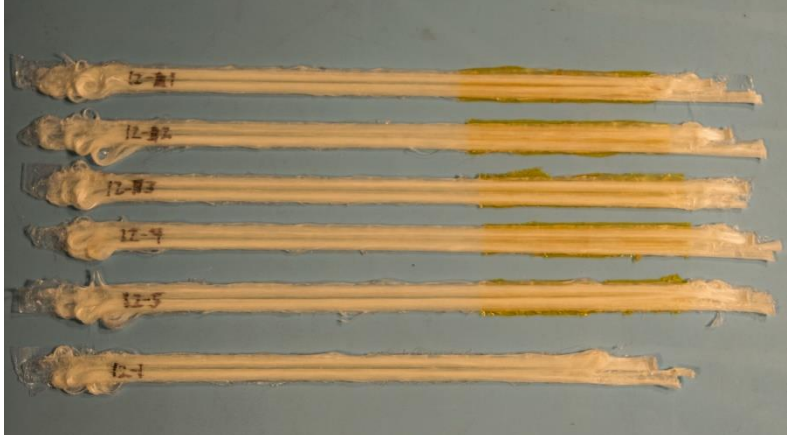
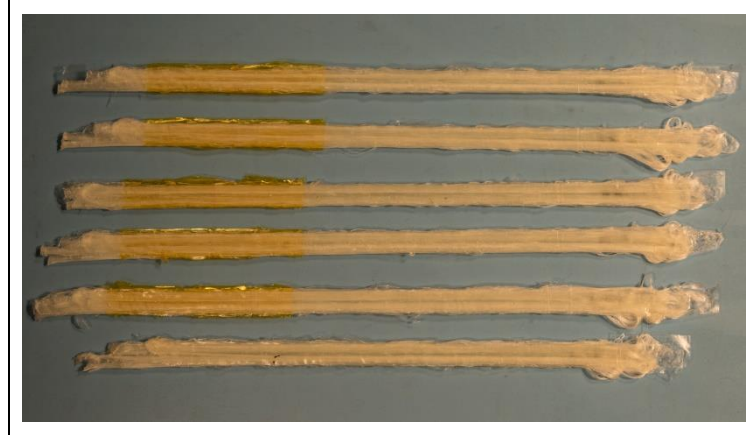
| Sample # | Front | Back |
|----------|---|--|
| 1 |  |  |
| 2 |  |  |

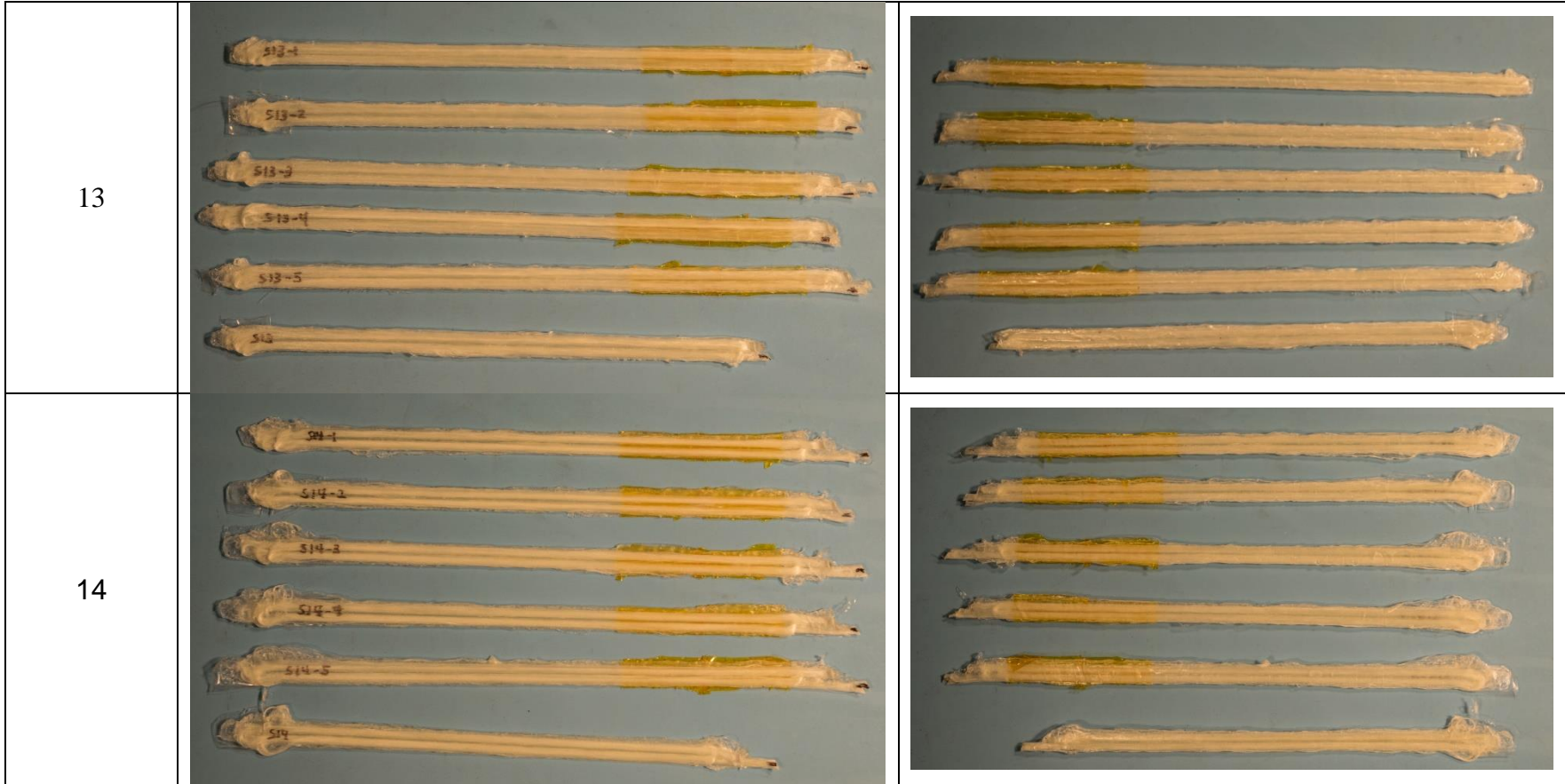



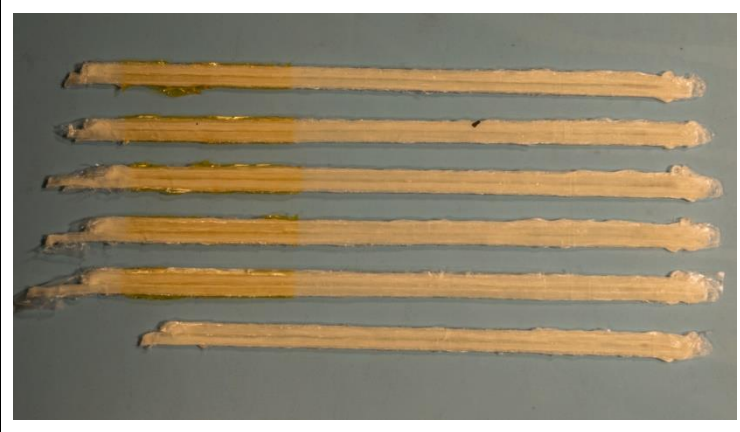

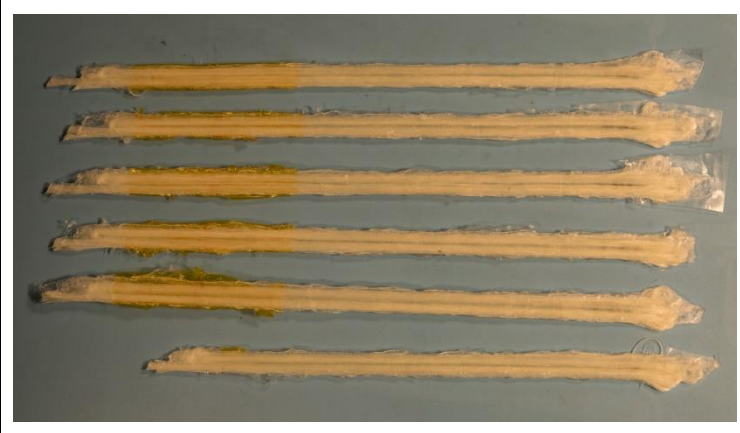


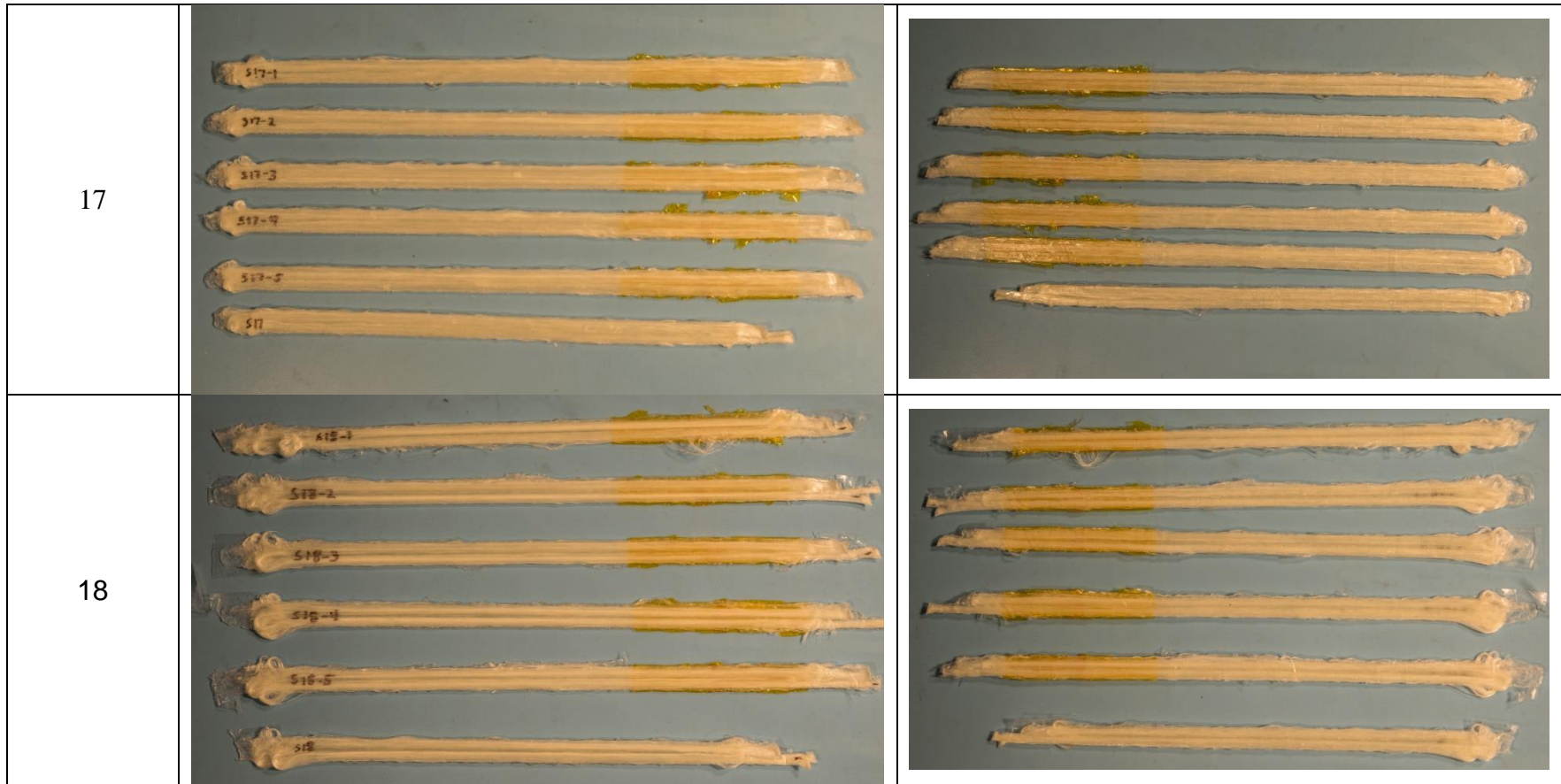


| | | |
|----|---|--|
| 9 |  |  |
| 10 |  |  |

| | | |
|----|---|--|
| 11 |  |  |
| 12 |  |  |

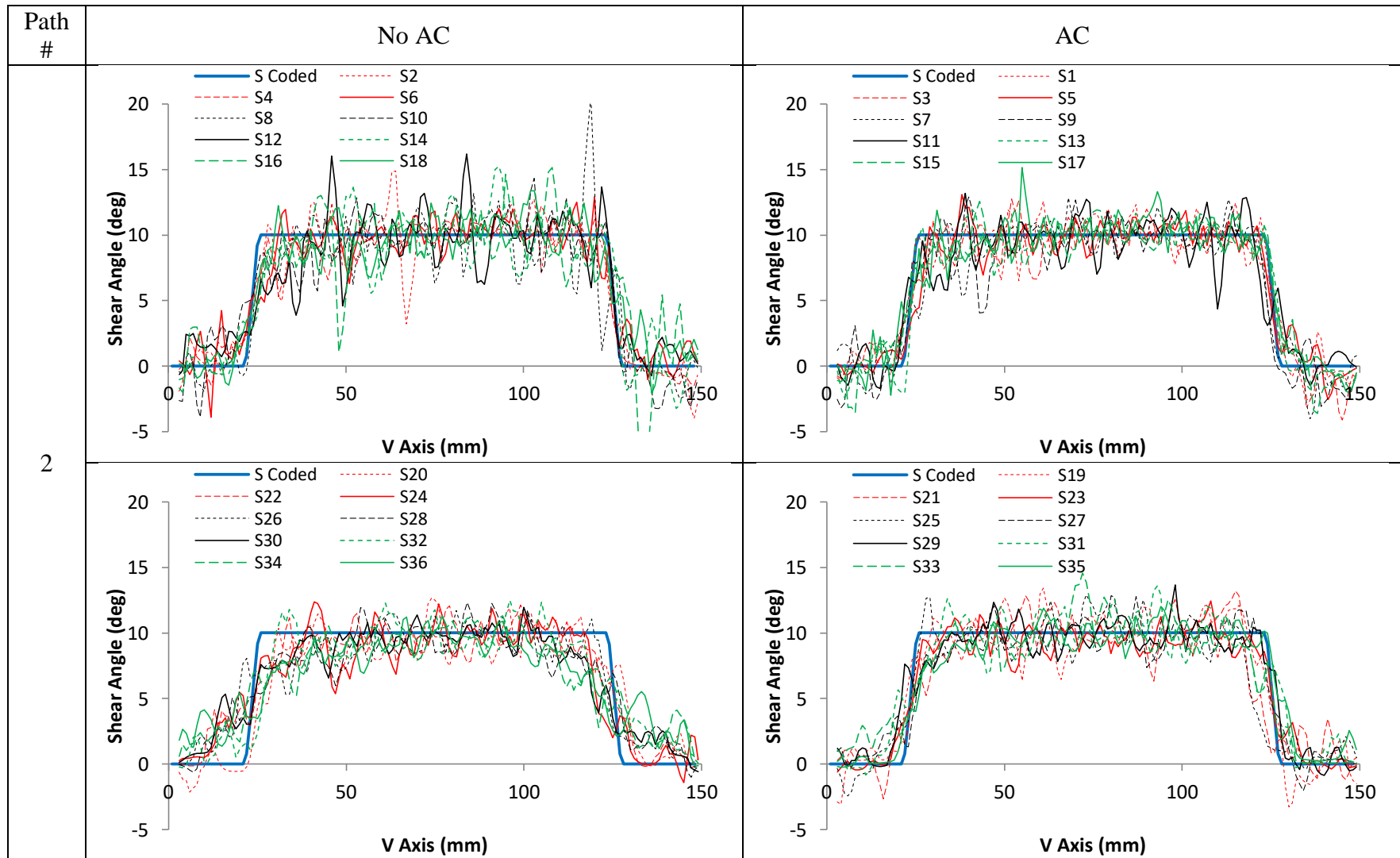


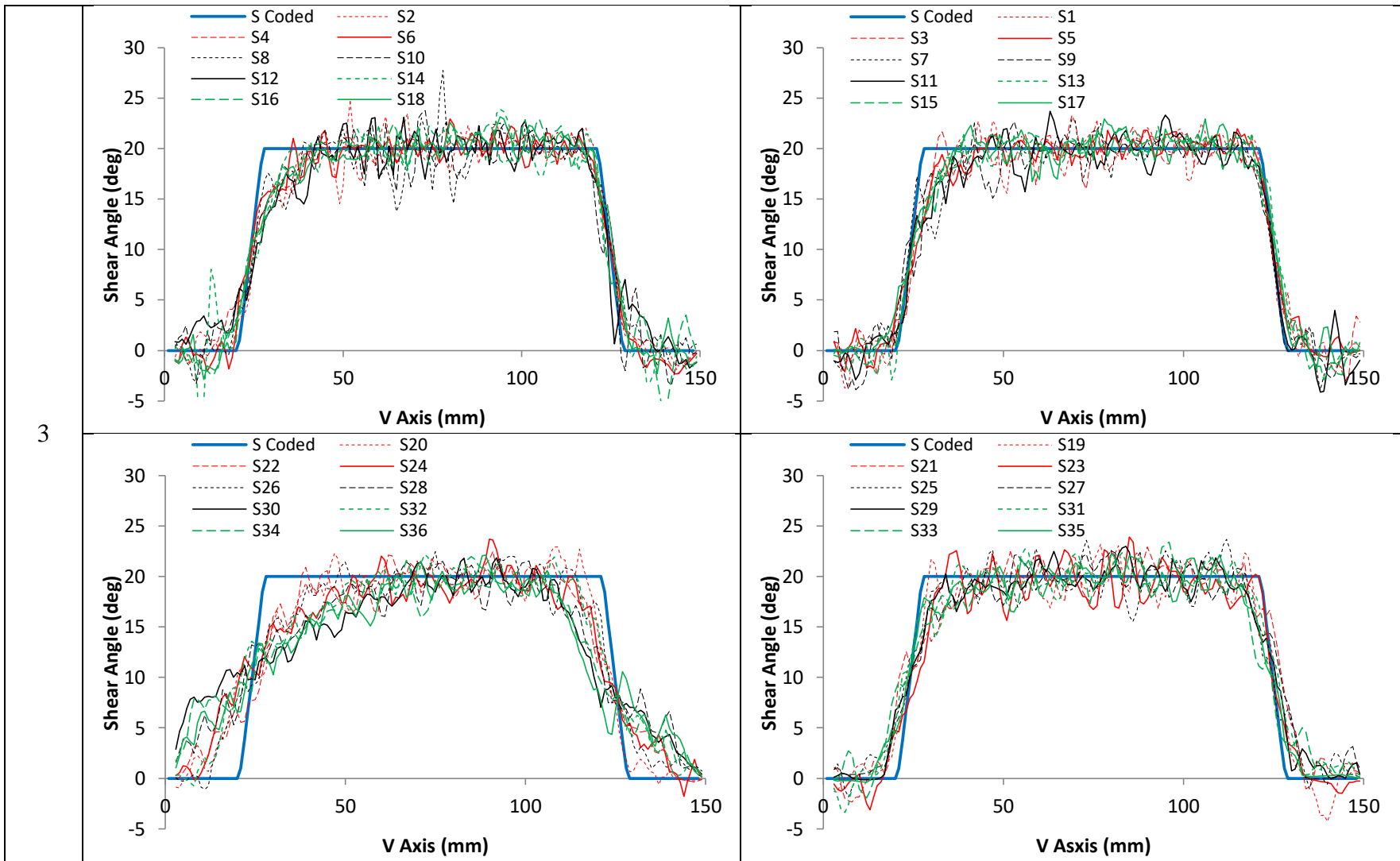
| | | |
|----|---|--|
| 15 |  |  |
| 16 |  |  |

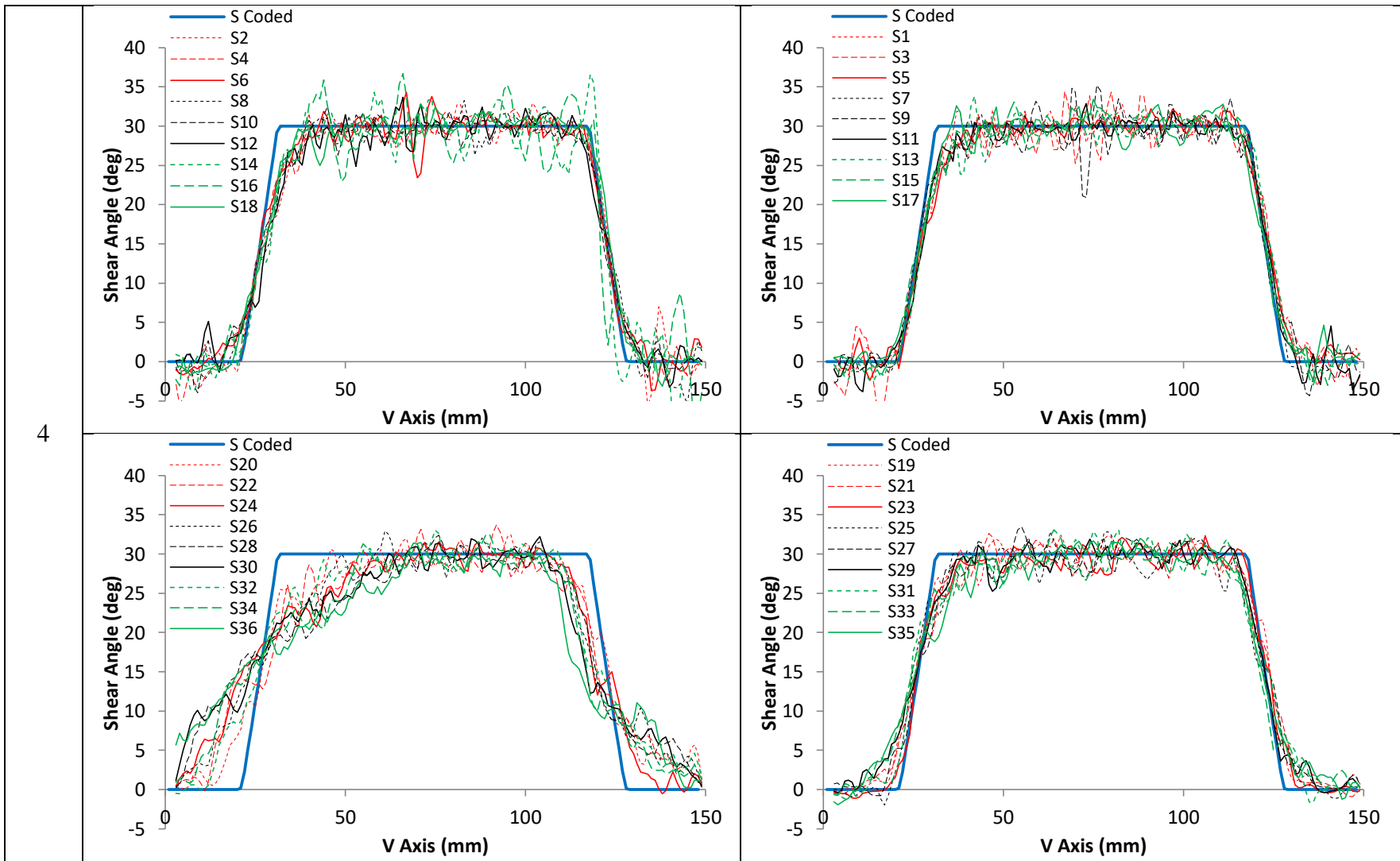


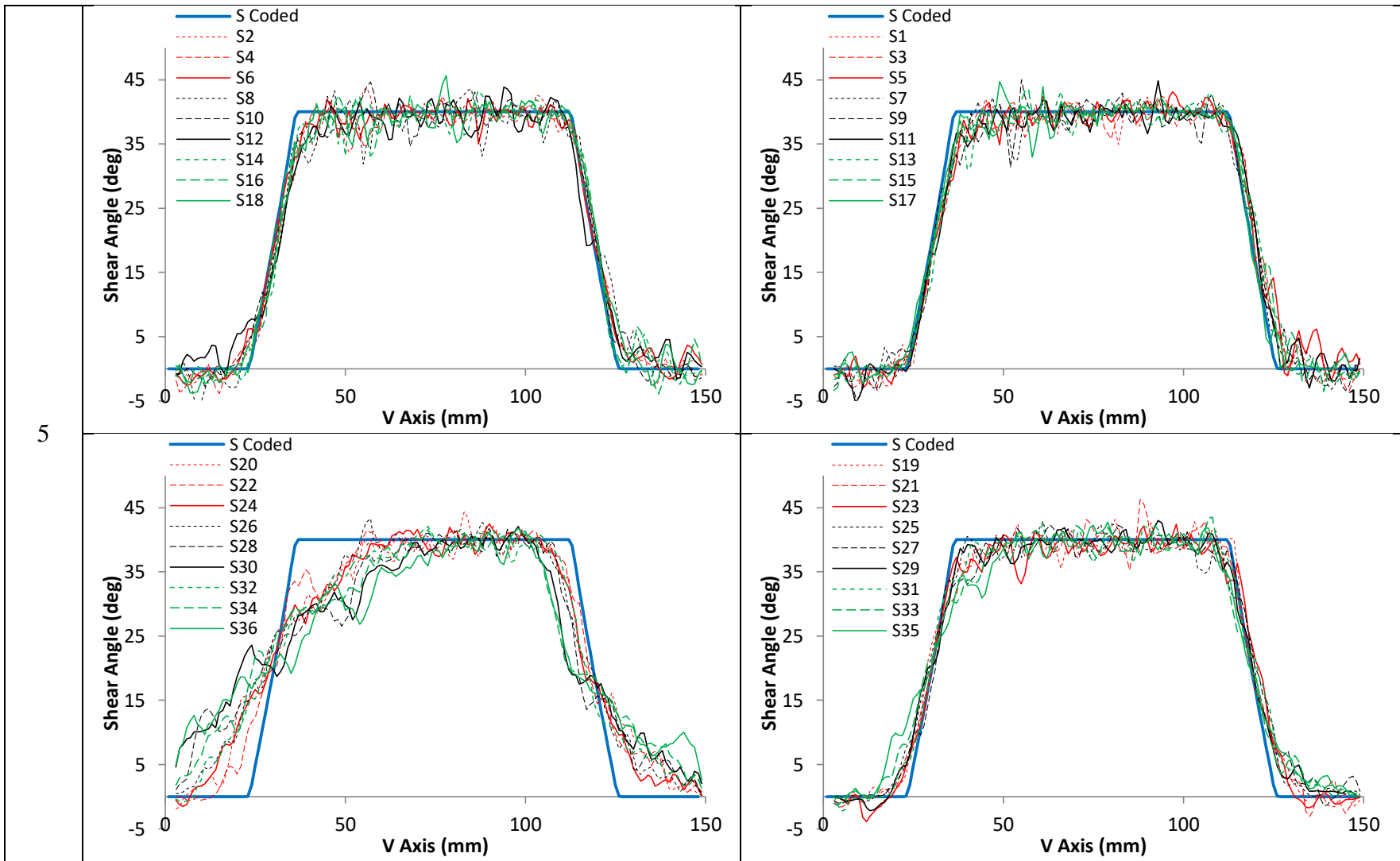
10.6 Shear Angle Graphs

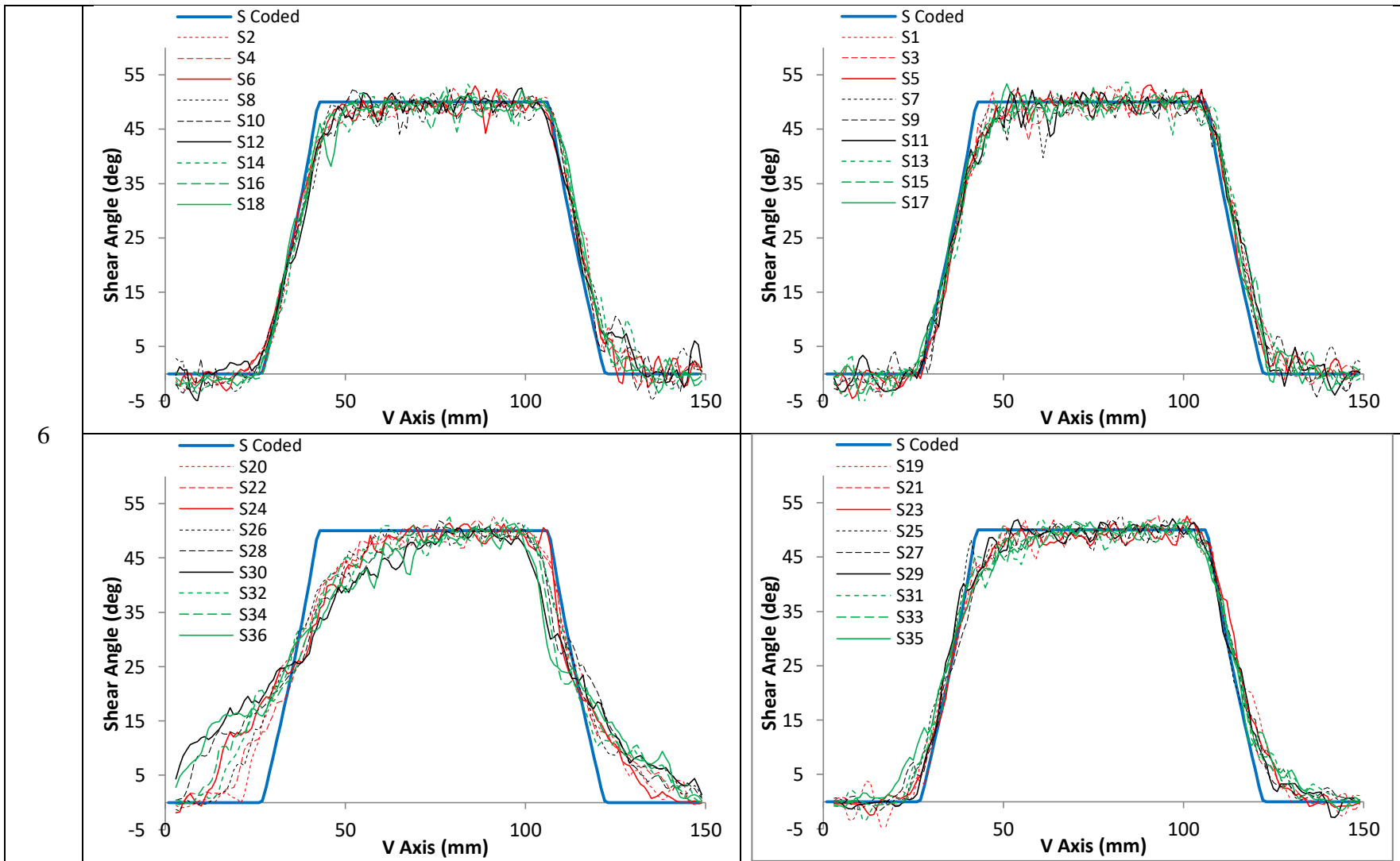
The following table displays additional shear angle results for each path analyzed as a part of the positional fidelity portion of this study.

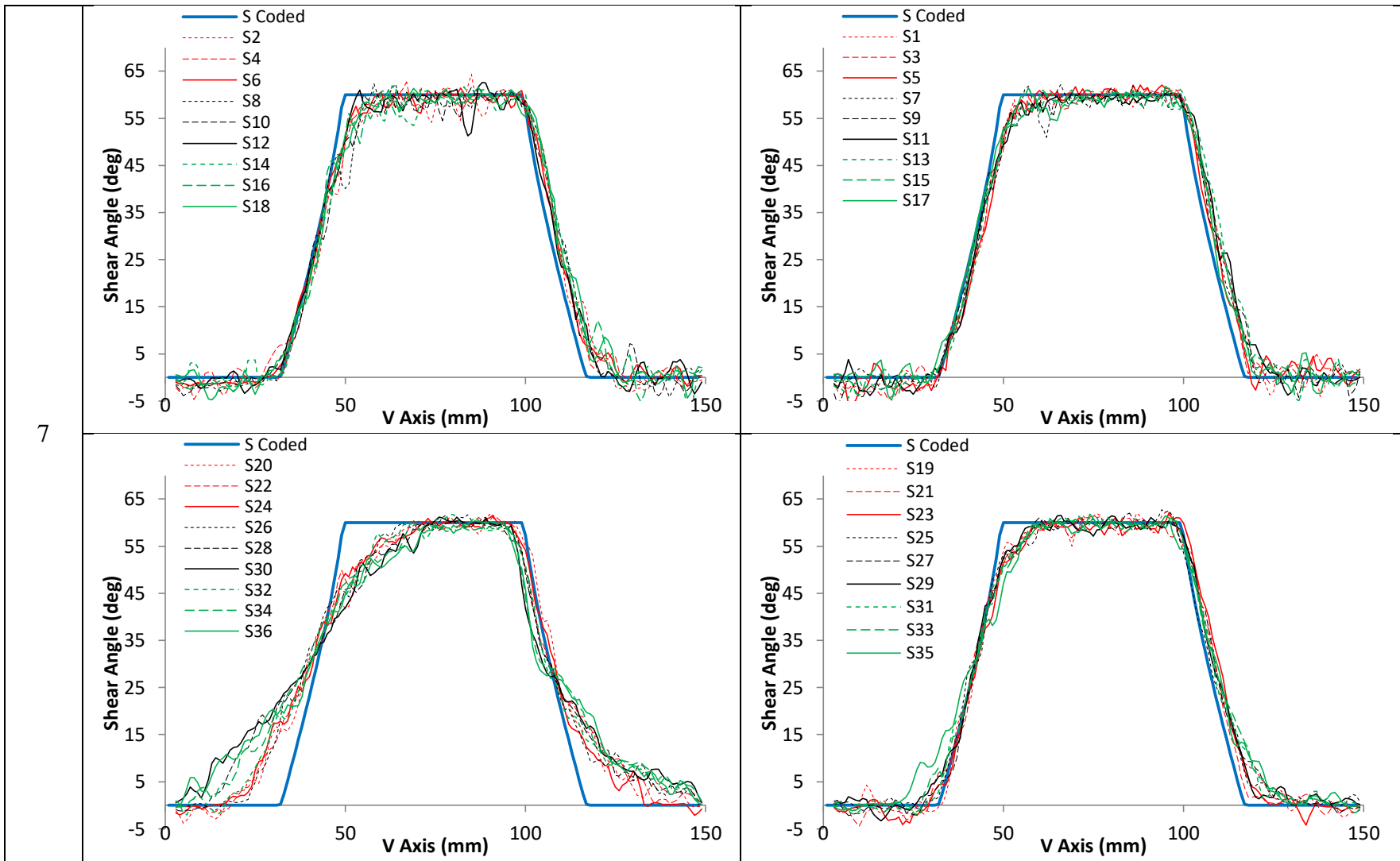


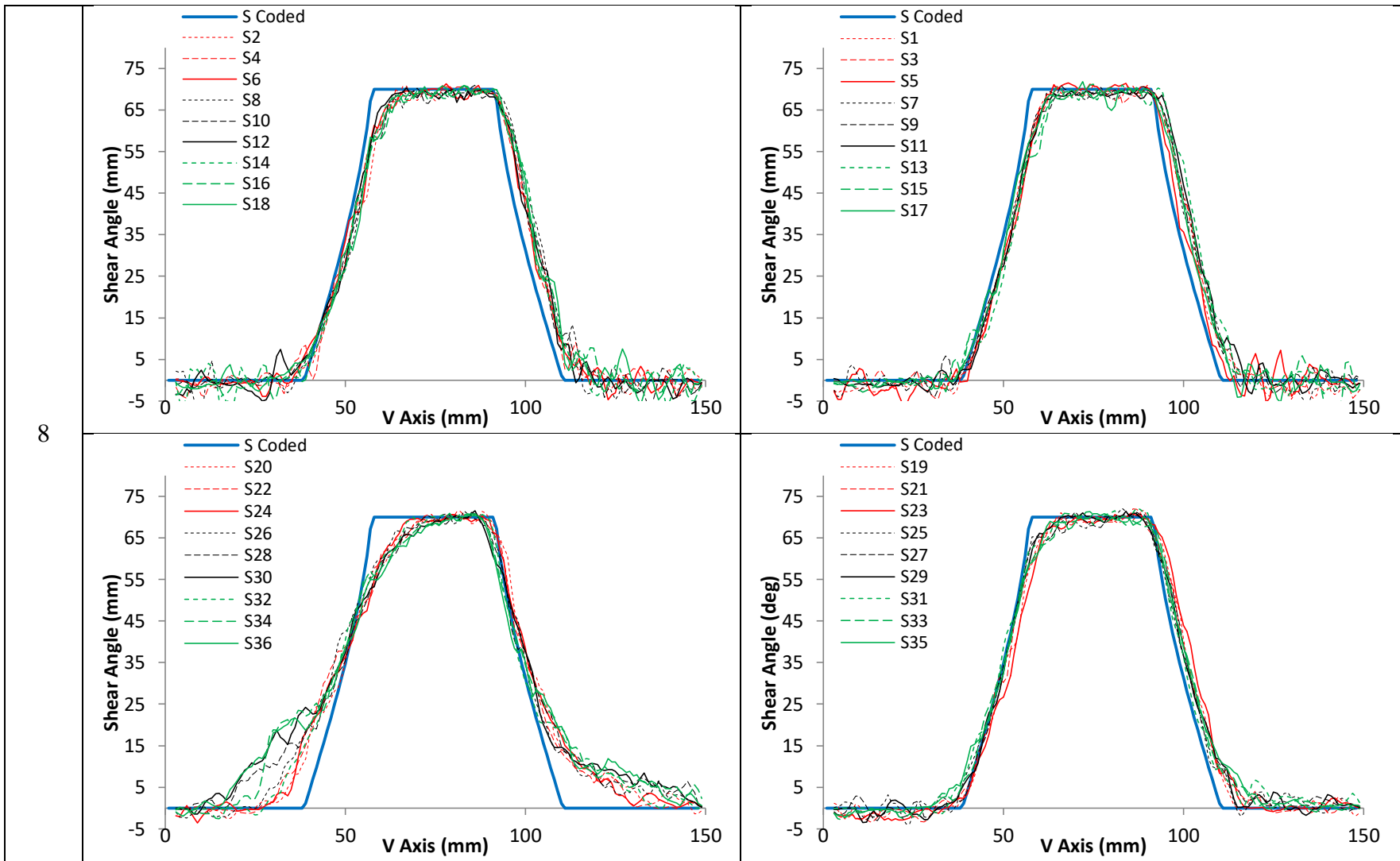






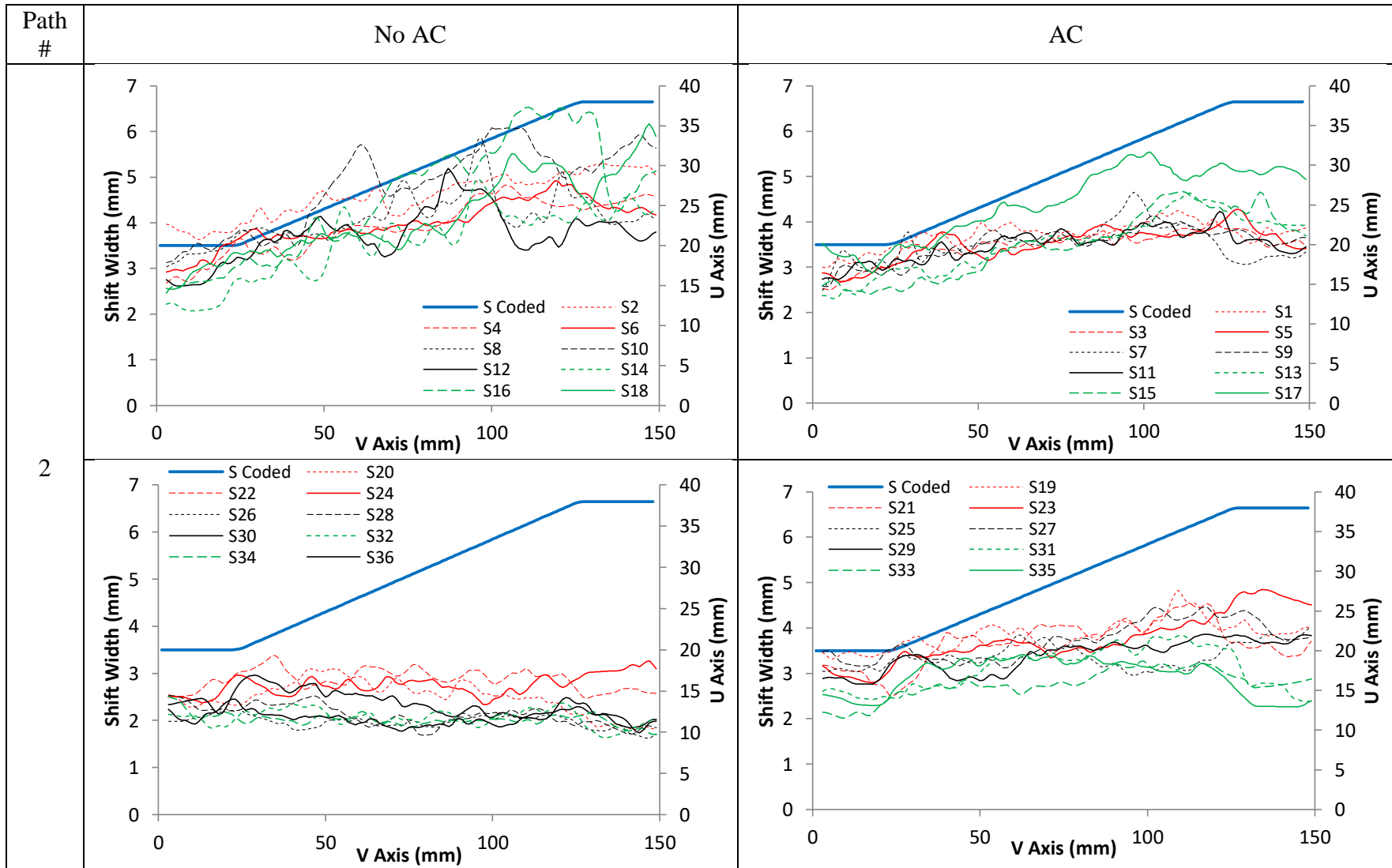


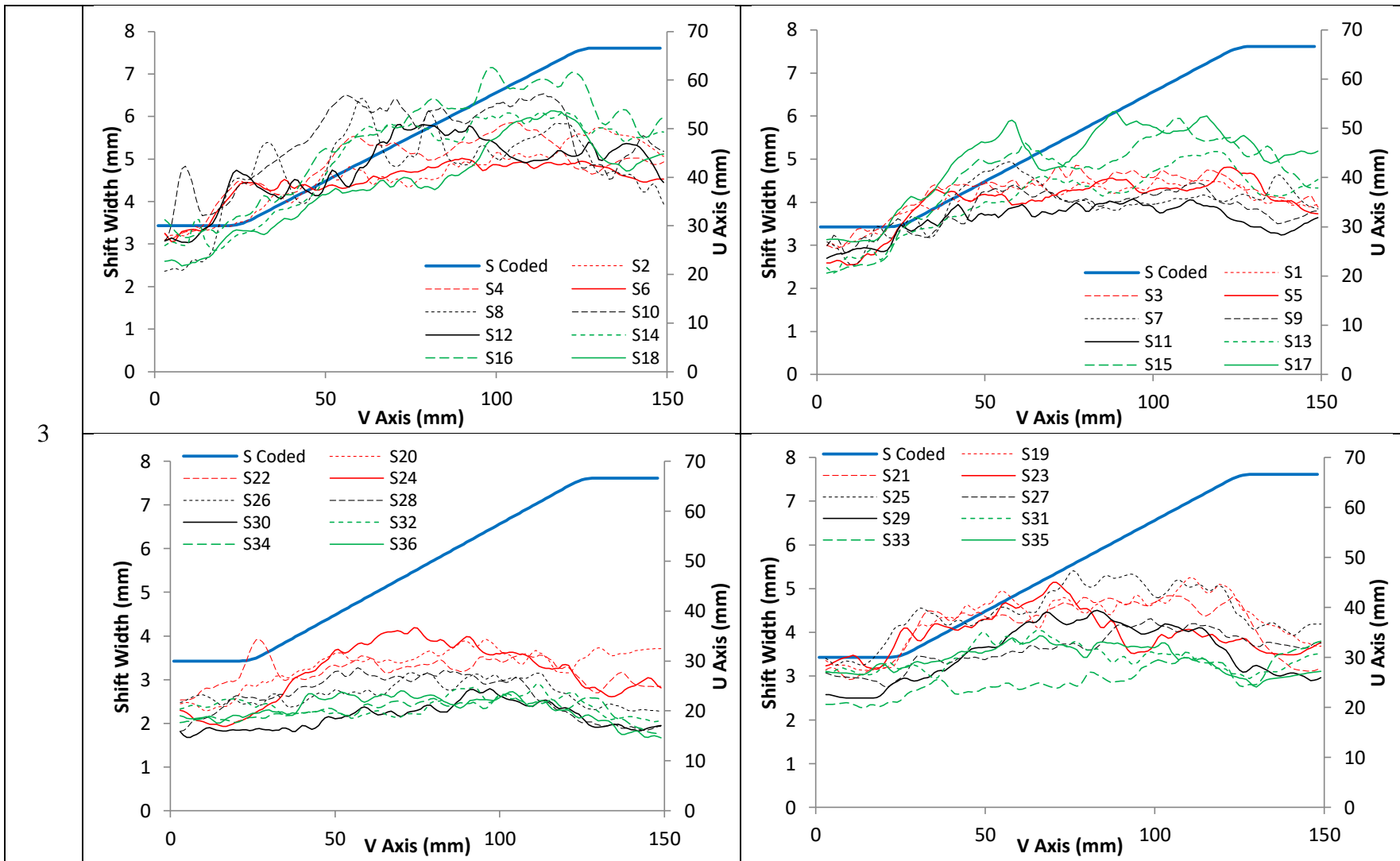


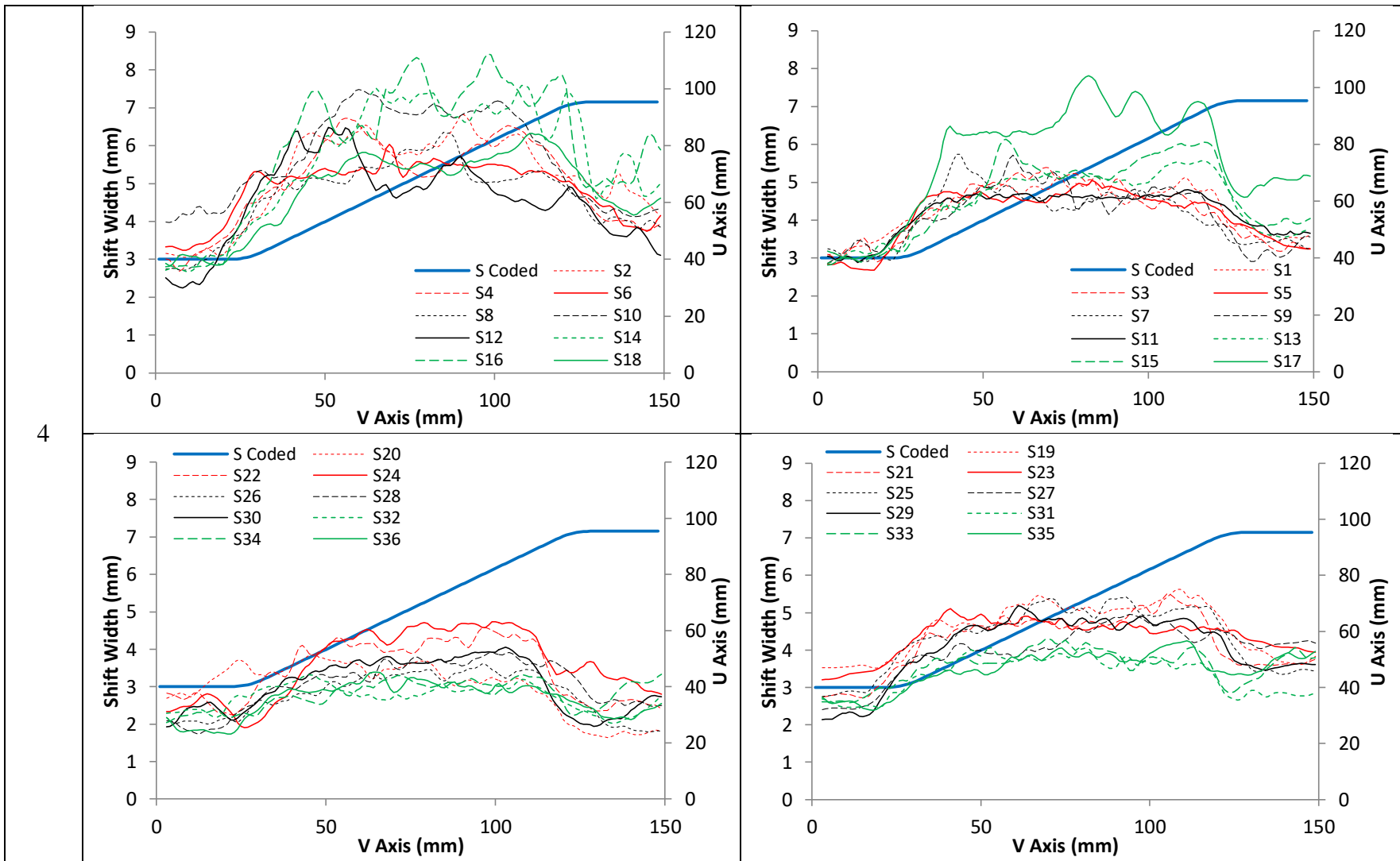


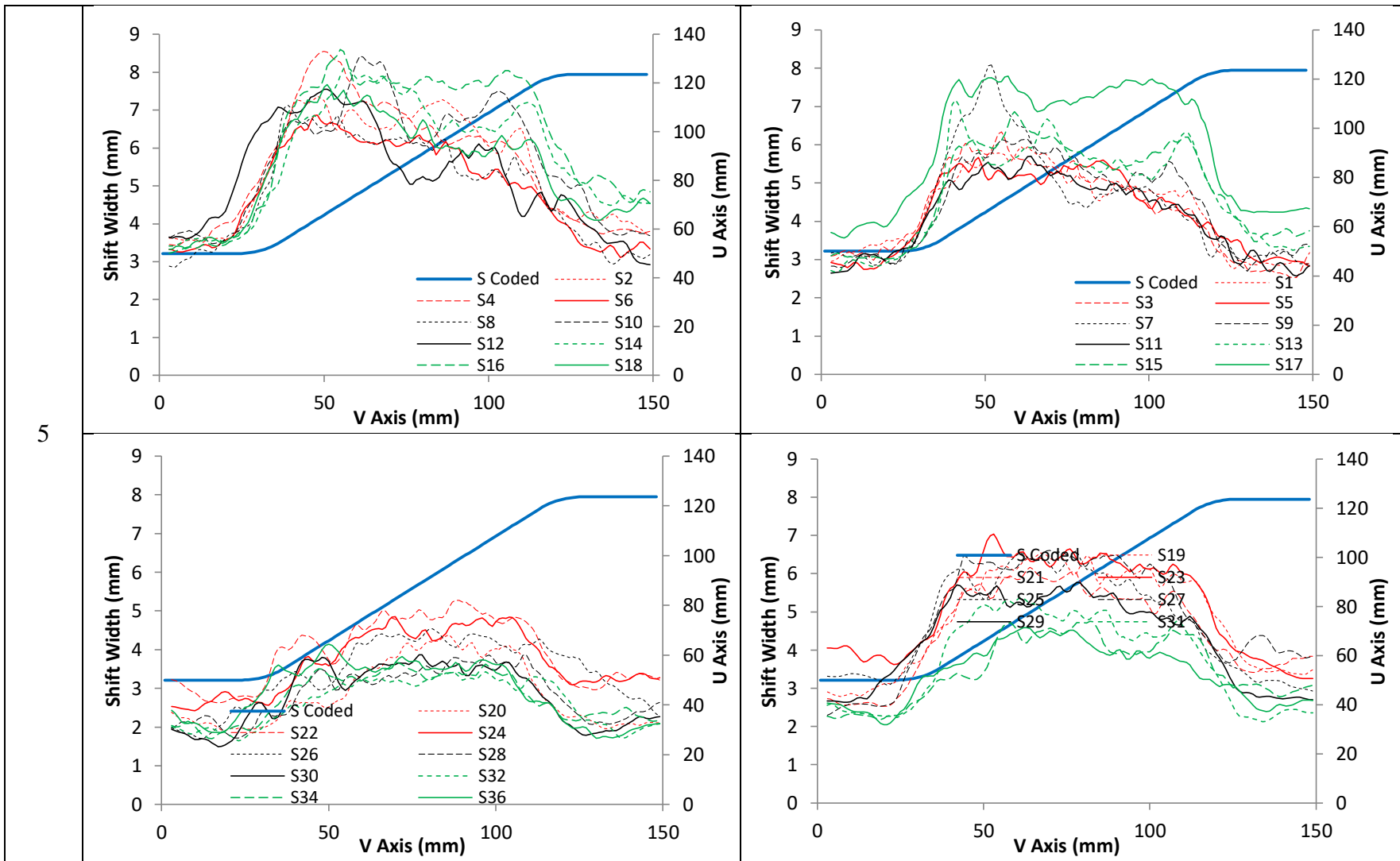
10.7 Shift Width Graphs

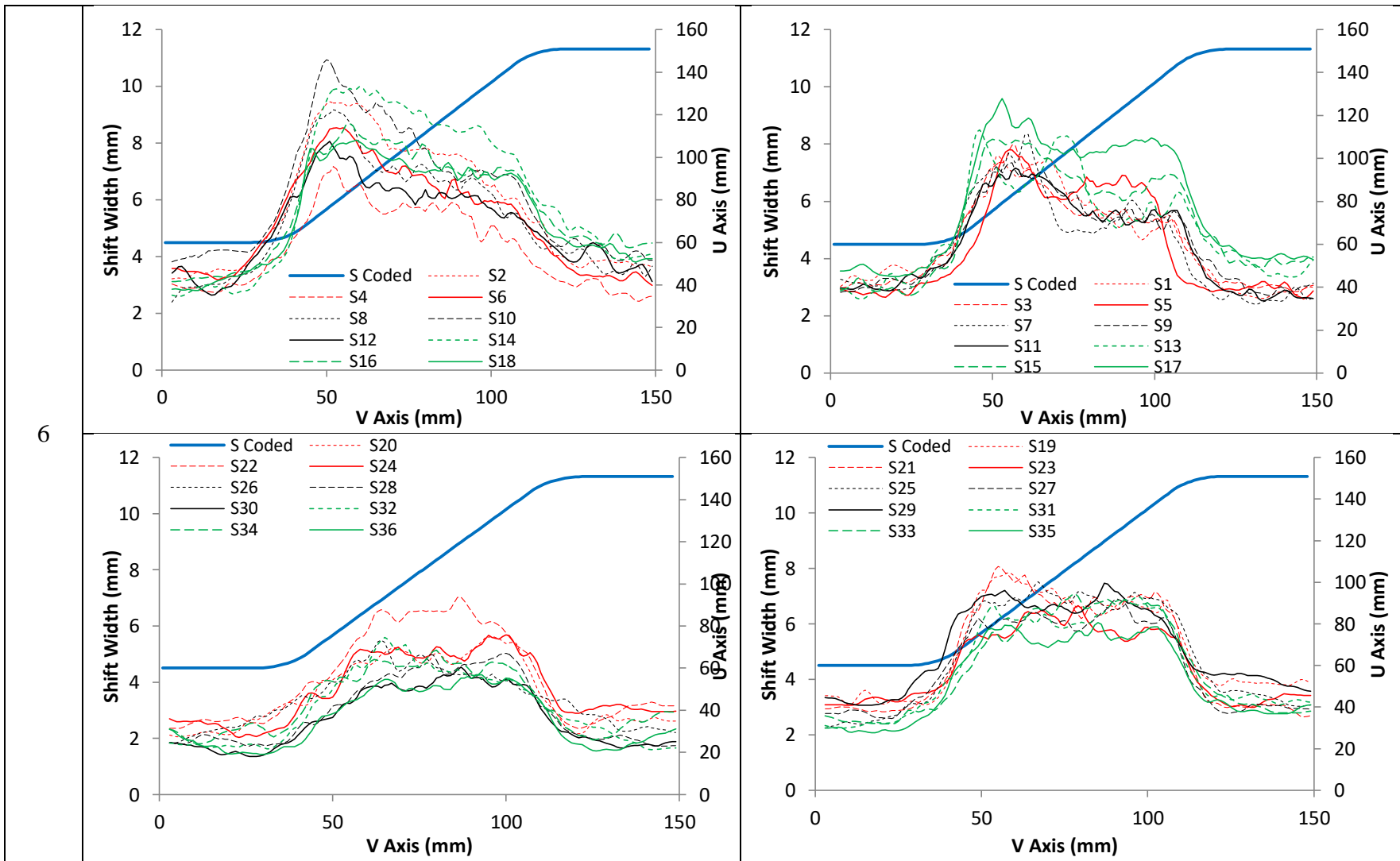
The following table displays additional shift width results for each path analyzed as a part of the positional fidelity portion of this study.

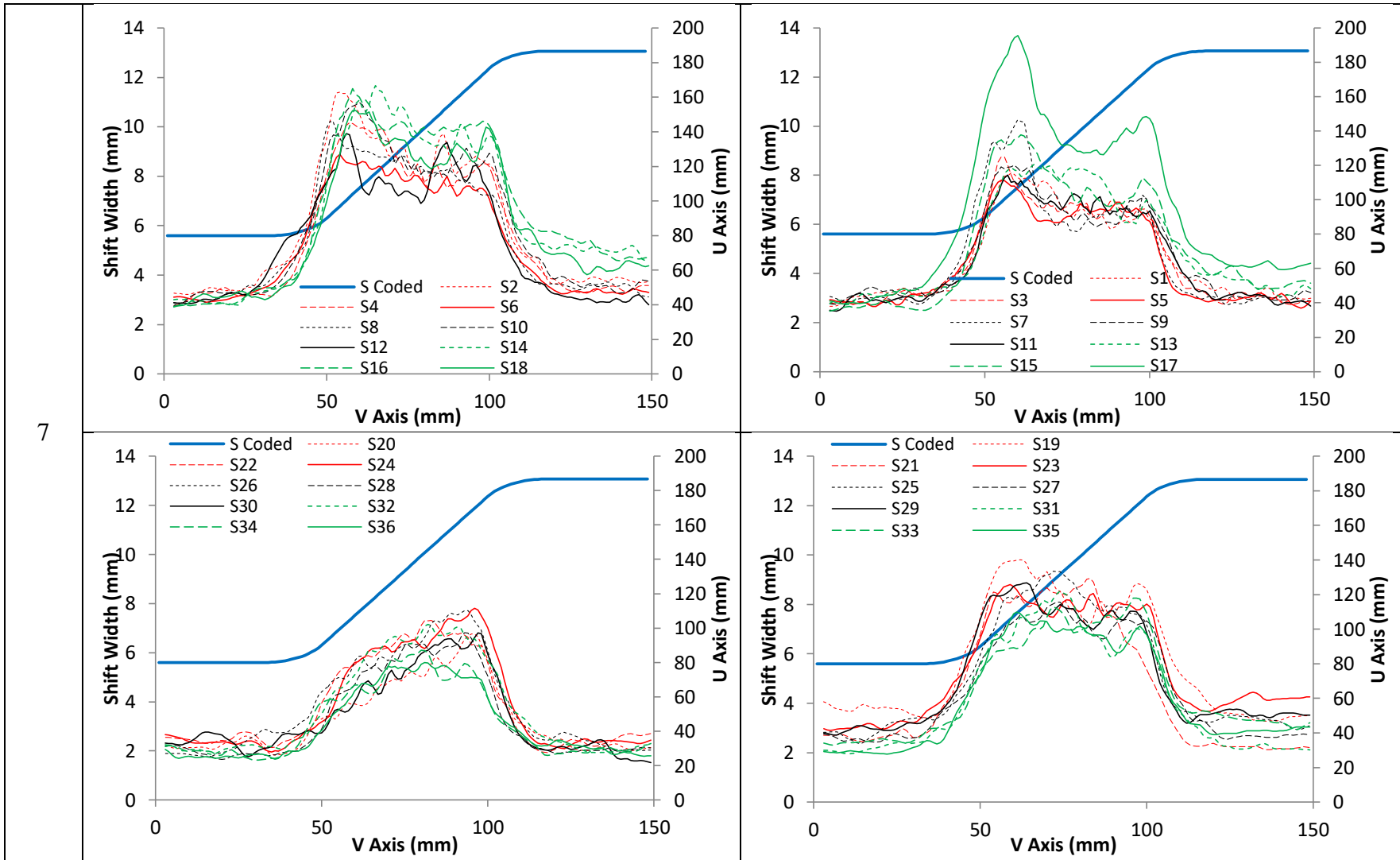


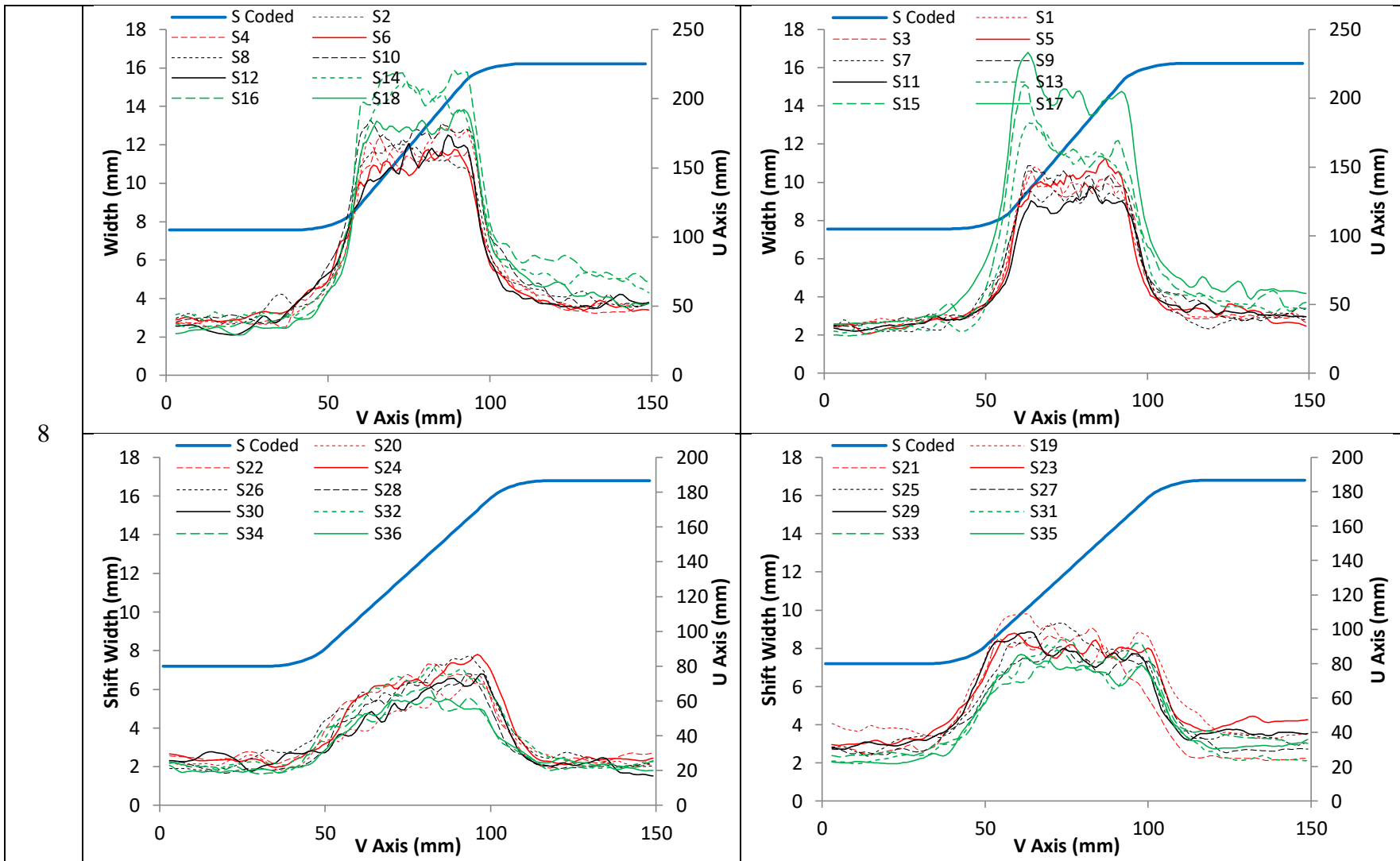






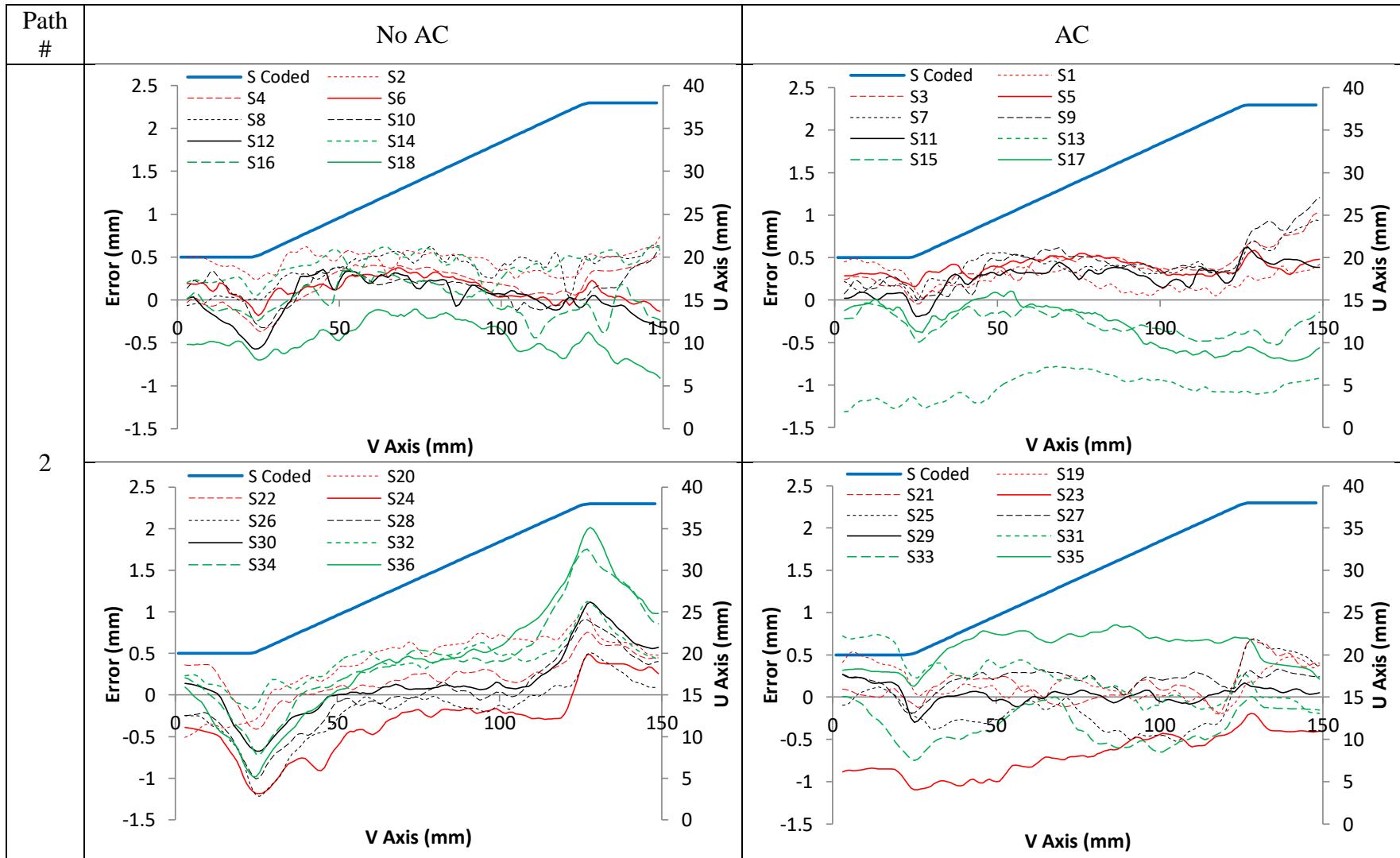


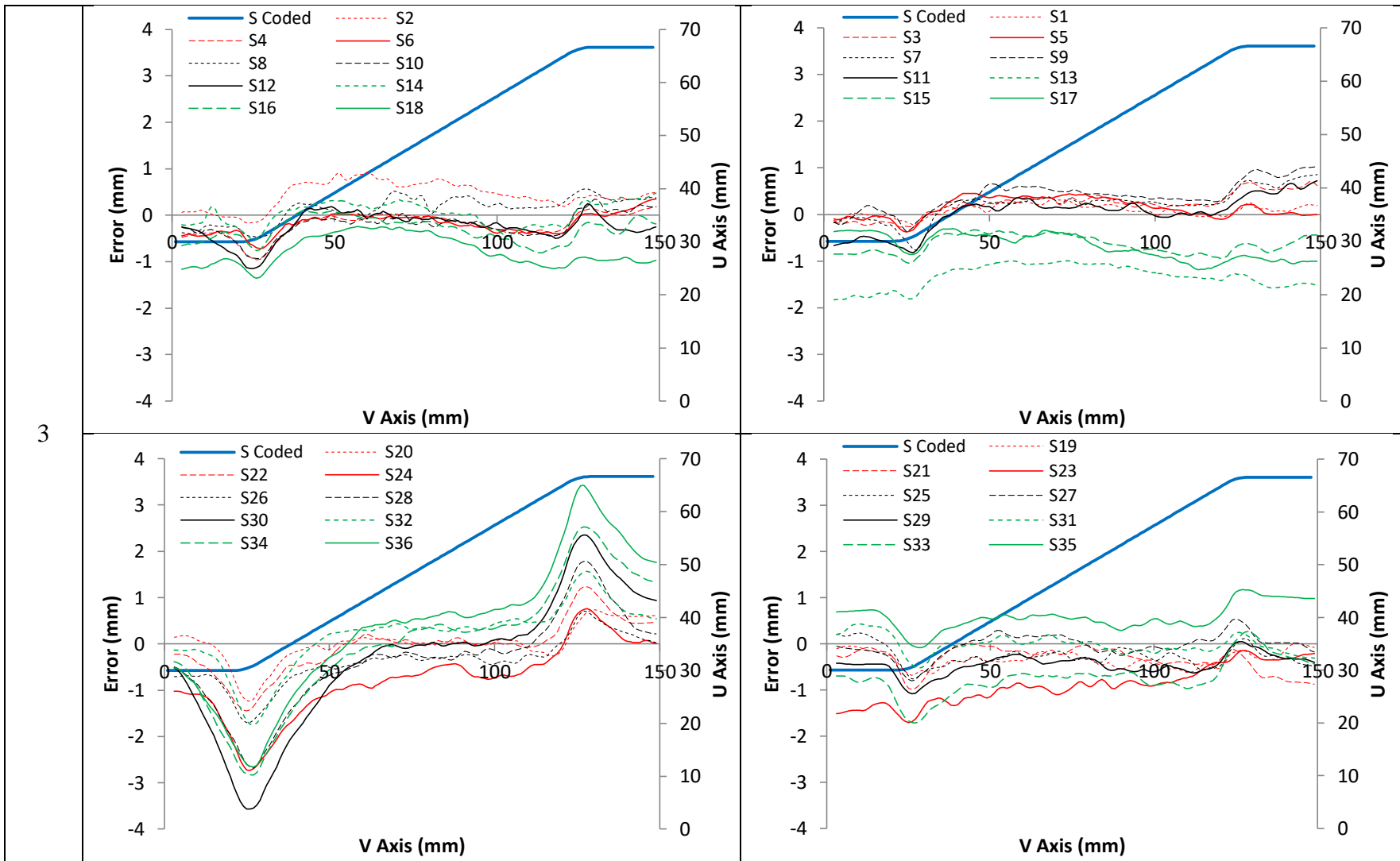


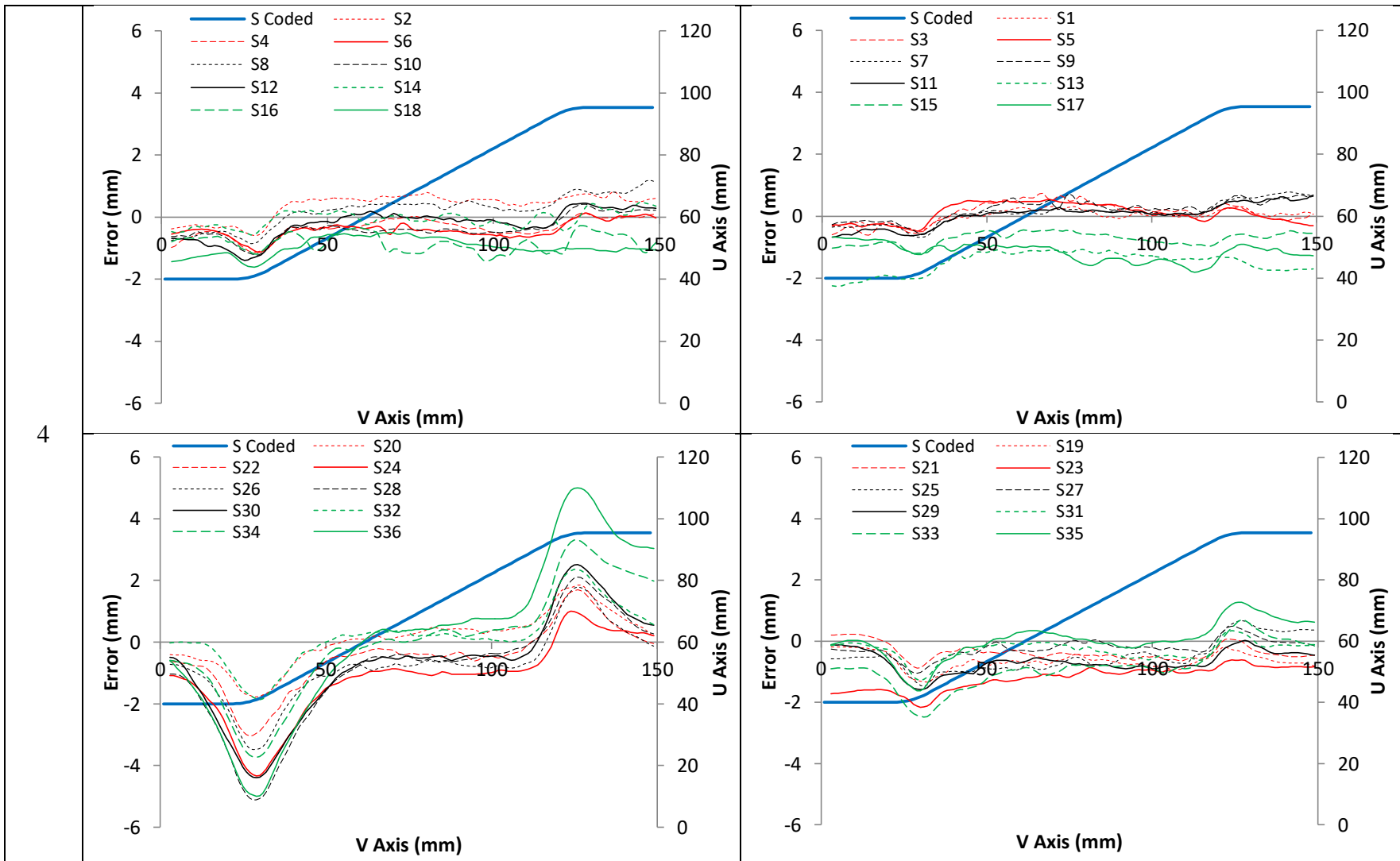


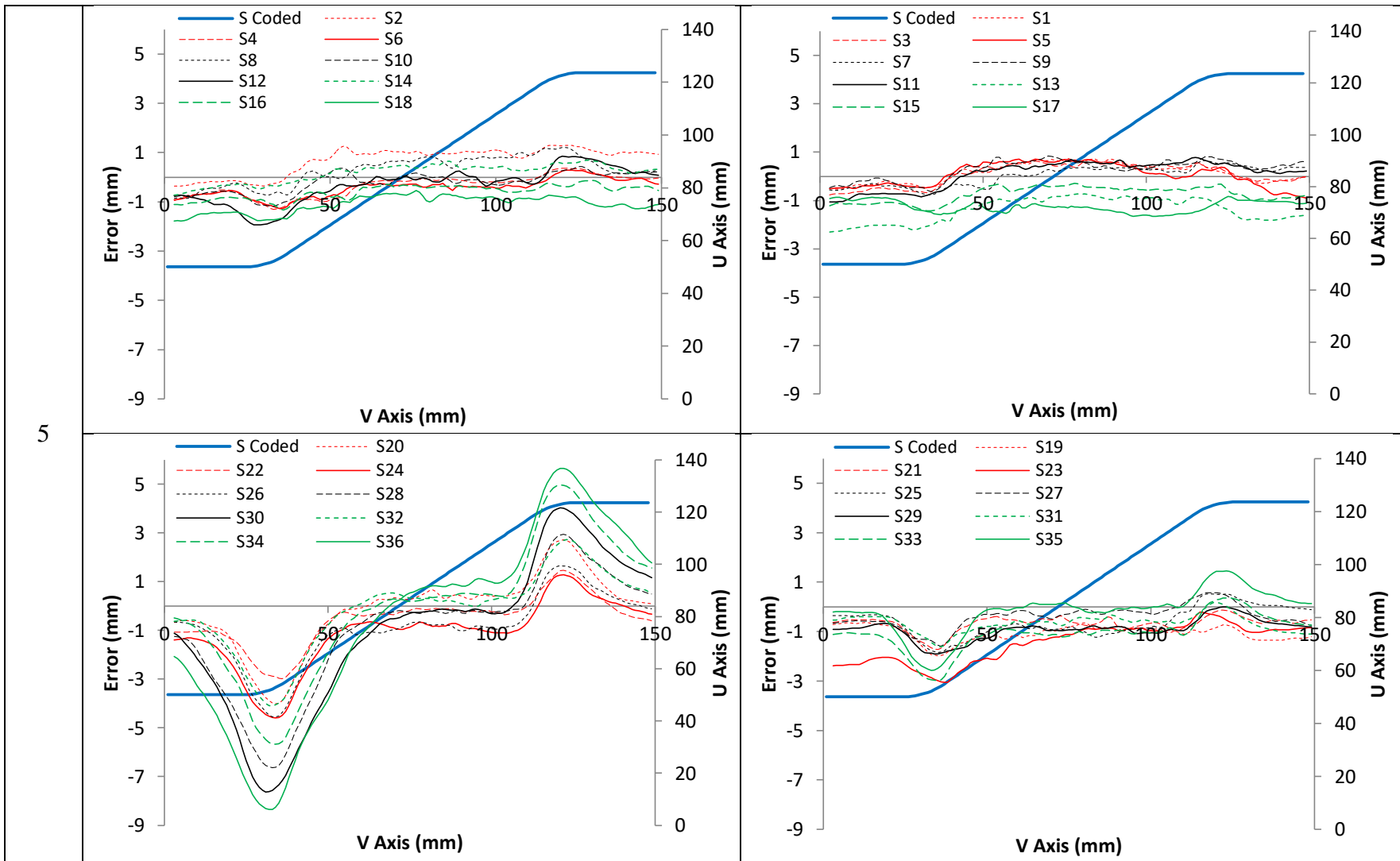
10.8 Error Graphs

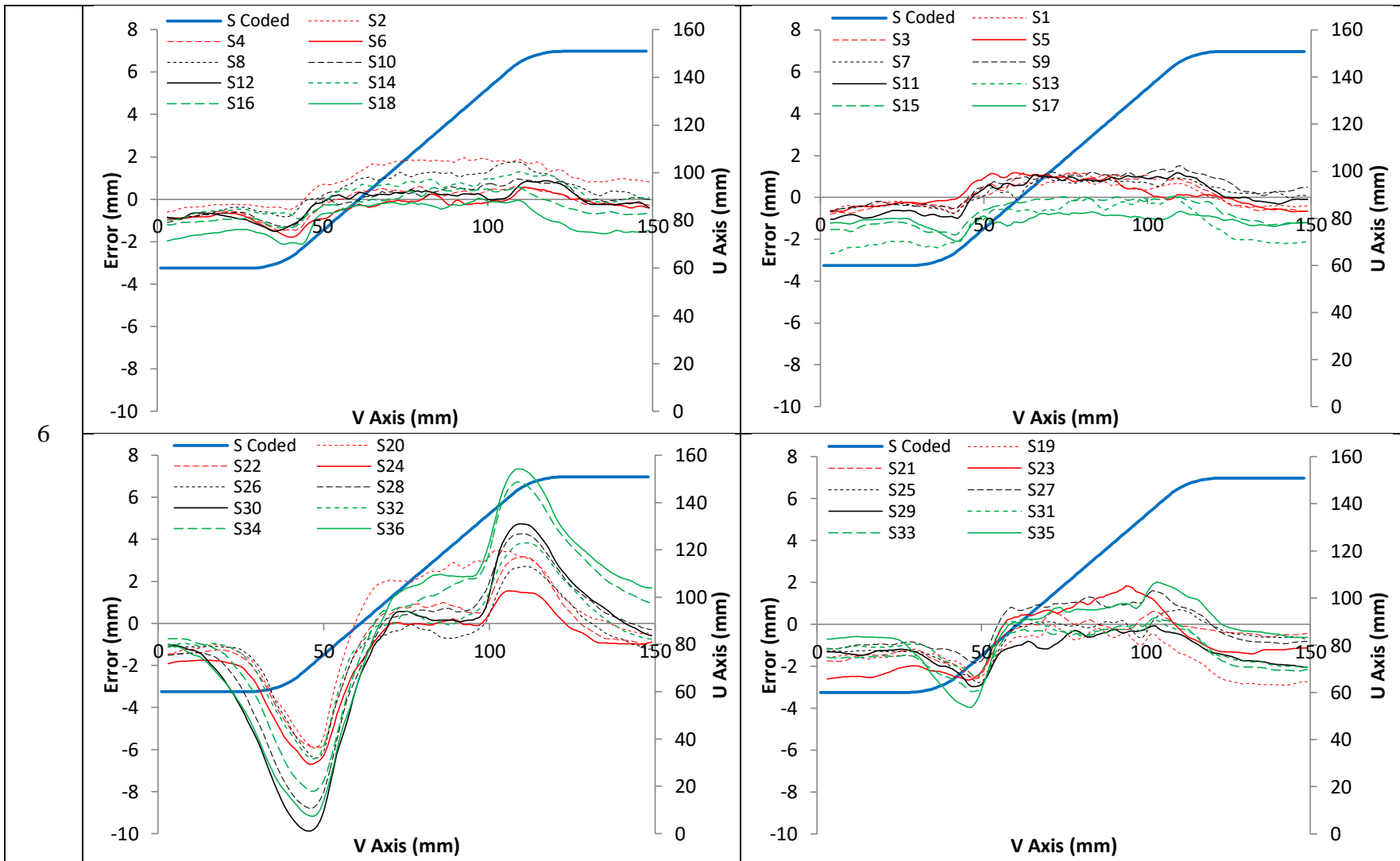
The following table displays additional error results for each path analyzed as a part of the positional fidelity portion of this study.











7

